# GROWTH AND CHARACTERIZATION OF Cu-O BASED SOLAR CELL

*By*

**MOHIT KUMAR**

**PHYS07201004005**

**INSTITUTE OF PHYSICS, BHUBANESWAR**

*A thesis submitted to the*

*Board of studies in physical sciences*

*In partial fulfilment of requirements*

*For the degree of*

**DOCTOR OF PHILOSOPHY**

*of*

**HOMI BHABHA NATIONAL INSTITUTE**

**September, 2016**

# HOMI BHABHA NATIONAL INSTITUTE

## Recommendations of the Viva Voce Board

As members of the Viva Voce Board, we certify that we have read the dissertation prepared by Mohit Kumar entitled “Growth and Characterization of Cu-O based Solar Cell” and recommend that it may be accepted as fulfilling the dissertation requirement for the Degree of Doctor of Philosophy.

**Date:**

**Chairman-**

**Date:**

**Convener-**

**Date:**

**Member1-**

**Date:**

**Member2-**

**Date:**

**Member3-**

Final approval and acceptance of this dissertation is contingent upon the candidate's submission of the final copies of the dissertation to HBNI.

I hereby certify that I have read this dissertation prepared under my direction and recommend that it may be accepted as fulfilling the dissertation requirement**.**

**Date:**

**Guide-**

**Place:**

# STATEMENT BY AUTHOR

This declaration has been submitted in partial fulfillment of requirement for an advanced degree at Homi Bhabha National Institute (HBNI) and is deposited in the Library to be made available to borrowers under rules of HBNI.

Brief quotation from this dissertation are allowable without special permission, provided that accurate acknowledgement of source is made. Requests for permission for extended quotation from the reproduction of this manuscript in whole or in part may be granted by the Competent Authority of HBNI when in his or her judgement the proposed use of the material is in the interests of scholarship. In all other instances, however, permission must be obtained from the author.

**MOHIT KUMAR**

# DECLARATION

I, hereby declare that the investigation presented in the thesis has been carried out by me. The work is original and has not been submitted earlier as a whole or in part for a degree / diploma at this or any other Institution / University.

**Mohit Kumar**

***To my wife and parents***

# Acknowledgements

The journey of Ph. D. life and all the achievements that I have accomplished during my stay at Institute of Physics, Bhubaneswar won’t be possible without the support, help, and guidance of my advisor, Prof. T. Som. I take this opportunity to express my sincere and deep gratitude to him, for his constant encouragement and enormous energy towards my cause. His innovative ways of looking into the problem with an admixture of professionalism and perfectionism will remain as assets for the rest of my life. I sincerely thank him and his family for their care and hospitality which never let me feel to be away from home during my stay in IOP. It has been truly a life time privilege for me to work under his guidance.

I would like to thank Prof. P. Ayub, TIFR, Mumbai, Dr. B. Satpati, SINP, Kolkata, Dr. P. K. Sahoo, NISER, Bhubaneswar, Prof. A. Kanjilal, SNU, Greater Noida, and Dr. S. Mookerjee, IUAC, New Delhi, for extending their facilities and precious time towards my research and relevant discussion. My special thanks to Prof. S. Kar, NISER, Bhubaneswar for his time to discuss with me at various points of time.

I would also like to acknowledge my senior group members Dr. S. K. Garg, Dr. T. Basu, Dr. D. P. Datta, and Dr. S. P. Patel and for our valuable discussion and providing me a chance to work with them. My special thanks go to Dr. S. Chatterjee, Dr. S. Nandy, Dr. S. K. Hazra, and Mr. S. A. Mollick for valuable discussion and their helps during various stages of my research life. I would like to thank my other lab mates,  Mr. Jyoti Ranjan Mohanty, Mr. Ranveer Singh, and Mr. Mahesh Saini for their constant helps in every aspects of my life. I must acknowledge Mr. Lingraj for his dedicated service, given to the SUNAG lab and keeping it always clean for the cause of maintaining a high standard.

I thank all my teachers who taught me during the pre-doctoral course work and all the experimental condensed matter group faculties of IOP, Bhubaneswar for their generous support. I also thank to scientific staff of IOP, especially Mr. S. K. Choudhury, Mr. Arun Dash, and Dr. S. N. Sarangi for making themselves available wherever their expertise was required for the lab. In fact, I have learnt a lot about various experimental systems from Mr. S. K. Choudhury.

I am grateful to the former directors: Prof. A.M. Jayannavar, Prof. A.M. Srivastava, and the present director, Prof. S. Panda, Dean HBNI at IOP, Prof. Pankaj Agrawal, members of my Doctoral committee: Prof. A. M. Jayannavar, Prof. S. Varma, and Prof. S. K. Patra and other members of the Institute (academic and non-academic) for their timely help, cooperation, and support whenever I needed the same.

A special acknowledgement goes to my friends who have been invaluable to the success of my research and to my happiness during these Ph. D. days. In particular: my batch mates Shailesh, Shalik, and Himanshu are among the best friends that I can ever have. Thanks to all the seniors and junior scholars of IOP for their direct or indirect assistance on many occasions during my stay at IOP.

Most importantly, I have always been fortunate in being able to count on continuous support from my parents, brother, relatives, and my wife, Priti. They have always believed in me and their love and affection has kept me going during all these years. In particular, I am indebted to my parents for providing me with their love, education, and it is because of them that I was able to become the person I am today.

Date:

Place: Mohit Kumar

# List of Publications

## Published In Journal

1. *Effect of grain-boundaries on electrical properties of *n*-ZnO:Al/*p*-Si heterojunction diodes by **Mohit Kumar**, Aloke Kanjilal, and Tapobrata Som: AIP Advances 3 (2013) 092126.

2. *Role of metallic-like conductivity in unusual temperature-dependent transport in *n*-ZnO:Al/*p*-Si heterojunction diode by **Mohit Kumar**, S. K. Hazra, and T. Som: Journal of Physics D: Applied Physics, 48 (2015) 455301.

3. *Ultra-violet absorption induced modifications in bulk and nanoscale electrical transport properties of Al-doped ZnO thin films by **Mohit Kumar**, Tanmoy Basu, and Tapobrata Som: Journal of Applied Physics 118 (2015) 055102.

4. *Structural defect-dependent resistive switching in Cu-O/Si studied by Kelvin probe force microscopy and conductive atomic force microscopy by **Mohit Kumar** and Tapobrata Som: Nanotechnology 26 (2015) 345702.

5. *Local probe microscopic studies on Al-doped ZnO: Pseudoferroelectricity and band bending at grain boundaries by **Mohit Kumar**, Tanmoy Basu, and Tapobrata Som: Journal of Applied Physics 119 (2016) 014307.

6. Thickness-dependent blue shift in the excitonic peak of conformally grown ZnO:Al on ion-beam fabricated self-organized Si ripples by Tanmoy Basu, **Mohit Kumar**, S. Nandy, B. Satpati, C. P. Saini, A. Kanjilal and T. Som: Journal of Applied Physics 118 (2015) 104903.

7. Surface modified Al doped ZnO hydrogen sensor-temperature dependent dual sensing response by D. Gupta, D. Dutta, **Mohit Kumar**, P.B. Barman, T. Som, and S.K. Hazra: Journal of Applied Physics 118 (2015) 164501.

8. Tunable antireflection from conformal Al-doped ZnO films on nanofaceted Si templates by T Basu, **Mohit Kumar**, P K Sahoo, A Kanjilal and T Som: Nanoscale Research Letters 9, 192 (2014).

9. Thickness-controlled photoresponsivity of ZnO:Al/Si heterostructures: Role of junction barrier height by T. Basu, **Mohit Kumar**, and Tapobrata Som: Materials Letters 135 (2014) 188.

10. Improved broadband antireflection in Schottky-like junction of conformal Al-doped ZnO layer on chemically textured Si surfaces by C. P. Saini, A. Barman, **Mohit Kumar**, P. K. Sahoo, T. Som, and A. Kanjilal: Applied Physics Letters 105 (2014) 123901.

11. Efficient Field Emission from Vertically Aligned $Cu_2O_{1-\delta}$ (111) Nanostructure Influenced by Oxygen Vacancy by S. Nandy, R. Thapa, **Mohit Kumar**, T. Som, N. Bundaleski, O. M. N. D. Teodoro, R. Martins, E. Fortunato: Advanced Functional Materials. 25 (2015) 947.

12. Influence of surface topography on the field emission of nanostructured copper oxide thin films grown by oblique incidence deposition by S. Chatterjee, **Mohit Kumar**, A. pal, I. Thakur, T. Som: Journal of Materials Chemistry C 3 (2015) 6389.

13. Cold cathode emission studies on topographically modified few layer and single layer $MoS_2$ films, A. P. S. Gaur, S. Sahoo, F. Mendoza, A. M. Rivera, **Mohit Kumar**, Saroj P. Dash, Gerardo Morell, and Ram S. Katiyar, Applied Physics Letters 108, 043103 (2016).

14. An oblique angle radio frequency sputtering method to fabricate nanoporous hydrophobic $TiO_2$ film by S. Chatterjee, **Mohit Kumar**, S. Gohil, T. Som: Thin Solid Films 568 (2014) 81.

15. Semi-insulating behaviour of self-assembled tin(IV) corrole nanospheres by W. Sinha, **Mohit Kumar**, A. Garai, C. S. Purohit, T. Som, and S. Kar: Dalton Transactions 43 **(**2014) 12564.

16. Synthesis, electron transport, and charge storage properties of fullerene–zinc porphyrin hybrid nanodiscs by A. Garai, **Mohit Kumar**, W. Sinha, S. Chatterjee, C. S. Purohit, T. Som, S. Kar: RSC Advances 4 (2014) 64127.

17. Tailoring room temperature photoluminescence of antireflective silicon nanofacets by T. Basu, **Mohit Kumar**, A. Kanjilal, J. Ghatak, P. K. Sahoo, and T. Som: Journal of Applied Physics 116 (2014) 114309.

18. A low temperature hydrogen sensor based on palladium nanoparticles by D. Gupta, D. Dutta, **Mohit Kumar**, P. B. Barman, C. K. Sarkar, S. Basu, S. K. Hazra: Sensors and Actuators B 196 (2014) 222.

**Communicated**

1 *****Field-induced doping-mediated tunability in work function of Al-doped ZnO: Kelvin probe force microscopy and first-principle theory by **Mohit Kumar**, S. Mookerjee, and T. Som: Nanotechnology.

2 *Microscopic evidence of inhomogeneous work function at the surface of pseudoferroelectric Al-doped ZnO thin films by **Mohit Kumar**, T. Basu, A. Kanjilal, and T. Som Journal of Physics D: Applied Physics.

**To be communicated**

1. *Tunable optoelectronic properties of pulsed dc sputter deposited ZnO:Al thin films at room temperature: Role of growth angle by **Mohit Kumar**, R Singh, and T. Som: Journal of Applied Physics.

2. *Intrinsic inhomogeneous barrier height at the *n*-$TiO_2$/*p*-Si hole blocking junction by **Mohit Kumar**, R Singh, M. Saini, and T. Som: Applied Surface Science.

3. *Growth angle-dependent transitions on Mo-films: From highly reflecting to anti-reflecting and hydrophilic to hydrophobic surfaces by **Mohit Kumar** and T. Som: Journal of Applied Physics.

4. *An efficient hole blocking Cu-O based solar cell by **Mohit Kumar**, R. Singh, M. Saini, and T. Som: Applied Physics Letters.

(*) indicates papers on which this thesis is based.

# Synopsis

Energy is one of the most fundamental needs in our daily life. In fact, energy is a necessary requirement to do work, light our cities, power our vehicles, control temperature at our homes and offices, cook our food, play our music, and power machineries in factories [1]. Thus, fulfilling the demand for energy becomes a more critical challenge for the world's population as it grows rapidly with more industrialization. Therefore, a competitive, sustainable, and secured energy supply is an even more demanding issue [2].

Presently, different sources of energy such as coal, petroleum, wind, thermal, and solar are naturally found on the earth [3]. Out of these, the fossil fuel-based energy sources faces a number of challenges including their limited resources, rising prices, security of supply, and pollution by carbon dioxide emission, etc. [4]. Carbon dioxide causes the greenhouse effect, which increases the global temperature by reducing the outward radiation and causing the anthropogenic climate change [4]. With the current rate of fossil fuel consumption, it is expected that the concentration of $CO_2$ will reach the critical level of 750 ppm by 2050 [5]. Since, there is no natural decomposition of $CO_2$ in the atmosphere, it will take 500 to 2000 years to overcome the environmental effect of this level of pollution.

Alternative potential energy sources can be the solar, geothermal, hydroelectric, and wind powers because these resources do not deplete as opposed to fossil fuels [6]. Currently, the total global energy consumption is estimated to be around 13.5 TW and will increase up to 27 TW by the year 2050 [2]. Thus, out of these, only the solar energy has a huge potential capacity of 1,20,000 TW, which is around 10,000 times higher than the current annual global energy consumption [7]. This means one hour of sun light on earth can provide us our annual energy used. In other words, at 10% efficiency in solar cells, only 0.1% of the earth's surface is sufficient to satisfy our present need of energy [7]. But getting a hold on this huge energy reservoir remains an enormous challenge. In fact, in order to meet a sizeable part of the world's energy demand, solar energy conversion with photovoltaics (PV) will have to reach the terawatt (TW) scale. In addition, price reductions are still required for solar energy to be cost competitive with respect to the conventional energy sources used in the majority of the world [6,7].

The requirement of higher efficiency at a lower cost can be fulfilled by designing the dye-sensitized or metal oxide (MO) semiconductor-based solar cells. Out of these, the dye-sensitized solar cells use an organic dye, coating a porous electrode, and metal-oxide with high surface area to absorb more light. Presently, the maximum achieved efficiency for dye-sensitized solar cells is around 11%, however, the use of a liquid electrolyte in the cells is a source of reliability issue [8]. On the other hand, most of the MOs are found to be abundant, non-toxic, and chemically stable in nature which allows us to design low cost solar cell.

In order to get a desired efficacy, different combinations of MOs have been tested. For instance, $TiO_2/Cu_2O$, $rGO/TiO_2$, $ITO/Cu_2O$, $FTO/Cu_2O$, ZnO:Al(AZO)/$Cu_2O$, and $Ga_2O_3/Cu_2O$ [9]. Out of many oxides, copper oxide (Cu-O) based solar cells, in the form of AZO/$TiO_2$/Cu-O heterostructures, have not only attracted the researchers' attention because of its band gap, which is close to the optimal band gap (~1 eV) under AM1.5 radiation spectrum but also its high absorption coefficient and large minority carrier diffusion length. Theoretically, the efficiency of copper oxide-based solar cells should be around 20%, however, the experimentally achieved efficiency is still less than 3% [10]. This poor cell performance is not only attributed to the less understanding on the charge transport process with in the used layers but also on the interface quality at the junctions [10,11]. In fact, an excellent control on interfaces in thin-film solar cells has been proved to be of prime importance to achieve high-efficiency devices, albeit it is still lacking in case of Cu-O based solar cells. Thus, a systematic experimentation on the study of charge transport as well as the formation of highly quality interfaces are needed to achieve a desired efficiency of a Cu-O based solar cell.

The topmost layer (e.g. AZO) works as a transparent conductive electrode for a copper oxide-based solar cell and is considered to be the most important part of the same. In fact, this electrode collects the photo-induced charge carriers from the underneath Cu-O layer and transfers it into the metal electrode. Thus, in order to improve the efficiency of such a cell, a smooth charge transport should take place through the AZO layer. In addition, it is mentioned here that a higher temperature (>300° C) is required to achieve a better quality thin film of AZO, although at higher temperatures an interfacial diffusion takes place which in turn reduces the efficiency of the same [12]. Thus, it is exigent to first optimize the room temperature (RT) growth process of the used layers and then explore their possible use to design full solar cell.

In this thesis, we have used pulsed dc/rf magnetron sputtering technique for the growth of different thin films towards constructing a copper oxide-based solar cell. To analyse the morphology, microstructure, composition, and crystallinity of these layers, surface profilometry, atomic force microscopy (AFM), scanning electron microscopy (SEM), transmission electron microscopy (TEM), energy dispersive x-ray spectrometry (EDS), x-ray photoelectron spectroscopy (XPS), and x-ray diffraction (XRD) were used, respectively. In addition, the optical properties of the used layers are investigated using ultra-violet-visible (UV-Vis) spectroscopy. Moreover, the optoelectronic properties of different thin films used in the heterojunction solar cell, are studied by bulk *I-V*, *C-V*, and photoresponsivity measurements. Further, various AFM-based local probe microscopic techniques such as conductive atomic force microscopy (cAFM), electrostatic force microscopy (EFM), Kelvin probe force microscopy (KPFM), and piezoresponse force microscopy (PFM) are used in order to understand the nanoscale (local) charge transport properties in different layers.

The thesis is organized in eight chapters. The first chapter provides a brief introduction on the topic and the second chapter describes the experimental techniques used in this thesis. In chapter 3, the experimental results are presented where we describe the growth of Al-doped ZnO thin films at RT and have studied the role of grain boundaries in the charge transport. In particular, we demonstrate the RT diode characteristics of ZnO:Al (AZO)/Si heterostructures by current-voltage measurements where we show that with increasing AZO film thickness, a systematic reduction in the turn-on potential (from 3.16 to 1.80 V) and the film stress take place. Complementary capacitance-voltage (*C*-*V*) measurements reveal a decreasing trend in the barrier height at the junction with the increasing AZO film thickness. In addition, gradual decrease in the resistivity takes place with increasing AZO film thickness. Above observations are explained in the framework of AZO thickness-dependent variation in grain size and in turn trap (defect) density at the grain boundaries, influencing carrier transport across the adjacent grains.

Following this, we have tried to reduce the defect density by thermal annealing and studied the role of the same in the charge transport process. In fact, we have investigated the effect of temperature on the transport mechanism of an *n*-AZO/*p*-Si heterojunction diode where an unusual variation in the *I*-*V* characteristics (with temperature) is observed. In particular, temperature-dependent transition from a direct tunnelling to the thermionic emission is observed in the *I*-*V* characteristics. In order to explain this behaviour, temperature-dependent resistivity of AZO film, deposited on soda-lime glass (SLG) substrate, is also investigated. The measured resistivity reveals a semiconducting nature at low temperatures (up to 343 K), which subsequently transforms into a metallic-like behavior at higher temperatures (>343K). In addition, we have made use of the optical absorption spectroscopy before and after the thermal annealing, which shows a reduction in the band gap of the AZO layer. The experimental results are explained in terms of annihilation of oxygen vacancies (during annealing in air) in the AZO thin films, present mainly at the grain boundaries (GBs). As a matter of fact, these vacancies at GBs play an important role in charge transport.

These observations indicate that, in order to make use of AZO thin films for solar cell applications, an in-depth understanding on the trap states at the grain boundaries as well as the role of the same in charge transport are needed. To address this issue, we have employed combined KPFM and cAFM measurements at RT. For instance, the donor concentration is mapped by KPFM in which a variation in the carrier density is observed. Since the carrier density as well as UV light absorption are known to play a significant role in controlling the local charge transport, we have measured the nanoscale electrical conductivity as well by cAFM before and after UV-exposure. An enhancement in the local conductivity, after UV-exposure, is observed which is explained in terms of experimentally measured bulk persistent photoconductivity. Further, UV-induced enhancement in the spectral response (during photoresponsivity measurements) of an *n*-AZO/*p*-Si solar cell is observed, manifesting UV absorption in the AZO overlayer should not cause a loss in the efficiency of a solar cell which is in contrary to the common belief.

Up to this point, it has been revealed that defects (mostly in the form of oxygen vacancies) at the GBs play a significant role in the charge transport process in AZO thin films. In fact, a potential barrier is formed at the GBs which is expected to govern the charge transport across the same. Thus, in order to control the charge transport in AZO, the true nature of the potential barrier at GBs should be understood. In doing so, in Chapter 4, we have undertaken the study of nanoscale charge transport properties of an AZO layer by using cAFM, EFM, KPFM, and PFM. Here we make use of these local probe techniques to show the novel pseudoferroelectric behaviour in AZO thin films at RT and how the barrier forms at the GBs due to defects and it takes part in the charge conduction process from one grain to the next. We also show how the barrier height is affected by the orientation of polarization. In fact, we show the roles of defects and polarization in the local band bending of AZO thin films at the grain boundaries.

In addition, we show the role of polarization on the work function at the surface of AZO thin films. In particular, using KPFM studies, the work function of an AZO film is mapped which is found to be spatially inhomogeneous. Further, the effect of polarization on the charge transport process is also confirmed by cAFM. As a matter of fact, the presence of polarization in AZO films opens up a new avenue to control the charge transport in the same. In particular, using KPFM and contact-mode (cont-mode) AFM, we demonstrate that work function of an AZO film can be tuned by inducing charge carriers through an applied electric field. For instance, we show that by applying a positive or negative bias on the top of an AZO film, electrons or holes can be induced on the surface, which in turn decrease or increase the work function of the same, respectively. Further to this, the role of electric field-induced doping in nanoscale charge transport is also demonstrated by performing local *I-V* measurements using cAFM. This study is not only important to design an Ohmic contact for different optoelectronic devices but also to address a fundamental aspect of physics.

As mentioned earlier, Cu-O is the main absorbing layer and thus, in Chapter 5, we have undertaken the studies on the growth and charge transport across the same. It is observed that the structural defects in a Cu-O film can be reduced by growing the film at an oblique angle. Following this, we have shown the importance of structural defects on the charge transport properties of rf magnetron sputter deposited Cu-O thin films. In doing so, XRD is used to investigate the crystalline nature and evaluate the dislocation density of the films, while KPFM is used to quantify the carrier density and cAFM studies demonstrate the crystallinity-dependent presence and absence of bipolar resistive switching. Further, we present the experimental evidence on nanoscale filament formation from cAFM images and discuss the mechanism of the observed switching behavior at nanoscale in detail. These studies help us to optimize the growth of high quality Cu-O films at RT, showing a smooth charge transport property, which is exigent for its use in a solar cell. These results also corroborate well with the high quality of AZO top electrode used in the present cell, where we see the absence of FE property in the same.

Under the present architecture, the sandwich layer between Cu-O and AZO is $TiO_2$ which is used to block the positive charges (e.g. holes) and thus, it makes an interface with the Cu-O as well as the AZO layer. As mentioned above, the interface of a MO-based solar cell plays an important role in determining the efficiency of a solar cell. Thus, in Chapter 6, we have optimized the growth of the $TiO_2$ buffer layer and investigated the variation in the nanoscale potential at its surface using KPFM. In addition, the charge transport across the $n$-$TiO_2$/$p$-Si heterojunction has been studied using temperature-dependent $I$-$V$ characteristics where they show a non-ideal behaviour. Moreover, it is observed that the barrier height decreases with increasing temperature, while the ideality factor increases, suggesting a strong variation in the barrier height. This behaviour corroborates well with the variation in the work function, measured by KPFM. Following this, we have also extended the hole blocking nature of the $TiO_2$ layer by depositing it on a Cu-O layer.

The bottom electrode for the presently studied cell configuration is a molybdenum thin film. For a better efficiency, this electrode should have high optical reflectivity and charge collection efficiency. Thus, in Chapter 7, first we have optimized the growth of Mo thin films at various angles and studied there structural, electrical, and optical properties. It is observed that the resistivity increases with the increasing growth angle, and thus, the film deposited under normal incidence shows the lowest resistivity (~$10^{-6}$ Ω-cm) and highest reflectivity (~65%), which is considered to be the optimised ones for the present architecture of the Cu-O based cell. Finally, based on our experimental findings on individual layers, we have constructed a full solar cell and demonstrated that the efficiency of a copper oxide-based solar cell can be increased up to 5.2%.

In chapter 8, we provide a summary of the present thesis work, which deals with the growth and characterization of heterostructures towards constructing a copper oxide-based solar cell. In particular, we have studied the bulk as well as nanoscale charge transport properties across the used layers. For the optimization of growth, thin films have been deposited using a large angular window (0°-80°). Based on our experimental findings on individual layers, we have optimized the growth conditions at RT and thicknesses of different layers, viz. Mo, Cu-O, $TiO_2$, and ZnO:Al. Following the same, structural, morphological, microstructural, compositional, and electrical properties of all these layers have been critically evaluated. Finally, we have constructed a fully functioning Cu-O based solar cell whose efficiency has been demonstrated to be 5.2%. This, to the best of our knowledge, is by far the highest among the Cu-O based solar cells, using the similar architecture and thus, shows an improvement by a factor of 2.5 times. We believe that the cell efficiency can be increased further by enabling more light trapping in the active layers through the use of textured substrates and/or individual layer.

# Bibliography

[1] T. B. Johansson, H. Kelly, A. K. N. Reddy, R. Williams, T. E. Drennen, Renewable energy: sources for fuels and electricity. 1992: Washington (D.C.).

[2] M. Asif, T. Muneer, Rene. Sus. En. Rev. 11 (2007) 1388.

[3] J. Twidell, T. Weir, Renewable Energy Resources. 1986: London, UK.

[4] G. Bahgat, International Affairs 82 (2006) 961.

[5] P. Hunter, EMBO Rep. Dec, 8 (2007) 1104.

[6] http://www.ecology.com/2011/09/06/fossil-fuels-renewable-energy-resources/

[7] T. Jackson, RE. Renewable energy sources. Background paper for the Royal Commission on Environmental Pollution, Centre for Environmental Strategy. 1998: University of Surrey, UK.

[8] K. C. Kao and W. Hwang, Electrical Transport in Solids. 1981: Pergamon, Oxford.

[9] M. Pavan, S. Rühle, A. Ginsburg, D. A. Keller, H-N Barad, P. M. Sberna, D. Nunes, R. Martins, A. Y. Anderson, A. Zaban, E. Fortunato, Sol. Energy Mats. Solar Cells 132 (2015) 549.

[10] Y. Abdu, A.O. Musa, J. Pure Appl. Sci. 2 (2009) 8.

[11] A. Bhaumik, A. Haque, P. Karnati, M.F.N. Taufique, R. Patel, K. Ghosh, Thin Solid Films 572 (2014) 126.

[12] B. D. Yuhas, P. Yang, J. Am. Chem. Soc. 131 (2009) 3756.

# Table of contents

# List of figures

# CHAPTER 1

# 1. Introduction

## 1.1 Preamble

Energy is one of the most fundamental needs in today's world [1]. Energy lights our cities, powers our vehicles, trains, planes and rockets, warms our homes, cooks our food, plays our music, gives us pictures on television, and powers machinery in factories. Thus, to fulfill the demand of energy becomes a more critical challenge for the world's population as it grows rapidly and becomes more industrialized [2]. Therefore, a competitive, sustainable, and secure energy supply is an ever more demanding issue.

Presently, different sources of energy such as coal, petroleum, wind, thermal, and solar are naturally found on the earth [3]. Out of these, the fossil fuel-based energy sources face a number of challenges including their limited resources, rising prices, security of supply, and pollution by carbon dioxide emission, etc. [4]. Carbon dioxide causes the greenhouse effect, which increases the global temperature by reducing outward radiation and causing anthropogenic climate change [4]. With the current rate of fossil fuel consumption, it is expected that the concentration of $CO_2$ will reach the critical level of 750 ppm by 2050 [5]. Since, there is no natural decomposition of $CO_2$ in the atmosphere, it will take 500 to 2000 years to overcome the environmental effect of this level of pollution.

Alternative potential energy sources can be solar, geothermal, hydroelectric, and wind powers because these resources do not deplete as opposed to fossil fuels [6]. Currently the total global energy consumption is estimated to be around 13.5 TW and will increase up to 27 TW by the year

2050 [2]. Thus, out of these, only the solar energy has a huge potential capacity of 1,20,000 TW, which is around 10,000 times higher than the current annual global energy consumption [7]. This means one hour of sun light on earth can provide us our annual energy used. In other words, at 10% efficiency in solar cells, only 0.1% of the earth's surface is sufficient to satisfy our present need of energy [7]. But getting a hold on this huge energy reservoir remains an enormous challenge. In fact, in order to meet a sizeable part of the world's energy demand, solar energy conversion with photovoltaics (PV) will have to reach the terawatt (TW) scale. In addition, price reductions are still required for solar energy to be cost competitive with respect to the conventional energy sources used in the majority of the world [6,7].

## 1.2 Overview: Solar Cell basics

A solar cell is an electronic device that can directly convert the solar energy into the electric one and the process is known as photovoltaic effect [8]. In fact, electric current or voltage is created across such a device if light shines on the same. The key factors behind this process are the intensity, the spectral distribution of radiation, capacity of light absorption by the material, and the need for a suitable design of the external circuit [9]. These requirements can be potentially fulfilled by a variety of materials, however, for efficient photovoltaic energy conversion, semiconducting materials in the form of a *p-n* junction device are essential [10]. When light falls on this junction, photons having an energy greater than the band gap of the used semiconductors are absorbed in the device and in turn create negatively charged electrons in the conduction band, leaving behind positively charged vacancies (i.e. holes) in the valence band. In fact, electron-hole pairs created in this processes exist only for a time scale equal to the minority carrier lifetime and thereafter they recombine [9,10]. Thus, the generated electron-hole pairs should be separated and collected before their recombination takes place. In order to do so, the action of the electric field is used which is created at the interface of the *p*-*n* junction. In fact, electrons diffuse from the *n*- to *p*-type semiconductor and holes diffuse in the opposite direction and in turn generate an internal electric field at the interface of the *p*-*n* junction [11].

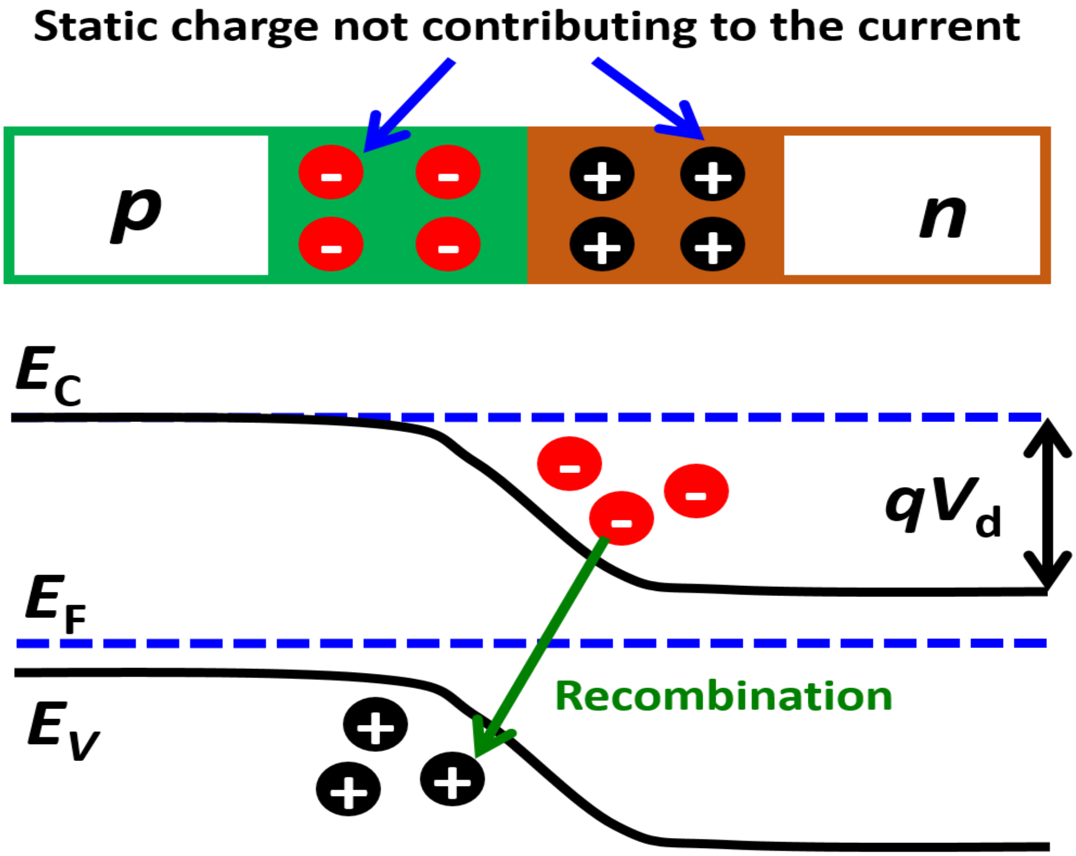

Figure 1.1: Schematic diagram of a *p*-*n* junction and its band diagram [8].

This electric field sweeps out the photo-generated carriers (electrons and holes) in the opposite direction, leading to the generation of a potential difference at both the ends of device (Fig. 1.1). The magnitude of this potential drop is called the open circuit voltage ($V_{oc}$) and it depends on the intensity of the incident light, although for a fixed intensity it remains constant with time [10,11]. In addition, if the terminals of a solar cell are connected together, the photo-generated carriers can flow through the external circuit and the magnitude of the current depends on the generated voltage. Thus, for an efficient solar cell, a higher open circuit voltage is required [8-11].

On the other hand, the ratio of the number of carriers collected by the solar cell to the number of photons having a given energy, incident on the solar cell, is called the ‘quantum efficiency’ (QE) and it can be expressed either as a function of the wavelength or the energy [10,11]. It becomes unity at a particular wavelength if all photons of that wavelength are absorbed and the resulting minority carriers are collected. On the other hand, it becomes zero for photons having energy below the band gap of the main absorbing layer. However, QE for most of the solar cells is found to be between zero and one because of recombination for which the charge carriers are not able to move into the external circuit (Fig. 1.1). Thus, for a better cell efficiency, the impacts of surface passivation and diffusion length on the collection probability are important [9-11]. This can be achieved by placing the *p-n* junction closer to the surface rather than the bulk so that the separated carriers have a shorter distance to travel within the cell, resulting in a lesser probability of recombination and in turn increasing the efficiency the cell.

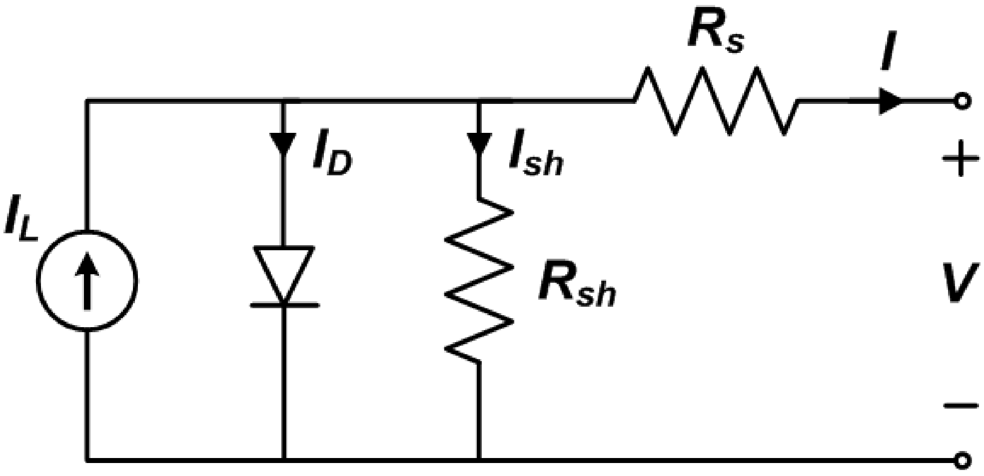

Figure 1.2: Equivalent circuit diagram of a solar cell.

A solar cell can be seen as a current generator where current is produced by injection of carriers from incident light [11]. The equivalent circuit in Fig. 1.2 describes the static behavior of the solar cell. This circuit is composed of a current source, a *p-n* junction diode, and a shunt resistor ($R_{SH}$) in parallel to a parasitic series resistor ($R_S$). As a matter of fact, $R_S$ is the total Ohmic resistance of the solar cell, which is essentially the bulk resistance caused by the fact that a solar cell is not a perfect conductor. To construct a better efficient cell, a smaller $R_S$ value is required. On the other hand, $R_{SH}$ accounts for the recombination and leakage currents from one terminal to the other due to a poor insulation. Thus, a larger $R_{SH}$ value is required for a more efficient cell, where the recombination and leakage currents are reduced. From the equivalent circuit, it is evident that the current produced by the solar cell is equal to:

$$I = I_L - I_D - I_{SH}, \tag{1.1}$$

where $I$, $I_L$, $I_D$, and $I_{SH}$ are output current, photo-generated current, diode current, and shunt current, respectively. The current through these elements is governed by the voltage across them:

$$V_J = V + IR_{SH}, \tag{1.2}$$

where $V_j$ and $V$ are voltages across both diode and resistor $R_{SH}$ and voltage across the output terminals. By the Shockley diode equation, the current diverted through the diode is:

$$I_D = I_0 \left[\exp\left(\frac{qV_J}{nk_B T}\right) - 1\right], \tag{1.3}$$

where $I_0$, $n$, $q$, $k_B$, and $T$ are reverse saturation current, diode ideality factor (1 for an ideal diode), elementary charge, Boltzmann's constant, and absolute temperature, respectively [11]. At 25°C, $k_B T/q$ is approximated to 0.0259 V. From Ohm's law, the current diverted through the shunt resistor is:

$$I_{SH} = V_J / R_{SH}, \tag{1.4}$$

Substituting these in Eq. (1.1) produces the characteristic equation of a solar cell, which relates solar cell parameters to the output current and voltage in the following manner:

$$I = I_L - I_0[exp\{q\left(V + \frac{IR_S}{nk_BT}\right)\} - 1] + (V + IR_S)/R_{SH} \ . \qquad (1.5)$$

The [-1] term in the above equation can usually be neglected since the exponential term is >>1 [11]. In principle, this equation can be solved by given a particular operating voltage $V$ and measuring the operating current $I$ at that voltage. However, since $I$ appears on both sides of the equation, it has no general analytical solution. Hence, the parameters $I_0$, $n$, $R_S$, and $R_{SH}$ cannot be measured directly. The most common application of this characteristic equation is a nonlinear regression to extract the values of these parameters on the basis of their combined effects on the solar cell behavior.

Most solar cell parameters can be obtained by carrying out $I$-$V$ measurements and its performance can be demonstrated by few parameters such as short circuit current ($I_{sc}$), open circuit voltage ($V_{oc}$), fill factor ($FF$), power ($W$), and conversion efficiency ($\eta$). The $I_{sc}$ (or $I_L$) is the current through the solar cell when the voltage across the solar cell is zero and $V_{oc}$ is the voltage across the solar cell when the current through the solar cell is zero and it is the maximum voltage available from the solar cell. The fill factor ($FF$) and the conversion efficiency ($\eta$) are metrics used to characterize the performance of the solar cell. The fill factor is defined as the ratio of maximum power point ($P_{max}$) divided by the products of $V_{oc}$ and $I_{sc}$. $P_{max}$ is the condition under which the solar cell generates its maximum power, while $V_{max}$ and $I_{max}$ are voltage and current at maximum power point, respectively. In fact, FF is essentially a measure of the quality of the solar cell and is expressed by the following equation:

$$FF = V_{max}I_{max}/V_{oc}I_{sc} \ . \qquad (1.6)$$

The conversion efficiency is defined as the ratio of $P_{\max}$ to the product of the input light irradiance ($E$) and the solar cell surface area ($A$) or simply power input.

$$\eta = P_{max}/E \times A \quad . \tag{1.7}$$

## 1.3 Perspective of solar cell research: A brief literature survey

The high cost and relatively low conversion efficiency are currently the two main problems to be resolved before solar energy can become a major contributor on the energy market [1,2,11]. The highest efficiencies have been demonstrated in GaAs-based cells for both single and multijunction devices [12]. Multijunction solar cells use multiple layers that are tailored (based on the band gap of the layers) to convert different portions of the solar spectrum more efficiently [13]. However, GaAs solar cells have generally been limited to space applications because of their high cost [12]. Presently, the majority of solar cells used for general applications are based on silicon [14]. In fact, silicon-based solar cells fabricated with single crystalline, poly crystalline, and amorphous forms dominate the PV market by 85%. It is known that silicon is found to be abundant in nature, however, in order to get a better efficiency, a pure silicon crystal is required while the fabrication processes of the same is very expensive [14]. Therefore, to have cost-effective solar cells, silicon should be replaced by some other materials which have the band gap nearby the optimum value (e.g. ~1 eV). In addition, used materials should be non-toxic and found abundant in nature [10,11]. In this regard, various types of solar cells such as GaAsInP, CdTe/CdS, copper indium gallium (di)selenide (CIGS), organic, and photochemical have been tested but all of them are facing various challenges [15]. For instance, the band gap of GaAsInP, CdTe/CdS, *CIGS* and its family strongly depends on the defect and deposition processes and is very difficult to control [15]. In addition, the toxicity of cadmium itself is a major concern for CdTe-based solar cells and the limited amount of indium reserves poses a long-term issue for CIGS. On the other hand, the development of materials for photochemical and dye-sensitized solar cell is still not completed [16]. Dye-sensitized solar cells use an organic dye, coating a porous electrode with high surface area to absorb more light. Presently, the maximum achieved efficiency for dye-sensitized solar cells is around 11%, however, the use of a liquid electrolyte in the cells is a source of reliability issues [16]. Another organic technology is thin-film solar cells based on solid-state organic semiconductors [16,17].

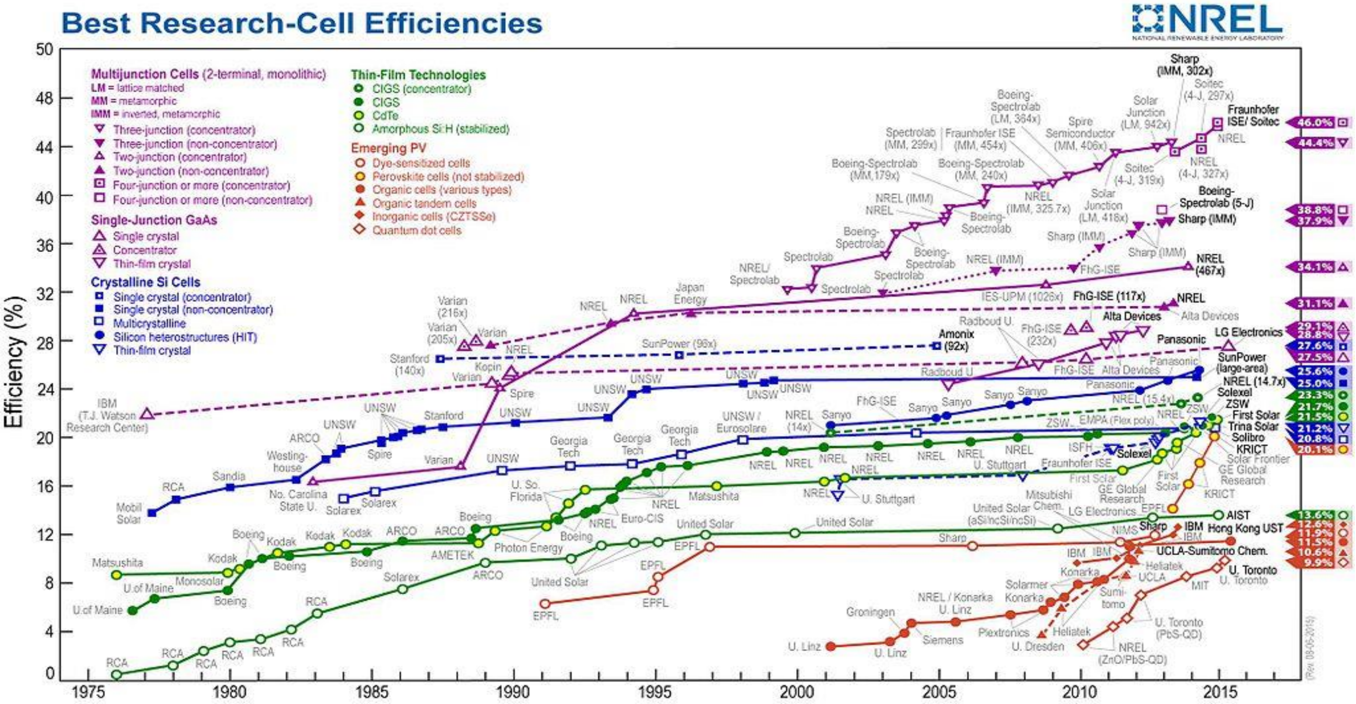

Figure 1.3: Timeline of highest efficiencies in various solar cell technologies [18].

Organic semiconductors can have their chemical and electrical properties tailored in numerous ways by modifying the chemical structures and can allow new processing methods. Organics have great potential for light-weight and flexible devices fabricated with high-throughput processes from low-cost materials in a variety of colors. However, organic semiconductors still belong to a relatively young field, and the highest efficiencies are only around 8% for the very best organic thin film cells [16].

Fig. 1.3 summarizes the highest efficiencies in various solar cell technologies obtained throughout the years [18]. It should be noted that sometimes commercially available solar cells have drastically lower efficiencies compared to the records because of additional complexities while manufacturing cells on a large scale. While multijunction concentrators and GaAs cells have the highest record efficiencies, crystalline and multicrystalline silicon are still the market leaders. Even with their lower efficiencies, thin-film solar cells are making significant market penetration because of the trade-off between the efficiency and cost. However, it is clear that there are many different approaches to reach the same goal of converting sunlight to electricity and each technology may be able to fill an appropriate role based on its individual advantages and trade-off.

## 1.4 Motivation

The requirement of high efficiency solar cells at a low cost can be fulfilled by designing the metal oxide (MO) semiconductor based solar cells [19]. In fact, most of the MOs are found to be abundant, non-toxic, and chemically stable in nature which allows us to deposit these materials even under ambient conditions. In fact, heterojunctions based on MOs are recently attracting considerable attention due to their promising potential for price reduction using cheap materials and production methods [19,20]. In addition, MOs are also used as active or passive components in a broad range of available commercial applications such as active channel layer in transistors that constitute the active matrix of displays or in solar cells as transparent conducting front electrodes, and as an electron or hole transport layers [19,20].

Out of many oxides, copper oxide (Cu-O) based solar cells are not only due to attract the researchers because of its band gap being close to the optimal band gap under the 1.5 solar mass (AM1.5) radiation spectrum but also its high absorption coefficient and high minority carrier diffusion length [21]. Fig. 1.4 shows a schematic representation of a Cu-O based solar cell.

Theoretically, the efficiency of this type of solar cell should be around 20% [22], albeit the experimentally achieved efficiency is still less than 3% [23]. This low efficiency is due to the lack of clear understanding of charge transport properties within the Cu-O layer and its fellow constituent layers. On the other hand, a higher temperature is also required to get a better quality solar cell, although at higher temperatures an interfacial diffusion takes place, reducing the efficiency of the same [19-24]. Thus, in order to improve the efficiency of the Cu-O based solar cell, beside room temperature processing, an in-depth understanding of the charge transport process in it and in the other constituent layers are required.

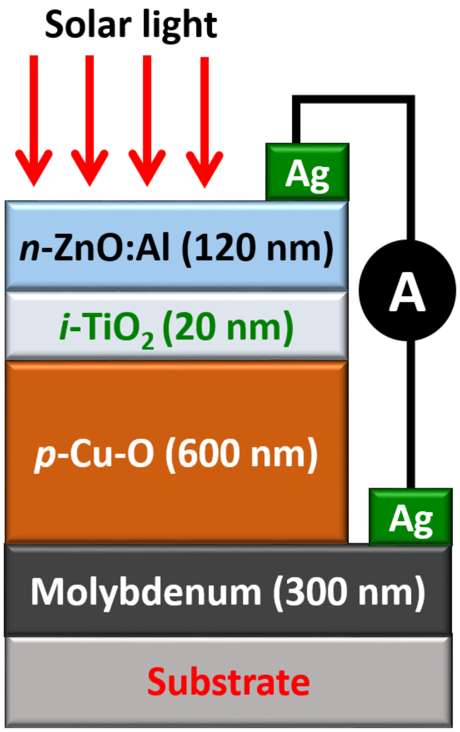

Figure 1.4: Schematic representation of a Cu-O based solar cell.

The present thesis deals with the optimization of the growth of the constituent layers at room temperature (RT) and studies on their electrical, optical, structural, and compositional aspects, leading to a superior cell efficiency (>5%). In fact, there are various points which have been addressed towards achieving a better efficiency and are described below.

**(a) Growth of Al-doped ZnO (AZO) films and understanding the charge transport:** The top most layer of the studied solar cell is an AZO film and it works as a transparent electrode. Generally, different methods such as chemical vapour deposition, sputtering, and pulsed laser deposition are used to grow AZO films [25]. In most of these cases, a high deposition temperature (>300° C) is required to meet the desired level of transparency and conducting property. In fact, achieving the metal-like resistivity and a high transmittance (at RT) in AZO is still challenging. In addition, for a better realization of the transparent contact properties, it is necessary not only to understand the bulk but also the nanoscale (local) electrical transport properties of AZO thin films, which are also considered to be quite challenging. In this thesis, we will focus on these issues and demonstrate how one can resolve the same.

**(b) Ultra-violet (UV) absorption in AZO and role of polarization in charge transport:** Nanoscale conductivity in AZO films not only depends on the carrier concentration alone but can be influenced by external excitation in terms of photo-absorption. For instance, ultra-violet (UV) absorption enhances the conductivity of an AZO window layer by direct photo-generation even though it is considered to be an optical loss for the underneath absorbing layer of a solar cell, leading to a poor cell performance [26]. This can be directly assessed by studying photoresponsivity and thus, it becomes quite important to have an in-depth understanding on UV-exposure and the corresponding photoresponse in nanoscale charge transport in an AZO layer. In addition, due to structural defects, a polarization can be generated in the doped-ZnO systems, which can play an important role in charge transport as well. However, one-to-one correlation between polarization and charge transport is still lacking, which is being addressed in this work.

**(c) Growth of Cu-O layer and role of structural defects in charge transport:** This is the main absorbing layer and hence, for a better efficiency a smooth charge transport process in necessary across this layer for which a better crystalline thin film is exigent. However, the growth of better crystalline films of Cu-O, at RT, is a challenging task. In general, Cu-O films grown by various methods are known to consist of a large number of defects, such as oxygen vacancies, copper interstitials, etc [27]. These vacancies govern the charge transport in Cu-O films. Normally, change in the defects concentration leads to a shift in the Fermi level position. This in turn changes the work function of a material, which has a one-to-one correspondence with its nanoscale conductivity. However, optimization of the growth of the Cu-O layer at RT and the influence of defects in the charge transport process in the same is still lacking. In this thesis, we have addressed these issues in detail.

**(d) Understanding the hole blocking nature of $TiO_2$ and the interfacial barrier formation:** Under the present architecture, we use a sandwich layer, in the form of $TiO_2$, between the AZO and Cu-O layer. In this thesis work, we have optimized the growth of the $TiO_2$ layer and show that it works as a hole blocking layer and is thus, expected to increase the cell efficiency. However, the formation of interfacial barrier and charge transport across this layer it is still lacking.

**(e) Growth of back contact:** A back contact is an essential part of the solar cell. It should have a low resistivity and a high reflectivity. In the present work, we have chosen Mo as the back contact layer and optimized its growth parameters to achieved better optoelectronic properties towards the construction of an efficient Cu-O based solar cell.

## 1.5 Background of the used layers

The oxide-based solar cells are known to a low cost, enviroemental friendly, and non-toxic solutions and thus, various combinations of oxide materials such as CuO/ZnO, $TiO_2$/CuO, etc.

have been tested to design an efficient solar cell [28,29]. As mentioned above, this thesis deals with a ZnO:Al/$TiO_2$/Cu-O/Mo heterostructure solar cell (Fig. 1.4). In this section, we will provide layer-by-layer discription (from the top towards the bottom) and adress their various physical properties.

### 1.5.1 ZnO:Al (AZO): The transparent conducting top electrode

Transparent conducting oxide (TCO) layers as a top contact is an essential component for most of the thin film solar cells [25]. As a front contact, the TCO layer should have a high optical transmission in the relevant spectral range and a low electrical resistivity at the same time. Generally, Sn-doped $In_2O_3$ (ITO) is used as a transparent contact material for above-mentioned devices [25]. However, due to its high cost, and toxicity researchers are searching for an alternative of the same. In this regard, non-toxic zinc oxide (ZnO) is considered to be a suitable replacement because it is cost-effective and found to be abundant in nature [25,30].

ZnO is a direct and wide band gap (3.37 eV at RT) II-VI binary compound semiconductor and it crystallize in two main forms: hexagonal wurtzite and cubic zinc blende structures (Fig. 1.5) [25,30]. The hexagonal wurtzite structure of ZnO is the most common phase having a crystal group of C6v or P 63 mc, which occurs almost exclusively at ambient conditions [30]. On the other hand, the wurtzite ZnO structure consists of alternating zinc (Zn) and oxygen (O) atoms (Fig. 1.5). The ZnO structure has a polar surface (0001), which is either Zn- or O-terminated and non-polar surfaces (1120) and (1010) as well, possessing an equal number of both atoms. The polar surface of ZnO is highly metastable in nature and is responsible for several unique and astonishing properties including piezoelectric properties [30]. Generally, ZnO exhibits *n*-type conductivity which can be attributed to the presence of a donor level arising from interstitial zinc atoms and/or oxygen vacancies. It is known that this conductivity can be enhanced up to three to four orders of magnitude after doping with Group-III elements, especially Al-doping [25]. It is interesting to mention that similar to ZnO, ZnO:Al (AZO) is also found to be more stable in the hexagonal wurtzite form.

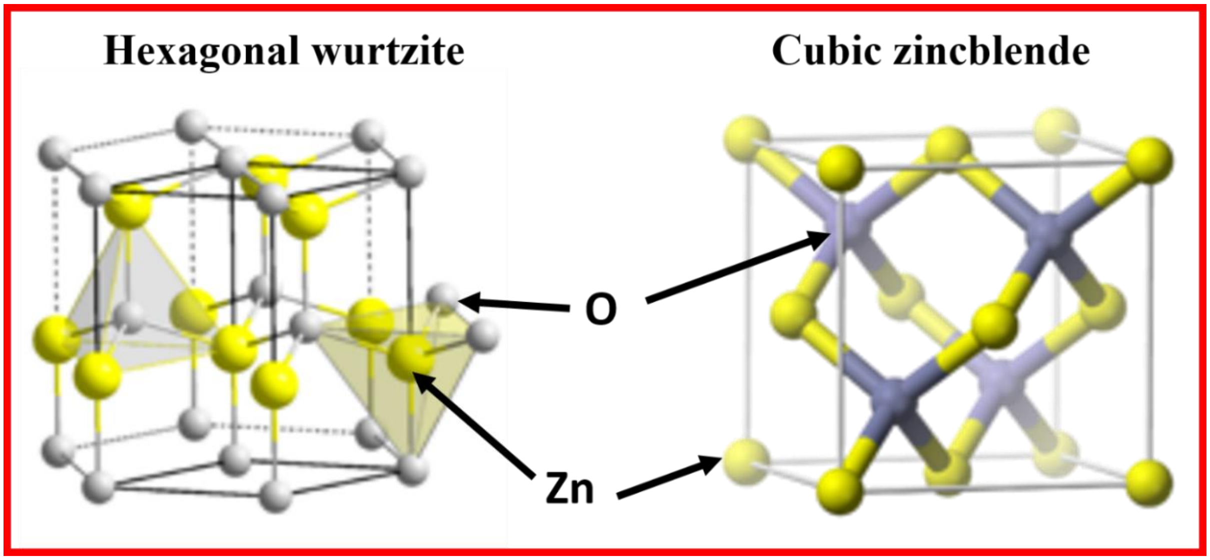

Figure 1.5: Possible stable crystal structures of ZnO [25].

AZO, in the hexagonal wurtzite crystal structure, has alternating planes of tetrahedrally coordinated $O^{2-}$ and $Zn^{2+}$ stacked along the *c*-axis (Fig. 1.6) [25]. In addition, the ionic radius of $Al^{3+}$ (0.053 nm) is smaller compared to $Zn^{2+}$ (0.074 nm) and thus, Al atom can substitute the Zn atom, which in turn donates an electron in the ZnO matrix, causing a metal-like conductivity (Fig. 1.6). In addition, the above mentioned defects (e.g. oxygen and zinc) are also found in the AZO matrix, giving rise to a non-stoichiometric nature of the film. This non-stoichiometric nature not only changes the conductivity of the AZO film but also gives rise to a shift in the optical band gap of the same [25]. In fact, Al-doping pushes the Fermi level in the conduction band (CB) and as a result, an increment in the effective optical band gap is observed – known as Burstein-Moss (BM) effect [31].

.

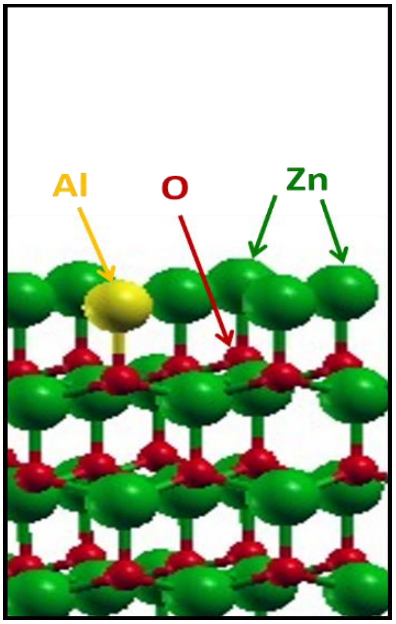

Figure 1.6: Crystal structure of Al-doped ZnO [25].

In fact, Al-doping as well as the presence of oxygen vacancies in the AZO matrix play an important role in the tuning of other physical properties as well. In order to understand the role of these defects, AZO thin films have been grown by various techniques, such as chemical vapor deposition, sputtering, and pulsed laser deposition [25,28,32]. In most cases, depending on the thermodynamic driving force, isolated islands coalesce and form grain boundaries (GBs). GBs give rise to a large number of defects which go on to influence the physical properties such as band bending and charge transport process in case of thin films [32]. Generally, changes in the doping level and surface defects lead to a shift in the Fermi level position, leading to a change in the work function of AZO thin films.

### 1.5.2 Cu-O: The main absorbing layer

Because of its novel properties, such as low cost, non-toxicity, fairly high minority carrier diffusion lengths, high absorption coefficient in the visible region, and large excitonic binding energy, copper oxide is considered as an attractive material for photovoltaic applications [39]. This is the main absorbing layer of a copper oxide-based solar cell and found to be in two stable forms, viz. cupric oxide (CuO) and cuprous oxide ($Cu_2O$) [40]. These two forms of Cu-O have different physical properties, different colors, crystal structures, and electrical properties. For instance, the band gap of CuO [copper oxide(I)] and $Cu_2O$  [copper oxide(II)] is found to be around 1.2 and 2.1 eV, respectively and thus, a much higher solar spectrum can be absorbed in copper oxide(I). Thus, $Cu_2O$ is being frequently studied as an absorber layer for low cost production of a metal oxide-based solar cell, even though its optical band gap is not optimum.

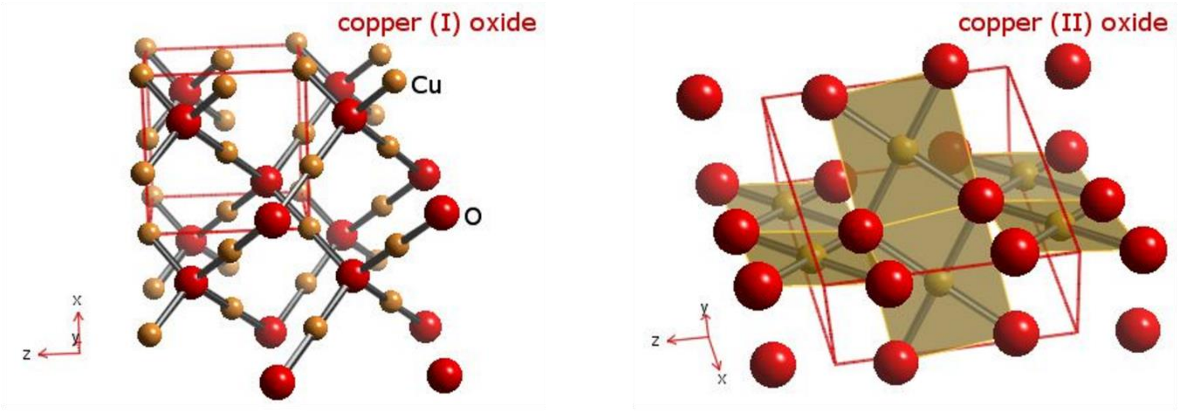

Figure 1.7: Crystal structures of copper oxides [41].

The crystal structure of $Cu_2O$ is found to be that of a simple cubic structure where the copper atoms arrange themselves in a face-centered cubic (fcc) sublattice and the oxygen atoms in a body-centered cubic (bcc) sublattice (Fig. 1.7). This structure has a lattice constant, $a$=4.2696 Å and one sublattice is shifted by a quarter of the body diagonal. In this lattice, each copper atom is linearly coordinated by two neighboring oxygen atoms and each oxygen atom is surrounded by four copper atoms, making the stoichiometry to be 2:1. On the other hand, the crystal structure of CuO is found to be in the monoclinic phase where each copper atom is coordinated by four oxygen atoms in an approximately square planar configuration (Fig. 1.7).

It is known that a slight deviation in the compositional ratio of Cu:O generates a nonstoichiometry of the same and in turn changes the physical properties [39,41]. Generally, this deviation from the stoichiometry, $\delta$, can be identified either as vacancies, interstitials or both [42]. In particular, copper vacancies (defects) in (both CuO and $Cu_2O$) Cu-O act as a *p*-type dopants (acceptors), making this oxide behave as a *p*-type semiconductor, whereas oxygen vacancies are found at donor sites and are attributed to be responsible for the *n*-type conductivity of Cu-O [41].

These defects not only tune the optical property of both these materials but also are involved directly in the charge transport process. In fact, the electrical conductivity and the hole density of *p*-type Cu-O films vary with the concentration of copper vacancy which act as shallow acceptors. In fact, it has been demonstrated that an increase in temperature increases the conductivity of CuO and $Cu_2O$ due to an increase in the hole concentration [42]. Thus, it is possible to tune the electrical properties (resistivity, carrier concentration and mobility) of Cu-O by changing the stoichiometry and crystallinity of the Cu-O films during the deposition process.

Optical properties of Cu-O also depend on the defects. In fact, the Cu-O crystal structure is formed by two interpenetrating three-dimensional Cu and O networks. Theoretical studies have been developed to clarify the interrelation between the structural and optical properties of undoped and doped Cu-O and have shown a dependence on the $Cu_2O$ band gap with Cu–Cu interactions [43]. In fact, the attenuation of Cu–Cu interaction leads to an enhancement in the band gap.

### 1.5.3 $TiO_2$: The hole blocking layer

Titanium di-oxide ($TiO_2$) thin films are widely used in various fields such as optical and protective coatings, and optical fibers because of their excellent chemical stability, mechanical hardness, and optical transmittance with a high refractive index [33]. In addition, recently, $TiO_2$ thin films have become the most promising material for environmental cleaning such as photocatalytic purifier and photochemical solar cells [34].

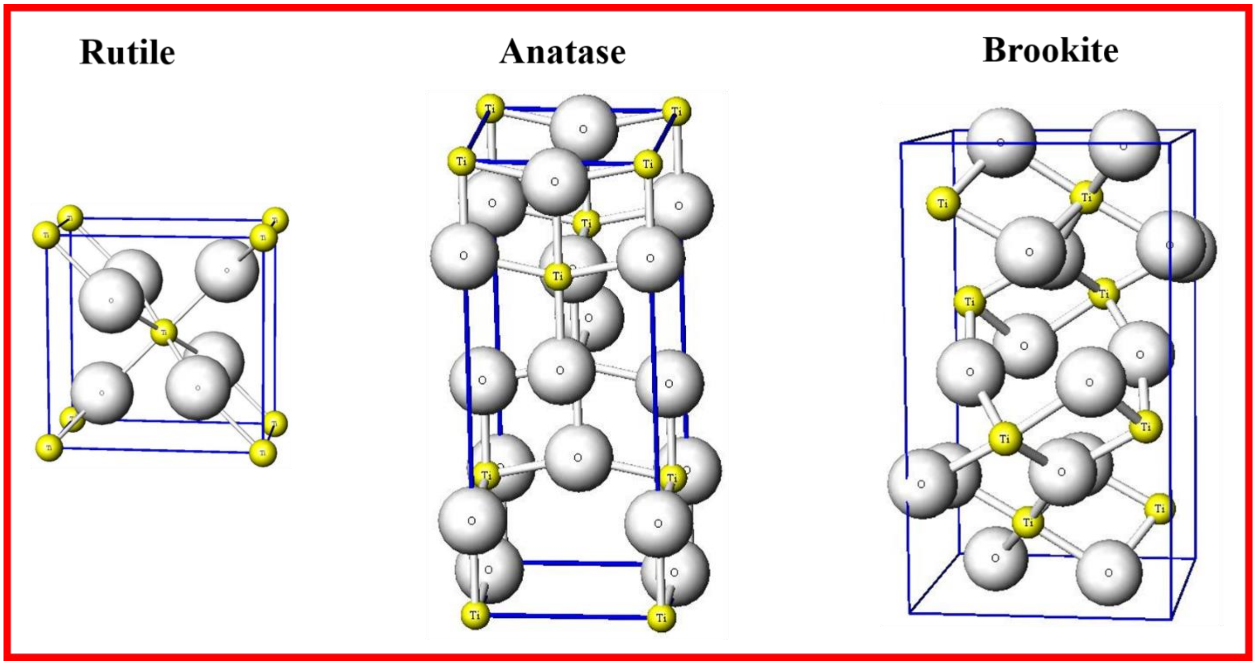

Figure 1.8: Crystal structures of different phases of $TiO_2$ [35].

Generally, $TiO_2$ is found to be in three main phases, e.g. rutile, anatase, and brookite (Fig. 1.8) whereas [33-36]. It is known that out of these phases, rutile is found to be thermodynamically the most stable one, whereas anatase and brookite have high kinetic and thus, show a degradation with time [28]. However, the anatase phase is found to be more useful in solar cells compared to the rutile phase, while a very little is known about the brookite phase [35]. Therefore, most studies discuss about pure anatase or rutile thin films. A number of techniques, such as chemical vapour deposition, sol-gel, plasma source ion implantation, pulsed laser deposition, and magnetron sputtering have been used to grow $TiO_2$ thin films onto several of substrate materials [33]. Out of these, magnetron sputter deposition of $TiO_2$ films has attracted special attention because it is an industrial process capability to large-area deposition and high quality $TiO_2$ films can be grown at lower substrate temperatures [36]. In addition, the grain size, nature of crystallinity, morphology, and planer orientation of the $TiO_2$ layers can be controlled by the process parameters such as sputtering gases, growth angle, $O_2$ partial pressure, substrate temperature, and/or annealing process [37]. However, only the anatase and rutile phases have generally been observed through the high temperature sputtering deposition of $TiO_2$. In addition, amorphous $TiO_2$ films are often observed if the substrate temperature is low during deposition (at room temperature) [33,36]. The physical properties of $TiO_2$ films, prepared by reactive magnetron sputtering, strongly depend on the sputtering conditions, namely power, partial pressure of the reactive gas, and substrate to target distance.

Depending on crystalline the structure of $TiO_2$, optical band gap exhibits both direct and indirect characteristics. For instance, the rutile phase of $TiO_2$ has both direct and indirect band gap of 3.06 eV and 3.10 eV, respectively and the anatase $TiO_2$ has only an indirect band gap of 3.23 eV [38]. Generally, $TiO_2$ exhibits an *n*-type conductivity, which is attributed to the donor type defects including oxygen vacancies and titanium interstitial atoms. The main advantage of $TiO_2$ is that it can be used to make a heterojunction where it shows the ability to selectively block the flow of either electrons (via the conduction band barrier) or holes (via the valence band barrier). This indeed opens up a new avenue to design photocatalytic devices [38].

### 1.5.4 Molybdenum: Back contact for solar cell

Naturally abundant Mo is considered to be a suitable contact material for various optoelectronic application [44]. Mo has a low solubility in water as well as low oxidation rate. Generally, Mo is found to have the body cubic crystal structure (Fig. 1.9). Mo thin films show high thermal stability and good electrical conductivity and are thus, chosen for making electrical contacts in different nano-electronics applications. In addition, Mo is also used as a back electrode for solar cell applications where it is used not only as a conducting layer but also as a reflecting mirror.

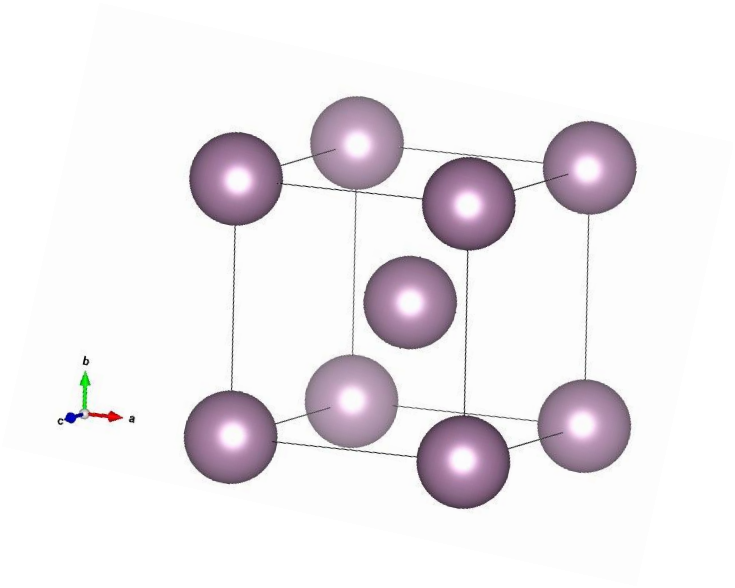

Figure 1.9: Crystal structure of Molybdenum [44].

## 1.6 Outline of the thesis

**Chapter 1:** In this chapter, a brief introduction of the solar cells and related issues covered in the studies are presented. The introductory description also includes some basics and models of solar cells. In this chapter, we have also described the motivation behind our study. In addition, we describe the physical properties of the layers used in our study, especially their crystal structures, electrical, and optical properties, and explain the role of each layer.

**Chapter 2:** This chapter describes the experimental techniques employed for carrying out the studies presented in this thesis.

**Chapter 3:** In this chapter, we demonstrate how better quality Al-doped ZnO (AZO) films can be deposited at room temperature. In fact, we show the effect of deposition angle on the structural, optical, and electrical properties of AZO films. Following this, we demonstrate the role of grain boundaries on the charge transport of AZO films. Above observations are explained in the framework of AZO thickness dependent variation in the grain size and in turn the trap density at the grain boundaries, influencing the carrier transport across the adjacent grains. In addition, we investigate the effect of temperature on the transport mechanism of an *n*-AZO/*p*-Si heterojunction diode. In particular, temperature-dependent transition from direct tunnelling to thermionic emission is observed in the (*I*-*V*) characteristics. We have made use of optical absorption spectroscopy before and after temperature treatment, which shows a reduction in the band gap of the AZO layer. These observations are discussed in terms of annihilation of the oxygen vacancies in the AZO layer.

Further, we will show how UV light absorption can influence the bulk as well as nanoscale conductivity of AZO thin films. To address this issue, we have employed combined Kelvin probe force microscopy (KPFM) and conductive atomic force microscopy (cAFM) measurements at room temperature (RT). For instance, the donor concentration is mapped by KPFM in which a variation in the carrier density is observed. Further, UV-induced enhancement in the spectral response of *n*-AZO/*p*-Si solar cell is observed, manifesting UV absorption in the AZO overlayer should not cause a loss in the efficiency of a solar cell which is in contrary to the common belief.

**Chapter 4:** In this chapter, we demonstrate an experimental evidence on polarization-mediated band bending at the grain boundaries of an AZO thin film using Kelvin probe force microscopy and conductive atomic force microscopy. In particular, we demonstrate the presence of polarization and nanoscale pseudoferroelectricity at the grain of the same using piezoresponse force microscopy. The presence of polarization is believed to open up a new avenue to control the charge transport by tuning the work function of AZO with an applying an electric field. Hence, our experimental investigation, using KPFM, shows that by applying a positive or negative tip bias, the work function of an AZO film can be enhanced or reduced which corroborates well with the measured charge transport using the conductive atomic force microscopy. Our experimental findings are further confirmed by calculations based on the first-principle-based density functional theory.

**Chapter 5:** In this chapter, first we optimize the growth of Cu-O thin films and then demonstrate the role of structural defects on the charge transport of rf magnetron sputter deposited copper oxide thin films. X-ray diffraction (XRD) is used to investigate the crystalline nature and evaluate the dislocation density of the films. In addition, we have used Kelvin probe force microscopy and conductive atomic force microscopy to show the structural defect mediated presence of resistive switching. These findings match well with the existing theoretical model on the resistive switching. In particular, understanding the role of structural defects in resistive switching can be considered as critically important to take a step forward for designing advanced nanoscale memory devices.

**Chapter 6:** In this chapter we show the growth and hole blocking behaviour of *rf* magnetron sputtered grown amorphous $TiO_2$ thin films. Initially, we demonstrate the role of deposition angle on the physical properties of $TiO_2$ thin films. Following this, we have made an attempt to understand the charge transport through the same. In fact, we perform temperature dependent current-voltage measurements of a $TiO_2$/Si heterojunction. Using KPFM and temperature-dependent current-voltage characteristics, we study the charge transport across $TiO_2$/Si heterojunction. In particular, the KPFM result shows a variation in the work function at $TiO_2$ surface. Further, the temperature-dependent current-voltage characteristics depict non-ideal hole blocking behavior. In addition, the measured barrier height is found to decrease with temperature, strongly suggesting its inhomogeneous nature at the interface. The observed result on the barrier inhomogeneities is attributed to the interfacial disorders arising due to the growth dynamics and corroborates well with the KPFM map. Following this, we first confirm the hole blocking nature of $TiO_2$ grown on a thick Cu-O layer and go ahead to demonstrate that an *n*-$TiO_2$/*p*-Cu-O junction possesses a better hole blocking property compared to that of *n*-$TiO_2$/*p*-Si junction.

**Chapter 7:** The bottom electrode for the presently studied cell configuration is a molybdenum thin film. For a better efficiency, this electrode should have high optical reflectivity and charge collection efficiency. Thus, in Chapter 7, first we have optimized the growth of Mo thin films on silicon substrate and studied its structural, electrical, and optical properties. In fact, the film deposited under normal incidence shows the lowest resistivity ($\sim 10^{-6}$ Ω-cm) and highest reflectivity (~65%) and thus, has been considered for the present architecture of the Cu-O based solar cell. In the quest of fabricating a $TiO_2$-based hole blocking solar cell, we have constructed two solar cells viz. AZO/Cu-O/Mo/Si and AZO/$TiO_2$/Cu-O/Mo/Si by optimizing the growth of individual layers and studying their microstructural, optical, and electrical properties. Based on these measurements, it has been demonstrated that the latter cell shows an efficiency of 5.2%, which is nine times higher than the former one, exhibiting the efficacy of a hole blocking solar cell. This is by far the best cell efficiency (viz. 2.5 times higher) among the Cu-O based solar cells, using the similar architecture.

**Chapter 8:** In chapter 8, we provide a summary of the present thesis work, which involves the growth and characterization of room temperature grown multilayers using various local probe microscopic. In fact, we have demonstrated the highest known efficiency, to the best of our knowledge, for a $TiO_2$ and Cu-O-based hole blocking solar cell, which is 2.5 times higher than the ones fabricated using the similar architecture. Further, we have outlined the future scope of experimental studies based on our results and their importance towards a deeper understanding of the oxide based solar cell and possible applications.

# Bibliography

[1] T. B. Johansson, H. Kelly, A. K. N. Reddy, R. Williams, T. E. Drennen, Renewable energy: sources for fuels and electricity. 1992: Washington (D.C.).

[2] M. Asif, T. Muneer, Rene. Sus. En. Rev. 11 (2007) 1388.

[3] J. Twidell, T. Weir, Renewable Energy Resources. 1986: London, UK.

[4] G. Bahgat, International Affairs 82 (2006) 961.

[5] P. Hunter, EMBO Rep. Dec, 8 (2007) 1104.

[6] http://www.ecology.com/2011/09/06/fossil-fuels-renewable-energy-resources/

[7] T. Jackson, RE. Renewable energy sources. Background paper for the Royal Commission on Environmental Pollution, Centre for Environmental Strategy. 1998: University of Surrey, UK.

[8] https://en.wikipedia.org/wiki/Solar_cell

[9] http://www.pveducation.org/pvcdrom/solar-cell-operation/solar-cell-structure

[10] M. Buresch, Photovoltaic energy systems: design and installation. 2008: McGraw-Hill, New York, USA.

[11] P. Würfel, U. Würfel, Physics of Solar Cells: From Basic Principles to Advanced Concepts. 2009: John Wiley & Sons.

[12] H. Cotal, C. Fetzer, J. Boisvert, G. Kinsey, R. King, P. Hebert, H. Yoon, and N. Karam, Energy Environ. Sci. 2 (2009) 174.

[13] M. S. Leite, R. L. Woo, J. N. Munday, W. D. Hong, S. Mesropian, D. C. Law, and H. A. Atwater, Appl. Phys. Letts. 102 (2013) 033901.

[14] T. Saga, NPG Asia Materials 2 (2010) 96.

[15] S. J. Fonash, Solar Cell Device Physics. 1981: Academic Press, New York, USA.

[16] T. W. Hamann, J. W. Ondersma, Energy Environ. Sci, 4 (2011) 370.

[17] K. C. Kao and W. Hwang, Electrical Transport in Solids. 1981: Pergamon, Oxford.

[18] http://www.nrel.gov/ncpv/

[19] S. Calnan, Coatings 4 (2014) 162.

[20] M. Pavan, S. Rühle, A. Ginsburg, D. A. Keller, H-N Barad, P. M. Sberna, D. Nunes, R. Martins, A. Y. Anderson, A. Zaban, E. Fortunato, Sol. Energy Mats. Solar Cells 132 (2015) 549.

[21] L. Zhu, G. Shao, and J. K. Luo *Semicond. Sci. Technol.* 26 (2011) 085026

[22] Y. Abdu, A.O. Musa, J. Pure Appl. Sci. 2 (2009) 8.

[23] A. Bhaumik, A. Haque, P. Karnati, M.F.N. Taufique, R. Patel, K. Ghosh, Thin Solid Films 572 (2014) 126.

[24] Y. Abdu, and A.O. Musa, Bajopas 2 (2009) 2.

[25] Y. Liu, Y. Li, H. Zeng, J. Nanomater 2 (2013) 9.

[26] B. D. Yuhas, P. Yang, J. Am. Chem. Soc. 131 (2009) 3756.

[27] D. Gao, J. Zhang, J. Zhu, J. Qi, Z. Zhang, W. Sui, H. Shi, D. Xue, Nanoscale Res Lett 5 (2010) 769.

[28] Y. Liu, Y. Li, and H. Zeng, J. Nano. 83 (2013) 23.

[29] Z. L. Wang, J. Phys.: Condens. Matter 16 (2004) R829.

[30] B. K. Sharma and N. Khare, J. Phys. D: Appl. Phys. 43 (2010) 465402.

[31] T. Minami, H. Nanto, and S. Takata, Jpn. J. Appl. Phys. 23 (1984) L280.

[32] A. Kushwaha, H. Tyagi, and M. Aslam, AIP Advances 3 (2013) 042110.

[33] S. M. Gupta and M. Tripathi, Chin. Sci. Bull. 56 (2011) 1639.

[34] M. Li and Y. Chen, Sensors and Actuators B 32 (1996) 82,

[35] S-C Zhu, S-H Xie, and Z-P Liu, J. Am. Chem. Soc., 137 (2015) 11532.

[36] C. J. Tavares, J. Vieira, L. Rebouta, G. Hungerford, P. Coutinho, V. Teixeira, J. O. Carneiro, A. J. Fernandes, Mat. Sci. Eng. B 138 (2007) 139.

[37] H. Y. Wang, T. M. Wang and P. Xu, J. Mater. Sci.: Materials in Electronics, 9 (1998) 327.

[38] G. Filipič and U. Cvelbar, Nanotechnology 23 (2012) 194001

[39] A. O. Musa, T. Akomolafe, M. J. Carter, Sol. En. Mat. Solar Cells 51 (1998) 305.

[40] A. Mittiga, E. Salza, F. Sarto, M. Tucci, and R. Vasanthi Appl. Phys. Letts 88 (2006) 163502.

[41] M. Heinemann, B. Eifert, and C. Heiliger, Phys. Rev. B 87 (2013) 115111.

[42] S. Nandy, R. Thapa, M. Kumar, T. Som, N. Bundaleski, O. M. N. D. Teodoro, R. Martins, and E. Fortunato, Adv. Funct. Mater. 25 (2015) 947.

[43] C. Rödl, F. Sottile, and L. Reining, Phys. Rev. B 91 (2015) 045102.

[44] https://en.wikipedia.org/wiki/Molybdenum.

# CHAPTER 2

# 2. Experimental techniques

The experimental studies presented in this thesis covers the growth of various thin film and their characterizations such as structural, compositional, optical, and electrical properties. The deposition was carried out using dc/rf sputtering techniques where various experiments were carried out by varying deposition angles. The surface morphologies were investigated *ex-situ* using atomic force microscopy (AFM) and scanning electron microscopy (SEM). In addition, x-ray diffraction (XRD) and transmission electron microscopy (TEM) were employed to check the crystallinity and microstructure of the films, whereas energy dispersive x-ray spectrometry (EDS) and x-ray photoelectron spectroscopy (XPS) were used for their compositional analyses. Optical absorption, transmittance, and surface reflectance were measured by UV-Visible spectroscopy. The charge transport process in the films was studied by bulk *I*-*V*, *C*-*V*, and photoresponsivity measurements. Further, nanoscale charge transport was also studied using various local probe microscopic techniques. In this chapter, we briefly introduce the basic principles of these experimental techniques and describe the instruments.

## 2.1 dc/rf magnetron sputtering

Sputter deposition is a physical vapour deposition (PVD) process where atoms are sputtered from a target material by collision with gas ions and gets deposited on a substrate surface [1]. In this process, a plasma is created and positively charged ions from plasma are accelerated towards a negatively charged electrode or “target”. Upon striking the target, these ions possess sufficient energy to dislodge the surface atoms of the target. The atoms which are getting ejected from the surface of the target condense on surfaces that are placed in the proximity of the magnetron sputtering cathode [2]. In addition, magnetron sputter deposition technique uses a closed magnetic field near the target to trap electrons. As a result, the efficiency of the initial ionization process gets enhanced [3]. It also allows a plasma to be generated at lower pressures which reduces both background gas incorporation in the growing film and energy loss of the sputtered atoms through gas collisions.

Arcing is a common source of numerous issues in magnetron sputtering. In contrast to the preferred uniform glow for stable sputtering, arcs are characterized as intense, localized concentrations of plasma supported by collective emission of electrons from the sputtered surface. Multiple mechanisms promote the formation of arcs in the sputtering process [4]. Reactive sputtering of dielectrics is particularly problematic because of the formation of insulating regions that can promote severe arcing [4]. It is well established in reactive sputtering that uses reverse-voltage pulsing can dramatically reduce arcs in even the most arc-prone reactive processes. Thus, properly chosen pulsing parameters are necessary to optimize the output, but once implemented, the result can be a significant reduction of the arc activity. From the schematic (Fig. 2.1), it is seen that a main deposition chamber coupled with a load lock chamber is the heart of the deposition. A turbo molecular pump (Varian, USA) backed by a rotary pump is used to maintain the high vacuum condition. A small inlet is fixed to the main chamber which is required to inject the sputtering gas into the main chamber. Generally, a sample manipulator is needed to align the substrate at different angles with respect to the incoming flux. This enables us to deposit films at a particular oblique angle other than normal incidence (Excel Instruments, India). Four magnetron sputtering guns can be attached to the main chamber. Different important parts of the setup are highlighted in yellow colour. The pulsed dc magnetron sputtering setup (Fig. 2.2) has a spherical high vacuum chamber.

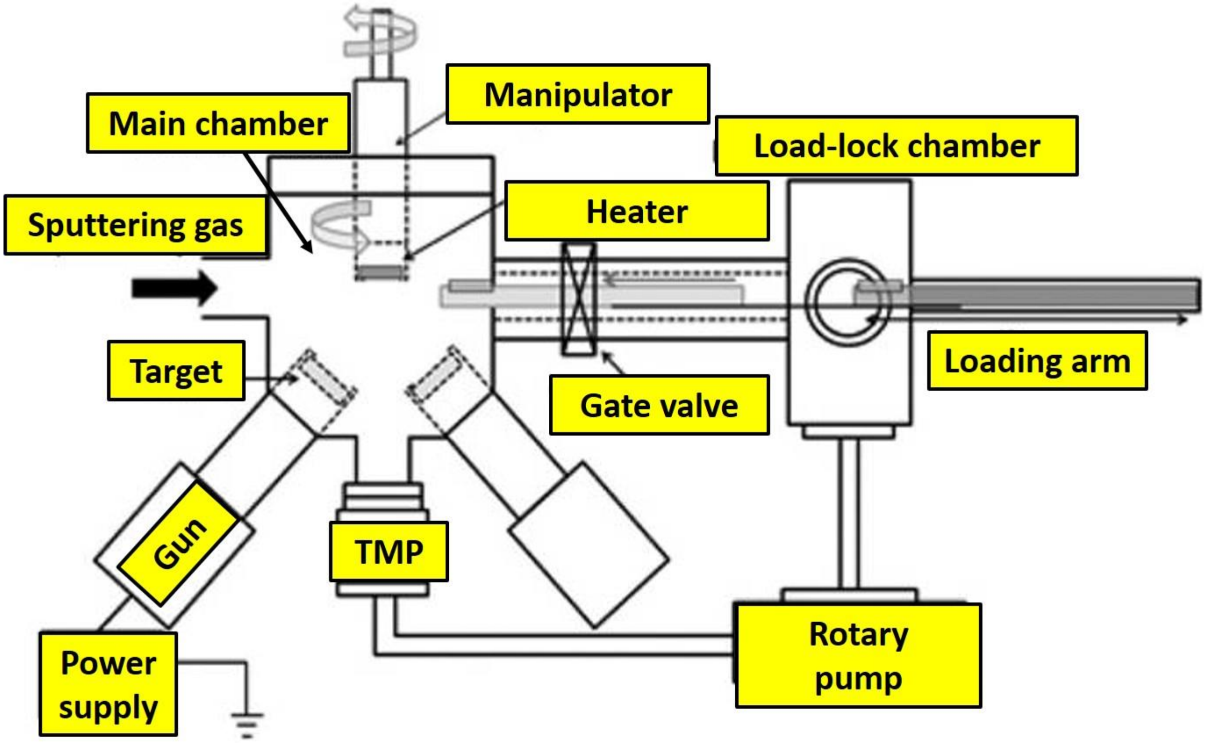

Figure 2.1: A schematic diagram of a dc/rf magnetron sputtering process.

These guns are equipped with chimneys to prevent the cross contamination between targets. In addition, the temperature of the target holders was kept below 19˚C by using a continuous chilled-water flow. Different films, used in the present thesis, are prepared using the present setup at room temperature (RT). The substrates are mounted on the top of the rotating substrate holder at a distance of 80 mm from the target. This substrate holder is equipped with a glancing angle deposition (GLAD) attachment. Prior to sputtering, a base vacuum of $3\times10^{-7}$ mbar was achieved. Following that ultra-pure (99.999%) Ar gas is injected into the chamber at a flow rate of 30 sccm (standard cubic centimetres per minute) until it reaches a working pressure of $5\times10^{-3}$ mbar. Before each deposition, pre-sputtering for a time duration of 10 min is conducted to remove the trapped impurities from the surface of the target. During this process, a movable shutter is used to protect the substrate from getting contaminated.

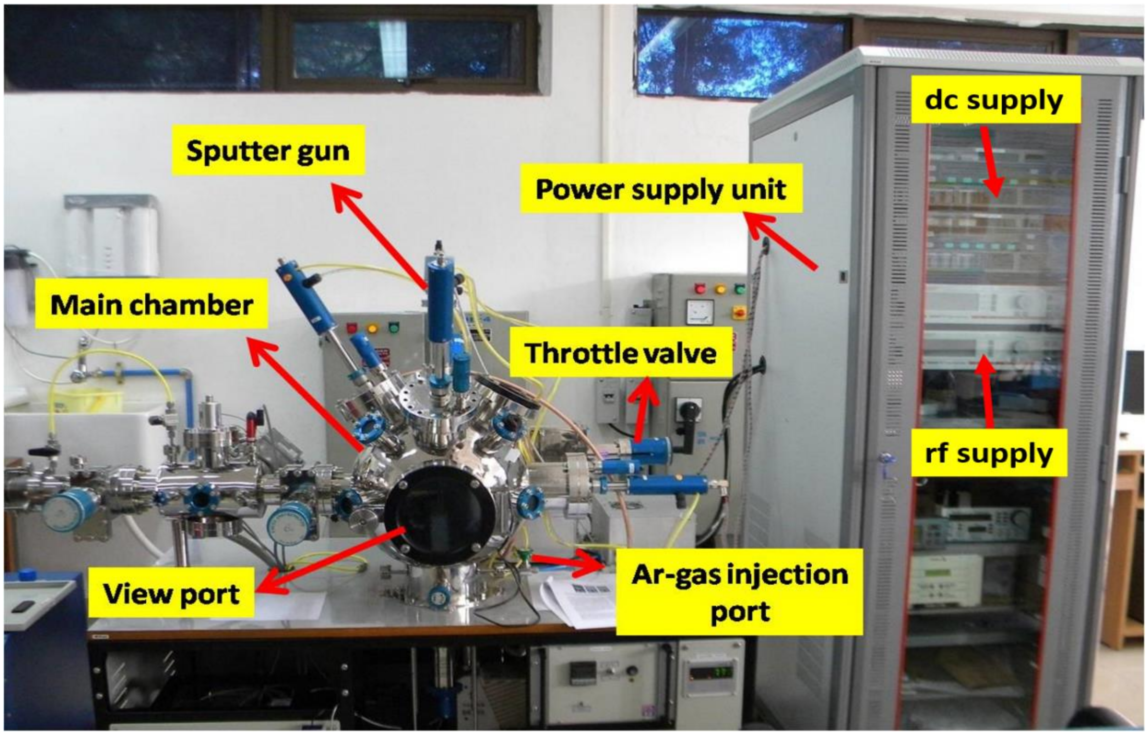

Figure 2.2: Pulsed dc magnetron sputtering setup at SUNAG laboratory.

## 2.2 Surface profilomenter

Surface profilometry is one of the common techniques to measure the film thickness [5]. A stylus is a small tool similar to a modern ball point pen. In a surface profilometer, a diamond stylus is moved across the surface to measure the vertical displacement corresponding to the studied feature. This process involves some mechanical and electronic devices in order to perform the conversion [6]. The sample is mounted on a stage which can move in X- and Y- directions. The measurement of the height or Z-axis is done by the stylus in contact with the surface. The stylus is located at the end of a cantilever arm. The opposite end of the cantilever is counter-balanced by a weight that is mounted in a screw system actuated by a motor; the motor can move the counter-weight closer or further from the pivoting centre of the cantilever, regulating the pressure of the tip. By dragging the stylus over the surface, the cantilever will move in Z- direction (up/down) and the force that the stylus impinges over the sample is controlled by the counter-weight system. The linear Z displacement is converted to an electric signal at the end.

Thickness measurement of the deposited films was carried out by using a surface profilometer (Ambios XP-200, USA) (Fig. 2.3). The stylus is housed in an acoustic isolation hood to reduce vibrational noise during scanning and placed on a large vibration damped sandstone block. The vertical range of the profilometer is 400 μm and its vertical resolution is 0.1 nm at a 10 μm scan length, 1.5 nm at 100 μm scan length, and 6.2 nm at 400 μm scan length [7]. The XP-200 profilometer's stylus is diamond coated one and has a tip radius of 2.0 ± 0.1 μm with an adjustable force range between 0.05–10 mg.

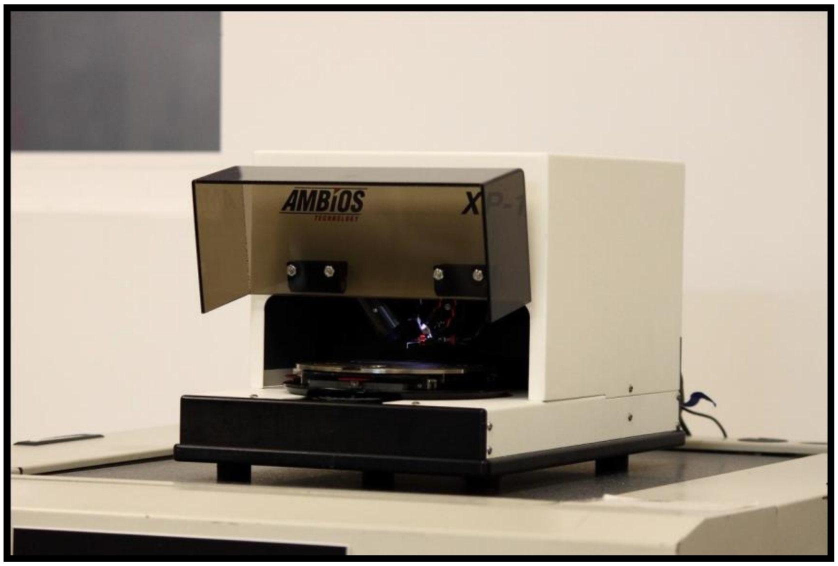

Figure 2.3: Surface profilometer.

The XP-200 profilometer can also calculate surface roughness, waviness, and perform stress analyses on thin films [8]. The film thickness is measured with respect to the substrate where a portion of the substrate is masked prior to the film growth deposition. This helps to get a reasonably good step height during thickness measurement.

## 2.3 Atomoc force microscopy (AFM)

Scanning probe microscopy (SPM) has a family of techniques for studying surface morphology and various nanoscale physical properties [9]. In the process of generating surface topography, a probe moves mechanically over the surface and records the probe-surface interaction as a function of position [10]. This interaction can be manifested in different forms, e.g. tunnelling current, inter-atomic, magnetic, electrical, and frictional force etc. which actually decides the mode of microscopy [10]. The most important among the SPM based techniques is the atomic force microscope (AFM) [9]. AFM is a microscopic technique which is applicable to all types of materials–insulators, semiconductors as well as conductors. This technique measures nanoscale variation in the surface topography by measuring the deflection of a tip (10-30 nm in diameter) attached to the end of a cantilever, as the tip is brought to a close proximity of the surface to be probed.

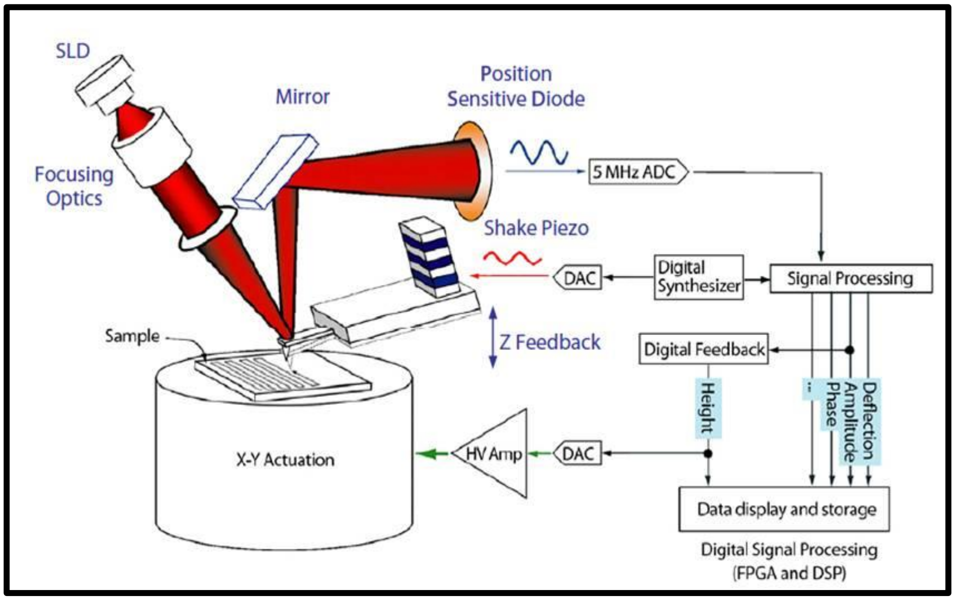

Figure 2.4: Schematic diagram of AFM setup [9].

A schematic diagram on the working principle of AFM is shown in Fig. 2.4. A laser beam is focused on the tip of a highly reflective cantilever head such that the laser beam is reflected onto the surface of a position-sensitive photodetector. The sample is scanned underneath the tip via a piezoelectric scanner made of PZT (lead zirconium titanate). A feedback loop is used to maintain either a constant deflection (contact mode) or oscillatory amplitude (tapping mode) of the cantilever, as the tip is scanned over the sample surface. The force associated with the tip and the sample during scanning is the inter-atomic Van der Waals force. The dependence of this Van der Waals force upon the distance between the tip and the sample is shown in Fig. 2.5, where three regimes of tip-surface distance are labelled: the contact regime, the non-contact regime, and the tapping regime.

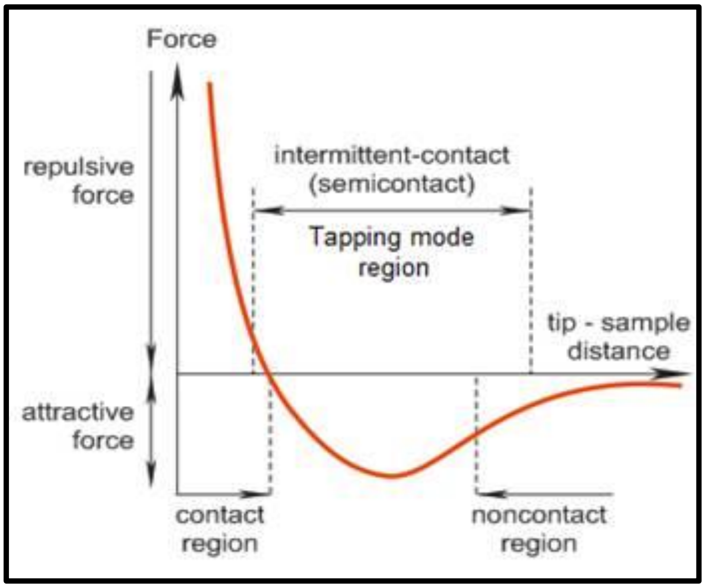

Figure 2.5: Van der Waal’s force as a function of tip to surface distance [9,10].

**Contact or repulsive mode:** In contact-AFM mode, also known as repulsive mode (due to the repulsive nature of the force in this regime), an AFM tip makes soft ‘physical contact’ with the sample by bringing the tip very close to a surface (a few angstroms) [11]. The tip is attached to the end of a cantilever with a low spring constant. As the scanner gently traces the tip across the sample (or the sample under the tip), the contact force causes the cantilever to bend to accommodate changes in the topography. This mode is usually used for hard crystalline surface because strong force involved may cause deformation of soft surfaces [11].

**Non-contact mode or attractive mode:** Non-contact mode AFM is one of several vibrating cantilever techniques in which an AFM cantilever vibrates near the surface of the sample keeping the tip-to-surface distance in the range of tens to hundreds of angstroms [11]. The major advantage of the non-contact mode AFM is its truly non-invasive character.

**Tapping mode:** This mode is also known as intermittent-contact mode [11]. In this case the vibrating cantilever is brought closer to the sample surface so that it just barely hits or ‘taps’ the sample. This mode is a compromise between the contact and the non-contact mode where the cantilever is made to oscillate with or near to the resonant frequency using a piezoelectric crystal so that the tip remains very close to the sample for a short time and then goes far away for a short time. As the oscillating cantilever begins to contact the surface intermittently, the cantilever oscillation necessarily reduces due to energy loss caused by the tip in contacting the surface. The reduction in the oscillation amplitude is used to identify and measure the surface features. This mode allows one to scan soft adsorbates on a substrate with better resolution than in the non-contact mode but with a small interaction (and consequently less modification of the samples) between the tip and adsorbate as in the non-contact mode. Thus, this tapping mode overcomes certain problems associated with conventional AFM scanning method viz. friction, adhesion, electrostatic forces, and other difficulties [9].

**AFM System and measurements:** AFM images in this thesis were acquired with the help of an MFP-3D AFM from Asylum Research, an oxford instrument company, USA in the different modes. The resonant frequency of the cantilevers used for tapping mode is around 300 kHz and the spring constant is 42 N $m^{-1}$. Special attention was given to prevent artefacts in the measurements. Among many advantages of this AFM, an important one is its large area-high precision facility because of which we can scan areas up to 90×90 μ$m^2$ with very high accuracy. Figure 2.6(a) shows different parts of the AFM setup. A zoomed image of the main part of this AFM setup is also shown in Fig. 2.6(b) which shows the scanner, head, base, and thumbwheel. Initially, the head is used to manually bring the tip near the surface. In the next stage, close approach to the surface (separation between the tip and sample remains 80 nm) is controlled by the software to prevent the damage in the tip. A XY-motorized sample stage, attached with the AFM, helps in precise positioning of a sample and checking large scale uniformity in surface morphology within a precision of 500 μm.

### 2.3.1 Conductive atomic force microscopy

Conductive AFM (cAFM) is a powerful current sensing technique that can simultaneously map the topography and current distribution of a sample [12]. In fact, it can be used for electrical characterization of conductivity variations at nanoscale in resistive samples. It allows to measure the current in the range of few picoamps (pA) to tens of nanoamps (nA) [13]. It is useful in a wide variety of materials characterization applications including thin dielectric films, ferroelectric films, nanotubes, conductive polymers, and others [13].

The present system has an ORCA module that consists of a specially-designed cantilever holder and includes a transimpedance amplifier. The gain of the amplifier can be chosen by the user while the standard values range from $5\times10^7$ to $5\times10^9$ V $A^{-1}$. The cantilever holder is used with conductive AFM probes to make the measurement possible. This technique, for measuring the localized conductivity of a sample, is combined with the contact mode AFM imaging. All electrical images used in this thesis were acquired using the contact mode with a Pt-Ir coated Electri-Lever tip, having a nominal spring constant of 1-2 N $m^{-1}$ and good wear characteristics.

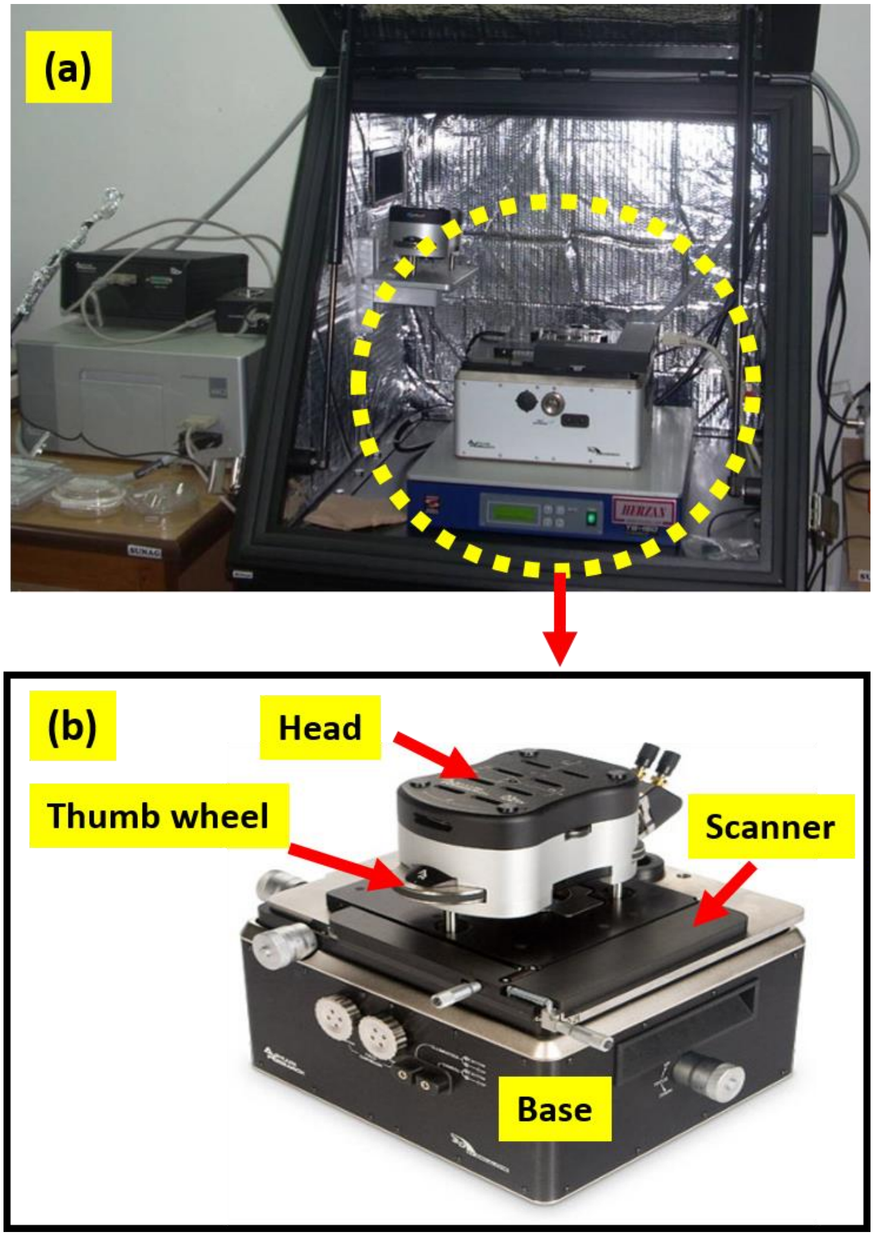

Figure 2.6: (a) AFM setup and (b) various parts of the AFM.

In addition, this system is equipped with the nanopositioning closed loop sensors (NPS™) which make it possible to reproduce the position of the cantilever at a point of interest [13]. The tip is positioned in the centre of the colored circles using the MFP-3D's "pick a point" force curve interface. In fact, the ORCA conductive AFM option for the MFP-3D provides low-noise, flexible transport measurements at the nanoscale. Further, the flexible software environment enables a variety of standard measurements to be made, as well as allowing the researcher to define their own experiments.

## 2.3.2 Kelvin probe force microscopy

Kelvin probe force microscopy (KPFM) is a technique that attempts to ascertain the potential difference between the tip and the sample [14]. The data collected by this sample will represent a combination of three contributing factors: the difference in work function, trapped charge, and any permanent or applied voltage between the tip and the sample. The technique relies on an ac bias applied to the tip to produce an electric force on the cantilever that is proportional to the potential difference between the tip and the sample [15]. In this mode tip is moved at a lift height (>40 nm) and thus, there is no mechanically induced drive. In fact, the only oscillations that the probe will have is to induced by an applied AC bias. An AC bias applied between the tip and the sample produces an electrostatic force between the two. If they are modelled as a parallel plate capacitor (c), then the force between the two plates is proportional to the square of the applied voltage ($V$):

$$F = \frac{1}{2}\frac{\partial C}{\partial Z}V^2 . \tag{2.1}$$

The total potential difference between the probe and the sample is the sum of the applied ac bias ($V_{\text{ac}}$), the potential difference we are trying to measure ($V_{\text{sp}}$), and any dc voltage we wish to apply ($V_{\text{dc}}$).

$$V = V_{sp} + V_{dc} + V_{ac}\sin(\omega t) \quad , \tag{2.2}$$

where, $\omega$ is the angular frequency of the applied ac signal.

If we substitute this into Eq. 2.1 and do some rearrangements, we get [15] the following:

$$F = \frac{1}{2}\frac{\partial C}{\partial z}\left( [(V_{dc} - V_{sp}) + \frac{1}{2}V_{ac}^2] + 2[(V_{dc} - V_{sp})V_{ac}\sin(\omega t)] - [\frac{1}{2}V_{ac}^2\cos(2\omega t)] \right) \tag{2.3}$$

Note that there are three force terms here which are summed together. The first force is the static one, meaning it has no frequency dependence. The second occurs at the ac signal drive frequency, while the third force oscillates at twice the drive frequency. The most important term here, as far as the surface potential is concerned, is the second one since this depends not on the square of the voltage but rather on the potential difference between the tip and the sample and multiplied by the magnitude of the applied ac voltage. This means that if there is a potential difference between the tip and the sample, then when an AC voltage is applied there will be an oscillatory force at the frequency of the drive and it will be proportional to the magnitude of the applied voltage and to the potential difference.

The probes used for KPFM measurements are generally conductive or heavily-doped semiconductors. Insulating probes do not work on the MFP-3D, as the bias is applied to the tip. To implement this technique on the MFP-3D, a two pass technique is used. On the other hand, the first pass is used to determine the topography of the surface, and is done exactly like a standard tapping mode scan line. The second one is used to find the surface potential and the tip is raised above the surface. To do this, a technique called ‘*nap$^{TM}$ mode’* is implemented. During a nap scan, the tip is raised over the surface on a point-by-point basis while the potential feedback loop is implemented.

## 2.3.3 Electrostatic force microscopy (EFM)

EFM maps the electrostatic force gradient between the AFM tip and the sample surface [16]. It is a tapping mode technique using a conductive probe and an applied tip-sample bias. After measuring the topography, the probe retraces each line at a fixed distance (typically 50 nm) above the surface (“*nap mode*”). During this *nap mode* pass, the cantilever is still driven mechanically with the tapping piezo, while the electrostatic force between the tip and the sample surface shifts the resonance frequency of the probe, resulting in changes in both the amplitude and phase of the cantilever. The user can view these directly or apply a phase lock loop (PLL) in order to track the resonance frequency. EFM is useful for measuring conductors embedded near the surface in insulating and semiconducting materials [16]. It can also be used to measure variations in gradient of the capacitance between the tip and the sample.

### 2.3.4 Piezoresponse force microscopy (PFM)

One of the fundamental mechanisms underlying the functionality of materials is electromechanical coupling [17]. These include inorganic materials, such as piezo- and ferroelectrics as well as many biological systems. These type of materials can be used in different applications such as sonar, ultrasonic and medical imaging, sensors, actuators, and energy harvesting [17]. The ability of ferroelectric materials to switch polarization orientation and maintain the polarized state in a zero electric field has led to the emergence of concepts of non-volatile ferroelectric memories and data storage devices [18]. Similarly, the necessity of probing the electromechanical functionalities has led to the development of PFM as a tool for local nanoscale imaging, spectroscopy, and manipulation of piezoelectric and ferroelectric materials. PFM measures the mechanical response when an electrical voltage is applied to the sample surface with a conductive tip of an AFM. In response to the electrical stimulus, the sample then locally expands or contracts, as is shown in Fig. 2.7. When the tip is in contact with the surface and the local piezoelectric response is detected as the first harmonic component of the tip deflection, the phase, $\varphi$, of the electromechanical response of the surface yields an information on the polarization direction below the tip. For $c^-$ domains (polarization vector oriented normal to the surface and pointing downward), the application of a positive tip bias results in an expansion of the sample, and the surface oscillations are in phase with the tip voltage, $\varphi = 0$. On the other hand, for $c^+$ domains, the response is opposite and $\varphi =$ 180° [17,18].

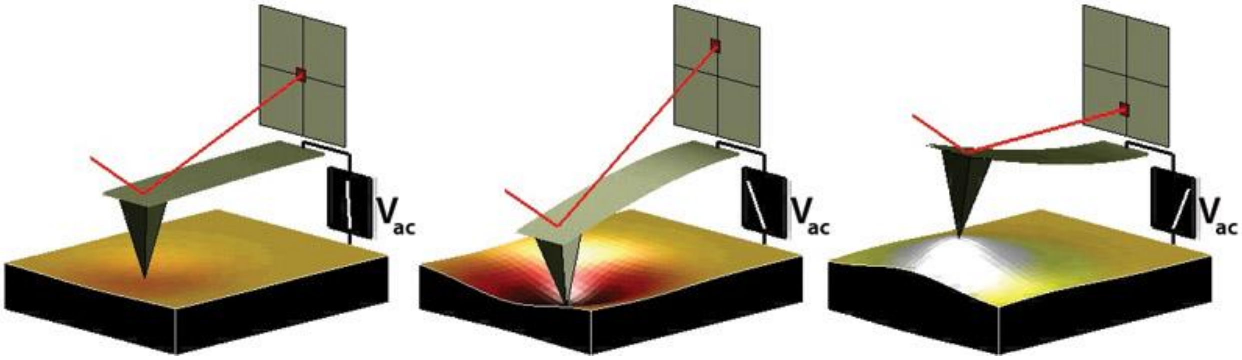

Figure 2.7: Depiction of the PFM operation. The sample deforms in response to the applied voltage. This, in turn, causes the cantilever to deflect, which can then be measured and interpreted in terms of the piezoelectric properties of the sample [17].

Detection of the lateral components of tip vibrations provides information on the in-plane surface displacement, known as lateral PFM. A third component of the displacement vector can be determined by imaging the same region of the sample after rotation by 90°. When the vertical and lateral PFM signals are properly calibrated, the complete electromechanical response vector can be determined, an approach referred to as the vector PFM. Finally, the electromechanical response can be probed as a function of the applied dc bias to the tip, providing information on the polarization switching for ferroelectrics, as well as more complex electrochemical and electro capillary processes.

PFM requires detection of small tip displacements induced by relatively high amplitude and high frequency voltages measured at the same frequency as the drive. Any instrumental crosstalk between the drive and the response will result in a virtual PFM background that can easily be larger than the PFM response itself, especially for weak piezo materials. However, minimizing the crosstalk between the driving voltage and the response imposes a number of serious engineering limitations on the microscope mechanics and electronics. In the past, significant post-factory modifications were required to decouple the drive and the response signals. To overcome this problem, Asylum Research PFM module uses a unique and proprietary design of the head and the high voltage sample holder to eliminate the drive crosstalk.

**Piezo Effect:** The relationship between the strain and the applied electric field (often referred to as the "inverse piezo effect") in piezoelectric materials is described by a rank-3 tensor [19]. The most important component of this tensor for typical "vertical" PFM is the $d_{33}$ component, since it couples directly into the vertical motion of the cantilever. The voltage applied to the tip is

$$V_{tip} = V_{cd} + V_{ac} cos\ (\omega t), \tag{2.4}$$

resulting in a piezoelectric strain in the material that causes cantilever displacement due to the piezoelectric effect.

$$z = z_{dc} + A(\omega, V_{ac}, V_{dc}) \cos(\omega t + \Phi), \tag{2.5}$$

When the voltage is driven at a frequency well below that of the contact resonance of the cantilever, this expression becomes:

$$z = d_{33} V_{dc} + d_{33} V_{ac} \cos(\omega t + \Phi), \tag{2.6}$$

where we have implicitly assumed that $d_{33}$ depends on the polarization state of the material. From this last equation, the magnitude of the oscillating response is a measure of the magnitude of $d_{33}$ and the phase is sensitive to the polarization direction of the sample. Because of this small signal to noise ratio (SNR), piezoelectricity is most frequently detected by a lock-in amplifier connected to the deflection of the AFM cantilever. By employing an oscillating electric field, the low-frequency noise and drift can be eliminated from the measurement [20].

**Spectroscopy Modes:** PFM spectroscopy refers to locally generating hysteresis loops in ferroelectric materials [21]. From these hysteresis loops, information on local ferroelectric behaviors such as imprint, local work of switching, and nucleation biases can be obtained. Understanding the switching behavior in ferroelectrics on the nanometer scale is directly relevant to the development and optimization of applications such as ferro-electric non-volatile random access memory (FRAM), and high-density data storage. Multiple studies have addressed the role of defects and grain boundaries on domain nucleation and growth, domain wall pinning, illumination effects on the built-in potential, and domain behavior during fatigue [22].

## 2.4 Scanning electron microscopy

In scanning electron microscopy (SEM), a finely focused electron beam is scanned in vacuum over the sample surface [22-24]. The novelty of SEM lies in its capability of producing 10-1,00,000 times magnified, three dimensional-like image of surface features of length scale starting from micrometer down to nanometer scale. In SEM, the sample needs to be conducting to prevent charging of the sample surface due to electron emission. In case of non-conducting samples, a very thin gold layer is coated over the sample surface or special beam conditions are applied such as low beam energy or high beam spot size and special detectors are used to prevent only surface charging. As the energetic electrons undergo a series of elastic and inelastic scattering events inside a material, different signals result from these interactions, viz. backscattering of electrons and production of characteristic x-rays, emission of secondary electrons etc. In the most standard imaging mode, the secondary electrons are used. Secondary electrons produce topographic contrast with high resolution and large depth of field. The secondary electron coefficient depends strongly on the electron beam energy; at lower energies, they are generated closer to the surface and thus, they have higher escape possibility.

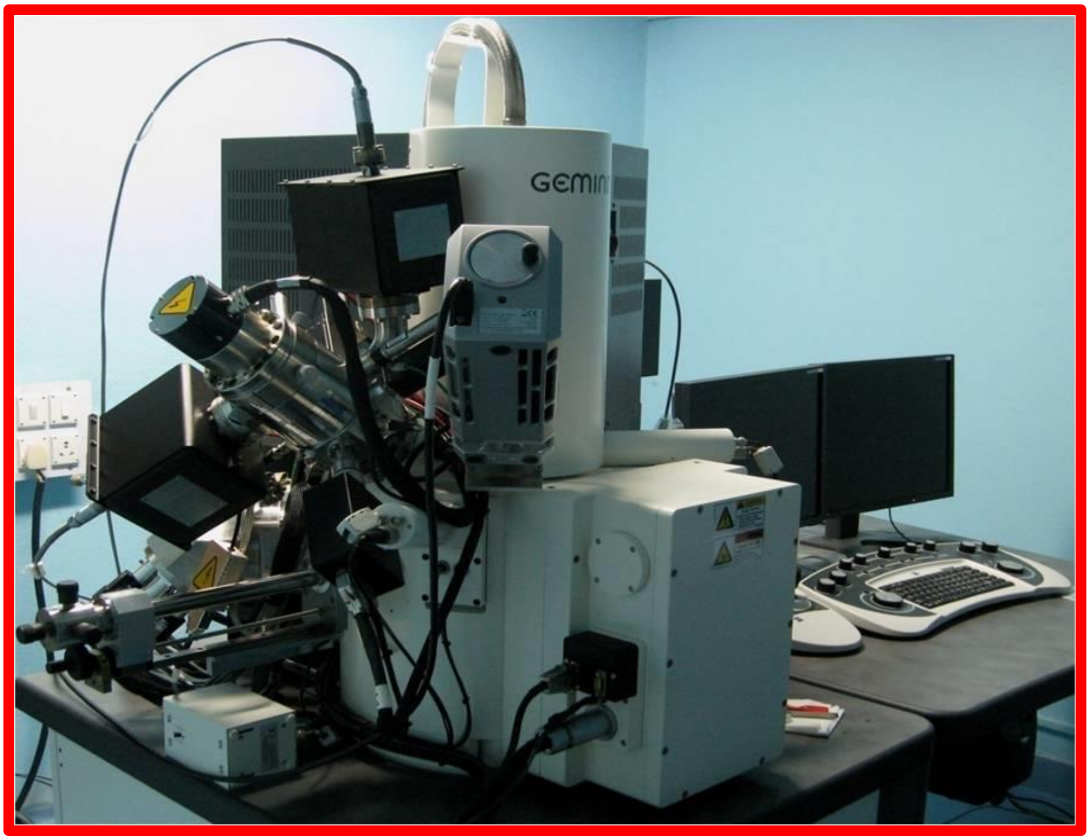

Figure 2.8: Scanning electron microscopy setup.

At higher electron beam energies, the number of secondary electrons increases but they are excited deeper in the specimen. The secondary electron yield depends also on the surface gradient and increases with the increasing tilt angle. Thus, more secondary electrons are produced from the tilted regions of the specimen, and this provides an important mechanism for the surface topographic imaging.

A scanning electron microscope (Fig. 2.8) contains an electron column containing an electron gun and a demagnification system, consisting of electromagnetic lenses for focussing of the electrons from the electron gun to a nanometer size spot on the sample mounted in the sample chamber below the electron column. Detectors for electrons and x-rays emitted from the sample are also mounted inside the sample chamber and a computer interface is coupled with the detectors for displaying the image. In a field emission gun, the cathode is a very sharp tungsten tip attached to a hairpin- shaped tungsten wire. A high voltage bias applied on the cathode causes the development of an intense electric field around the tip, which results in electron emission from the sharp tip. The source size of the electron beam can be of the order of 20 nm in a field emission gun, offering a better resolution in SEM. For the studies presented in this thesis, a Carl Zeiss-make SEM was used [25]. The microscope works with a probe current up to 100 nA and for acceleration voltages from 0.2 to 30 kV.

## 2.5 Transmission electron microscopy (TEM)

Transmission electron microscopes [26,27] are usually used to study sample microstructures, crystallinity aspect, etc. The ideal thickness of the sample may, in some cases, be of the order of 100 nm or even less [27] which transmits electron with relatively less energy loss. The power of the TEM relies on its better resolving power and production of diffraction data and images. The configuration of a transmission electron microscope (TEM) is shown schematically in Fig. 2.9. The electron gun at the top of the microscope produces a stream of energetic electrons. Electron guns with $LaB_6$ crystal filament is commonly used in TEMs. Electrons emerging from the electron gun are focused to a thin, almost parallel beam by a pair of condenser lenses. Some of the electrons in the beam which travel at relatively larger angles with respect to the optic axis is restricted from falling on the sample by a condenser aperture of controllable size placed below the condenser lenses. The sample to be examined is placed at the object plane of the objective lens of the TEM. To obtain a clearly visible image on the phosphor screen, the sample is required to be electron transparent, i.e., thin enough so that a large portion of the incident electron beam is transmitted through the sample. The thickness of any material that the electrons can penetrate through is dependent upon the energy of the incident beam and the elemental composition of the material. In general, it is necessary to thin a sample below 100 nm for observation in TEM and below 50 nm for high resolution TEM (HRTEM). The transmitted portion of the electron beam is focused by the objective lens. An electron diffraction pattern of the sample area, illuminated by incident parallel beam of electrons, is formed at the focal plane of the objective lens (called the back focal plane). The image of the illuminated sample area is formed at the image plane (called the first image plane) of the objective lens, as is indicated in Fig. 2.9. The electron diffraction pattern or the image formed at the image plane is magnified on the viewing screen by the first and the second intermediate lens and the projector lens assembly. In diffraction mode of operation, the first intermediate lens is adjusted in such a way that the back focal plane of the objective lens becomes the object plane of the first intermediate lens. In this case, an electron diffraction pattern is seen on the viewing screen which consists of a bright central spot on the optic axis and spots due to the diffracted electrons. An aperture of a controllable size (called the selected area aperture) is placed at the first image plane. An area of interest can be selected from the sample image formed on the first image plane by the selected area aperture. This selected area acts as a virtual source for the intermediate lens assembly so that only electron diffraction from this area can be observed in the viewing screen and is known as selected area electron diffraction (SAED) imaging. In the imaging mode operation of the TEM, a spot from the electron diffraction pattern can be chosen for imaging by another aperture placed above the SAED aperture, which is called the objective aperture. To obtain an image of the sample, the first intermediate lens is adjusted so that the first image plane becomes its object plane. If the central spot on the optic axis is chosen for imaging by the objective aperture then the TEM image is called a bright field image. If any other diffraction spot is chosen for imaging then the image is called a dark field image. In this thesis, TEM measurements have been carried out using a field emission gun based 300 keV FEI Tecnai G2 S-Twin machine.

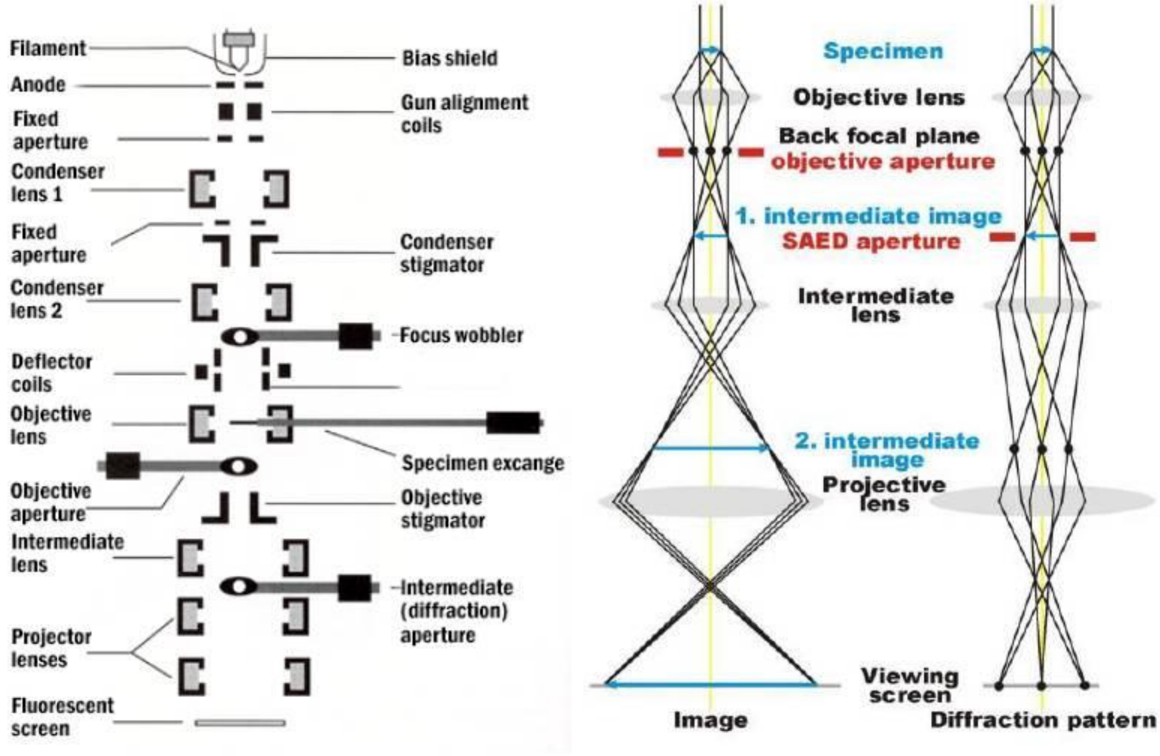

Figure 2.9: Schematic diagram of TEM parts, image formation and diffraction pattern formation process [26].

In case of HRTEM, the image formation is based on the phase contrast mode, which is the most difficult contrast mechanism to image in transmission electron microscopy, but it is also the mode that provides images with a higher resolution. It is related to the phase lag in the electron wave front introduced by the passage of the electrons through the sample. The retarded phase interferes with another wave, giving rise the phase contrast.

It has been mentioned above that for the analysis of solid samples like ion bombarded Si wafers in TEM, thinning of the sample down to 50-100 nm is necessary for a good transmission of the electron beam through the sample. The sample thinning process involves several steps, especially in case of preparing sample for the cross-sectional observation [28].

## 2.6 X-ray diffraction (XRD)

One of the most widely used techniques for evaluating the crystallinity and phase of materials is x-ray diffraction (XRD) [29]. Since the wavelength of x-rays (1-10 nm) are similar in size to interatomic spacing of materials, the waves diffract and scatter upon filling on them. The scattered waves contain information on the atoms and their arrangement in a materials. When a beam of monochromatic x-rays impinges on a sample, most of the radiation gets scattered from the atoms and interferes destructively with radiation scattered from other atoms. Hence, no signal is detected. However, when there is a long range order in the atomic arrangement of a material, scattered x-rays interfere constructively. This condition of interference is defined by Bragg's law (Fig. 2.10):

$$2d\sin\theta = n\lambda, \tag{2.7}$$

where $\theta$ is half the angle between the diffracted beam and the original beam direction, $\lambda$ is the wavelength of the x-rays, and $d$ is the inter-planar spacing between the planes that cause constructive reinforcement of the beam.

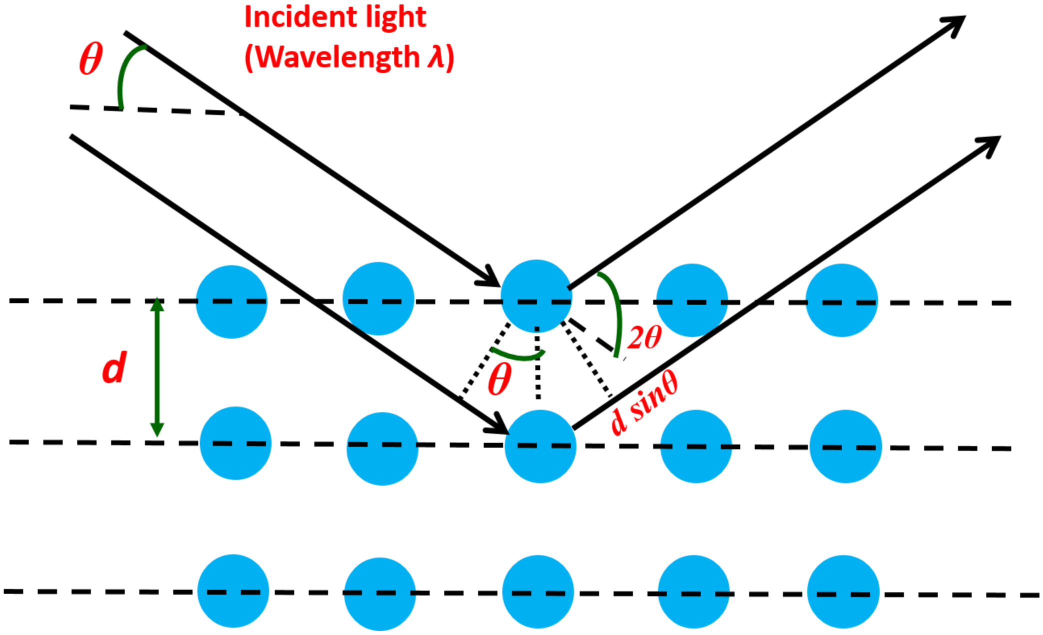

Figure 2.10: Schematic diagram of Bragg's reflection.

The average crystallite size is given by the Scherrer's formula [30]:

$$D = \frac{k\lambda}{\beta \cos\theta} \quad , \tag{2.8}$$

where $D$ is the average crystallite size, $\beta$ is the FWHM of the diffraction peak, $\lambda$ is the wavelength of the incident x-ray, and $k$=0.9 has been chosen according to the literature [30]. Additionally, the relative strain in polycrystalline materials can be measured–based on the shift in the central location of the reflection peak.

Figure 2.11: XRD setup

A Bruker D8 Discover diffractometer (Fig. 2.11) with Cu-Kα radiation source has been used for the studies presented in this thesis. The x-ray source is operated at a voltage of 40 kV. Göbel mirror attachment is used to produce a parallel beam of x-rays, whereas single bounce Ge (220) monochromator is used for high-resolution measurements.

## 2.7 Compositional analysis

Compositional analysis of samples have been carried out using energy dispersive x-ray spectroscopy (EDS) and x-ray photoelectron spectroscopy (XPS). The basic principles and a brief description of these two techniques are presented in the following paragraphs.

### 2.7.1 Energy dispersive x-ray spectrometry (EDX)

Energy dispersive x-ray spectrometry is an analytical technique used for the elemental analysis or chemical characterization of a sample [31,32]. In case of EDX, characteristic x-rays are emitted from a material due to energetic electron beam irradiation which are used to identify the elements present in the material and their relative amounts. An incident electron is inelastically scattered and knocks out a core electron. An electron from a higher orbital fills the empty state (hole) in lower (core) orbital. The energy difference between these two orbitals is released in the form of photons (when the core level electron of high enough atomic number is knocked out, the emitted photons have energy in the x-ray regime), whose energy is characterized for the transition in the respective target atom by following Mosley's law:

$$\sqrt{v} = a\,(Z-b)\,, \tag{2.9}$$

where $v$ is the characteristic x-ray frequency, $a$ and $b$ are constants, and $Z$ is the atomic number of the target atom. The emitted x-rays are detected by spectrally resolved (the number of counts in a given energy width of typically few eV/channel) with an appropriate energy dispersive detector, like Si(Li) or SDD (Si drifted detector).When an incident x-ray photon strikes the detector crystal, its energy is absorbed by electrons in the valence band of the semiconductor and electrons are raised in the conduction band, creating holes in the valence band. A high bias voltage at the front and back face of the detector sweeps this electrons and holes producing a charge signal. The size of the charge signal is proportional to the energy of the incident x-ray photon. The charge signal is converted into a voltage signal by the field effect transistor (FET) circuit attached to the backside of the detector. The electronics in the pulsed processor is used for amplification of the x-ray signal from FET, analog to digital conversion of the data, and measurement of energy of the x-ray photons incident on the detector from the digital voltage signal. The output of the pulsed processor is read by the multichannel analyser inside the control computer where each channel corresponds to a definite energy interval. For each measurement of x-ray energy by the pulsed processor, the count in the channel of the multichannel analyser corresponding to the x-ray energy is increased by one. The total number of counts at different channels are displayed as an x-ray spectrum. The resolution of the x-ray detector (given by the FWHM of the peak of a characteristic x-ray line) is 132 eV as measured for Mn-$K_\alpha$ line (5.9 keV). An EDX spectrum displays peaks corresponding to the energy levels for which the most x-rays had been received. Each of these peaks is unique to an atom, and therefore, corresponds to a single element. The higher the intensity of a peak in a spectrum, the more concentrated the element is in the specimen. An EDX spectrum not only identifies the element corresponding to each of its peaks, but the type of x-ray to which it corresponds as well. For example, a peak corresponding to the amount of energy possessed by x-rays emitted by an electron in the L-shell going down to the K-shell is identified as a $K_\alpha$ peak. In this compositional analysis of selective samples were examined by X-Ray Energy Dispersive Spectroscopy (EDX) in the SEM coupled with an EDX arrangement (Carl Zeiss).

### 2.7.2 X-ray photoelectron spectroscopy (XPS)

X-ray photoelectron spectroscopy (XPS) is a spectroscopic technique which quantitatively measures the elemental composition, chemical state, and charge state of elements present in a material. Since the discovery of photoelectric effect by Heinrich Rudolf Hertzin 1887, it has become the most interesting light-matter phenomenon which was successfully explained later in 1905 by Albert Einstein. Kai Siegbahn and his group in 1954 from Uppsala University (Sweden) developed and recorded the first high-energy-resolution XPS spectrum of the cleaved sodium chloride (NaCl) material [33]. XPS spectra are obtained by irradiating a material with a beam of X-rays, while simultaneously measuring the kinetic energy and number of electrons that escape from the top 1 to 10 nm of the material being analyzed. XPS requires ultra-high vacuum (UHV) conditions.

When x-ray photons interact with a solid, it leads to ionization and the emission of a core (inner shell) electron from the atoms of the solid. Because the energy of the incoming x-ray photon is known, the binding energy of the emitted electrons can be determined by

$$E_{\mathrm{binding}} = E_{\mathrm{photon}} - (E_{\mathrm{kinetic}} + \varphi) \tag{2.10}$$

where $E_{\mathrm{photon}}$ is the energy of the x-ray photon, $E_{\mathrm{kinetic}}$ is the kinetic energy of the electron and is measured by an electron analyzer, and $\varphi$ is the work function of the material. These analyzers use electrostatic and/or magnetic lens units focused through apertures to effectively separate out electrons in a desired narrow band of energies from the wide range of energies contained in all other electrons entering the spectrometer.

For every element there will be a characteristic binding energy associated with each core atomic orbital. This gives rise to a characteristic set of peaks in the photoelectron spectrum at kinetic energies, determined by the photon energy and the respective binding energies. The presence of peaks at particular energies therefore, indicates the presence of a specific element in the sample under study. Intensity of the peaks is related to the concentration of the element within the sampled region.

In the present thesis, the XPS experiments were performed using a setup procured from VG Instruments (the schematic of the system setup is shown in Fig. 2.12). The base pressure of the main chamber is maintained at $1\times10^{-10}$ Torr. The load-lock chamber is equipped with low energy Ar-ion gun. The XPS system is equipped with twin Mg/Al anodes, a hemispherical analyzer, and a channeltron detector unit. The dual anodes generate non-monochromatic X-ray emissions of energies 1253.6 eV for Mg-$K_\alpha$ and 1486.6 eV for the Al-$K_\alpha$ lines. The analyzer is operated with the pass energy of 200 eV for the large survey scans in the range of 1−1000 eV, and 20 eV for the high-resolution scans. The instrumental resolution of the setup is 0.9 eV. The data are acquired at an angle of 45° between the sample normal and the analyzer axis. The final spectra are fitted using the VGX-900 and CASA softwares to get the binding energy positions of the elements.

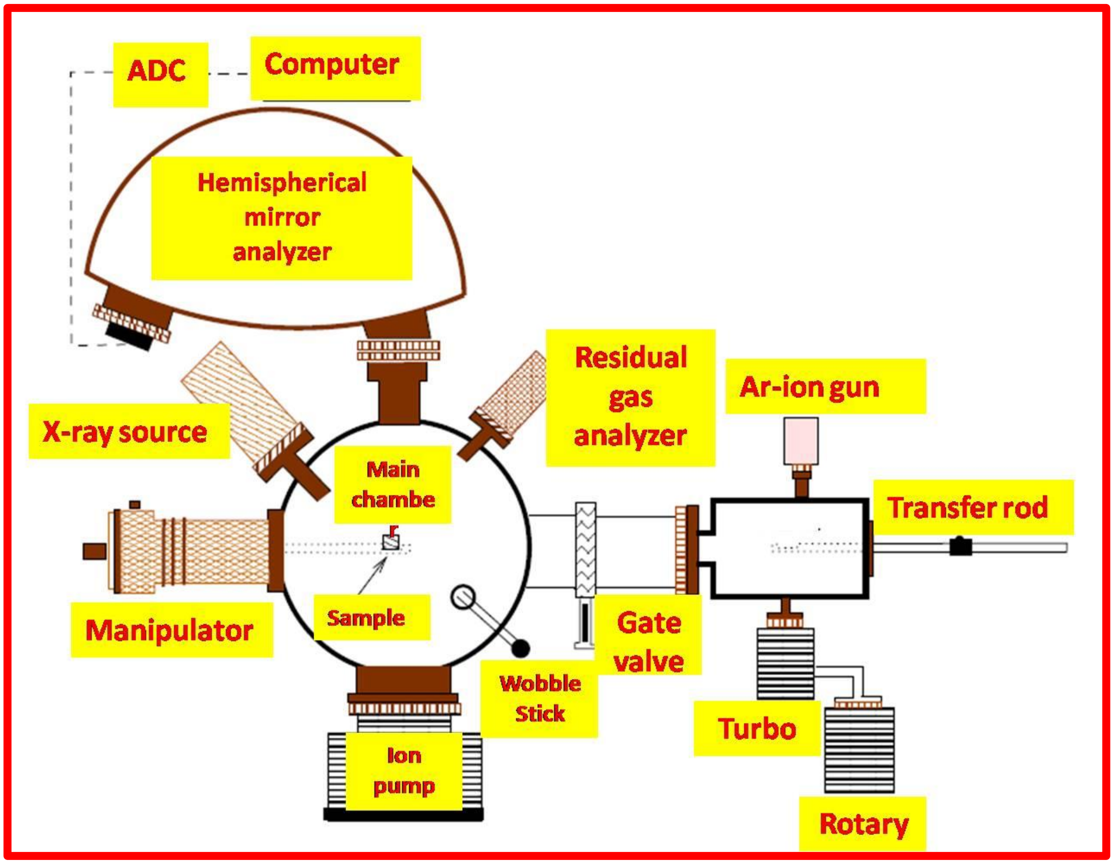

Figure 2.12: Schematic diagram of the XPS setup displaying different components.

## 2.8 Optical studies

Transmittance, absorption, and reflectance measurements have been carried out for various heterojunctions studied in this thesis. The working principles of these techniques are described below.

### 2.8.1 Transmittance

Transmission is the process of passage of radiant flux through a medium through diffusion and scattering. Both processes can undergo scattering (also called diffusion), which is the deflection of the unidirectional beam of radiation into other directions [34]. When no diffusion occurs, the beam of radiation obeys the laws of geometrical optics and the unidirectional beam results in unidirectional beam called specular (or regular) reflection and direct (or regular) transmission. The wavelength of radiation is unchanged in these processes if the medium is stationary. The transmittance, $T$, of a medium is defined by the ratio of transmitted radiant flux to the incident radiant flux. The total transmittance $T$ is subdivided into specular transmittance $T_r$ and diffuse transmittance $T_d$ and the terminology for transmittance follows the same definitions as reflectance except the process is transmission and the word reflectance is replaced by transmittance.

**The absorptance:** The absorptance, $A$, of a medium is defined by the ratio of absorbed radiant flux to incident radiant flux [35]. By the conservation of energy principle, the following relationship holds: $R+T+A= 1$. The emittance (also called emissivity) of a body at a given temperature is equal to the absorptance. Therefore, based on the above expression, the emittance of a body can be deduced in principle by measuring $R$ and $T$. For the opaque materials, no transmission takes place and $T$ is zero. In such cases, the absorptance/emittance can be derived from the measurement of reflectance, $R$, alone. These quantities are defined using an independent vocabulary to account for the effects of geometry and other parameters such as polarization and temperature of the material, etc.

### 2.8.2 Reflectance

Reflectance is the amount of incident light that is reflected by a surface [36]. Optical reflectance measurements have been carried out using a Shimadzu (Model: UV 3101PC)–make ultra-violet-visible-near infrared (UV-Vis-NIR) spectrophotometer (Fig. 2.13) equipped with a specular reflectance measurement accessory. The spectral range that can be studied with this instrument is 200 to 3200 nm. However, in the present thesis, most of the spectra have been collected over a wavelength range of 300–800 nm using 1 nm increment. The reflectance mode works in the specular reflection geometry arrangement with $45^0$ incidence angle of light.

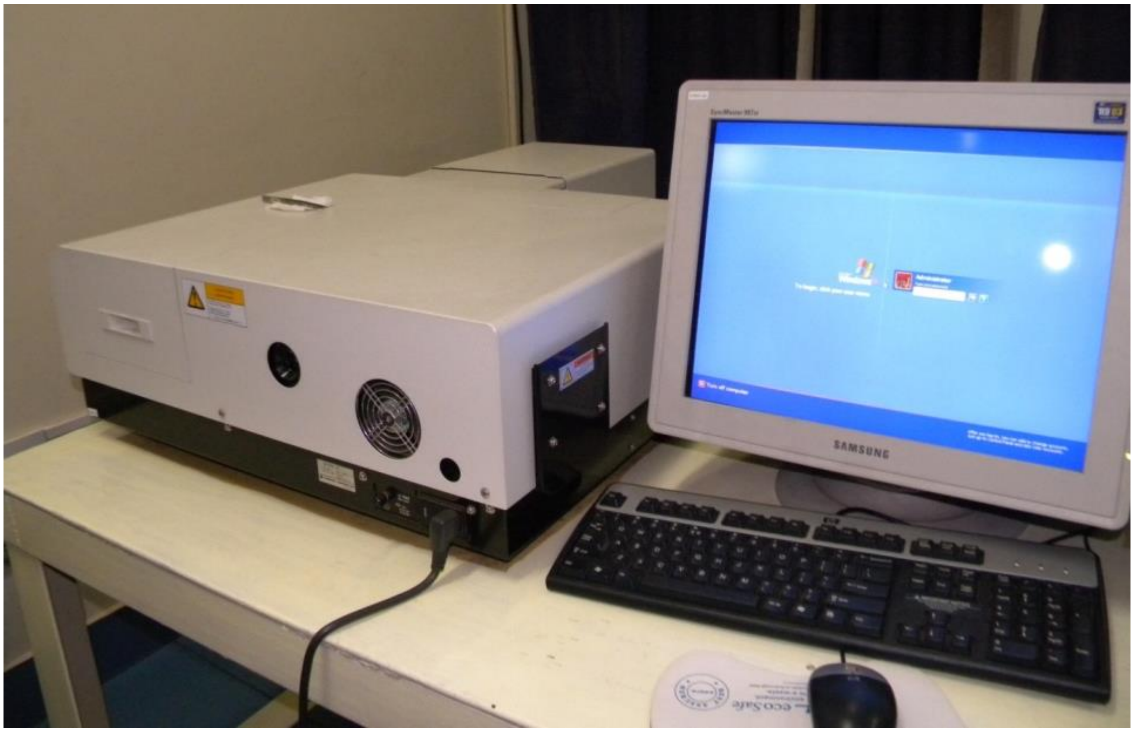

Figure 2.13: UV-Vis spectrophotometer.

## 2.9 Electrical measurements

The electrical properties of thin films, such as electrical conductivity and resistivity, are most commonly performed in the semiconductor industry using a four-point probe system [37]. The four-point probe is often used on test structures throughout the semiconductor fabrication process to ensure and verify the condition of the device between the various processing steps. Two-point probe systems must take into account contact resistance and therefore, it makes the measurements much more difficult and erroneous [Fig. 2.14].

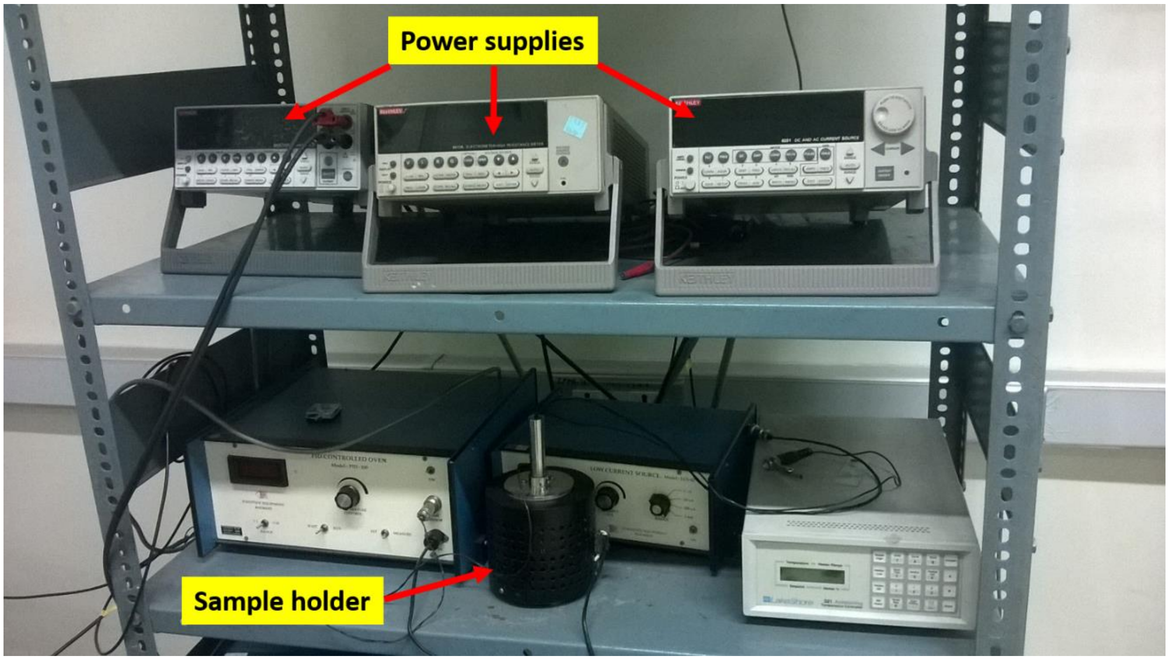

Figure 2.14: Resistivity measurements setup.

### 2.9.1 Resistivity

The resistivity of the films have been determined by the four-probe method with the electrodes in the planar geometry [37]. High conductivity silver paste (SPI Supplies) was used for making contacts. The Ohmic nature of these contacts was confirmed with current-voltage ($I$-$V$) measurements which show a linear behaviour. The resistivity ($\rho$) of the films is calculated applying the Ohm's law, by using the relation $\rho = RA/L$. Here $R$ is the resistance given by the slope of the current-voltage characteristics, $A$ is the area of the film in the planar geometry given by the product of the film thickness and the width of the film, and $L$ is the spacing between the electrodes. The current voltage measurements are carried out using a Keithley source meter unit (Model 2410).

### 2.9.2 *I-V* characteristics

*I-V* characterization consists of basically applying a voltage between two probes in the sample and measuring the current that flows through the sample. *I-V* measurements are carried out using a Keithley 2410 source meter. Each source meter instrument is both a highly stable dc power source and a true instrument-grade 6½-digit multimeter. The power source characteristics include low noise, and precision. The result is a compact, single-channel, dc parametric tester. To do the characterization, we have used a computer program which scans the voltage at a constant rate up to the maximum desired voltage.

### 2.9.3 *C-V* characteristics

Capacitance-voltage (*C-V*) profiling is used for characterizing various semiconductor materials [Fig. 2.15]. In this technique, the applied voltage is varied and the corresponding capacitance (across a junction) is measured and plotted as a function of the applied voltage. Generally, a metal-semiconductor junction or a *p-n* junction are characterized using this technique where the formed depletion region (with its ionized charges) behaves like a capacitor. By varying the applied voltage, one can vary the width of the depletion region. The dependence of the depletion width on the applied voltage provides information about the doping profile, defect densities, and junction barrier height etc. *C-V* measurements can be carried out using a dc or an ac signal. In the present thesis, the capacitance measurements are useful in determining the built-in voltage ($V_{bi}$) as per the following equation mentioned below, where $\varepsilon_0$ is the permittivity of free space, $K_s$ is the dielectric constant, $A$ is the cross-sectional area, and $N_A$ is the acceptor concentration.

Figure 2.15: Capacitance-Voltage measurements setup.

Eq. 2.10 is the depletion capacitance equation for a metal-semiconductor, which is a good approximation and applicable for a highly doped *n*-AZO layer deposited onto a *p*-Si.

$$\frac{1}{C^2} = \frac{2(V_{bi} - V_A)}{qN_A K_S \varepsilon_0 A^2} \tag{2.11}$$

In an ideal system, plotting $1/C^2$ versus $V_A$, the applied voltage, yields a straight line intercepting at $1/C^2 = 0$ with the voltage axis. Following the above equation, the slope of this line is proportional to the carrier density and therefore, a straight line is indicative of a uniform doping distribution. Capacitance measurements, which are ideally frequency independent, indicate the capacitance of the space charge layer. It is however, often the case that these plots are frequency dependent. Two types of plots are possible: curves that are parallel to each other and therefore, having different built-in voltages and curves that have different slopes, converging to the same built-in voltage. The latter behaviour is attributed to the presence of surface irregularities and/or surface states in the semiconductor.

According to the equation, a nonlinear relationship between $1/C^2$ and $V$ are expected when deep levels are present and exposed and when their sites are ionized. Concentration levels increase in a nonlinear fashion as a result of bias changes. Nonlinearity in $1/C^2$ versus $V$ curves is therefore, a direct result orientating from the effect of deep level charges [38]. The studies presented in this thesis have been carried out using a precision LCR meter (HP 4284A).

### 2.9.4 Photoresponsivity studies

In general, optoelectronic property of a heterojunction is categorized in two groups, viz. the generation of photocurrents due to absorption of photons and the emission of photons as a result of electronic excitation in the heterojunction. In this thesis, we concentrate on the former one. The current–voltage characteristics of a heterojunction gets changed under the presence of a light source. The modified expression can be written as [39]:

$$J = J_S\left[\exp\left(\frac{qV}{k_BT}\right)-1\right]-J_R \quad , \qquad (2.12)$$

where $J_R$ is the photocurrent density, $J_S$ is the dark reverse saturation current density, $V$ is the applied voltage, $q$ is electronic charge, and $k_B$ is the Boltzmann's constant. In absence of recombination or generation of carriers, $J_R$ is voltage independent and is equal to the short-circuit photocurrent density, $J_{SC}$. The open circuit voltage, $V_{OC}$, across the heterojunction ($J$=0) can be expressed as:

$$V_{OC} = \frac{k_BT}{q}\ln\left[1+\frac{J_R}{J_S}\right] \quad , \qquad (2.13)$$

The saturation current ($J_S$) depends on the heterojunction structure, while $J_R$ depends on a geometrical dimension of the heterojunction.

The most commonly used mode of illumination for a heterojunction is the perpendicular illumination where the photons are incident on the front surface of the wide–band gap material and are perpendicular to the plane of the junction. In this case the high energy photons are absorbed in the wide band gap material, while the low energy ones penetrate through the wide band gap material and are absorbed in the narrow band gap material near the interface. This phenomenon is called the ‘window effect’.

A heterojunction which responds to the incident photons is known as ‘photon detectors’. The photon detectors measure the rate of arrival of quanta and show a selective wavelength dependence of the response (in the form of current or voltage) per unit incident radiation power. Photovoltaic cell (solar cell) is a type of the photo detector where the energy of sun light is directly converted into electricity.

A solar cell under illumination is characterized by the following parameters: responsivity, short-circuit current, open-circuit voltage, the fill factor, and the power conversion efficiency. In the following paragraphs these parameters are clarified [40].

**Responsivity:** Responsivity ($R_\lambda$) is defined as the ratio between the output electrical signals [voltage or current ($I_{ph}$)] to the incident radiation power ($P_{in}$). The responsivity for monochromatic light of wavelength, $\lambda$, incident normally is given by [41]:

$$R_\lambda = \frac{I_{ph}}{P_{in}} \quad . \tag{2.14}$$

The photovoltaic testing system (PTS, Sciencetech, Canada), used for the present case, includes a 150 W Xe lamp and a monochromator to tune the light source. A setup is shown in Fig. 2.16 for better realization. A source meter is used as an active load permits operating the test cell at various load conditions, including the short-circuit, compensating for a series resistor required to sense the current produced by the modulated monochromatic light.

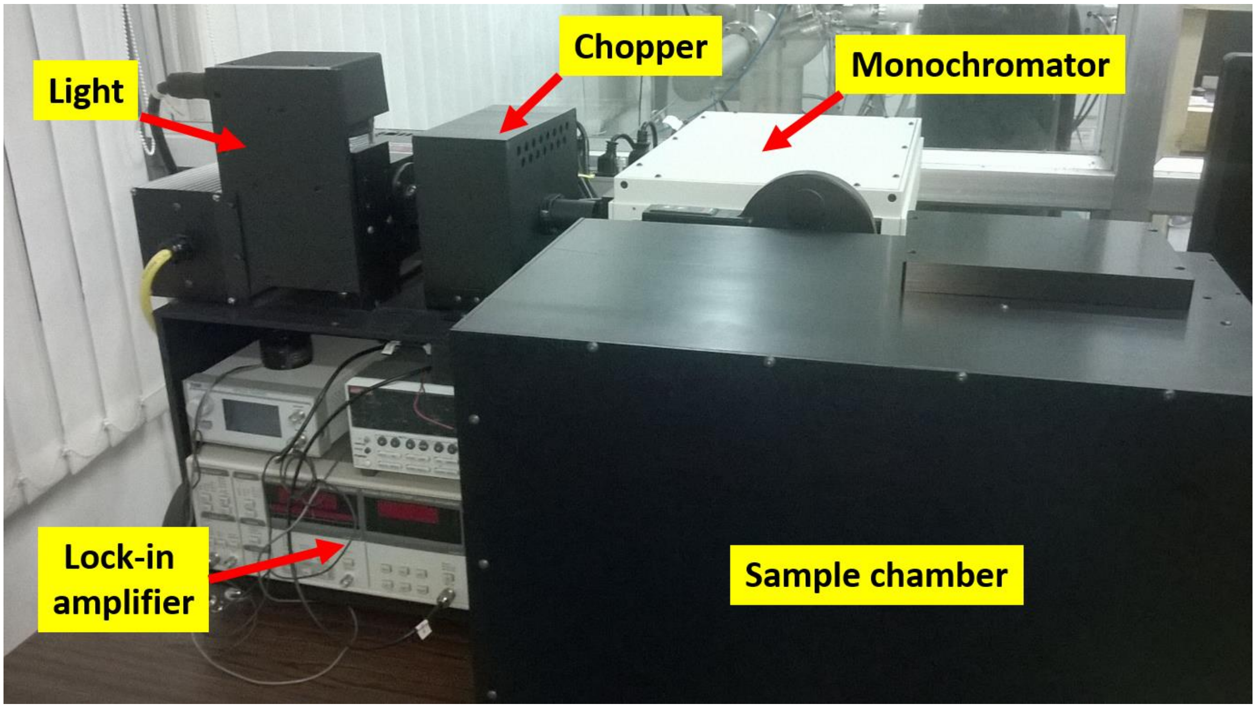

Figure 2.16: Experimental setup of the Photoresponsivity measurement setup.

This sensed current plus a reference signal at the frequency of the light modulation are both fed into the precision lock-in amplifier to allow measurement of the photocurrent generated by the modulated monochromatic light. PTS1 software, provided by the supplier, allows us to measure the spectral response (*SR*) and *I*-*V* characteristics of the cell. It includes a SCIRUNSR *I*-*V*-Test measurement system, precision lock-in amplifier, and the system software. The software controls the monochromator, the source meter, and lock-in amplifier to automatically measure the *I*-*V* characteristics and *SR* versus wavelength, plotting the results on the screen and providing the calculated values, including $V_{OC}$, $I_{SC}$, $P_{max}$, fill factor (*FF*), and the raw measurements to a standard file format. Key features of this instrument are listed below:

- Monochromator with automated order sorting filters
- Monochromatic probe light area adjustable from 2 mm to 5 mm diameter
- Monochromatic probe light power of 125 mW total (white light)

- Keithley 2400 Series source meter
- Bias voltage ranges from 0-200 V
- Calibrated reference detector
- Optical chopper and drive
- Stanford SR800 series lock-in amplifier
- Photocurrents measurable from 1 pA to 1 μA
- Automated switching of lock-in input signals from the reference detector to the sample current measurement
- Target table with dual cell holder having a 150 mm height adjustment.

# Bibliography

[1] R.V. Stuart, Vacuum technology, thin film, and sputtering. 1985: Academic Press, Inc.

[2] J. B. Webb, Thin films for free atoms and particles, Chapter 6. 1985: Academic Press, Inc.

[3] A. Anders, Thin solid Films 502 (2006) 22.

[4] P. J. Kelly, P. S. Henderson, R. D. Arnell, G. A. Roche, D. Carter, J. Vac. Sci. Technol. A 18 (2000) 6.

[5] www.advanced-energy.com.

[6] D. H. Lee and N. G. Cho, Meas. Sci. Technol. 23 (2012) 105601.

[7] http://www.rochester.edu/urnano/facilities/Ambios_profilometer/index.html.

[8] http://imel.demokritos.gr/docs/Facilities/SURFACE-PROFILER-EQUIPMENT.pdf

[9] G. J. Legget, "Scanning Tunneling Microscopy and Atomic Force Microscopy", in Surface Analysis: The Principal Techniques, edited by J. C. Vickerman. 1997: John Wiley & Sons, Chichester.

[10] K. S. Birdi, Scanning Probe Microscopes: Applications in Science and Technology. 2003: CRC Press, Boca Raton.

[11] Y. Sugawara, "Atomic Force Microscopy", in Roadmap of Scanning Probe Microscopy, edited by S. Morita. 2007: Springer, Berlin - Heidelberg.

[12] https://www.asylumresearch.com/Applications/Orca/Orca.shtml.

[13] http://www.asylumresearch.com/Applications/ElectricalCharacterization/ElectricalSuite.pdf

[14] L. Nony. Principles of Kelvin Probe Force Microscopy and applications. DEA. Laurent NONY, 1st German-French Summer School on noncontact -AFM Porquerolles. 2013: France.

[15] W. Melitz, J. Shena, A. C. Kummel, S. Lee, Surface Science Reports 66 (2011) 1.

[16]http://www.parkafm.com/images/spmmodes/dielectric/Electrostatic-Force-Microscopy-(EFM).pdfver=1.2.

[17] https://www.asylumresearch.com/Applications/PFMAppNote/PFM-ANHR.pdf

[18] J. S. Meena, S. M. Sze, U. Chand, and T. Y. Tseng, Nanoscale Research Letters 9 (2014) 526.

[19] file:///C:/Users/Mohit%20kumar/Downloads/246.full.pdf

[20] https://www.asylumresearch.com/Products/PFM/PFMDataSheetHR.pdf

[21] A. Gruverman and A. Kholkin, Rep. Prog. Phys. 69 (2006) 2443.

[22] D. K. Schroder, Semiconductor material and device characterization. 2006: John Wiley & Sons, Inc., Hoboken, New Jersey, 3rd ed.

[23] B. G. Yacobi, D. B. Holt, and L. L. Kazmerski, "Scanning Electron Microscopy", in Microanalysis of solids, edited by B. G. Yacobi, D B Holt, and L. L. Kazmerski. 1994: Plenum Press, New York.

[24] P. S. Turner, C. E. Nockolds, and S. Bulcock, "Electron Microscope Techniques for Surface Characterization", in Surface Analysis Methods in Materials Science, edited by D. J. O'Connor, B. A. Sexton, and R. St C. Smart. 2003: Springer, Berlin Heidelberg.

[25] http://www.zeiss.de.

[26] A. J. G. Reed, "Transmission Electron Microscopy", in Microanalysis of Solids, edited by B. G. Yacobi, D. B. Holt, and L. L. Kazmerski. 1994: Plenum Press, New York.

[27] N. Yao and Z. L. Wang (eds), Handbook of microscopy for nanotechnology. 2005: Kluwer Academics Publishers, New York.

[28] B. Satpati (Ph. D. Thesis, Institute of Physics, Bhubaneswar)

[29] http://www.bruker.com/products

[30] A. L. Patterson, Phys. Rev. 56 (1939) 978.

[31] D. K. Schroder Semiconductor material and device characterization, second edition. 1998: A Wiley publication, New York.

[32] P. E. J. Flewit and R. K. Wild, Physical methods for material characterization, second edition. 2003: IOP publishing, London.

[33] K. Siegbahn, and K. I. Al. Edvarson, Nuclear Physics 1 (1956) 137.

[34] I. Chambouleyron, E. G. Birgin and J. M. Martínez, in Optical Interference Coatings 9, OSA Technical Digest Series. 1998: Optical Society of America, Washington, DC.

[35] I. Chambouleyron and J. M. Martínez, Handbook of Thin Film Materials, edited by H. S. Nalwa. 2001: Academic, San Diego.

[36] F. L. Forgerini and R. Marchiori, Biomatter. 4 (2014) 28871.

[37] F. M. Smits, Measurement of Sheet Resistivities with the Four-Point Probe. Bell System Technical Journal, 37 (1958) 711.

[38] http://www.evaluationengineering.com/articles/200812/fundamentals-of-semiconductor-c-v-measurements.php

[39] B. Sharma and R. Purohit, Semiconductor Heterojunctions First edition. 1974: Pergamon Press.

[40] A. Tom, PhD thesis (2006): https://lirias.kuleuven.be/bitstream/1979/402/5/PhD.

[41] http://www.nrel.gov/docs/legosti/fy98/23878.pdf.

# CHAPTER 3

## 3. Electrical transport in AZO thin films: Roles of grain boundaries, metal-like conductivity, and UV absorption

In this chapter, we optimized the growth and demonstrate the role of grain boundaries in charge transport for Al-doped ZnO (AZO) thin films. In particular, we study on room temperature (RT) diode characteristics of *n*-AZO/*p*-Si heterostructures by current-voltage and capacitance-voltage measurements. In addition, the current-voltage characteristics of an AZO/Si heterojunction diode is investigated over a temperature range of 293 and 423 K. Further, temperature-dependent resistivity measurement performed on AZO thin films grown on glass substrates show metallic-like conductivity, which is explained on the basis of local annealing of defects, mainly vacancies, in the AZO layer. Based on our experimental findings, we construct a parametric phase diagram to elucidate the transition from one to the other conduction mechanism. Following that, using conductive atomic force microscopy and Kelvin probe force microscopy, we study the local electrical transport properties of AZO thin films. In addition, a strong enhancement in the local current at grains is observed after exposing the film to ultra-violet (UV) light which is attributed to persistent photocurrent. Further, it is shown that UV absorption gives a smooth conduction in AZO film which in turn gives rise to an improvement in the bulk photoresponsivity of an *n*-AZO/*p*-Si heterojunction diode. This finding is in contrast to the belief that UV absorption in an AZO layer leads to an optical loss for the underneath absorbing layer of a heterojunction solar cell. The present study will be useful to understand the roles of grain boundaries as well as self-heating for AZO-based devices.

## 3.1 The growth of low resistive and high transitive AZO thin film at room temperature

### 3.1.1. Experimental detail

A film thickness of 120 nm was deposited on ultrasonically cleaned SLG and Si substrates at RT using a pulsed dc magnetron sputtering system (Excel Instruments; Advanced Energy System). Commercially available (MTI Corporation), 99.99% pure $ZnO:Al_2O_3$ (2 wt.%) sputtering target (50.8 mm dia×6.35 mm thick) was used to grow AZO thin films. Ultra-pure (99.999%) argon gas was injected into the chamber with a flow rate of 30 sccm to maintain the working pressure of $5\times10^{-3}$ mbar during sputtering. A dc power of 100 W (frequency=150 kHz, reverse time=0.4 μs) was supplied to the AZO target and the substrate was rotated with a speed of 3 rpm for achieving uniform film thickness, where the target-to-substrate distance was maintained at 80 mm. The deposition was carried out at various angles ($\theta$) in the range of 0-80° where the angle of incident flux was measured with respect to the target normal. The optical properties of as-deposited AZO films was measured by an ultra-violet-visible-near infrared (UV-Vis-NIR) spectrophotometer in the wavelength range of 300-700 nm. In addition, linear four-probe technique was used to measure the growth angle-dependent change in resistivity of AZO films.

Kelvin probe force microscopy was employed to measure the work function of AZO films in lift-mode using an Ir/Pt-coated silicon tip (Nano world) with a resonant frequency of about 75 kHz and force constant of about 2.8 N $nm^{-1}$. Simultaneously, the surface topography also also recorded by atomic force microscopy in tapping mode. The commercial software (IGOR PRO 6.05) together with the Asylum Research code (version 080501-1804C) were used to get the statistical distribution of contact potential.

### 3.1.2 Results and discussion

The optical transmittance spectra of all the films deposited at different deposition angles are shown in Fig. 3.1(a). From this figure, it is observed that the average transmittance of all the AZO films (in the visible range) is greater than 80% till the growth angle of 70°, whereas it reduces a bit (<75°) for the film grown at an angle of 80°. In addition, the observed sharp decrease in the transmittance around 360 nm can be attributed to the fundamental absorption edge of AZO [2,3].

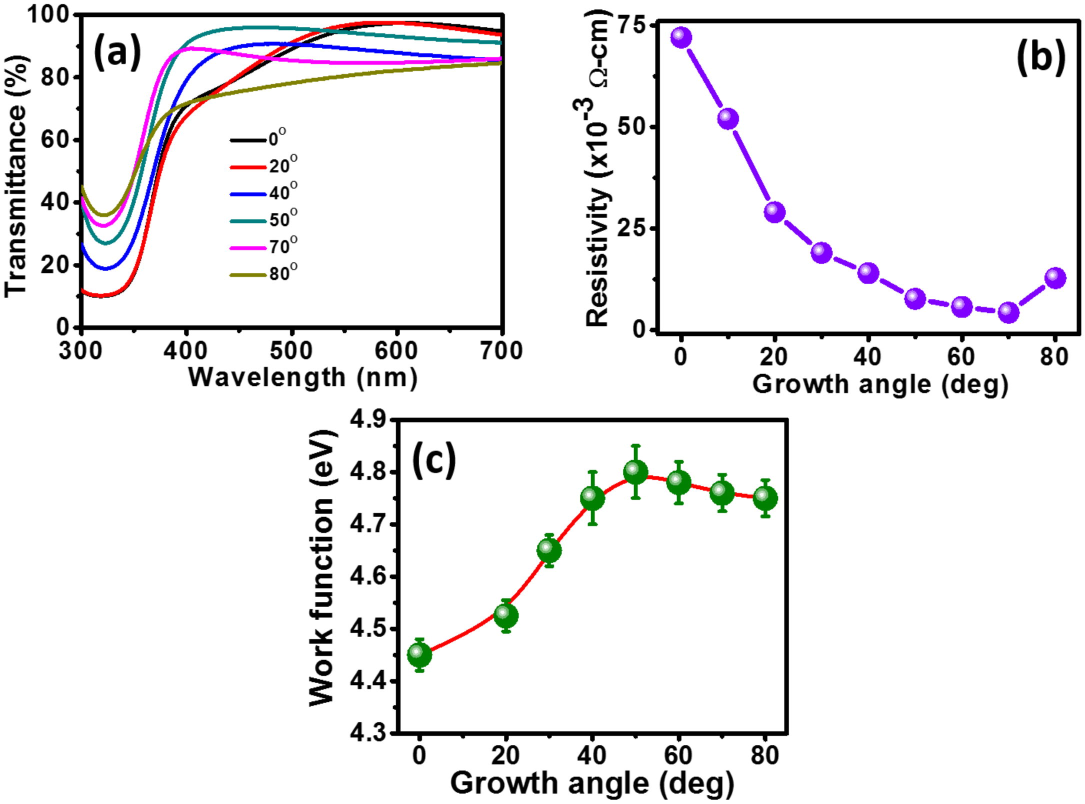

Figure 3.1: (a) show the optical transmittance data for AZO films grown at different angles (b) Variation in the resistivity of AZO films as a function of deposition angle, and (c) shows the growth angle-dependent variation in the work function of the AZO films.

Fig. 3.1(b) shows the growth angle-dependent variation in the resistivity, measured by the linear four-probe technique. A sharp decrease in the resistivity is evident with an increase in the deposition angle from 0° to 70°, whereas a little increment is observed corresponding to the growth angle of 80°. The minimum resistivity is found to be in the range of $5.6\text{-}4.3\times10^{-3}$ Ω-cm corresponding to the growth angles of 50°-70°. On the other hand, a small increment in the resistivity at $80^0$ can be attributed to the presence of porosity in the films at higher angles. The change in crystallinity with the growth angle can also influence the nanoscale electrical properties [2]. In order to address this issue, KPFM measurement is employed to extract the work function of the AZO films. It is known that the observed $V_{\mathrm{CPD}}$ can be converted into the work function of a material, using the following relation [3]: $W_{\mathrm{sample}} = W_{\mathrm{tip}} - qV_{\mathrm{CPD}}$, where $W_{\mathrm{sample}}$ and $W_{\mathrm{tip}}$ are the work function of the sample and the tip, respectively and $q$ is the electronic charge. The measured work function is seen to increase up to 50° (4.78 eV), whereas it decreases slightly for the films deposited up to an angle of 80° [Fig. 3.1(c)]. Since, for a better electrical contact, a higher work function is desired and thus, it is infer that the film grown at an angle of 50° can be an optimized one. The observed results indicate that not only the bulk but also the nanoscale properties can be tuned by changing the growth angle.

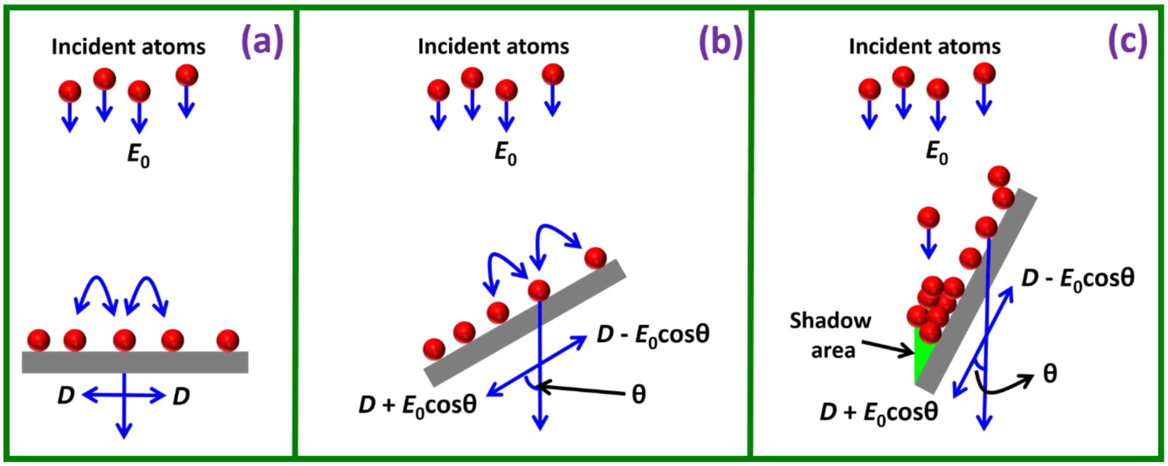

Figure 3.2: (a): Schematic representations of the films deposited at normal incidence, an arbitrary oblique angle, and a grazing incidence angle are presented in (a), (b) and (c), respectively.

The observed experimental findings can be attributed to the growth dynamics of the films. It is known that grain growth in a thin film is governed by the surface diffusion [4]. In fact, a higher surface diffusion leads to a higher grain size. Generally, surface diffusion increases due to an increase in the substrate temperature [5]. Thus, the observed results can also be understood in light of surface diffusion. For instance, for the film deposited at 0°, the atoms have an equal diffusion energy ($D$) in all directions [Fig. 3.2(a)] [4,5]. In this case, the presence of a large number of grain boundaries in the film will give rise to a large number of defects produced due to incomplete atomic bonding, resulting in an increase in the scattering centres (or resistivity) of the same. On the other hand, for an oblique angle deposition, the incident atoms on the substrate will undergo an asymmetric diffusion [Fig. 3.2(b)]. In fact, incident atoms have an initial energy ($E_0$) where a component of this energy ($E_0\cos\theta$) will enhance the atomic diffusion [Fig. 3.2(b)] on the surface, giving rise to an improvement in the grain growth or crystallinity. As the growth angle increases further, the surface diffusion increases, albeit at higher angles (>70°), the shadowing effect also comes in the picture [Fig. 3.2(c)]. This causes an increase in the porosity of the film, which in turn increases the resistivity of the film. In fact, there is an interplay between the surface diffusion and shadowing in case of oblique angle deposition [4,5]. One can infer that, for the films grown at low oblique incidence angles, the formation of nanostructures are governed by the surface diffusion, whereas for the films grown at higher angles, shadowing will be the dominating factor.

### 3.1.3 Conclusions

Further, we demonstrate that low resistive films ($5.6\text{-}4.3\times10^{-3}$ Ω-cm) can be obtained for the growth angle between 50° to 70°. A continuous change in the work function with growth angle is also observed, which becomes the highest (4.78 eV) corresponding to 50°. Thus, it can be concluded that the AZO film grown at 50° shows the best optimized physical properties to use it as a transparent conductive contact and for further experiments we will use this angle for deposition.

## 3.2 Effect of grain-boundaries on electrical properties of *n*-ZnO:Al/*p*-Si heterojunction diodes

### 3.2.1 Introduction

ZnO is a good candidate for fabricating solar cells [6], heterojunction diodes [7] and photodetectors [8] due to its wide band gap ($E_g$~3.3 eV at RT), large binding energy (60 meV), and high transparency. Recently, doping of group III elements in ZnO films [9] (especially Al-doping) has also generated considerable interest. For instance, they are not only important for different applications including fabrication of transparent conductive oxide [6,10,11] but also from the fundamental standpoints. However, the thickness dependent optimization of optical and electrical properties of AZO films is essential for photovoltaic and optoelectronic applications, where the carrier concentration dependent resistivity can reach the value as low as $10^{-4}$ Ω-cm [12] considering the substitution of Zn (atomic radius:0.054 nm) by Al (atomic radius:0.074 nm) atoms. For a moderate Al-doping, it is known that the broadening of $E_g$ is associated with the partial filling of states above the conduction band minimum of AZO – known as Burstein-Moss effect [13], whereas the carrier concentration above the Mott critical density is known to be associated with the decreasing $E_g$ due to the modification in the bands through electron-electron and electron-impurity interactions [14]. Different techniques have been employed so far to synthesize AZO films, which include pulsed laser deposition, [10] chemical processing [15], direct current (dc) magnetron sputtering [8] etc.

In this work, we study the effect of AZO thickness on the current-voltage (*I-V*) and capacitor-voltage *(C-V)* characteristics of *n*-AZO/*p*-Si heterojunction diodes and how the grains contribute in the same. In fact, we will show systematic reductions in the turn-on potential and electrical resistivity with increasing AZO film thickness. In order to explain these behaviour, thickness-dependent evolution of grains in the deposited AZO films was investigated by atomic force microscopy (AFM) and scanning electron microscopy (SEM), while their nature of crystallinity was examined by x-ray diffraction (XRD).

## 3.2.2 Experimental

AZO films were deposited on ultrasonically cleaned *p*-type Si(100) wafers (with its native oxide) at RT using a pulsed dc magnetron sputtering system (Excel Instruments). Commercially available 99.99% pure AZO target having 50.8 mm diameter × 6.35 mm thickness and composed of 98 wt.% ZnO and 2 wt.% $Al_2O_3$ (Testbourne Ltd., England) was used for depositing AZO thin films in a vacuum chamber with a base pressure of $3\times10^{-7}$ mbar. Ultra-pure (99.999%) argon gas was injected into the chamber with a flow rate of 27 sccm to maintain the working pressure of $5\times10^{-3}$ mbar during sputtering. A dc power of 100 W (frequency=150 kHz, reverse time=0.4 µs) was supplied to the AZO target and the substrate was rotated with a speed of 3 rpm for achieving uniform film thickness, where the target-to-substrate distance was 80 mm.

Four AZO thin films were deposited for 5, 10, 20, and 30 min with an average deposition rate of 6.2 nm $min^{-1}$ on Si wafers (sliced into small pieces of $1\times1$ $cm^2$) and named as S1, S2, S3, and S4, respectively. The corresponding thicknesses were measured to be about 30, 70, 120, and 175 nm, respectively within the instrumental error, using a surface profilometer (Ambios, XP-200, USA). Many films were deposited to check the uniformity in thickness before making the devices. Phase identification and crystalline orientation were investigated by XRD using a Cu-$K_\alpha$ radiation ($\lambda$=0.154 nm) over a $2\theta$ scan range of 20-60°. Surface morphology was examined by *ex-situ* AFM in tapping mode. For each sample, several images were taken from different regions to check the uniformity and to estimate the average grain size as well as the root mean square (rms) roughness.

In addition, the deposition time dependent evolution of grains in AZO films was monitored by SEM in both plan-view and cross-sectional geometries using 5 keV electrons. Silver paste was used to make the electrical contacts on top of the AZO films and back side of the Si substrates. The formation of Ag/AZO/Si/Ag heterostructure diodes was verified by taking *I*-*V* characteristics using an electrometer based resistivity measurement setup. The junction barrier height was investigated by performing capacitance-voltage (*C*-*V*) measurements at a frequency of 1 MHz using precision LCR meter.

### 3.2.3 Results and discussion

Figures 3.3(a) and (b) show AFM images of S1 and S4 samples, exhibiting a gradual change in the surface morphology with increasing deposition time. It appears that the average grain size increases with deposition time (prominent in S4). The average grain size was measured to be 22, 26, 32, and 36 nm for S1, S2, S3, and S4, respectively (all images are not shown).

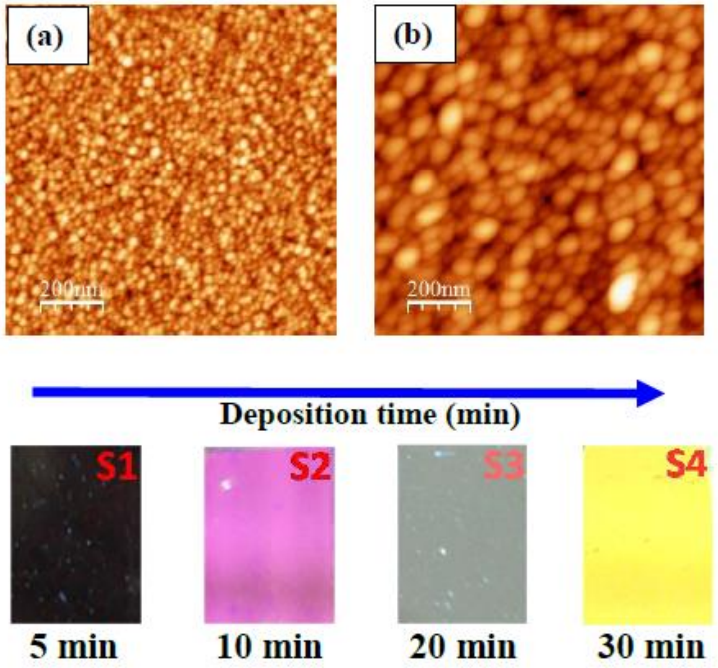

Figure 3.3: AFM micrographs (1µm×1µm) of AZO films deposited on Si: (a) S1 and (b) S4 with height scales of 6.3 nm and 22.18 nm, respectively. S1 to S4 are the original photographs of the films deposited for 5 min, 10 min, 20 min, and 30 min, respectively.

One can also see a clear change in colour on the surface (using a camera) with increasing thickness (photographs shown below the AFM images of S1 and S2) and can be explained in the framework of strain-induced variation in the band gap with increasing AZO film thickness [16]. On the other hand, the rms surface roughness is found to increase monotonically with increasing film thickness (Table 3.1). Besides investigating the thickness variation of the AZO films, as a function of deposition time, by SEM (under the cross-sectional geometry), we have seen the formation of elongated grains — tightly packed and aligned normal to the Si surface. Typical plan-view and cross-sectional SEM images of S3 are shown in Figure 3.4.

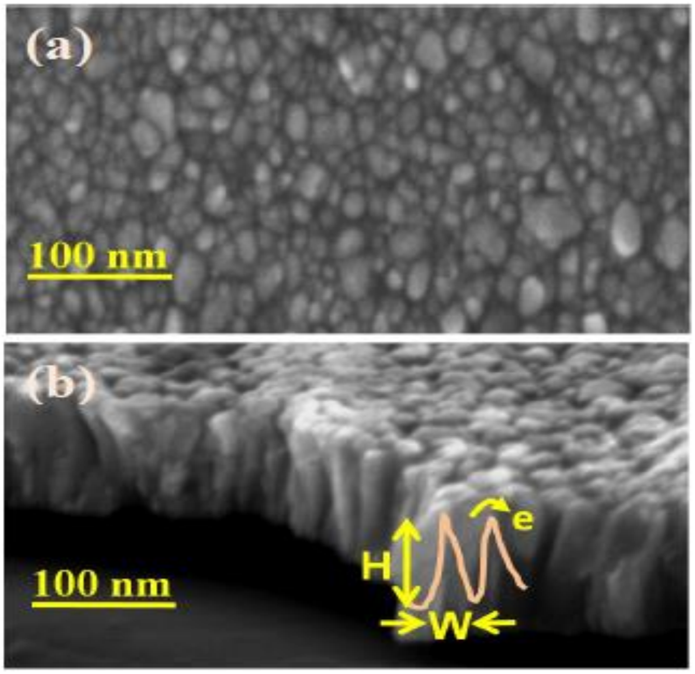

Figure 3.4: (a) Plan-view and (b) cross-sectional SEM images of S3 sample. Charge transport across potential barriers (shown by line profile) at grain boundaries is shown schematically on cross-sectional SEM image.

The XRD patterns of S1-S4, shown in Figure 3.5, confirm the formation of crystalline grains. The dominant peak located around 34.10° can be attributed to the (002) reflection of the hexagonal wurtzite structure [15], indicating the formation of highly oriented grains along the *c*-axis.

Formation of the preferentially oriented AZO (along the *c*-axis) grains suggests that the value of the surface free energy is minimum for the AZO (002) plane during the growth stage [17]. As the film thickness increases, the (002) peak intensity is found to increase systematically with a continuous decrease in full width at half maximum (FWHM), signifying the evolution of bigger grains with deposition time up to 30 min.

The average grain size was determined for all four samples S1-S4 using Scherer's formula [18]: $D = 0.9\lambda/\beta\cos\theta$ where $D$ is the crystallite size, $\beta$ is the FWHM, $\theta$ is the Bragg's angle, and $\lambda$ is the x-ray wavelength (Table 3.1). From this table, it is observed that the measured grain sizes from AFM are little bigger than the ones derived from XRD data.

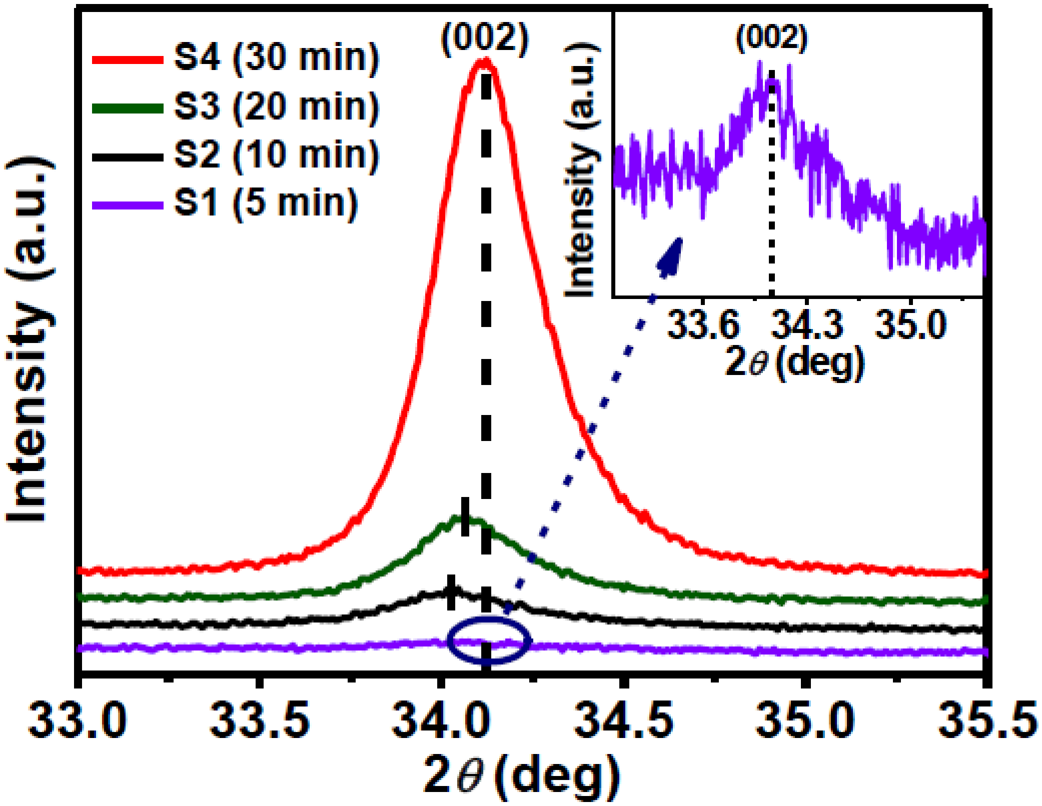

Figure 3.5: Thickness-dependent XRD patterns. For a better projection the magnified region around the (002) reflection of S1 is shown as the inset.

This is because of the limitation of AFM to resolve smaller crystallites within a bigger grain [18]. In addition, a systematic shift in the (002) peak position was observed with increasing AZO layer thickness. It is known that the peak shift towards a lower $2\theta$ value with respect to the ZnO can be attributed to the presence of compressive stress present in the films, originating from oxygen implantation during the sputtering process [16]. In-plane film stress is calculated on the basis of the biaxial strain model: $\sigma=[2C_{13}-C_{33}(C_{11}+C_{12})/C_{13}]\times(c-c_0)/c_0$ where elastic stiffness constants are: $C_{11}=2.1\times10^{11}$ Nm$^{-2}$, $C_{33}=2.1\times10^{11}$ Nm$^{-2}$, $C_{12}=1.2\times10^{11}$ Nm$^{-2}$, and $C_{13}=1.05\times10^{11}$ Nm$^{-2}$ [13,16,19]. After putting the above values, $\sigma$ becomes $-4.5\times10^{11}$ $(c-c_0)/c_0$ Nm$^{-2}$. For a hexagonal lattice with (002) orientation, $c = 2d_s$ and $c_0 = 2d_0 = 0.5206$ nm where $d_s$ is the inter-planar spacing derived from the (002) peak position (Figure 3.5) and $d_0$ is the corresponding one for stress-free system (0.2603 nm) [20]. Accordingly the calculated stress values for S1 to S4 are presented in Table 3.1 which reveals that the AZO films become relaxed with increasing thickness – in accordance with Ref. 16. From the above discussion one can derive the film strain using the relation [20]: $[(d_s-d_0)/d_0]\times100\%$ which are summarized in Table 3.1.

For resistivity measurements, we have used the AZO films grown on commercial glass slides simultaneously and under similar conditions as on Si substrates. Figure 3.6 shows the thickness-dependent variation in resistivity measured by the linear four-probe technique. A sharp decrease in resistivity is recorded for S1 to S2, whereas it remain almost constant for S3 and S4. It may be note that the linear variation in the *I-V* characteristics (inset, Figure 3.6) of the AZO films grown on glass substrates confirms the Ohmic nature of the silver contacts.

On the other hand, the *I-V* characteristics of all Ag/AZO/Si/Ag heterojunction diodes [Figure 3.7(a)] show the rectifying property where the schematic view of such a diode is depicted in the inset (bottom corner).

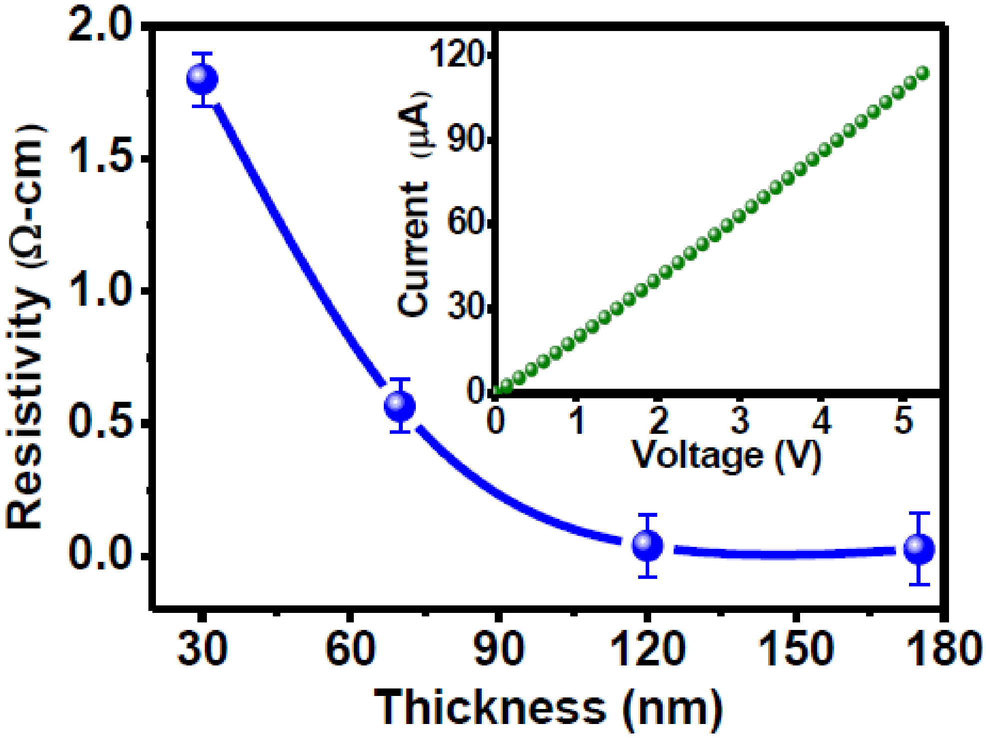

Figure 3.6: Variation in resistivity with AZO film thickness. Inset shows the linear variation of current with applied voltage corresponding to the silver contacts.

The diode series resistance and the ideality factor can be obtained from [16] $dV/d(\ln I) = [IR_s + nk_BT/q]$ where $V$ is the applied potential, $I$ is the measured current, $R_s$ is the series resistance, $n$ is the diode ideality factor, $k_B$ is the Boltzmann constant, $T$ is the sample temperature, and $q$ is the electrical charge. The calculated values of $n$ and $R_s$ from the slope and the intercept at zero voltage in the ln $I$ versus $V$ plot (not shown) are summarized in Table 3.1. Because of having a large lattice mismatch between the AZO layer and Si(100) substrate [11], dislocations appearing at the AZO/Si interface can lead to the increase in ideality factor, $n$ (Table 3.1). As the AZO/Si interface plays an important role in carrier injection, we believe that the AZO thickness-dependent increase in $n$ is most likely associated with the minority carrier injection and recombination [17].

This is consistent with the increase in the reverse saturation current ($I_0$) with increasing AZO film thickness, which in turn takes part in the suppressing turn-on potential by decreasing the barrier height, $\phi_B$, at the AZO/Si interface [Figure 3.7(a)]. The barrier height $\phi_B$ at a temperature of $T$ can be determined from: $I_0 = A^*ST^2\exp(-\phi_B/k_BT)$, where $S$ is the surface area of the diode, $k_B$ is the Boltzmann constant, and $A^*$ is the Richardson constant [23].

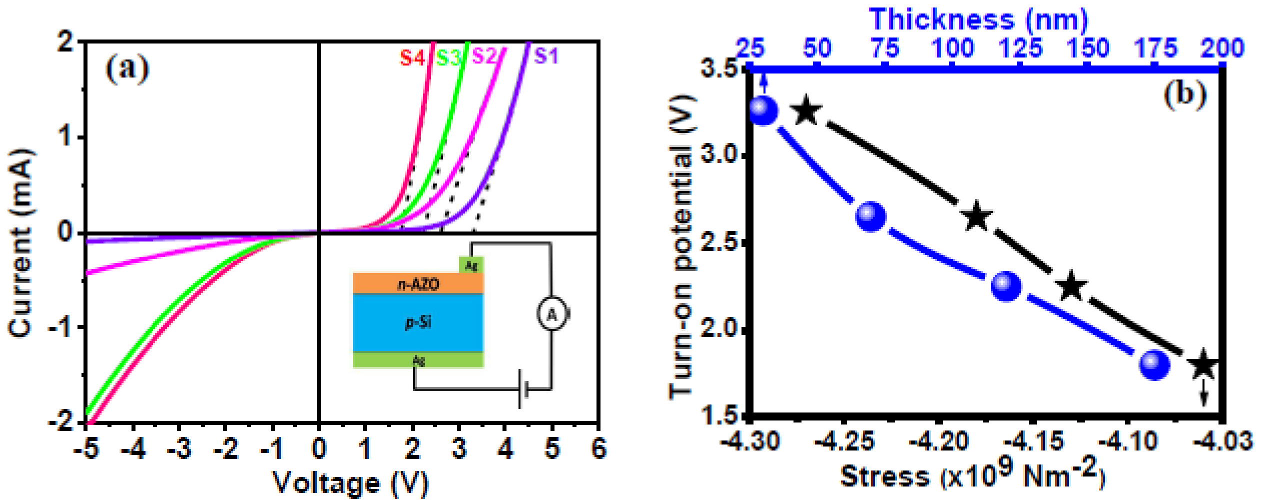

Figure 3.7: (a) Thickness dependent nonlinear *I-V* characteristics of all AZO/Si hetrojunction diodes (shown schematically in the bottom inset), (b) variations in turn-on potential with AZO thickness and film stress.

Since we cannot avoid the presence of a thin native $SiO_x$ between the AZO layer and the Si substrate, the extracted $\phi_B$ will be erroneous due to the active participation of the AZO/$SiO_x$ and $SiO_x$/Si interfaces, especially for the thin AZO layers ( below 70 nm) [see the reverse current profiles in Figure 3.7(a)]. This is due to the incorporation of a large amount of defects between the AZO/$SiO_x$ and $SiO_x$/Si interfaces which as a result can contribute in charge transfer process between the AZO film and the Si substrate [24,25]. In order to determine $\phi_B$, we did *C-V* measurements at 1 MHz under a forward and reverse bias sweeps of +4 to -4V.

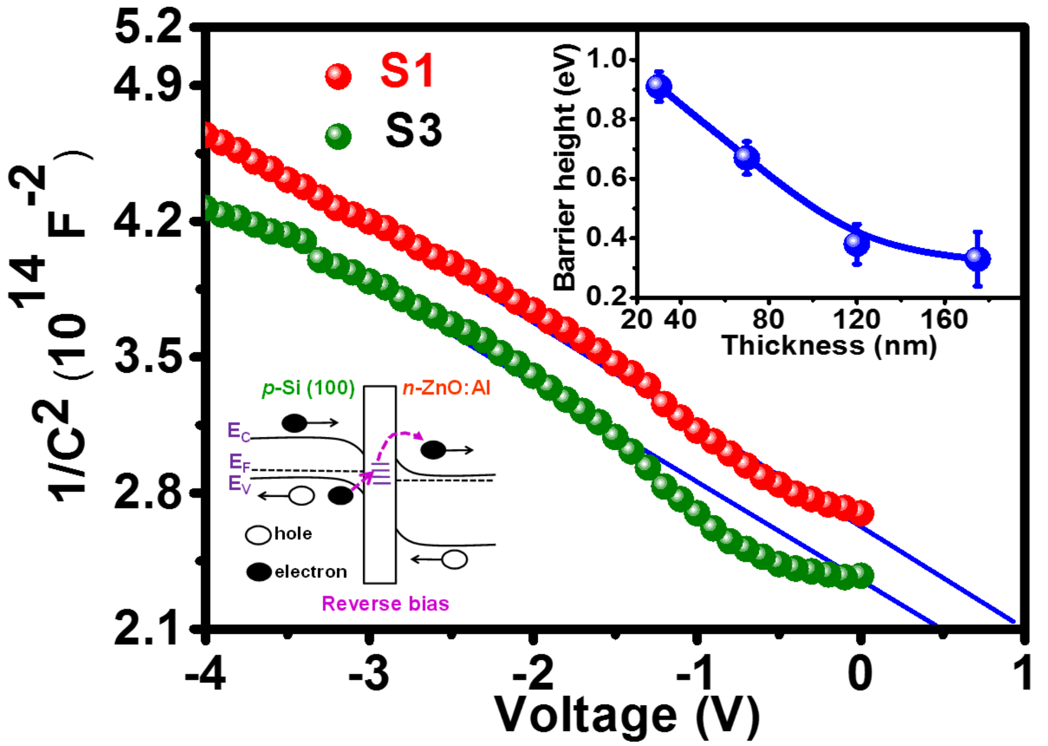

Figure 3.8: Typical $1/C^2$-$V$ characteristics for S1 and S3, where the inset depicts the variation of barrier height as a function of AZO film thickness.

For applied voltage $V >> k_B T/q$ and $N_A >> N_D$, the capacitance per unit area can be written as $1/C^2 = 2(V_{bi} - V)/q\varepsilon_s N_D$ where the $N_A$ and $N_D$ are the donor density in *n*-AZO and the acceptor density in *p*-Si, respectively, $V_{bi}$ is the built-in potential within Si, and $\varepsilon_s$ is the Si permittivity [23]. Using $1/C^2$-$V$ plot (Figure 3.8, shown only for S1 and S3 to maintain the clarity) the extrapolated straight line intercept of $1/C^2$ on the voltage axis is the measure of $\phi_B$ [26]. The AZO film thickness-dependent change in $\phi_B$ is displayed in the inset of Figure 3.8, showing a systematic decrease in it from 0.9 to 0.3 V with increasing thickness up to 175 nm. From the above results it can be inferred that the AZO/Si heterojunction diode characteristics, especially the turn-on potential is strongly influenced by the growth of AZO films and their thicknesses.

Different theoretical models have been proposed so far to explain the electrical properties of the AZO/Si hetrojunction diodes where the most acceptable one is the bandgap model with and without $SiO_2$ layer [7,8]. Earlier band alignment and the microstructure of the ZnO/Si hetrojunction were studied in detail and used to explain the nonlinear behaviour [8]. In the present scenario, the notable decrease in the turn-on potential with increasing AZO film thickness [Figure 3.7(b)] can be described in light of decreasing film stress. In fact, we observed strain relaxation with increasing AZO thickness (Table 3.1), which is possibly due to the increase in grain size. The presence of traps at the AZO grain boundary and their impact on transmission of electrons (or holes) have recently been demonstrated by scanning tunnelling microscopy [27]. Based on this concept, it is now possible to explain the observed phenomena in the framework of defect-induced potential barrier formation at the grain boundaries, while the magnitude of the barrier height ($H$) and width ($W$) are associated with the trap density between two adjacent grains [shown schematically in Figure 3.4 where the line profile represents the potential (due to traps) at grain boundaries]. This in turn controls the charge transport between two grains: the conduction increases with reducing $H$ and vice versa. Clearly, the boundary traps dominate in S1 compared to the samples like S2 to S4 due to a decrease in the surface-to-volume ratio with increasing grain size (Table 3.1).

Although the trap density reduces with increasing grain size, the decrease in $\phi_B$ as a function of AZO thickness (discussed above) can enhance the minority carrier injection in inversion through the reduction in the depletion width [22]. As a matter of fact, the probability of minority carrier recombination increases with increasing AZO film thickness, leading to an increase in the magnitude of $I_0$ by suppressing $R_s$ (Table 3.1). However, considering the existence of a thin native $SiO_x$ between the AZO layer and the Si substrate, the minority carrier injection may be influenced by the degree of tunnelling through the surface states [28]. Hence, the diode characteristics degrades with the increasing AZO layer thickness. On the other hand, with the increasing grain size as a function of AZO layer thickness can increase the mean free path of the electrons. In fact, the energy of electrons with increasing AZO film thickness becomes conserved with the long mean free path [29], which in turn reduces the scattering loss [30,31] and trapping of charge carriers, resulting a decrease in resistivity (Figure 3.4).

### 3.2.4 Conclusions

In conclusion, the variation in the grain size with increasing *n*-AZO film thickness on *p*-type Si(100) substrates is shown by AFM, whereas the XRD results confirm the enhancement of (002)-oriented crystalline grains. Thickness-dependent reduction in the compressive stress is also demonstrated from the XRD measurements. Further, we observe the rectifying property of AZO/Si heterojunction diodes from the recorded *I-V* characteristics, where the turn-on voltage undergoes a hitherto unseen systematic reduction with increasing AZO film thickness. Using the linear four-probe technique, a systematic decrease in the resistivity is found with increasing AZO film thickness. These phenomena have been modelled based on the thickness-dependent variation in grain size and in turn trap density at the grain boundaries, influencing the charge transport across the adjacent grains. In particular, the development of potential barrier at the grain boundary followed by the scattering of charge carriers were shown to be the controlling factors of the observed *I-V* characteristics. The barrier height at the junction, calculated from the *C-V* measurements, shows a decreasing trend with increasing AZO film thickness, which corroborates well with the observed thickness-dependent behaviour of the turn-on voltage of the heterojunction diodes. Such studies will have tremendous impact in developing the next generation silicon thin film solar cells [32] and UV detectors [33].

## 3.3 Role of metallic-like conductivity in unusual temperature-dependent transport in *n*-ZnO:Al/*p*-Si heterojunction diode

### 3.3.1 Introduction

Generally, ZnO exhibits *n*-type conductivity which can be enhanced up to three to four orders of magnitude after doping with Group-III elements, especially Al-doping [7,34,35]. This enhanced conductivity makes ZnO:Al (AZO) a suitable material not only for transparent conducting electrodes but also for various other applications, viz. ultra-violet detectors, junction diodes, etc. [34-41]. Generally, AZO-based device fabrication is studied in the simplest form of an *n*-AZO/*p*-Si heterojunction diode [34] where the performance of the heterojunction mainly depends on the factors like growth process, Al-doping, and the working temperature of the devices [7]. Recently, it has been reported that charge transport property of ZnO and doped-ZnO materials changes significantly with temperature. For instance, temperature-dependent metallic-like behaviour has been reported for ZnO, AZO, and Ga-doped ZnO thin films deposited on insulating substrates [42,43]. This unusual change in resistivity with temperature is expected to play an important role in the charge transport process of a device based on doped-ZnO systems. However, the role of temperature-dependent the resistivity of AZO in the current-voltage (*I*-*V*) characteristics of an AZO-based heterojunction diode is still lacking. Thus, in order to use AZO/Si heterojunctions for device applications, a detail understanding of changes occurring in its *I*-*V* characteristics due to external heating is exigent.

In this regard, it may be mentioned that often AZO-based heterojunctions are operated at high current densities (beyond the turn-on potential, $V_T$), which causes self-heating to occur in the device. This is expected to bring variation in the junction characteristics which can affect the device performance to a significant extent. It is envisaged that changes occurring in the *I*-*V* characteristics of the heterojunction due to self-heating should be similar to those observed under the influence of external heating. Therefore, it is important to investigate temperature-dependent changes in resistivity of AZO thin films and its effect on the performance of *n*-AZO/*p*-Si heterojunction diodes.

In this work, we investigate the effect of temperature on the transport mechanism of an *n*-AZO/*p*-Si heterojunction diode. A large variation in the *I*-*V* characteristics with temperature is observed. In particular, temperature-dependent transition from direct tunnelling to thermionic emission is observed in the (*I*-*V*) characteristics. In order to explain this behaviour, temperature-dependent resistivity of the AZO film, deposited on soda-lime glass (SLG) substrate, is also investigated. The measured resistivity reveals a semiconducting nature at low temperatures (upto 343 K), which subsequently transforms into a metallic-like behavior at higher temperatures (>343K). In addition, we have made use of optical absorption spectroscopy before and after temperature treatment, which shows a reduction in the band gap of the AZO layer. These observations are discussed in terms of annihilation of oxygen vacancies in the AZO layer due to annealing in air.

### 3.3.2 Experimental

AZO films of an optimized thickness of ~60 nm were simultaneously deposited on ultrasonically cleaned SLG and native oxide covered *p*-type Si(100) substrates at RT using a pulsed dc magnetron sputtering system using the similar experimental parameters (as described in section 3.1.2). An indigenously developed sample holder assembly (having a heating stage), whose temperature was precisely controlled (±0.5 K) by a proportional-integral-derivative (PID) temperature controller and sensed by a Platinum resistance temperature detector (RDT, A class) thermocouple, was coupled with a source meter to perform the temperature-dependent electrical studies. The *I*-*V* data were recorded using commercially available software (Lab-Tracer 2.0) during annealing (293-423

K) of the AZO/Si heterojunctions in air. In addition, the optical absorption of AZO films before and after temperature treatment was measured by a UV-Visible-NIR spectrophotometer in the wavelength range of 300-700 nm. The reproducibility of the results were confirmed on three different AZO thickness viz. 40, 60, and 120 nm.

### 3.3.3 Results and discussion

AZO films were analysed by SEM and XRD to look for a possible correlation between the charge transport and structural properties of the films. Figs. 3.9(a) and (b) show the SEM images of an AZO film deposited on Si substrate before and after the heat treatment. It is observed that in both cases the AZO film shows a granular nature, albeit the average grain size increases form 30 to 35 nm and the width of the grain size distribution decreases [respective insets in Figs. 3.9(a) and (b)]. In fact, as the temperature increases, thermal energy increases the diffusion of atoms and in turn smaller grains merge into a bigger grain.

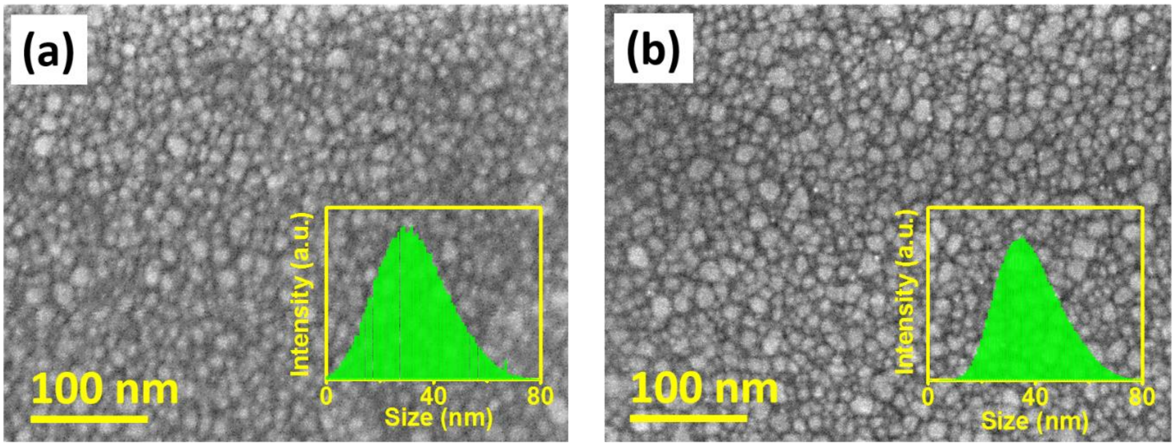

Figure 3.9: (a) and (b) Plan-view SEM images before and after heat treatment (at 423 K), respectively. The insets show the grain size distributions of corresponding film.

Fig. 3.10 shows the XRD pattern of an AZO film grown on Si which confirms the crystalline nature of the film. The dominant peak at $2\theta$=34.8° can be attributed to the (002) reflection of hexagonal wurtzite structure, indicating the formation of highly oriented grains along the *c*-axis [7,34,44]. The average grain size is determined using Scherer's formula: $D=0.9\lambda/\beta cos\theta$ where $D$ is the crystallite size, $\beta$ is the full width at half maximum, $\theta$ is Bragg's angle, and $\lambda$ is the Cu-$K_\alpha$ x-ray wavelength [7,34,44]. Thus, the average grain size of the film before and after heat treatment is found to be 17 nm and 21 nm, respectively. Further, a small shift (0.08°) in the peak position is observed. In-plane film stress is calculated on the basis of biaxial strain model: as is described in section 3.2.3.

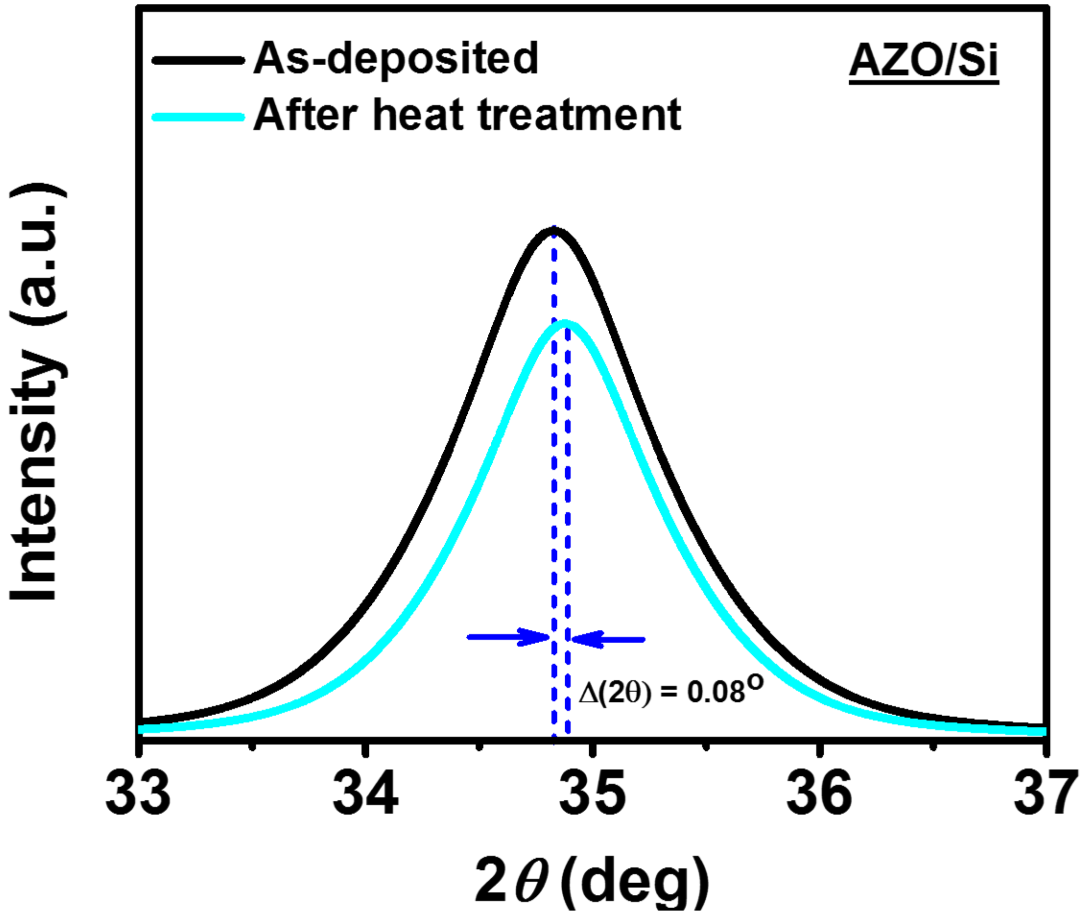

Figure 3.10: XRD patterns of an AZO film before and after heat treatment in air at 423 K.

The measured strain and stress values for the as-deposited AZO film are found to be -4.27×$10^9$ N $m^{-2}$ and -0.98%, respectively (Table 3.1), which are in good agreement with our results [34]. However, this decreases to -4.20×$10^9$ N $m^{-2}$ and -0.92%, respectively, indicating a relaxation of stress in the film due to heat treatment. Further, it may be mentioned that similar SEM and XRD behaviours are observed for the film deposited on glass substrates (data not shown).

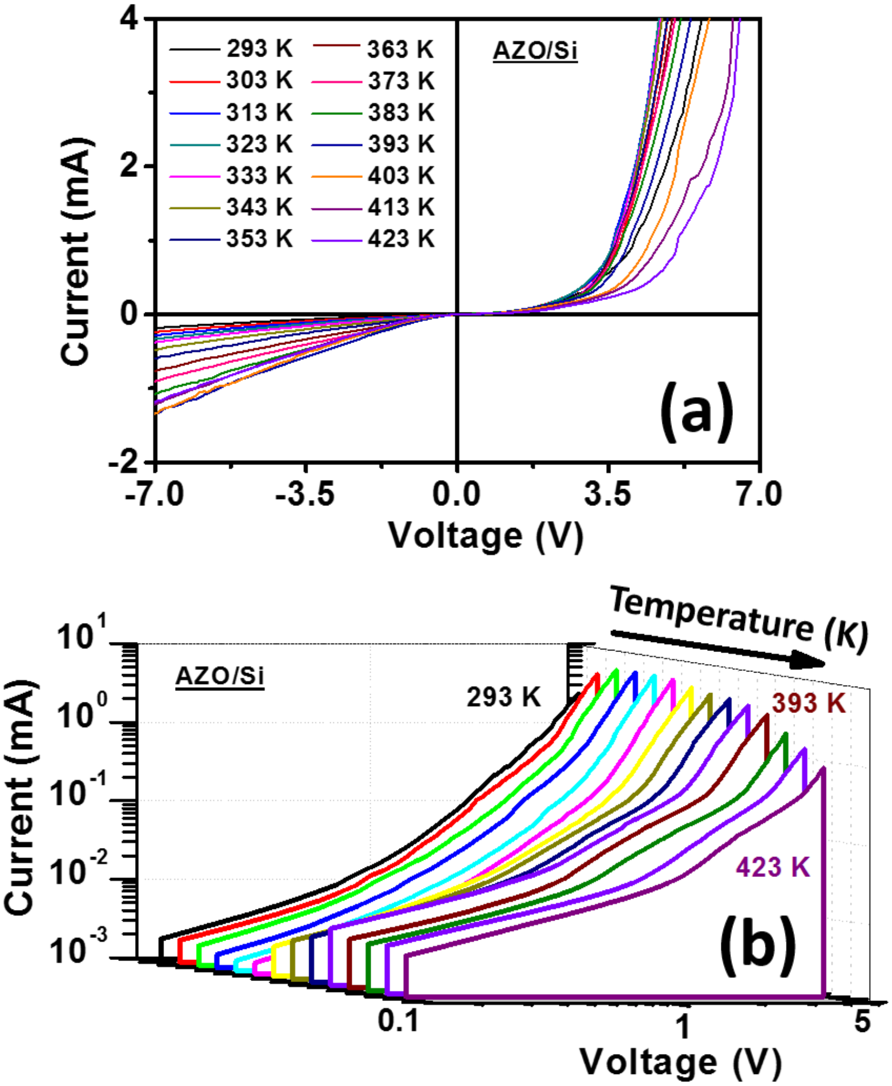

Figure 3.11: (a) Temperature-dependent *I-V* characteristics of AZO/Si heterojunction diode, (b) log-log plots of the forward bias characteristics of figure (a) where the arrow indicates the direction of increasing temperature.

Fig. 3.11(a) shows the *I*-*V* characteristics of an *n*-AZO/*p*-Si heterojunction diode at different temperatures, varying from 293 to 423 K, where all *I*-*V* curves show the rectifying property. It is evident from this figure that both forward and reverse currents are not only dependent on the applied voltage but also on the sample temperature. Theoretically, the $V_T$ of a semiconductor heterojunction diode should decrease with increasing temperature [45]. However, the present *I*-*V* data show unusual variation, where no significant change takes place in $V_T$ with increasing temperature in the range of 293-343 K, while it increases beyond 343 K (Table 3.2). The similar trend is observed in the reverse saturation current ($I_s$) as well (Table 3.2). The value of the ideality factor (*n*), determined from the slope of the linear region of the forward bias log (*I*-*V*) characteristics [46], has a typical value of 2.1±0.1. The values of *n* and the series resistance ($R_s$) at all temperatures are calculated from the corresponding *I*-*V* characteristics and summarized in Table 3.2. To understand the mechanism behind the variation in *I*-*V* characteristics more clearly, we have plotted the data using a log-log scale [46,47]. The log-log *I*-*V* characteristics of a heterojunction under forward bias from 293 to 423 K are shown in Fig. 3.11(b). In this figure, two interesting features are worth to be noted: (i) the current values at low voltages (<0.5V) shows inconsistency with increasing temperature and (ii) a clear hump at higher temperatures is observed for intermediate voltages (0.6<V<1.2). In fact, the behaviour up to a certain applied voltage (~0.6 V) is Ohmic in nature and thereafter, non-Ohmic behaviour is manifested due to the thermal effects which indicates defect activation and an increase in the electrical current [48]. For a better clarity, the log-log plot of *I*-*V* data, measured at 373 K, is shown in Fig. 3.12.

As a result, change in behaviour of the *I*-*V* characteristics at different voltages becomes very clear. In fact, the *I*-*V* plot can be divided into four different regimes as described below. Region-I: current is linearly dependent on voltage, i.e. Ohmic in nature, region-II: exponentially dependent on voltage, region-III: shows a power law dependence, $I \propto V^a$ where $a>1$, and region-IV: there is a sudden enhancement in current with voltage [26,49,50]. These four regions in the *I-V* characteristic are also strongly influenced by temperature, which is a signature of thermally activated charge injection mechanism [26,49,50]. However, at lower temperatures (<343 K), the *I-V* curves show a weak temperature-dependence, which can be well described by the tunnelling mechanism [26,49,50].

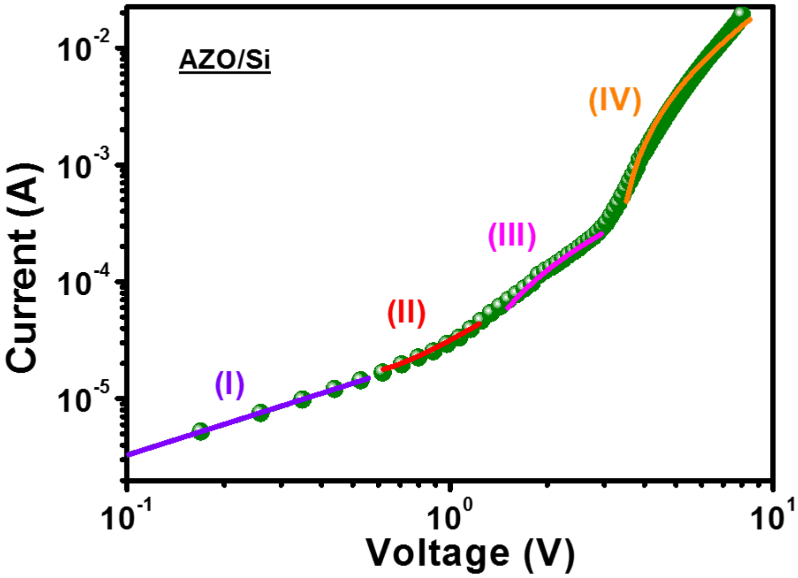

Figure 3.12: Log-log *I-V* plot under the forward bias corresponding to 373 K where (I), (II), (III), and (IV) show different conduction regimes.

Generally, temperature-dependent *I-V* characteristics are explained in the framework of Schottky-type conduction and/or space charge limited conduction (SCLC) [44]. However, the anomaly in our results indicates that possibly different conduction mechanisms are operative in different voltage-temperature regimes.

Fig. 3.13(a) shows $\ln(I)$ versus $V^{1/2}$ behaviour to establish the main current conduction mechanism in the *n*-AZO/*p*-Si heterojunction diode and these curves are further used to calculate the reverse saturation current. It is observed that $\ln(I)$ versus $V^{1/2}$ curves remain linear at lower voltages

(<0.6V) but deviate at higher voltages (>0.6V), ruling out the possibility of a Schottky-type conduction mechanism at higher voltages [51,52]. In addition, by extrapolating straight lines (not shown in the Figure) to 0 V [Fig. 3.13(a)], we obtain the leakage current ($I_0$) as a function of temperature, which is further used to calculate the barrier height ($\Phi$) at the AZO/Si interface. For the calculation of $\phi$, $\ln(I_0/T^2)$ is plotted as a function of $1000/T$ in Fig. 3.13(b), which reveals a linear relation at higher temperatures (>383 K).

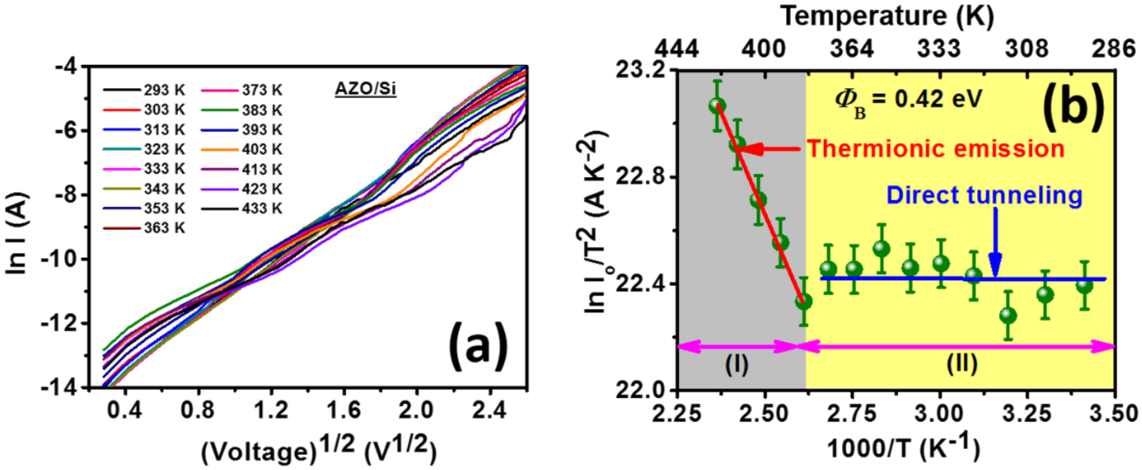

Figure 3.13: (a) ln ($I$) versus $V^{1/2}$ plot, (b) Arrhenius plot extracted from (a) for the AZO film deposited on Si substrate.

However, the plot remains constant below 383 K, indicating a weak temperature-dependence at lower temperatures. In fact, the constant value of ln ($I_0/T^2$), up to 383 K, indicates that the current at low bias voltages (<0.6V) is governed by direct tunnelling [51]. For this voltage regime, the current is described by the relation:

$$I \,\alpha\, V exp\left[\,2d\sqrt{2m^{*}\phi_{B}}\,/\hbar\,\right], \tag{3.1}$$

where $\hbar$ is reduced Planck's constant, $m^*$ is effective mass of the charge carrier, $d$ is the width of the interface barrier, and $\phi_B$ is the junction barrier height [52,53]. However, at higher temperatures, thermionic emission governs the charge transport process. The $I$-$V$ characteristics in this regime obey the Richardson-Schottky (RS) equation and the current is described by the relation:

$$I = A^{*}T^{2}exp\left[-\{\ \phi_{B} - \sqrt{\left(\frac{q^{3}V}{4\pi\varepsilon_{0}\varepsilon_{r}d}\right)}\ \}/k_{B}T\ \right], \tag{3.2}$$

where $A^*$ is the effective Richardson constant, $\varepsilon_r$ is the permittivity of AZO film, $\varepsilon_0$ is the permittivity of vacuum, and $q$ is the electronic charge [49]. Thermionic regime also shows a variation in the leakage current, $I_0$. Subsequent calculation of the junction barrier height corresponding to the thermionic regime reveals an activated behavior due to the high value of $\phi_B$=0.42 eV. In fact, when the temperature is low (383 K), thermal energy of the charge carriers is low, which is not sufficient to overcome this barrier height. This indicates that different mechanisms are operative at different temperatures [51].

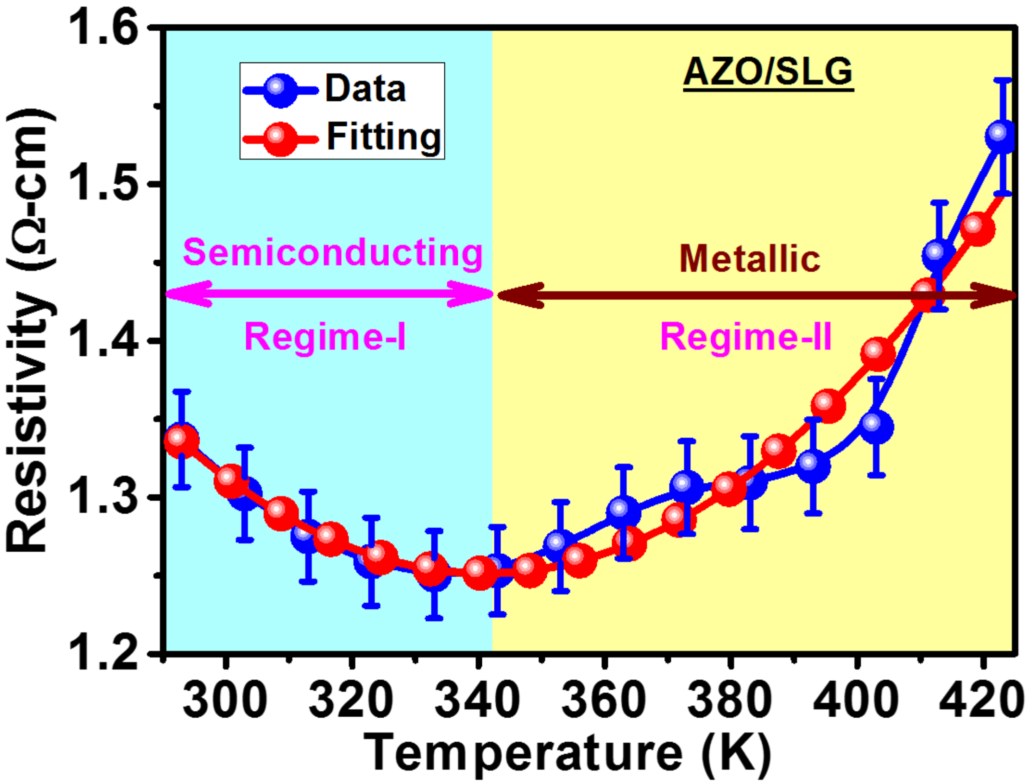

Figure 3.14: Temperature-dependent resistivity of an AZO film deposited on the SLG substrate.

Recently, it has been reported that electrical properties of ZnO and doped-ZnO change with increase in temperature, which play a significant role in electrical transport [42,43]. To understand the unusual *I-V* behaviour of AZO/Si heterojunction described above, we have carried out resistivity measurements of an AZO thin film at different temperatures. Fig. 3.14 shows the temperature-dependent resistivity of the AZO film deposited on a glass substrate. Interestingly, the experimental resistivity values show two different regimes: initially the resistivity decreases with temperature (<343 K) and thereafter, it increases at higher temperatures (≥343 K). The initial decreasing trend in Regime-I (highlighted by the cyan-coloured block) can be correlated to the semiconducting nature of the AZO film, whereas the subsequent trend in Regime-II (highlighted by the yellow-coloured block) is in contradiction since it resembles the metallic behaviour. It is observed from this figure that resistivity of the AZO film at 423 K is higher compared to that at RT (293 K). In addition, resistivity of the AZO film is also measured after bringing down the furnace temperature to RT which is found to be the same as 423K, indicating the irreversible nature of the metallic-like behaviour. Interestingly, it is observed that the AZO film after heat treatment has bigger gran sizes and less compressive strain and hence, should have shown a low resistivity. However, the resistivity increases after heat treatment, which indicates that some other mechanism is responsible for this behaviour.

Normally, Al acts as an effective donor either by substitution at the Zn sites or by creating oxygen vacancies after sitting as an interstitial atom which in turn leads to the low resistivity of AZO films [7,54]. In addition, these donor electrons (due to Al or oxygen vacancies), normally occupy the higher (deeper) energy levels in the conduction band, which in turn can initiate high energy photon absorption during the optical studies. As a result, the effective band gap ($E_g$) of an AZO film should be relatively higher when compared to the separation between the minima (of conduction band) and the maxima (of valence band) of this direct band gap semiconductor [shown in Fig. 3.15(a)].

Such a widening in the band gap is known as Burstein–Moss (BM) shift which depends on the carrier density of the film, *n*, according to $n^{2/3}$ [50].

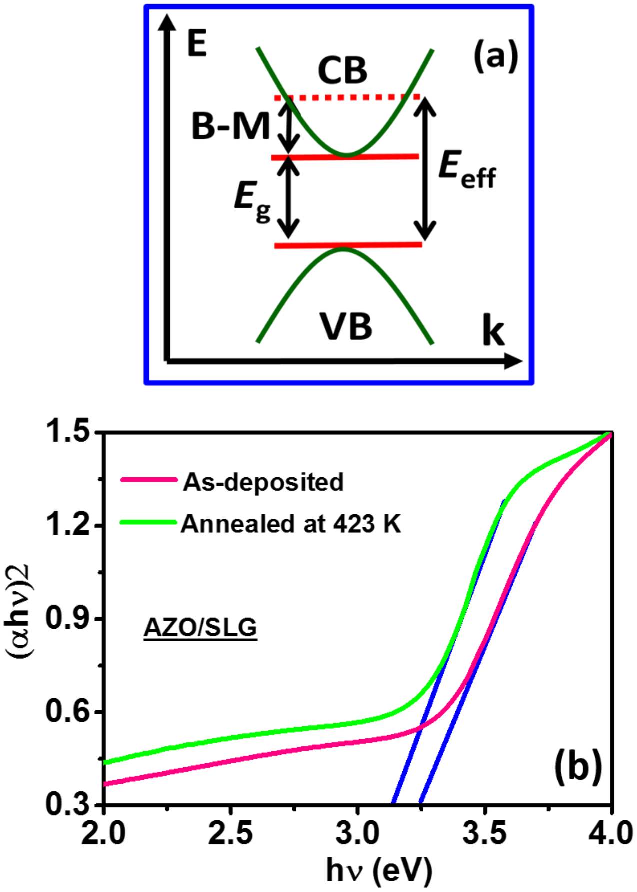

Figure 3.15: (a) Schematic representation of Burstein–Moss (B-M) shift, (b) the measured band gap of an AZO film (deposited on the SLG substrate) before and after heat treatment.

It is well-known that the electrical transport properties of AZO can be understood on the basis of the optical absorption studies. Thus, to understand the observed metallic-like behaviour of the AZO film, we have performed the optical absorption studies before and after the heat treatment. Since, the heat treatment is performed in air, oxygen adsorption in AZO film is likely to happen. This can lead to a more stoichiometric nature of the AZO film due to annihilation of oxygen vacancies, causing a decrease in the carrier concentration [42]. As a consequence, the band gap of the AZO film after heat treatment should be lower relative to the as-deposited one. Thus, to understand the reason behind the metallic-like conductivity, we have measured the energy gaps of the AZO film from the optical absorption spectra. It is observed that after annealing at 443 K, the absorption edge shifts towards a lower energy (3.27 to 3.13 eV) [Fig 3.15 (b)]. This behaviour can be attributed to the fact that at relatively lower temperatures (<383 K), oxygen atoms do not get absorbed at the surface because of insufficient activation energy, whereas beyond 383 K, the atmospheric oxygen atoms interact with the surface and in turn reduce the carrier density in the films. In fact, due to annealing in open air, electrons get accumulated at the AZO surface and can be trapped by oxygen molecules to form negatively charged oxygen ions [56]. These trapped electrons lead to a reduction in the effective donor density within the oxide. A similar behaviour has been reported in case of Ga-doped ZnO after annealing which confirms the reduction in oxygen vacancies [43]. To fortify this fact, similar heat treatment on the AZO film, deposited on glass substrate, is performed in vacuum ($8\times10^{-8}$ mbar) and subsequent change in the band gap (absorption spectra not shown) is measured. Interestingly, no change in the optical band gap is observed which confirms that annihilation of oxygen vacancies is responsible for the metallic-like behaviour of the AZO film under consideration. Therefore, the variation in resistivity of the AZO film has a one-to-one correspondence with the *I-V* characteristics of the *n*-AZO/*p*-Si heterojunction. Based on the above discussion, we infer that the temperature-dependent charge conduction mechanism in AZO/Si heterojunction diode is primarily governed by the AZO layer.

Based on our experimental observations, we have constructed a parametric phase diagram (voltage versus temperature) which defines the dominating charge conduction mechanism at a fixed temperature (Fig. 3.16). It is clear from this diagram that at lower temperatures the conduction mechanism is governed by diffusion; however, this changes to the thermionic emission process beyond a certain temperature.

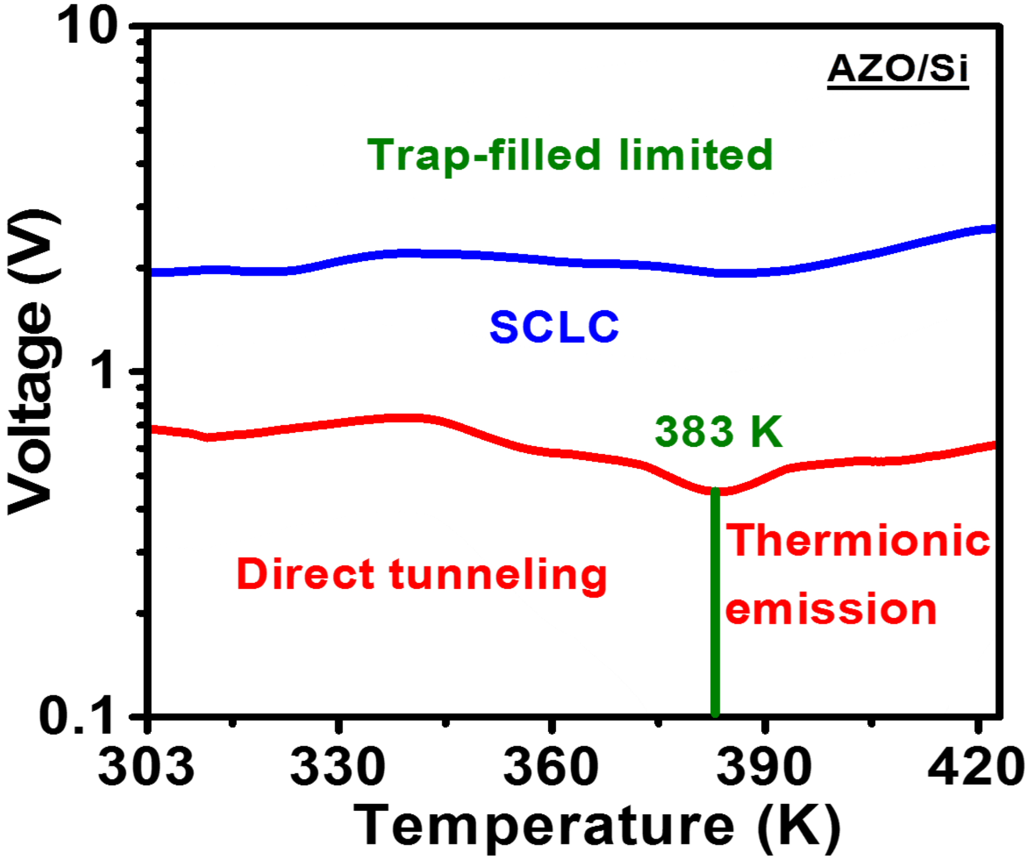

Figure 3.16: Voltage versus temperature parametric phase diagram for an *n*-AZO/*p*-Si heterojunction diode.

Reproducibility of the results have been checked on five different AZO samples (60 nm thick) grown on both Si and SLG substrates. Interestingly, similar behaviour is observed for three different AZO film thickness, viz. 40, 60, and 120 nm, grown on both SLG and *p*-Si substrates. Thus, we conclude that the present study will provide important input to understand the effect of self-heating of AZO-based devices, operating at high temperature.

### 3.3.4 Conclusions

In summary, we have deposited AZO films on SLG and *p*-Si substrates and performed temperature-dependent *I*-*V* studies. *I*-*V* characteristics of the *n*-AZO/*p*-Si heterojunction diodes, at different temperatures, reveal an unusual behaviour, which is correlated with the temperature-dependent resistivity of the AZO film deposited on the SLG substrate. At higher temperatures (423 K), an increase in the resistivity takes place which is attributed to the annihilation oxygen vacancies. The metallic-like conductivity of the AZO film, at relatively higher temperatures, is concluded to be responsible for the transition of the conduction mechanism from diffusion to the thermionic emission mode. The present study enables us to address the self-heating effect on AZO-based devices.

## 3.4 Ultra-violet absorption induced modifications in bulk and nanoscale electrical transport properties of Al-doped ZnO thin films

### 3.4.1 Introduction

Thin films of aluminum-doped zinc oxide (AZO), as a transparent conductive oxide (TCO), are widely studied for potential applications in flat panel displays, solar cells, and light-emitting diodes (LEDs) [57]. In most of these applications, the performance of AZO-based devices is strongly governed by the carrier density, which not only depends on the aluminum doping level but also on the presence of local defects in AZO films [13,32,57]. In addition, statistical distributions of the grain size, carrier density, and defects can vary from grain-to-grain which in turn give rise to a local variation in the conductivity [58]. Thus, for a better realization of the TCO properties, it is necessary not only to understand the bulk but also the nanoscale (local) electrical transport properties of AZO thin films, which are considered to be quite challenging.

In order to do so, various scanning probe techniques are employed which include scanning tunnelling microscopy (STM) [27], conductive atomic force microscopy (cAFM) [59], and Kelvin probe force microscopy (KPFM) [60]. For instance, using STM, Likovich *et al*. [27] have recently determined the trap density at the grain boundaries (GBs) of an AZO thin film to be $\sim 10^{13}$ cm$^{-2}$ which is ought to influence the electrical transport properties.

Generally, changes in doping and surface defects lead to a shift in the Fermi level position which in turn changes the work function of a material [60-63]. KPFM is considered to be a suitable non-contact technique, which is used not only to map the work function but also to quantify the carrier concentration [62]. The measurement of doping concentration without any contact on the sample surface has a considerable advantage because it avoids the presence of an extra Schottky barrier at the contact-specimen junction and has a direct correlation with nanoscale conductivity [61,63].

However, local conductivity is not only dependent on the carrier concentration alone and can be influenced by an external excitation in terms of photo-absorption [64]. For instance, ultra-violet (UV) absorption enhances the conductivity of an AZO window layer by direct photo-generation even though it is considered to be an optical loss for the underneath absorbing layer of a solar cell [65-67], leading to a poor cell performance. This can be directly assessed by studying photoresponsivity and thus, it becomes quite important to have an in-depth understanding of the effect of UV-exposure on the photoresponse of an AZO-based solar cell.

In this paper, we will show how UV light absorption can influence the bulk as well as nanoscale conductivity of AZO thin films. To address this issue, we have employed combined KPFM and cAFM measurements at RT. For instance, the donor concentration is mapped by KPFM in which a variation in the carrier density is observed. Since the carrier density is known to play a significant role in controlling the local charge transport, we have measured the nanoscale electrical conductivity as well by cAFM before and after UV-exposure. An enhancement in the local conductivity, after UV-exposure, is observed which is explained in terms of experimentally measured bulk persistent photoconductivity. Further, UV-induced enhancement in the spectral response (during photoresponsivity measurements) of *n*-AZO/*p*-Si solar cell is observed, manifesting UV absorption in the AZO overlayer should not cause a loss in the efficiency of a solar cell which is in contrary to the common belief [64-69].

### 3.4.2 Experimental detail

An optimized film thickness of 30 nm was deposited simultaneously on ultrasonically cleaned soda lime glass (SLG) and *p*-Si (100) (covered with a thin native oxide layer) substrates at RT using a pulsed dc magnetron sputtering system. Similar experimental conditions and the same commercially available target (as described earlier) was used for the growth the AZO thin films. The crystallinity and phase identification of AZO films were performed by XRD (Bruker, D8-Discover) in the Bragg-Brentano geometry, using the Cu-Kα radiation ($\lambda$=0.1542 nm). Field emission gun scanning electron microscope based energy dispersive x-ray (EDX) spectrometric analysis was performed for compositional analysis of the films.

Surface morphology, local electrical properties, and local donor distribution of AZO films were examined by atomic force microscopy in different modes using an Ir/Pt-coated silicon AFM tip with a resonant frequency of about 75 kHz and force constant of about 2.8 N nm$^{-1}$. For each sample, several images were taken from different regions to check the uniformity and to estimate the average grain size and root mean square (rms) roughness values. AFM, KPFM, and cAFM image analyses were carried out with the help of WSxM software [68].

The optical absorption of as-deposited AZO film (on SLG substrate) was measured by a UV-Visible-NIR spectrophotometer in the wavelength range of 300-700 nm which was further confirmed by bulk photoconductivity (PC) measurements. Silver paste was used to make electrical contacts on top of the AZO film and back side of the Si substrate for studying the spectral response. The spectral response was recorded using a commercial setup, equipped with a Keithley 2400 source meter and a lock-in amplifier where broadband illumination was provided by a xenon light source. The incident light power was measured with a calibrated silicon photodiode for data at wavelengths below 1100 nm and the spectrum was normalized to the power. The device was masked to attain an illuminated active area of 0.19 $cm^2$. In addition, bulk carrier density was determined using a Hall measurement setup (Ecopia, HMS-5000).

### 3.4.3 Results and discussion

Prior to the electrical measurements, AZO films are analyzed by AFM, XRD, and EDX to look for a possible correlation between the local charge transport and the structural properties of the films. It is observed that AZO films are granular in nature. The average grain size (22 nm) and distribution of grains are determined from the AFM image [Fig. 3.17(a)]. In addition, Fig. 3.17(b) shows the XRD pattern which confirms the crystalline nature of AZO films. The dominant peak at $2\theta$=34.1° can be attributed to the (002) reflection of hexagonal wurtzite structure, indicating the formation of highly oriented grains along the *c*-axis. It may be mentioned that no signature of Al or $Al_2O_3$ is observed in the films [13,33]. The average crystallite size (17 nm) is determined using Scherer's formula: $D=0.9\lambda/\beta cos\theta$ where $D$ is the crystallite size, $\beta$ is the full width at half maximum, $\theta$ is the Bragg angle, and $\lambda$ is the Cu-$K_\alpha$ x-ray wavelength [13,33]. In addition to the grain-related stress (described earlier), the development of intrinsic stress in polycrystalline films is also attributed to the presence of grain boundaries. In fact, as described earlier (section 3.1.3) recently it has been reported that with increasing grain size, the compressive stress of a crystalline AZO film can decrease [13]. In addition, the elemental composition of the samples is studied by EDX spectrometric analysis clearly shows the presence of Zn and O and the absence of Al or any other metallic impurity(es) in the film [22]. A representative EDX spectrum corresponding to AZO film grown on Si substrate is depicted in Fig. 3.17(c).

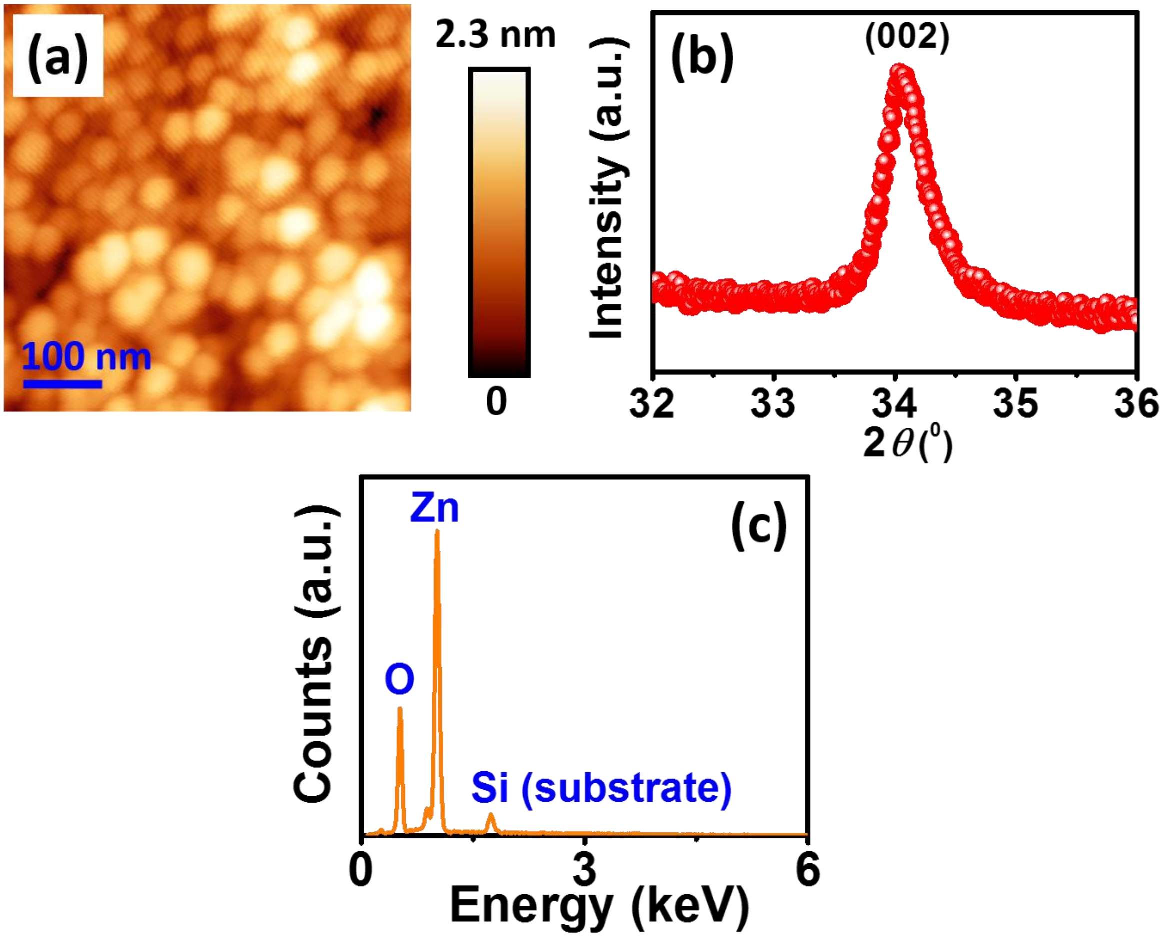

Figure 3.17: (a) AFM image of an AZO film grown on SLG substrate, showing the granular nature of the films, (b) shows the XRD pattern, and (c) depicts a representative EDX spectrum of the film [Similar data are obtained from AZO films grown on Si substrates not shown].

Fig. 3.18(a) shows the optical absorption spectrum of AZO film deposited on a SLG substrate where a sharp absorption edge around 365 nm corresponds to the bandgap (3.4 eV at RT). A close inspection reveals small absorption in the visible range (400-700 nm). In fact, the band-gap of the AZO film is measured from the Tauc plot [inset of Fig. 3.18(a)], which gives a value of 3.4 eV from the intercept of a line (on the absorption edge) with the abscissa. In addition, a tail in the range of 3.3 to 3.4 eV [Fig. 3.18(a)] can be assigned to band-edge absorption [69]. The band gap of AZO is also confirmed by carrying out photoconductivity measurements. Fig. 3.18(b) presents the photoconductivity spectrum, as a function of excitation wavelength in the range of 300-700 nm, exhibiting three distinct regions: (i) 300-380 nm, (ii) 380-500 nm, and (iii) 500-700 nm.

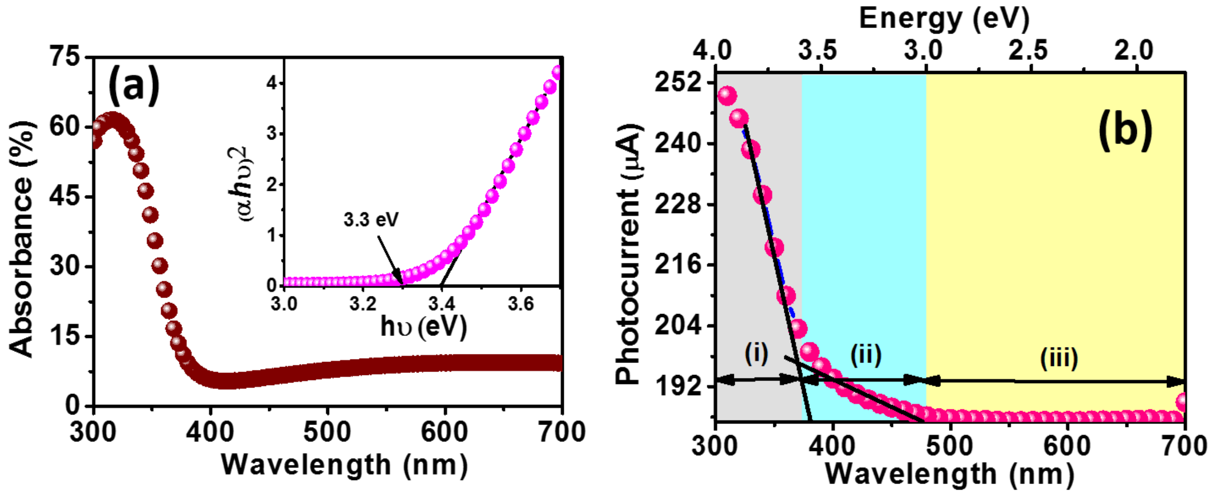

Figure 3.18: (a) Absorption spectrum of an as-grown AZO film at RT, where the inset depicts the Tauc plot, showing a direct band gap of ~3.4 eV, (b) photoconductivity spectrum of the film, in the spectra range of 300-700, taken at +5 V potential difference.

In region (i), a rapid decrease in the photocurrent is observed, which results from the band gap absorption of AZO. On the other hand, in region (ii), one can see a slow decrease in the photocurrent, which is a manifestation of the presence of mid-gap states induced by defects in grains and/or at GBs. Generally, mid-gap (trap) states in ZnO-based semiconductors are deep and therefore, show a slow photo-response [69,70]. At even higher wavelengths, i.e. in region (iii), photocurrent drops and gets saturated due to very low absorption, indicating that the defect-related electronic states are not sensitive to visible light (500-700 nm) [70]. In order to identify the exact location of trap states, in the present case, we have performed transient photoconductivity measurements, as shown in Fig. 3.19(a). As discerned, there is a low current prior to the UV (330 nm) exposure up to 100 s ─ called the dark current ─ from where it increases rapidly till the UV light is turned off (to check the retention time of the photocurrent) after ~220 s. Interestingly, the photocurrent is found to decrease slowly until 2000 s and it follows the same behaviour after multiple number of cycles (data not shown to maintain the clarity).

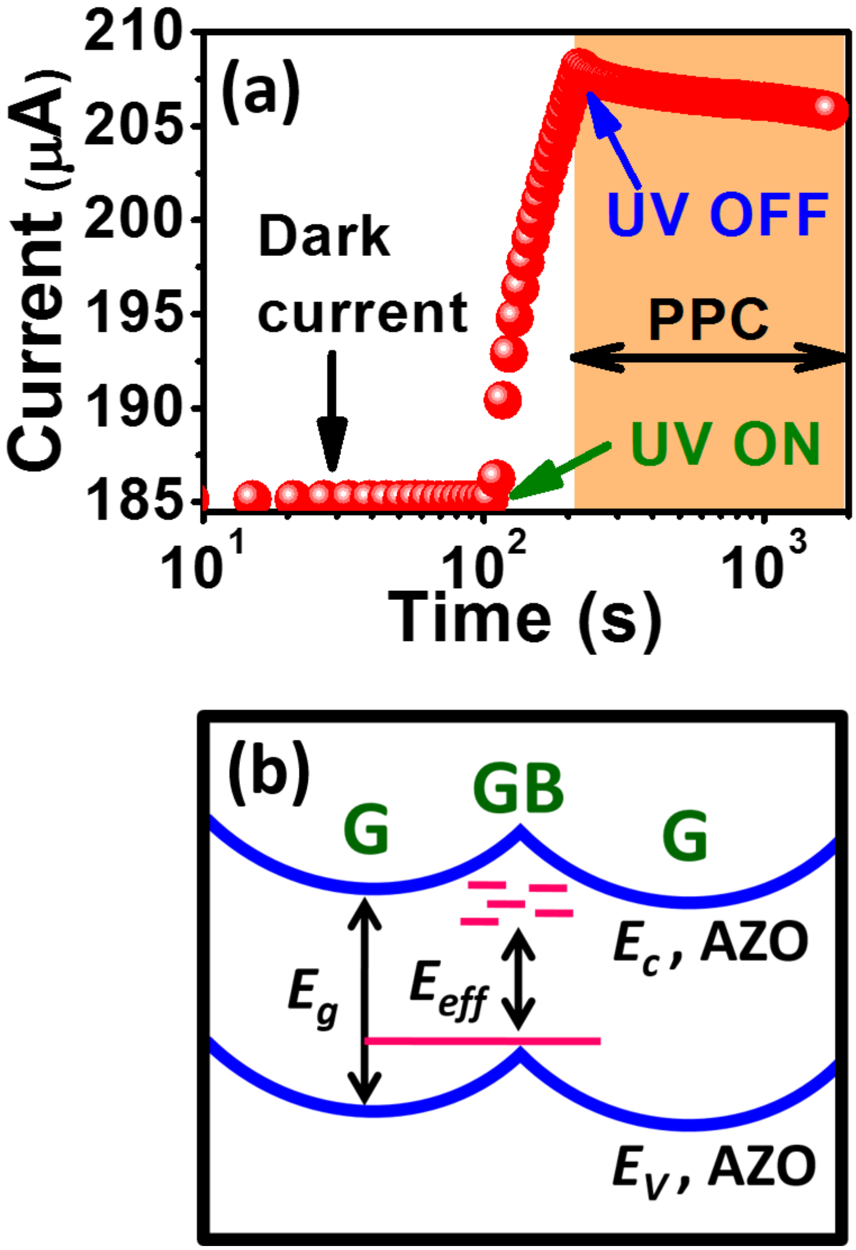

Figure 3.19: (a) Study of the transient photocurrent: a sharp rise in the photocurrent by switching the UV light ‘ON’ and the persistent photocurrent by switching it ‘OFF’ at the same voltage. (b) A schematic representation of conduction ($E_C$) and valance ($E_V$) bands of AZO, where G is the grain, GB is the grain boundary, and the pink lines represent the oxygen vacancy-mediated trap states.

An exponential fitting of this decay curve (or persistent photoconductivity), however, indicates that it should take more than 6 h to match the dark current. Persistent photoconductivity in such systems is attributed to fast oxygen desorption and slow absorption at GBs, due to respective UV light exposure and its subsequent withdrawal [69-71]. The slow response in photocurrent decay is related to the defects, which are located near the conduction band [69-71], as shown in Fig. 3.17(b) [72]. Thus, region (ii) in Fig. 3.16(b) can be correlated to the accumulation of defects at the GBs, leading to the evolution of defect states having distributed energy (~680 meV) within the AZO band gap [27]. These broadly distributed energy states will eventually cause a band gap narrowing ($E_{\mathrm{eff}}$) [73,74], as depicted schematically in Fig. 3.19(b), followed by its sensitivity in the visible range. In fact, most of the defects are present at the GBs, which in turn give rise to the local band bending of conduction and valance bands, opposing the smooth electrical transport [68].

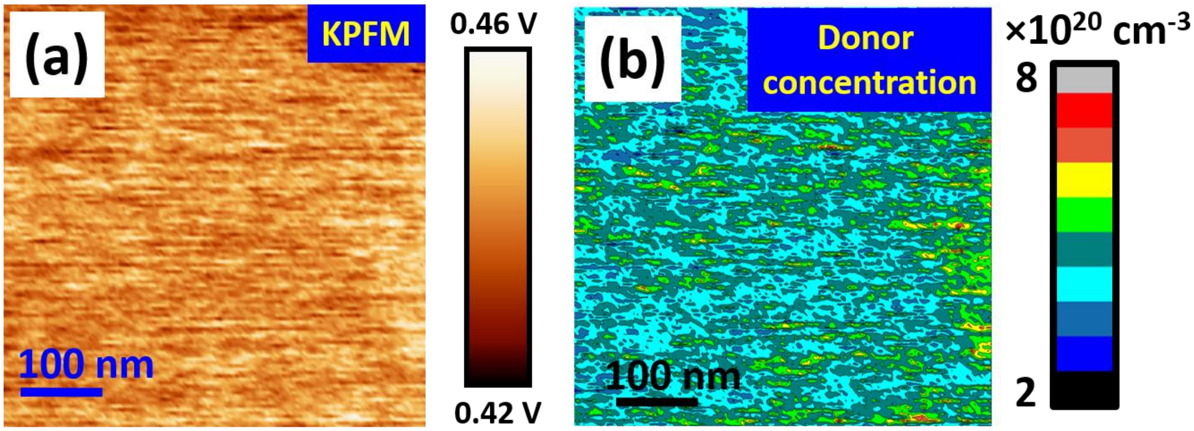

Figure 3.20: (a) Two-dimensional contact potential difference, $V_{\mathrm{CPD}}$, image (obtained from the KPFM measurements) of an as-grown AZO film deposited on SLG substrate. The image is recorded at a lift height of 60 nm. (b) Two-dimensional map of the charge carrier density.

Generally, electrical transport in a film depends on the work function and carrier concentration. Thus, to understand the local electrical transport, we employ KPFM for two-dimensional mapping of the work function and the carrier density. Mathematically, work function of a sample ($\Phi_{\mathrm{sample}}$) can be expressed as:

$$\Phi_{\mathrm{sample}} = \Phi_{\mathrm{tip}} - qV_{\mathrm{CPD}} \ , \tag{3.3}$$

where $\Phi_{\mathrm{tip}}$, $q$, and $V_{\mathrm{CPD}}$ are work function of the tip, electronic charge, and the substrate contact potential difference, respectively. Fig. 3.20(a) shows the measured $V_{\mathrm{CPD}}$ of AZO film grown on SLG glass. Since the work function of the tip (Si coated with Pt/Ir) is ~4.85 eV [54], the measured work function of the AZO film is found to be ~4.46±0.2 eV. The $V_{\mathrm{CPD}}$ between a metal tip and an $n$-type semiconductor can be written as:

$$V_{\mathrm{CPD}} = [\Phi_{\mathrm{tip}} - \chi + (E_F - E_{\mathrm{C}})]/q \ , \tag{3.4}$$

where $\chi$ is the electron affinity of the semiconductor, and $E_{\mathrm{F}}$, $E_{\mathrm{C}}$ are Fermi level and conduction band, respectively [61]. Following the above relation, $V_{\mathrm{CPD}}$ data obtained from our KPFM studies can be converted into the effective donor concentration, $C_{\mathrm{D}}$, as:

$$C_{\mathrm{D}} = N_{\mathrm{C}} \, exp[\frac{qV_{\mathrm{CPD}} - \Phi_{\mathrm{tip}} + \chi}{k_{\mathrm{B}}T}] \ , \tag{3.5}$$

where $N_{\mathrm{C}}$ is the effective density of states in the conduction band, $k_{\mathrm{B}}$ is the Boltzmann constant, and $T$ is the sample temperature [61]. After substituting $N_{\mathrm{C}}$=1×10$^{19}$ cm$^{3}$ [75], $\chi$ = 4.5 eV [76], and $\Phi_{\mathrm{tip}}$=4.85 eV [59], in Eq. (3.5) each pixel of the KPFM image is converted into an effective donor concentration and plotted as a separate image [shown in Fig. 3.20(b)]. From this image, the calculated average donor density turns out to be ~10$^{20}$ cm$^{-3}$, which is in good agreement with our Hall effect measurement (9.1×10$^{19}$ cm$^{-3}$). The measured donor concentration is found to be independent of thickness and matches well with literature [61], although it is known that donor concentration mapped by KPFM shows a large spatial variation in ZnO-based thin films [61]. Since the present AZO film shows persistent photoconductivity, we expose the film under UV light and measure the change in carrier concentration. However, a large variation in the calculated carrier density (obtained from KPFM studies) limits us to obtain any meaningful change in the measured donor concentration before and after UV-exposure. In absence of a reliable value of the donor concentration after UV-exposure, cAFM is employed to address the local electrical transport properties of AZO films.

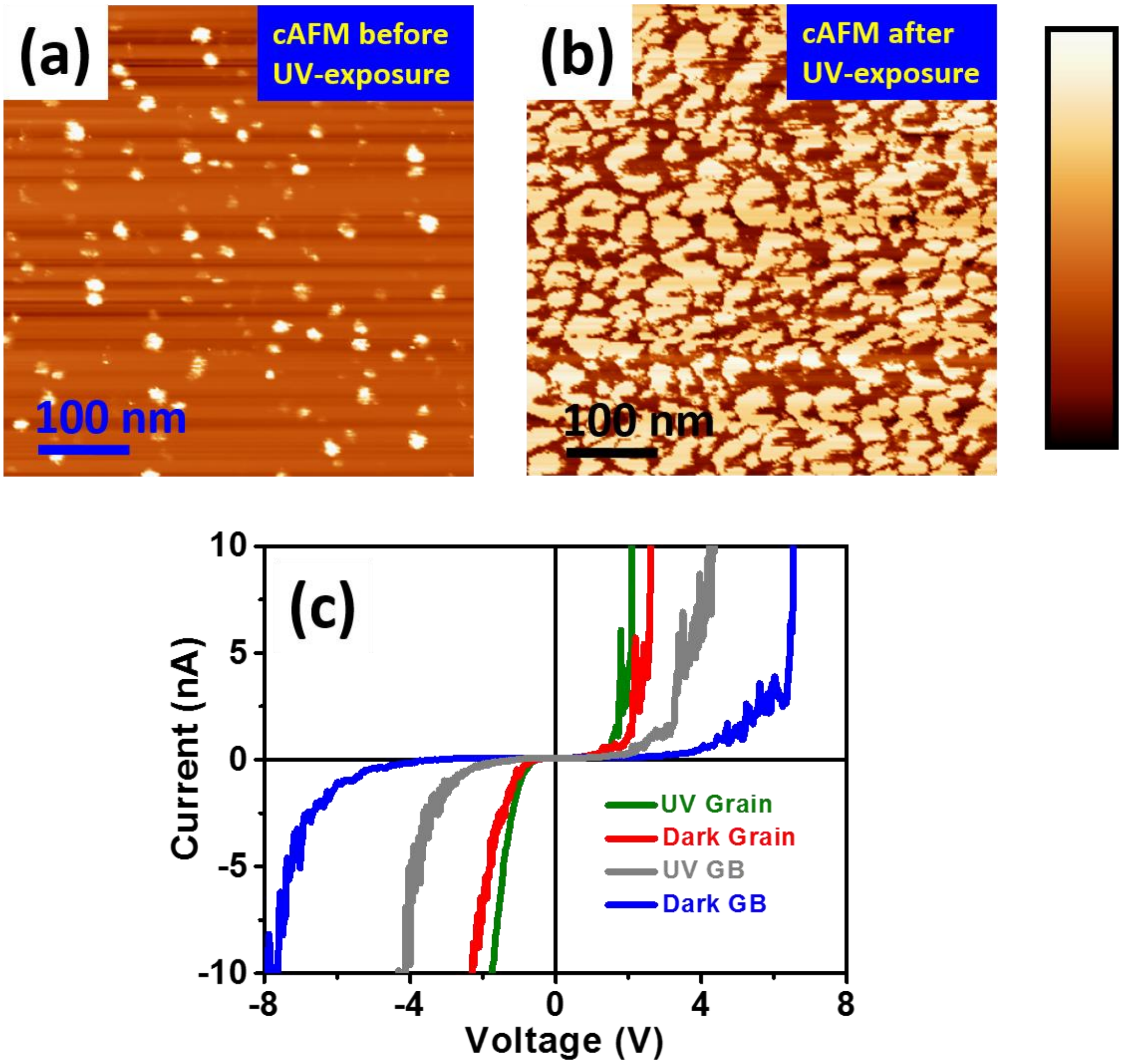

Figure 3.21: cAFM current maps of an AZO film deposited on a SLG substrate: (a) before and (b) after UV-exposure for 600 s. Here the scale bar varies from 0 to 5 nA for (a) and 0 to 18 nA for (b), respectively. (c) Local *I-V* characteristics at a grain and the GB before and after the UV-exposure.

Figs. 3.21(a) and (b) show cAFM images [at a tip voltage $V_{tip}$=+2 V] before (dark) and after UV-exposure, respectively. As a matter of fact, an AZO film is exposed to UV light (for a fixed wavelength of 330 nm) for 660 s and rapidly (within 102 s) set for the cAFM measurement. As expected, very low and distinct current spots are observed in dark [Fig. 3.21(a)], while following the UV-exposure, an enhanced current from grains is recorded at the same tip voltage [Fig. 3.21(b)]. It is known that a large number of charge carriers are generated after UV absorption in the AZO film, which in turn causes an enhancement in the current [33]. In fact, this enhanced and sustained current (in the bulk *I-V* characteristics) after UV-exposure is the persistent photocurrent (PPC) [as shown in Fig. 3.19(a)] [69]. In addition, from Figs. 3.20(a) and (b), it is clear that current signal is much higher at grains (compared to GBs) before and after UV-exposure. This low current at the GBs is a signature of the defect states which can trap the free carriers available for electrical transport [23]. Further, it is inferred that all the grains are not equally conducting, which is manifested from the local carrier concentration mapping (mentioned above). In fact, the spatial distribution of grain size and the presence of strain or stress can also be responsible for the observed nanoscale variation in the electrical conductivity [58]. In addition, the *I–V* characteristics of a single grain and a GB before and after UV-exposure are also performed.

Fig. 3.21(c) shows the *I-V* characteristics obtained from the grain and GB, using cAFM, suggesting the formation of a Schottky-like junction (in both cases) between the Pt tip and the AZO film [77,78]. As discerned, a clear difference in the conductivity of grains and GBs is observed. In this architecture, the AZO film is deposited on a SLG substrate and the Pt-coated AFM tip is used as the top electrode, making a metal-semiconductor configuration. Hence, the carrier transport in the metal-semiconductor contact is dominated by the majority carriers according to the thermionic emission theory for a Schottky barrier [77,78]. In this case, the current under the reverse bias can be expressed as [78]:

$$I = A^{*}ST^{2}\exp\left(-\frac{q\Phi_{\mathrm{e}}}{k_{\mathrm{B}}T}\right) \ , \tag{3.6}$$

where $A^*$ is the effective Richardson constant, $S$ is the area of the metal-semiconductor contact, $\Phi_e$ is the effective Schottky barrier height (SBH) in the presence of an image force. At a fixed temperature, $I$ depends on the SBH according to $I \propto exp(-q\Phi_e/k\mathrm{B}T)$. Thus, a change in the barrier height, $\Delta\Phi$, from a grain to the adjacent grain boundary can be calculated from the saturation current ratio ($I_G/I_{GB}$) under a forward bias, where $I_G$ is the saturation current for the grain and $I_{GB}$ is the saturation current at the grain boundary which turns out to be $\Delta\Phi = (k_BT/q)ln(I_G/I_{GB})$. Careful analysis results in $I_G$=79 pA, while $I_{GB}$ turns out to be 41 pA. After putting all required values, $\Delta\Phi$ turns out be 49 meV. It needs to be mentioned that $\Delta\Phi$ varies when measured at large number of places and on an average is found to be 50±10 meV. In fact, due to the variation in SBH from grains to grain boundaries, a modulation in the surface potential is generated which in turn gives rise to different electric transport properties at grains and grain boundaries [confirmed by cAFM measurements as shown in Figs. 3.21(a) and (b)]. The observed enhancement in the current at grains after UV-exposure gives rise to a smooth conduction of charge carriers in the AZO film deposited on the SLG substrate, which should potentially improve an AZO-based device performance. In order to understand the role of UV absorption in the photoresponsivity of AZO-based solar cell, we have fabricated an *n*-AZO/*p*-Si heterostructure diode and measured its photoresponsivity at different wavelengths [36,79,80].

Fig. 3.22 shows the photoresponse of a hetrojunction (fabricated by using 30 nm AZO on *p*-Si) as a function of wavelength under the forward bias condition. Plots (I), (II), and (III) represent photoresponse recorded in the wavelength ranges of 500-800 nm, 400-800 nm, and 300-800 nm, respectively. From this figure, two conspicuous behaviours are noticed. For regions (I) and (II), the recorded photoresponses are low in magnitude and remain almost constant in the visible range (400-800 nm). In fact, a wavelength independent the photoresponsivity is observed which can be attributed to the transport of photo-generated electrons (minority carriers) in *p*-Si. On the other hand, during photoresponsivity measurement, corresponding to plot (III), the sample got exposed to UV radiation leading to a strong enhancement in the photoresponsivity (by a factor of ~1.5) even in the visible range. This enhancement can be explained in the framework of different drifting of photogenerated electrons and holes in AZO and Si, respectively [36,79-81]. For instance, the photogenerated electrons in AZO can easily move into Si due to a relatively low potential barrier at the interfacial region but the holes in Si cannot tunnel through the high potential barrier [36,79-81].

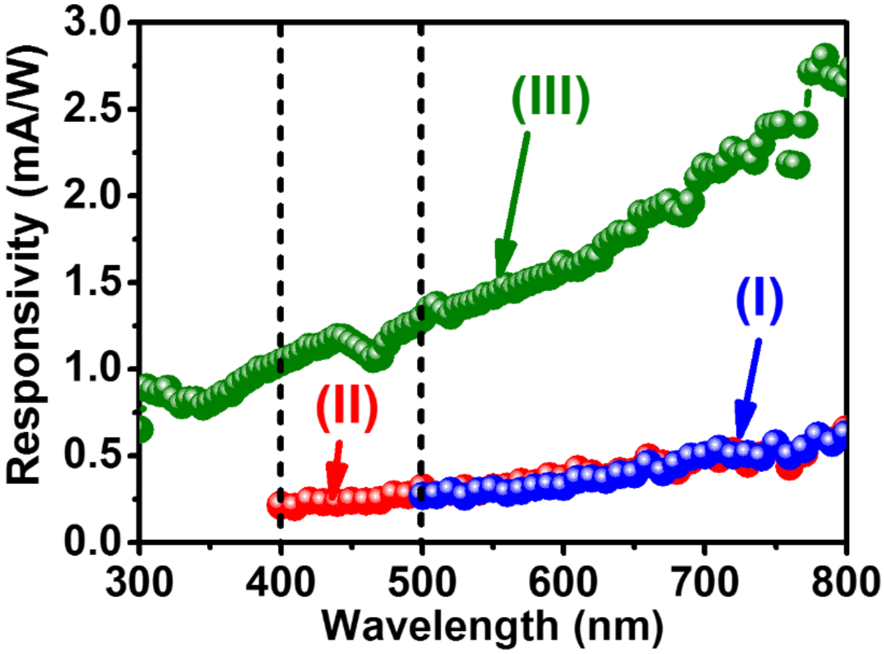

Figure 3.22: Photoresponsivity spectra of a 30 nm-thick AZO overlayer grown on *p*-type Si in different spectral ranges.

Thus, it can be inferred that UV absorption enhances the performance of an AZO-based solar cell instead of leading to a much believed optical loss in the underlying absorbing layer.

### 3.4.4 Conclusions

In conclusion, we have grown AZO thin films on soda lime glass and Si substrates at room temperature using pulsed dc magnetron sputtering technique. Optical band gap (~3.4 eV) of highly oriented AZO films is confirmed by optical absorption and photoconductivity measurements. cAFM investigation shows an enhancement in the local electrical conductivity at grains after UV-exposure which gives a smooth conduction in the film. In particular, our experimental observation on enhancement in the photoresponsivity of an AZO/Si heterojunction diode in the visible range, after UV-exposure, manifests that UV absorption in the AZO overlayer should not be considered as an optical loss for the underlying absorber layer of a solar cell which is in contrary to the common belief.

**Table 3.1:** Following parameters were determined for the AZO/Si hetrostructures in S1 to S4: rms surface roughness (nm), and average grain size (nm) from AFM; peak position (2$\theta$), FWHM (deg), average grain size (nm), strain (%), and stress (N $m^{-2}$) from XRD; turn-on potential (V), series resistance (kΩ), and the ideality factor (*n*) from the *I-V* characteristics. Negative signs in strain and stress values indicate their compressive nature.

| Sample No. | AFM | | XRD | | | | | *I-V* | | |
|---|---|---|---|---|---|---|---|---|---|---|
| | rms surface roughness (nm) | Av. grain size (nm) | Peak position (2$\theta$ in deg) | FWHM (deg) | Av. grain size (nm) | Strain (%) | Stress ($\sigma$ in 109 Nm-2) | Turn-on potential (V) | Series resistance (kΩ) | Ideality factor (*n*) |
| S1<br>(5 min)<br>30 nm | 0.63 | 22 | 34.06 | 0.53 | 17 | -0.98 | -4.27 | 3.26 | 7.5 | 1.7 |
| S2<br>(10 min)<br>60 nm | 1.19 | 26 | 34.07 | 0.44 | 21 | -0.93 | -4.18 | 2.65 | 7.4 | 1.7 |
| S3<br>(20 min)<br>120 nm | 2.32 | 32 | 34.10 | 0.37 | 26 | -0.91 | -4.13 | 2.25 | 7.2 | 2.4 |
| S4<br>(30 min)<br>175 nm | 2.78 | 36 | 34.14 | 0.32 | 30 | -0.90 | -4.06 | 1.80 | 6.1 | 2.7 |

**Table 3.2:** Various parameters extracted from *I-V* data.

| S.N. | Sample temperature (K) | Turn on potential, $V_T$ (V) | Reverse leakage current, $I_0$ (mA) | Series resistance (Ω) | Ideality factor, *n* |
|---|---|---|---|---|---|
| 1 | 293 | 3.48 | 0.32 | 444.62 | 2.04 |
| 2 | 303 | 3.45 | 0.28 | 342.19 | 2.05 |
| 3 | 313 | 3.45 | 0.24 | 317.05 | 2.06 |
| 4 | 323 | 3.44 | 0.19 | 313.53 | 2.05 |
| 5 | 333 | 3.43 | 0.32 | 303.24 | 2.03 |
| 6 | 343 | 3.50 | 0.40 | 309.99 | 2.03 |
| 7 | 353 | 3.54 | 0.50 | 333.91 | 2.10 |
| 8 | 363 | 3.62 | 0.78 | 367.11 | 2.12 |
| 9 | 373 | 3.71 | 0.92 | 444.76 | 2.15 |
| 10 | 383 | 3.91 | 1.02 | 514.88 | 2.19 |
| 11 | 393 | 4.25 | 1.13 | 466.79 | 2.15 |
| 12 | 403 | 4.56 | 1.16 | 372.35 | 2.14 |
| 13 | 413 | 5.12 | 1.01 | 349.41 | 2.13 |
| 14 | 423 | 5.43 | 1.10 | 350.46 | 2.11 |

# Bibliography

[1] I. Horcas, R. Fernandez, J.M. Gomez-Rodriguez, J. Colchero, J. Gomez-Herrero, A.M. Baro, Rev. Sci. Instrum. 78 (2007) 013705.

[2] M. Kumar, S. K. Hazra, and T. Som, *J*. Phys. D: Appl. Phys. 48 (2015) 455301.

[3] M. Kumar, T. Basu, and T. Som, J. Appl. Phys. 118 (2015) 055102.

[4] G. H. Gilmer and P. Bennema, J. Appl. Phys. 43 (1972) 1347.

[5] E. Chason, J. W. Shin, S. J. Hearne and L. B. Freund, J. Appl. Phys. 111 (2012) 083520.

[6] F. Khan, Vandana, S. N. Singh, M. Husain, and P. K. Singh, Sol. Energy Mater. Sol.Cells. 100 (2012) 57.

[7] C. Y. Huang, Y. J. Yang, J. Y. Chen, C. H. Wang, Y. F. Chen, L. S. Hong, C. S. Liu, and C. Y. Wu, Appl. Phys. Lett. 97 (2010) 013503.

[8] H. Huang, G. Fang, X. Mo, L. Yuan, H. Zhou, M. Wang, H. Xiao, and X. Zhao, Appl. Phys. Lett. 94 (2009) 063512.

[9] W. Körner, and C. Elsässer, Phys. Rev. B 81 (2010) 085324.

[10] B. Z. Dong, G. J. Fang, J. F. Wang, W. J. Guan, and X. Z. Zhao, J. Appl. Phys. 101 (2007) 033713.

[11] K. Ellmer, A. Klein, B. Rech, Eds. Transparent Conductive Zinc Oxides: Basics and Applications in Thin Film Solar Cells. 2007: Springer, Berlin.

[12] Z. L. Pei, X. B. Zhang, J. Gong, C. Sun, R. F. Huang, and L. S. Wen, Thin Solid Films 497 (2006) 20-23.

[13] J. G. Lu, Z. Z. Ye, Y. J. Zeng, L. P. Zhu, L. Wang, J. Yuan, and B. H. Zhao, J. Appl. Phys. 100 (2006) 073714.

[14] A. A. Ziabari, and S. M. Rozati, Physica B 407 (2012) 4512.

[15] P. C. Yao, S. T. Hang, Y. S. Lin, W. T. Yen, and Y. C. Lin, Appl. Surf. Sci. 257 (2010) 1441.

[16] B. C. Mohanty, Y. H. Jo, D. H. Yeon, I. J. Choi, and Y. S. Cho, Appl. Phys. Lett. 95 (2009) 062103.

[17] H. S. Lee, J. Y. Lee, T. W. Kim, D. W. Kim, and W. J. Cho, J. Mater. Sci. 39 (2004) 3525.

[18] S. Y. Hu, Y. C. Lee, J. W. Lee, J. C. Huang, J. L. Shen, and W. Water, Appl. Surf. Sci. 254 (2008) 1578.

[19] S. Maniv, W. D. Westwood, and E. Colombini, J. Vac. Sci. Technol. 20 (1982) 162.

[20] B. B. He, Two-Dimensional X-Ray Diffraction. 2009: John Wiley & Sons, New Jersey.

[21] K. Mohanta, and A. J. Pal, J. Appl. Phys. 105 (2009) 024507.

[22] S. Majumdar, S. Chattopadhyay, and P. Banerji, Appl. Surf. Sci. 255 (2009) 6141.

[23] F. Chaabouni, M. Abaab, and B. Rezig, Superlattices and Microstructures 39 (2006) 171.

[24] T. Hori, Gate Dielectrics and MOS ULSIs: Principle, Technologies, and Applications. 1997: Springer, Berlin.

[25] A. Kanjilal, L. Rebohle, W. Skorupa, and M. Helm, Appl. Phys. Lett. 94 (2009) 101916.

[26] B. He , H. Z. Wang , Y. G. Li , Z. Q. Ma , J. Xu , Q. H. Zhang , C. R. Wang , H. Z. Xing, L. Zhao , and Y. C. Rui, J. Alloy. Compd. 581 (2013) 28.

[27] E. M. Likovich, R. Jaramillo, K. J. Russell, S. Ramanathan, and V. Narayanamurti, Phys. Rev. B 83 (2011) 075430.

[28] L. C. Chen, and C. N. Pan, Eur. Phys. J. Appl. Phys. 44 (2008) 43.

[29] Y. M. Cui, Y. F. Tian, W. Liu, Y. F. Li, R. M. Wang, and T. Wu, AIP Adv. 1 (2011) 042129.

[30] H. Tong, Z. Deng, Z. Liu, C. Huang, J. Huang, H. Lan, C. Wang, and Y. Cao, Appl. Surf. Sci. 257 (2011) 4906.

[31] H. Wang, M. H. Xu, J. W. Xu, M. F. Ren, and L. Yang, J. Mater. Sci. Mater. Electron. 21 (2010) 589.

[32] P. Cuony, D. T. L. Alexander, I. Perez-Wurfl, M. Despeisse, G. Bugnon, M. Boccard, T. Soderstrom, A. Hesser-Wyser, C. Hebert, and C. Ballif, Adv. Mater. 24 (2012) 1182.

[33] M. Dutta, and D. Basak, Appl. Phys. Lett. 92 (2008) 212112.

[34] M. Kumar, A. Kanjilal, and T. Som AIP Adv. 3 (2013) 092126.

[35] T. Basu, M. Kumar, and T. Som Mat. Lett. 135 (2014) 188.

[36] T. Basu, M. Kumar, P. K. Sahoo, A. Kanjilal, and T. Som Nanoscale Res. Lett. 9 (2014) 1.

[37] A. K. Pradhan, R. M. Mundle, K. Santiago, J. R. Skuza, B. Xiao, K. D. Song, M. Bahoura, R. Cheaito, and P. E. Hopkins Sci. Rep. 4 (2014) 6415.

[38] M. M. Islama, S. Ishizuka, A. Yamada, K. Matsubara, S. Niki, T. Sakurai, K. Akimoto Appl. Surf. Sci. 257 (2011) 4026.

[39] G. Kaurn, A. Mitra, K. L. Yadav Prog. Nat. Sci.: Mater Int. 25 (2015) 12.

[40] G. V. Naik, J. Liu, A. V. Kildishev, V. M. Shalaeva, and A. Boltassev PNAS 109 (2012) 8834.

[41] S. Sarkar, S. Patra, S. K. Bera, G. K. Paul, and R. Ghosh Physica E 46 (2012) 1.

[42] O. Bamiduro, H. Mustafa, R. Mundle, R. B. Konda, and A. K. Pradhan Appl. Phys. Lett. 90 (2007) 252108.

[43] V. Bhosle, A. Tiwari, and J. Narayan Appl. Phys. Lett. 88 (2006) 032106.

[44] B. B. He, Two-Dimensional X-Ray Diffraction. 2009: John Wiley & Sons, New Jersey.

[45] S. Majumdar and P. Banerji, J. Appl. Phys. 105 (2009) 043704.

[46] A. Kargar, K. Sun, Y. Jing, C. Choi, H. Jeong, Y. Zhou, K. Madsen, P. Naughton, S. Jin, G. Y. Jung, and D. Wang Nano Lett. 13 (2013) 3017.

[47] F. Yang, M. Wei, and H. Deng J. Appl. Phys. 114 (2013) 134502.

[48] M. Asghar, K. Mahmood, M. Faisal, and M. A. Hasan J. Phys.: Conf. Seri. 439 (2013) 012030.

[49] C. W. Cao, W. N. Bao, X. Lin, X. Y. Liu, Y. Geng, H. L. Lu, Q. Q. Sun, P. Zhou, D. W. Zhang, and P. F. Wang ECS Solid State Lett. 2 (2013) 25.

[50] X. G. Zhang and S. T. Pantelides Phys. Rev. Lett. 108 (2012) 266602.

[51] D. Songand and B. Guo J. Phys. D: Appl. Phys. 42 (2009) 025103.

[52] B. K. Sarker and S. I. Khondaker ACS Nano 6 (2012) 4993.

[53] M. Kumar, T. Basu, and T. Som J. Appl. Phys.118 (2015) 055102.

[54] G. M. Ali and P. Chakrabarti Appl. Phys. Lett. 97 (2010) 031116.

[55] J. G. Lua, S. Fujita, T. Kawaharamura, H. Nishinaka, Y. Kamada, and T. Ohshima, Z. Z. Ye, Y. J. Zeng, Y. Z. Zhang, L. P. Zhu, H. P. He, and B. H. Zhao J. Appl. Phys. 101 (2007) 083705.

[56] M. W. G. Hoffmann, A. E. Gad, J. D. Prades, H-R Francisco, R. Fizc, H. Shen, S. Mathur Nano Energy 2 (2013) 514.

[57] H. Liu, V. Avrutin, N. Izyumskaya, U. Ozgur, H. Morkoc, Superlattices Microstruct. 48 (2010) 458.

[58] V. Consonni, N. Baier, O. Robach, C. Cayron, F. Donatini, and G. Feuillet, Phys. Rev. B 89 (2014) 035310.

[59] Y. Lv, J. Cui, Z. M. Jiang, and X. Yang, Nanoscale Res. Lett. 7 (2012) 659.

[60] W. Melitz, J. Shen, A. C. Kummel, and S. Lee, Surf. Sci. Rep. 66 (2011) 1.

[61] C. Maragliano, S. Lilliu, M. S. Dahlem, M. Chiesa, T. Souier, and M. Stefancich, Sci. Rep. 4 (2014) 1038.

[62] S. Nandy, R. Thapa, M. Kumar, T. Som, N. Bundaleski, O. M. N. D. Teodoro, R. Martins and E. Fortunato, Adv. Funct. Mater. 25 (2015) 947.

[63] W. Wu, Y. Horibe, N. Lee, S. W. Cheong, and J. R. Guest, Phys. Rev. Lett. 108 (2012) 077203.

[64] D. C. Coffey, O. G. Reid, D. B. Rodovsky, G. P. Bartholomew, and D. S. Ginger, Nano Lett. 7 (2007) 738.

[65] S. Siebentritt Sol. En. Mater. Sol. Cells 95 (2011) 1471.

[66] Y. S. Lee, D. Chua, R. E. Brandt, S. C. Siah, J. V. Li, J. P. Mailoa, S. W. Lee, R. G. Gordon, and T. Buonassisi, Adv. Mater., 26 (2014) 4704.

[67] U. Palanchoke, V. Jovanov, H. Kurz, P. Obermeyer, H. Stiebig, and D. Knipp, Optics Express 20 (2012) 6340.

[68] http://www.nanotec.es/products/wsxm/index.php.

[69] C. E. Benouis, M. Benhaliliba, A. Sanchez Juarez, M. S. Aida, F. Chami, F. Yakuphanoglu, J. Alloys and Comp. 490 (2010) 62.

[70] Z. Fan, P. Chang, J. G. Lu, E. C. Walter, R. M. Penner, C. Lin, and H. P. Lee, Appl. Phys. Lett. 85 (2004) 6128.

[71] H. S. Kim, S. H. Jeon, J. S. Park, T. S. Kim, K. S. Son, J. B. Seon, S. J. Seo, S. J. Kim, E. Lee, J. G. Chung, H. Lee, S. Han, M. Ryu, S. Y. Lee, and K. Kim, Sci. Rep. 3 (2013) 1459.

[72] Y. J. Kim and H. J. Kim, Mat. Lett. 41 (1999) 159.

[73]J. Wang, Z. Wang, B. Huang, Y. Ma, Y. Liu, X. Qin, X. Zhang, and Y. Dai, Appl. Mater. Interfaces, 4 (2012) 4024.

[74] V. Srikant and D. R. Clarke, J. Appl. Phys. 81 (1997) 6357.

[75] Ellmer, K “Transparent Conductive Zinc Oxide”, Springer Series in Materials Science: 2008, Springer Berlin.

[76] J. J. Robbins and C. A. Wolden, Appl. Phys. Lett. 83 (2003) 3933.

[77] S. M. Sze and K. K. Ng, Physics of Semiconductor Devices, Wiley, 2006.

[78] S. Nandy, G. Gonçalves, J. V. Pinto, T. Busani, V. Figueiredo, L. Pereira, R. F. P. Martins and E. Fortunato, Nanoscale 5 (2013) 11699.

[79] A. K. Pradhan, T. Holloway, R. Mundle, H. Dondapati, and M. Bahoura, Appl. Phys. Lett. 100 (2012) 061127.

[80] T. Basu, M. Kumar, and T. Som, Mater. Lett.135 (2014) 188.

[81] C. Y. Huang, Y. J. Yang, J. Y. Chen, C. H. Wang, Y. F. Chen, L. S. Hong, C. S. Liu, and C. Y. Wu, Appl. Phys. Lett. 97 (2012) 013503.

# CHAPTER 4

## 4. Role of polarization in charge transport: local band bending and grain boundaries, inhomogeneous work function and electric field induced doping

Up to this point, it has been revealed that defects (mostly in the form of oxygen vacancies) at the GBs play a significant role in the charge transport process in AZO thin films. In fact, a potential barrier is formed at the GBs which is expected to govern the charge transport across the same. Thus, in order to control the charge transport in AZO, the true nature of the potential barrier at GBs should be understood.

In doing so, in this chapter, we have undertaken the study of nanoscale charge transport properties of an AZO layer by using cAFM, EFM, KPFM, and PFM. Here we make use of these local probe techniques to show the novel pseudoferroelectric behaviour in AZO thin films at RT and how the barrier forms at the GBs due to defects and it takes part in the charge conduction process from one grain to the next. We also show how the barrier height is affected by the orientation of polarization. In fact, we show the roles of defects and polarization in the local band bending of AZO thin films at the grain boundaries.

In addition, we show the role of polarization on the work function at the surface of AZO thin films. In particular, using KPFM studies, the work function of an AZO film is mapped which is found to be spatially inhomogeneous. Further, the effect of polarization on the charge transport process is also confirmed by cAFM. As a matter of fact, the presence of polarization in AZO films opens up a new avenue to control the charge transport in the same. In particular, using KPFM and contact-mode (cont-mode) AFM, we demonstrate that work function of an AZO film can be tuned by inducing charge carriers through an applied electric field. For instance, we show that by applying a positive or negative bias on the top of an AZO film, electrons or holes can be induced on the surface, which in turn decrease or increase the work function of the same, respectively. Further to this, the role of electric field-induced doping in nanoscale charge transport is also demonstrated by performing the local *I-V* measurements using cAFM.

## 4.1 Local probe microscopic studies on Al-doped ZnO: Pseudoferroelectricity and band bending at grain boundaries

### 4.1.1. Introduction

As discussed earlier, aluminum-doped zinc oxide (AZO) offers not only high electrical conductivity but also high transmittance, which make this material suitable for use as a transparent conductive oxide [1-4] AZO thin films are grown by various methods such as chemical vapor deposition, sputtering, and pulsed laser deposition [2-6]. In most cases, depending on the thermodynamic driving force, isolated islands coalesce and the form grain boundaries (GBs). GBs give rise to a large number of defects and in turn influence the physical properties in case of thin films [6-10].

On the basis of Landau theory, Tagantsev has classified the doped-ZnO system as pseudoferroelectric materials [11]. Recently, Herng *et al*. have demonstrated oxygen vacancy-assisted pseudoferroelectricity model in much debatable ZnO by first-principle calculations [6], albeit theoretically inverse domains (polarization) cannot be formed in a perfect ZnO crystal due to a high energy barrier (>5 eV per Zn-O pair) for ion diffusion. Especially, they propose that a spontaneous nucleation of inverted domains can be developed at GBs due to the vacancies. Given a downward electric field, the positively charged Zn ion has been shown to move up in the vertical direction, causing a polarity inversion of Zn and O atoms at the adjoining sites. This in turn leaves a trail of inversion ferroelectric domains and forms an inversion domain wall through the GBs. Thus, the pseudoferroelectric behavior in ZnO and doped-ZnO materials may be considered to be driven by defect enhanced structural disorder [6,13-15]. In addition, the spatial distribution of carrier concentration, the grain size and structure, and the nature or type of GBs also play major roles in exhibiting the pseudoferroelectric property and the local band bending [7,12]. Thus, probing the impact of GBs on these physical properties in AZO is of immense importance and has drawn renewed interest in both fundamental and applied physics.

It is known that defect-induced local band bending at GBs may ultimately govern the performance of a device [6]. In fact, the presence of a potential barrier at the GB has even been shown to help improving the performance of a polycrystalline chalcopyrite thin film based solar cell device [8]. It can be mentioned that band bending at GBs of doped-ZnO has been reported using different indirect methods [9,12,16]. For instance, Bikowski *et al.* have studied the relation between the electronic transport and the structural properties in Al- and Mg-doped ZnO and tried to correlate their results on the basis of a predicted band bending at GBs [16]. However, a direct microscopic evidence on the local band bending at the GBs and determination of this potential barrier in doped-ZnO systems (e.g. AZO) is yet to be explored. Likewise, an experimental evidence on pseudoferroelectricity in AZO is also lacking.

In order to understand the local properties at GBs, the use of scanning tunneling microscopy has been in common place [5,8]. For instance, Likovich *et al*. [5] have recently demonstrated the accumulation of traps at AZO GBs, leading to a broad distribution of the defect states below the conduction band (~100 meV), which affects the electron transport properties. This may consequently create a potential barrier for the carrier transport, albeit it needs to be verified experimentally. Recently, versatile applications of scanning probe microscopy have made it suitable to study the local physical properties of materials as well [17]. For instance, suitably choosing the different modes of scanning probe microscopy viz. conductive atomic force microscopy [18], electrostatic force microscopy, Kelvin probe force microscopy [19], and piezoresponse force microscopy [20], one can build up information on the local electrical conduction across GBs. Recently, using scanning probe microscopy, the impact of GBs on the charge transport properties have been studied in detail for both polar and non-polar polycrystalline thin films [5,16,21]. In general, the local band bending at the GBs is explained in the theoretical framework of the double Schottky potential barriers (DSPB) in nonpolar materials and the polarization-meditated barrier in ferroelectric materials [11,12,21]. According to this model, the orientation of polarization can strongly affect the Schottky barrier height (SBH). In fact, an upward polarization leads to an increase in the barrier height, whereas a downward polarization is responsible for a decrease in the same. However, to the best of our knowledge, the role of polarization in the local band bending of pseudoferroelectric materials remains hitherto unexplored.

In this work, we show the roles of defects and polarization in the local band bending of AZO thin films at the grain boundaries. Since the defects at the GBs are known to play a significant role in controlling the overall charge transport, we have undertaken the study of nanoscale transport properties of an AZO layer by using cAFM, EFM, KPFM, and PFM. Here we make use of these local probe techniques to show the novel pseudoferroelectric nature of AZO at room temperature and how the barrier forms at the GBs due to the defects and it takes part in the charge conduction process from one grain to the next. We also show how the barrier height is affected by the orientation of polarization. The present study is due to help taking a step forward to understand the potential barrier formation (the local band bending) at the GBs for doped-ZnO systems in light of both polarization and electrostatic effects.

### 4.1.2 Experimental

Following the same methodology in Chapter 3 (section 3.2.2), we deposited AZO thin films on ultrasonically cleaned Pt/$TiO_2$/$SiO_2$/Si substrates (Radiant Technology, UK) at RT. Subsequently, the surface morphology and the local electrical properties of the AZO films were examined by an *ex-situ* AFM in different modes using conductive tips (AC240TM, Electric-Lever, Olympus), having a tip radius of 15 nm, the stiffness of 2 N $m^{-1}$, and a resonance frequency of 70 kHz. Further, EFM and KPFM measurements were performed in the lift mode with a user-defined lift height of 60 nm from the surface. Out-of- plane piezoresponse force microscopy and spectroscopy were used to characterize the pseudoferroelectric behavior at RT of as-grown AZO films. It may be mentioned that cAFM, EFM, and PFM measurements were accomplished on several films having thicknesses in the range of 30-120 nm. In addition, cAFM, EFM, KPFM, and PFM measurements were performed at large number of randomly chosen places with different scan speeds (0.2 to 1 Hz) and at various scan angles (by rotating the samples) on three sets of samples deposited under the similar conditions. However, no noticeable change in the results were found for either of them, confirming the absence of tip-related artifacts in the present data.

In the present case, samples were placed in the silica gel-filled boxes (immediately after taking out of the deposition chamber) and subsequently stored inside a controlled, low-humidity sample storage unit, which in turn reduced the possibility of adsorption of water molecules on the surface of samples. In addition, to reduce the adsorption of water molecules on film surfaces, the samples were taken out of the container boxes just before starting the respective cAFM, EFM, KPFM, and PFM measurements. Further, a low humidity environment was always maintained surrounding the main AFM setup. In fact, the used AFM setup was placed in a closed, low-vibration, and low-humidity enclosure – filled with sufficient amount of humidity absorber (silica gel bead-filled packets), which reduced the humidity level (close to 15%, as was measured by a commercially available and calibrated humidity meter) within the same. Such a low-humidity level was comparable to the one created by dry nitrogen (≈8-10%) and thus, in this study, the humidity-related issues might be safely considered as negligible to induce adsorbed water molecule-related artifacts during the current measurements and alter their lateral resolution.

It would be important to mention that the electric transport properties at nanoscale, in particular performed by cAFM measurements, would strongly depend on the applied force [22]. Hence, the spring constant of the tip and the detector sensitivity were calibrated with the help of a quartz crystal. These helped us to find out a relation between the set-points and the applied force and we used a fixed set-point (applied force: 2 nN) during all cAFM measurements. In fact, the use of a constant force set-point reduced the possibility of introducing tip-related artifacts to a significant extent [22]. The commercial software together with the Asylum Research code were used to get the statistical distribution of active domains. On the other hand, AFM image analysis was carried out by employing WSxM [23] and SPIP [24] softwares. For a better understanding of various physical properties of samples and a possible correlation with the local electrical properties, samples were also analyzed by scanning electron microscopy (SEM), x-ray energy dispersive analysis (EDX), and x-ray diffraction (XRD).

### 4.1.3 Results and discussion

Fig. 4.1(a) shows the schematics on the working principles of EFM and cAFM. Prior to performing the electrical measurements, the topography of the AZO films is investigated by AFM in the AC$^{TM}$ mode which provides an average grain size of 22 nm and the rms roughness of 2.3 nm [Fig. 4.1(b)].

When zoomed into a small region, the grains and GBs are clearly seen, as is depicted in the inset of Fig. 4.1(b). It is well-known that the grains and GBs may have different charge carrier densities. Generally, EFM is used for the spatial mapping of accumulation of the charge carriers [21]. In the present case, EFM image of an AZO film, recorded using a tip voltage ($V_{\text{tip}}$) of -3 V, provides the electrostatic force distribution on the surface [Fig. 4.1(c)]. The bright contrast at the GBs indicates the strong repulsive interaction (due to the trapped negative surface charges), while the dark contrast of the grains corresponds to a weak repulsive interaction [21]. This variation in the intensity relates to the different accumulation of different amount of charges at the grains and grain boundaries, which in turn leads to the different charge transport process.

Generally, cAFM is extensively used because it can build up simultaneous information on local electrical conduction and surface topography. In fact, a one-to-one correspondence between the surface morphology and the current mapping, with very high lateral resolution (~5 nm in topography and ~1 pA in current image), can be obtained from cAFM measurements [22]. In addition, for cAFM studies, a conductive tip is used as a top electrode which gives an easy control to perform the *I-V* measurements at a desired location [22]. Fig. 4.1(d) shows the current map, obtained from a cAFM measurement (for a tip voltage, $V_{\text{tip}}$=+4 V) where the bright spots represent the current signal. Thus, the current signal is much higher on the grains rather than that at the GBs, which manifests that the accumulated negative charge carriers at GBs remain trapped and hence, are not available for the electrical conduction. The trap states at GBs can create a space charge regime, which leads to a conduction band bending due to the formation of a back-to-back Schottky barrier at the GBs [7,12]. In order to quantify the local band bending, we have carried out the local current-voltage (*I-V*) characteristics at the grains and GBs using cAFM.

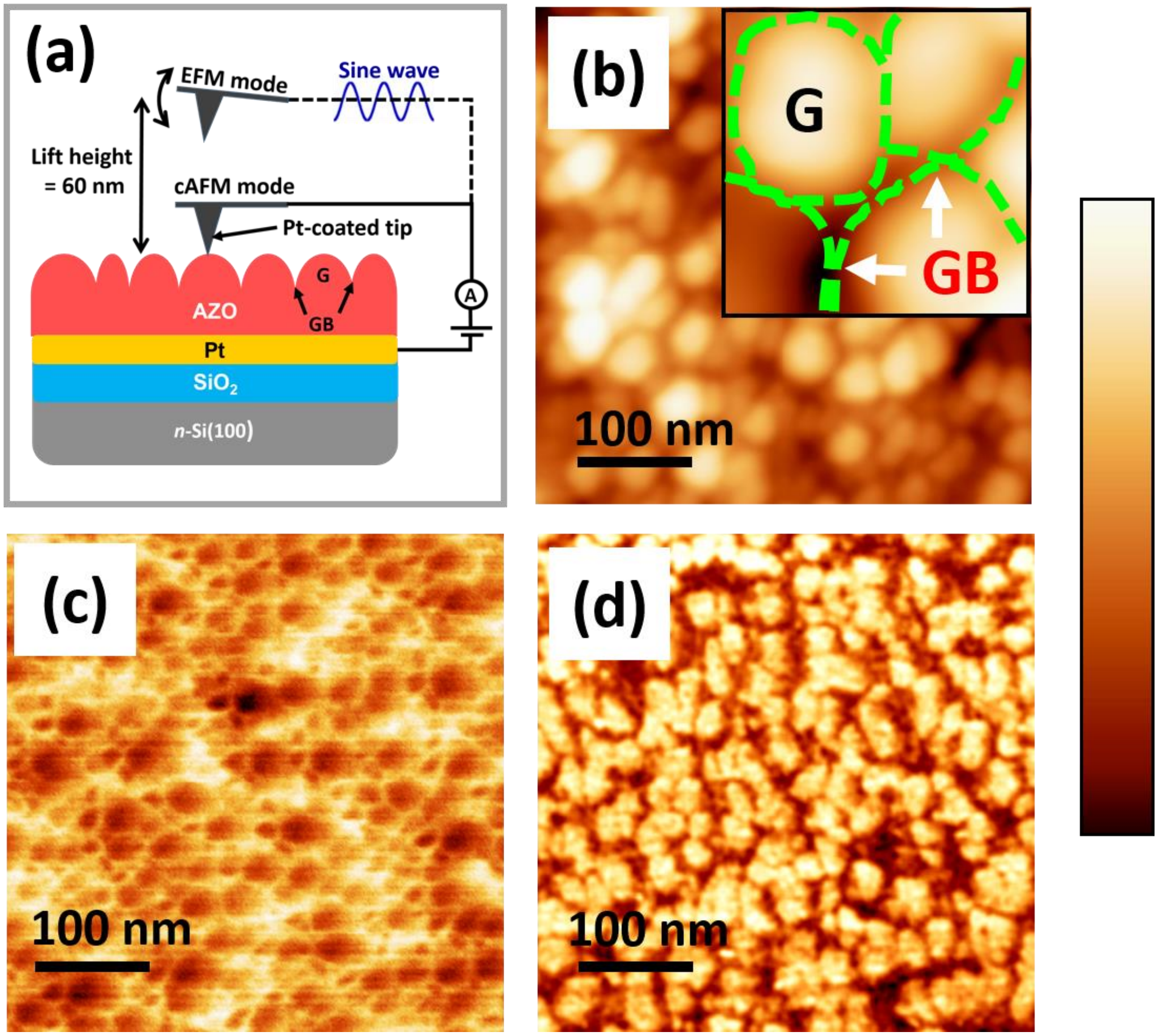

Figure 4.1: (a) Schematics of working principle of cAFM and EFM, (b) AFM topography taken in the tapping mode where a inset shows the magnified image (100×100 nm$^2$), representing grains (G) and grain boundaries (GB), (c) EFM image [corresponding to $V_{\text{tip}}$ = -3 V], showing the variation in electrostatic interaction on grains and at GBs, and (d) cAFM image for $V_{\text{tip}}$ = +4 V ($F$ = 2 nN) where the bright zones are conducting ones. The color bar represents 0 to 3.2 nm for (b), 0 to 2.5 nm for (c), and 0 to 10 nA for (d) [19].

Fig. 4.2(a) shows a zoomed area of the current distribution across a grain and a GB (corresponding to $V_{\text{tip}}$= +4V). In this image, the grain and the GB are marked by black and white texts, respectively, on which the local *I-V* measurements are carried out. The white line drawn across the G and GB [on Fig. 4.2(a)] yields the line profile as is shown in Fig. 4.2(b), clearly indicating a higher current at the grain. On the other hand, Fig. 4.2(c) shows the *I-V* characteristics obtained from the grain and the GB, using cAFM, suggesting the formation of a Schottky-like junction (in each case) between the Pt tip and the AZO film. As discerned, a clear difference in the conductivity of a grain and GB is observed. Since, in this architecture, AZO films are deposited on Platinized-Si substrates and the Pt-coated AFM tip is used as the top electrode, this combination makes a Pt/AZO/Pt or a metal-semiconductor-metal configuration.

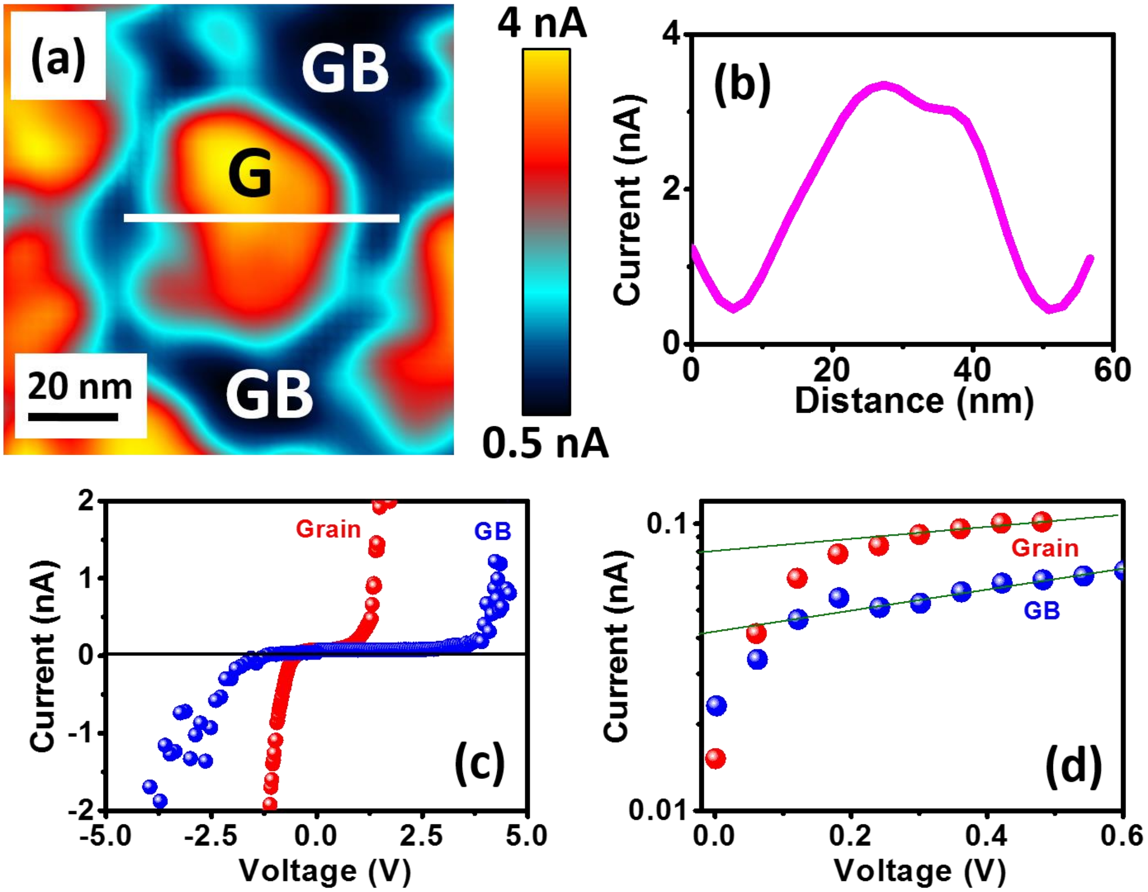

Figure 4.2: (a) Magnified image of current distributions of AZO grain (G) and grain boundary measured by cAFM, (b) corresponding line profile of the grain, as is obtained from (a), showing current distribution throughout the grain. (c) *I-V* characteristics of grain and GB using the cAFM tip and, (d) the semi-log (magnified) forward *I-V* characteristics obtained from grain and grain boundary [19].

Hence, the carrier transport through the metal-semiconductor (M–S) contact is dominated by the majority carriers [26,27]. At a fixed temperature, $T$, saturation current, $I_S$, depends on the Schottky barrier height or SBH, $\Phi$, according to the relation: $I_S \propto exp(-\Phi/nk_BT)$. It is known that the grains and GBs have different physical properties [18]. Thus, a change in the barrier height ($\Delta\Phi$), under the assumption that both the grain and grain boundaries make similar contacts, can be calculated from the saturation current ratio at forward bias, $I_{S_G}/I_{S_{GB}}$, where $I_{S_G}$ is the saturation current at grain and $I_{S_{GB}}$ is the same at grain boundary, leading to $\Delta\Phi = nk_BT \ln(I_{S_G}/I_{S_{GB}})$. Careful analyses result in $I_{S_G}$=79 pA, while $I_{S_{GB}}$ turns out to be 41 pA [Fig. 4.2(d)]. After substituting all the required values, $\Delta\Phi$ turns out be 49 meV. It may be mentioned that in the course of the present study, $\Delta\Phi$ has been measured at large number of places which varies and on an average is found to be 50±10 meV. In fact, due to a variation in the SBH from the grains to grain boundaries, a modulation in the surface potential is generated which in turn gives rise to the different electrical transport properties at the grains and grain boundaries [as confirmed by cAFM measurements, Fig. 4.1(d)].

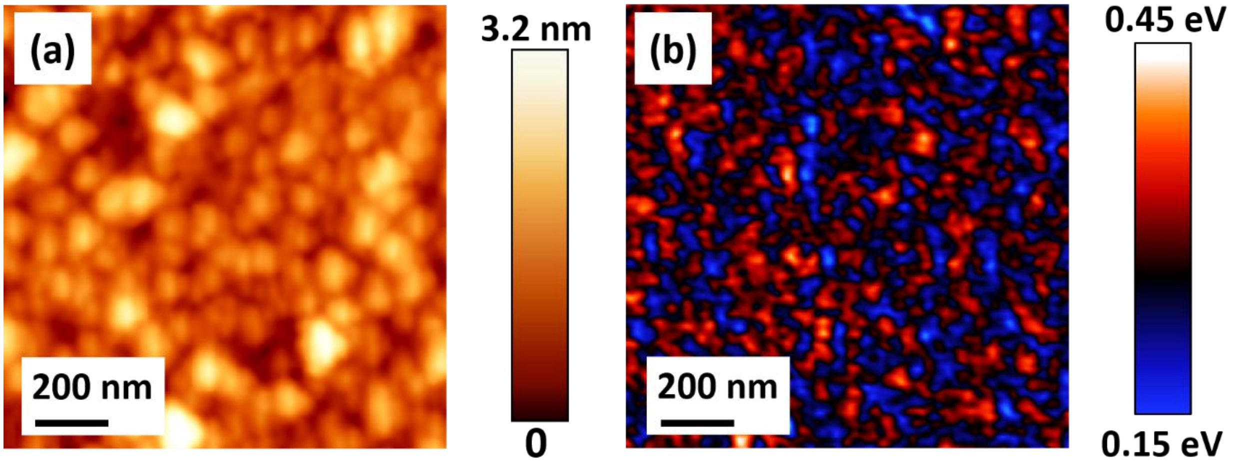

Figure 4.3: (a) Shows an AFM topographical image of an AZO film and (b) localized potential difference mapping of the corresponding surface. A close look at the scanning illustration indicates a clear variation in surface potential due to AZO nanostructures grains [19].

The variation in the surface potential can be directly measured using KPFM. KPFM is considered to be a non-destructive scanning probe microscopy based technique that helps to minimize the electrostatic interaction between the tip and the surface at each scanning point on the sample by applying an external dc bias [28]. This yields a contact potential difference ($V_{\mathrm{CPD}}$) between the tip and the surface, $V_{\mathrm{CPD}}=(\Phi_{\mathrm{sample}} - \Phi_{\mathrm{tip}})/e$, where $\Phi_{\mathrm{sample}}$ and $\Phi_{\mathrm{tip}}$ are the work functions of the sample and the tip, respectively. This technique can be directly interpreted in terms of the localized work function or the potential variation of the surface over nanoscale regions with simultaneous illustration of the sample topography. Figs. 4.3(a) and (b) show the topography and the surface potential distribution, respectively, of the AZO film. A clear variation in the nanoscale surface potential is observed from Fig. 4.3(b). In fact, the nanostructured film surface with blue contrasts have a lower work function with respect to the adjacent areas and the variation is found to be up to 300 meV. It may be mentioned that KPFM measurement is performed at the ambient and due to the inherent instrumental limitation, it is very difficult to probe a single GB by KPFM. Therefore, to a good approximation, the observed variation in the surface potential can be attributed largely due to the presence of the grains and grain boundaries [3,10,11].

In general, band bending at the GBs is explained, theoretically, in the frame work of double Schottky potential barrier (DSPB) model, based on the formation of a space charge regime, where grains are presumably separated by random GBs [12]. By solving Poisson's equation, the electrostatic potential barrier height ($\Phi_{ele}$) at the GBs and the depletion layer width ($d$) are given by $\Phi_{ele}=Q^2{}_i/8e\varepsilon_0\varepsilon_r N_0$ and $d=Q_i/2N_0$, respectively, where $Q_i=eN_t$ is the net surface charge, $e$ is the electronic charge, $N_t$ is the surface density of trapped charge carriers, $N_0$ is the volume density of ionized donors in the grains, $\varepsilon_0$ is the vacuum permittivity, and $\varepsilon_r$ is the static dielectric constant of AZO [7,12].

Under the assumption that the barrier is a symmetrical one and considering $N_t$=$10^{15}$ cm$^{-2}$ [5], $N_0$=$10^{20}$ cm$^{-3}$ (obtained from the Hall effect and KPFM measurements), and $\varepsilon_r$ = 8.5±1.3 [29], the calculated $\Phi_{ele}$ and $d$ are determined to be 28.6±3.2 mV and ~1 nm, respectively. The value of $\Phi_{ele}$ differs from the measured $\Delta\Phi$ value and thus, indicates that there may be some other process(es) involved in the local band bending at the GBs. It is observed that the measured local band bending at GBs for different AZO film thicknesses, (viz. 30, and 60 nm) turns out to be the same within experimental error, which matches well with the prediction of the DSPB model [12].

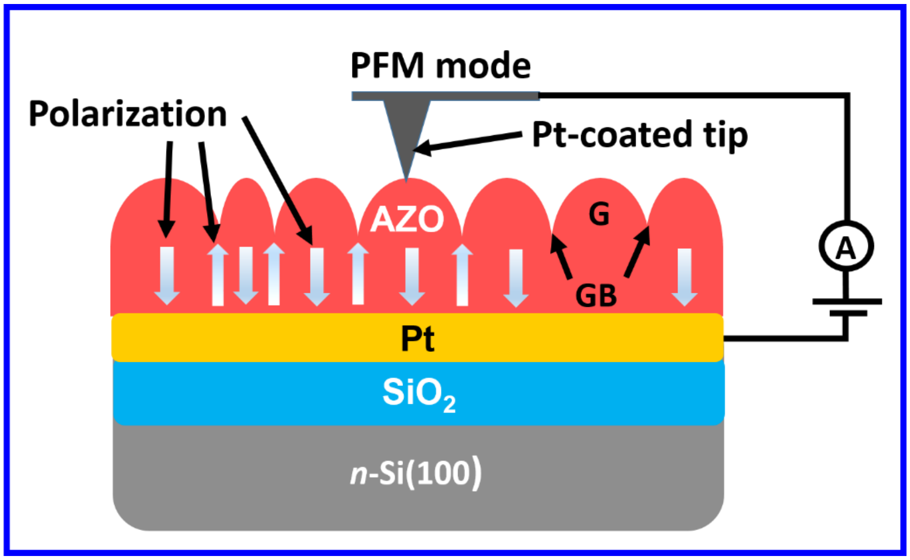

Figure 4.4: Schematic representation of PFM methodology [19].

As discussed above, the DSPB model may not be the sole governing mechanism for the observed band bending in polarized materials but some other effect(s) may also be responsible for the same, viz. polarization [6]. Thus, in order to study the involvement of polarization in band bending, we have performed PFM measurements. In may be noted that the high spatial resolution of PFM not only provides the information on very small (5-10 nm) domain sizes but also resolves the direction of polarization [30]. Figure 4.4 shows a schematic diagram, explaining the PFM methodology. Initially, PFM studies are carried out on as-obtained and cleaned Platinized-Si substrates (not shown) which show no signal, verifying their non-piezoelectric nature. On the other hand, Figs. 4.5(a) and (b) depict the PFM amplitude and phase images, respectively, obtained from an AZO film deposited on a Platinized-Si substrate.

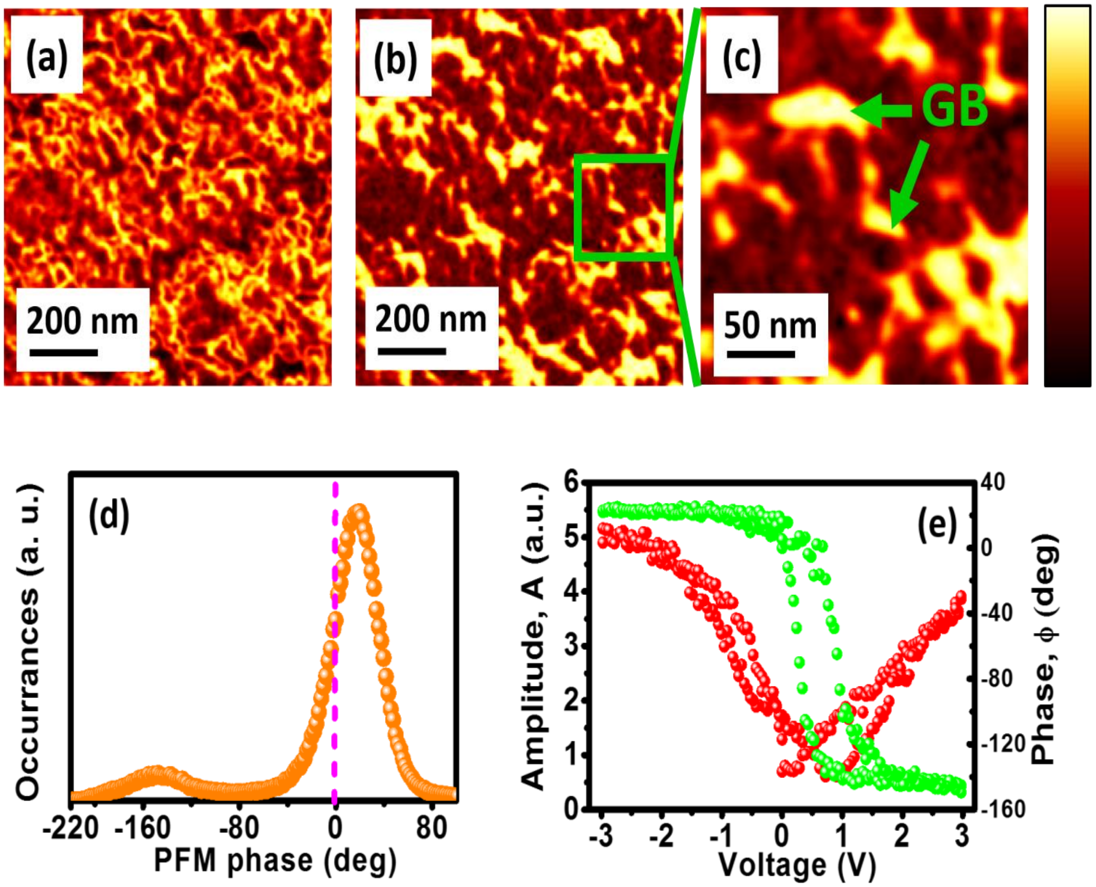

Figure 4.5: (a) and (b) show simultaneously recorded PFM amplitude and phase images, respectively, (c) a magnified view of the marked position on the phase image, depicting the clear presence of grains and grain boundaries, (d) PFM phase histogram [extracted from (b)], indicating opposite polarization at grains and GBs. (e) Hysteresis loop (obtained from switching spectroscopy), confirming the pseudoferroelectric nature of the AZO films. Colour scales: PFM amplitude (a) and PFM phase (b) images are 1.5 to 2.5 pm, and 120$^0$ to -220$^0$, respectively [19].

Fig. 4.5(c) shows a magnified view of the marked area on Fig. 4.5(b) from where it is clear that the phases at grains and GBs have opposite (180$^0$) orientations where the phase contrast is roughly proportional to the effective piezoelectric coefficient, $d_{33}$, which is determined from the projection of the polarization vector (***P***) normal to the surface (***N***) [30]. The bright and dark contrasts correspond to the polarization heads directed opposite (downward at grains) and towards (upward at GBs) the tip, respectively [31-33]. To understand the distribution of polarization with respect to the surface normal, we present a histogram [Fig. 4.5(d)], extracted from the PFM phase image [Fig. 4.5(b)]. The histogram clearly shows two asymmetric peaks: one at around $18^0$ and the other one at around $-145^0$. Interestingly, the area under the former peak is found to be much higher than the latter one, suggesting the number of dipoles at the grains with downward polarization exceeds the oppositely oriented dipoles at the GBs (with upward polarization). At the same time, the peak broadening represents the variation in the effective polarization [30].

It may be mentioned that the PFM response image alone is not sufficient to distinguish between the polarization and electrostatic interaction [34]. Thus, the presence of polarization in the AZO film is also confirmed by switching spectroscopy in PFM mode (for a fixed grain and with a dc voltage being swept in a cyclic manner), which shows the butterfly amplitude loop and the hysteresis loop [Fig. 4.5(e)]. Since the amplitude loop gets saturated at higher voltages, it can be inferred that the response is piezoelectric in nature instead of an electrostatic one [34]. In addition, the phase ($\Phi$) of the piezoresponse data can be flipped by $180^0$ beyond the coercive voltage of –1 V at the negative side and 1.8 V at the positive side which further confirms the piezoelectric nature of the films. It is interesting to note that the hysteresis loop is asymmetric in nature and one of the possible reasons behind this observed asymmetry can be the presence of strain in the studied film. In fact, for ferroelectric materials, this type of asymmetric behaviour originates from the presence of strain [35,36]. On the other hand, the presence of noise in the butterfly loop [Fig. 4.5(e)] can originate particularly in the case of a weakly polarized material like AZO (unlike ZnO). Thus, our measurements provide direct and clear evidence of pseudoferroelectricity in AZO films at RT. It can be mentioned that Herng *et al*. have recently reported pseudoferroelectricity even in ZnO [6].

As discussed above, the downward polarization at grains reduces the barrier height through direct polarization induced charges [21]. The change in the barrier height due to polarization ($\Phi_{\text{pol}}$) can be calculated using the simple dielectric gap model [21,37]. According to this model, the change in the barrier height due to polarization is given by $P\delta/\varepsilon_0\varepsilon_r$, where $P$ is the polarization and $\delta$ is thickness of the interface layer (e.g. length of a single unit cell along the *c*-axis for wurtzite ZnO) [29]. After substituting all the required parameters, such as $P$=5.5 μC cm$^{-2}$ [38], $\delta$=0.5206 nm [3], and $\varepsilon_r$=8.5±1.3 [28], $\Phi_{\text{pol}}$ is found to be 330 meV which is quite consistent with our KPFM measurements. However, further studies, namely, temperature-dependence of *I*-*V* spectroscopy in conjunction with first-principle calculations, are needed to reveal the exact nature of the metal-pseudoferroelectric barrier at the AZO surface.

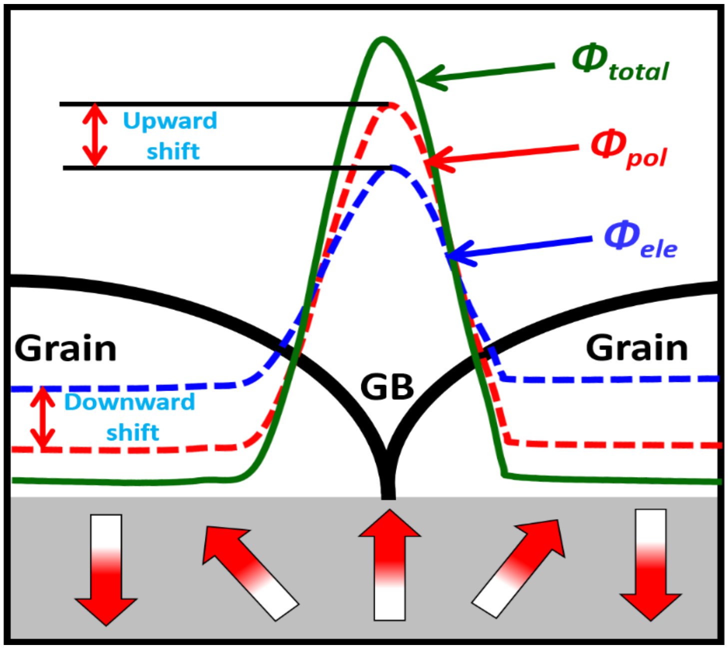

Figure 4.6: Schematic representation of band bending at GB where blue and red lines represent the Schottky barrier ($\Phi_{\text{ele}}$), the polarization-induced barrier ($\Phi_{\text{pol}}$), and the total barrier height ($\Phi_{\text{total}}$), respectively. Pseudoferroelectric domains are marked by arrows.

Based on these information, the SBH and polarization-induced berried height (PBH) are presented schematically in Fig. 4.6, where the grains and GBs show downward and upward polarization, respectively (shown by the up and down arrows). These polarization induced charges are due to give rise to the local band bending, affecting the local electrical transport. Reproducibility of these results are checked on three different AZO thicknesses (30 and 60 nm) grown on Platinized-Si substrates. Interestingly, similar behaviour is observed for all samples. These direct measurements confirm that in case of AZO films, the local band bending at the GBs takes place through the local Schottky barrier formation and direct piezoelectric effects.

### 4.1.4 Conclusions

In summary, we demonstrate a first conclusive experimental evidence on nanoscale room temperature pseudoferroelectricity in preferentially oriented thin films of aluminium-doped zinc oxide (AZO). Local probe microscopic measurements like cAFM, KPFM, and PFM indicate that pseudoferroelectricity in the films gives rise to the polarization-driven barrier formation, which in conjunction with the defect-induced electrostatic potential barrier match well with the experimentally observed local band bending at the grain boundaries. The present observation of the polarization-driven potential barrier formation can be a benchmark for understanding the charge transport process across the GBs in AZO films and even in other pseudoferroelectric materials. However, more detail investigations are underway to address the local band bending at AZO grain boundaries in light of roles played by the type and nature of the grains and GBs. The present findings are also crucial to design AZO-based polarization controlled transparent transistors, memory devices, and window layers.

## 4.2 Field-induced doping-mediated tunability in work function of Al-doped ZnO: Kelvin probe force microscopy and first-principle theory

### 4.2.1 Introduction

An electrical contact, having a metallic-like conductivity and high optical transparency, is an essential part of modern optoelectronic devices such as solar cells, light emitting diodes, etc. [1]. This contact is directly connected to the active material which is generally a semiconductor and hence, from the application point of view, a smooth charge transport should take place between them [39,40]. However, the work function ($W$) of a contact material is found to be different from the active material, which in turn generates an electrostatic potential barrier at the interface. This potential opposes the charge transport across them and as a consequence, the efficiency of the device gets reduced [3]. Thus, to achieve a state-of-the-art performance of a device, the key requirement is to have a minimal mismatch between the work functions of a contact and the active material [41].

Generally, Sn-doped $In_2O_3$ (ITO) is used as a transparent contact material for above mentioned devices [42]. However, due to its high cost and toxic nature, Al-doped ZnO (AZO) thin films have emerged as one of the most promising candidates to replace ITO [43]. In fact, an Al atom replaces a Zn one and acts as an electron donor in the ZnO matrix, causing a metallic-like conductivity [25,43]. In addition, Al-doping pushes the Fermi level in the conduction band (CB) and as a result, an increment in the effective optical band gap is observed – known as Burstein-Moss (BM) effect [44]. This effect not only reduces the work function of AZO, in comparison to ZnO, but also opens a new avenue to explore the possibility of tuning the Fermi level (or the work function) by varying the Al-doping level [45]. In fact, using the first-principle theory (density functional theory), it has been predicted that electron density in the CB can be changed by varying Al-doping which in turn gives rise to an upward shift in the Fermi level [45]. However, experimentally, it is found that the maximum carrier density or minimum resistivity of ZnO can be achieved by adding most soluble level (e.g. ~2 wt.%) of Al-doping [43]. In fact, large Al-doping (>2 wt.%) leads to the formation of insulating $Al_2O_3$ in the ZnO matrix, which in turn increases its resistivity and makes this material unsuitable for use as a transparent conductive contact [43]. Thus, tuning of the Fermi level or the work function of an AZO film, having an optimized Al-doping (e.g. 2 wt.%) level, is not only important for fundamental point of view but also to design a suitable Ohamic contact for advanced functional devices.

In the present scenario, it has been reported that the charge density in a semiconductor can also be controlled by applying an external electric field [46]. In fact, recently, using the local probe microscopic techniques, Kumar *et al*. have shown that the work function of Cu and Co-doped ZnO can be tuned by applying an external electric field, albeit due to high resistivity of these materials, they cannot be used as transparent contacts [46,47]. However, to the best of our knowledge, achieving a field-induced doping-mediated tunable work function and in turn its effect on charge transport in Al-doped ZnO, which offers a good optical transmittance and low resistivity, is yet to be explored.

In this paper, using Kelvin probe force microscopy (KPFM) and contact-mode (cont-mode) atomic force microscopy (AFM), we demonstrate that work function of an AZO film can be tuned by inducing charge carriers through an applied electric field. For instance, we show that, by applying positive or negative bias on the top of an AZO film, electrons or holes can be induced on the surface, which in turn decrease or increase the work function of the same, respectively. Further to this, the role of electric field-induced doping in nanoscale charge transport is also demonstrated by performing local *I-V* characteristics using conductive atomic force microscopy (cAFM). Our experimental findings are confirmed by first-principle density functional theory (DFT)-based calculations. This study is not only important to design an Ohamic contact for different optoelectronic contact but also for fundamental aspect of physics.

### 4.2.2 Details on first-principle simulations

In order to understand the role of field-induced charge doping on the work function of AZO, *ab initio* DFT was used by employing the PWscf code of the Quantum ESPRESSO distribution [48]. We employed fully-relativistic, projector-augmented wave potentials. The Perdew-Burke-Ernzerhof functional (PBE) for the exchange-correlation energy was used. Initially, we used the experimentally measured lattice parameters of AZO as the starting geometry and then it was minimized to the total energy as a function of the lattice parameters until it changed by less than 2 meV. The Brillouin zone (BZ) integration was performed with a Monkhorst-Pack grid of 12×12×4 *k*-points and using a Gaussian broadening of 0.002 Ry≈27 meV. The convergence with respect to the number of *k*-points as well as the wave-function and charge density cut off was checked. The self-consistent solution of the Kohn-Sham equations was obtained when the total energy changed by less than $10^{-8}$ Ry and the maximum force on all atoms was less than $5\times10^{-6}$ Ry $a^{-1}$ ($a\approx0.529$ Å is the Bohr radius).

### 4.2.3 Experimental

Following the same methodology in Chapter 3 (section 3.2.2), we deposited AZO thin films on ultrasonically cleaned Pt/$TiO_2$/$SiO_2$/Si substrates (Radiant Technology, UK) at RT. The local charge transport properties of AZO films were studied using similar techniques as described in section 4.2.2. In addition, the compositional analysis of AZO thin film was carried out by using x-ray photoelectron spectroscopy.

### 4.2.4 Basics of KPFM measurements and electric filed-induced doping

Figs. 4.7(a)-(c) depict the schematic of the working principles of charge doping and KPFM measurement. In fact, electric field-induced charge doping (field doping) and KPFM measurements are performed using a two-fold overwriting process. In this process, first we scan an area in the cont-mode, without [Fig. 4.7(a)] and with [Fig. 4.7(b)] a positive or negative tip bias which in turn induces charge carriers over this area accordingly (so far their polarity is concerned). In the second step, a larger area, around the first scanned area as the central one, is scanned in tapping mode – with a lift height of 60 nm and at the zero tip bias – which maps essentially the contact potential difference ($V_{\mathrm{CPD}}$) between the tip and the sample [Fig. 4.7(c)].

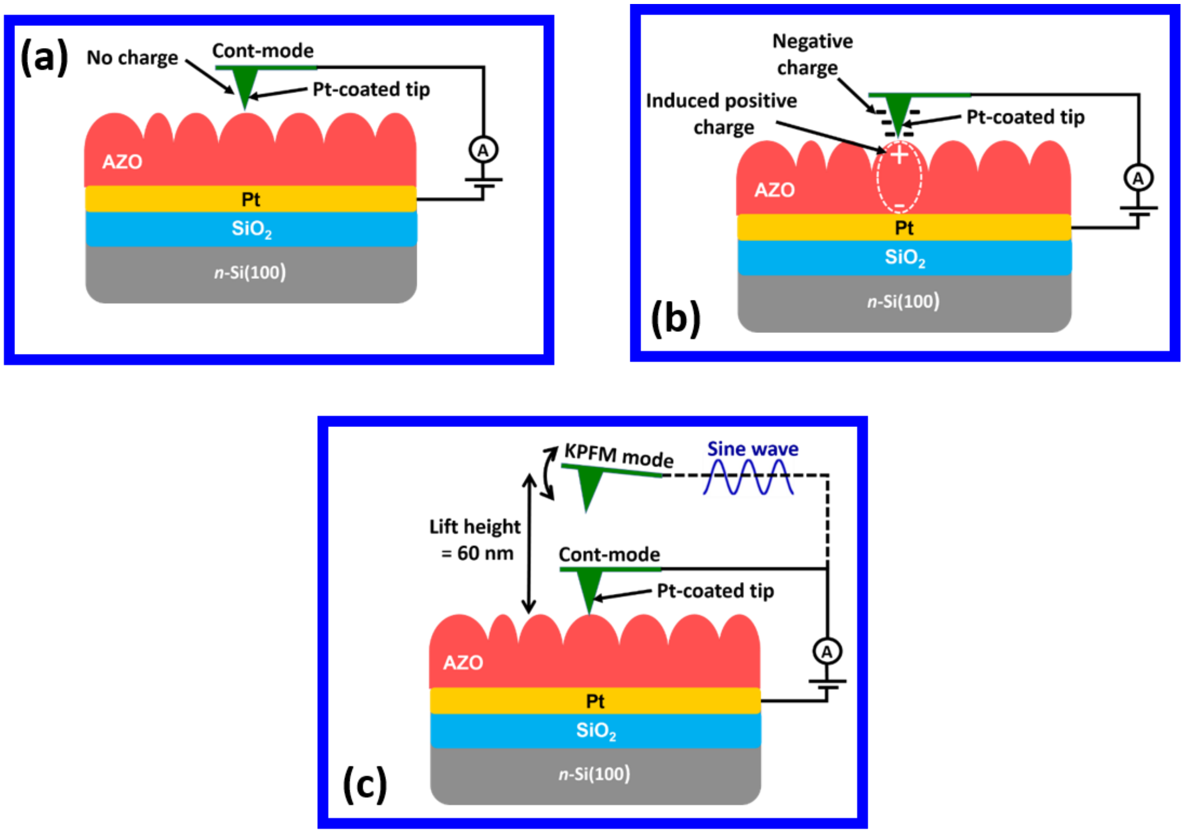

Figure 4.7: (a)-(c) show the schematic representation of charge induction using contact-mode (cont-mode) and subsequently mapping using KPFM technique.

### 4.2.5 Results and discussion

Compositional analysis of AZO films is carried out by XPS measurements. The survey spectra (not shown) of all samples do not reveal the presence of any undesirable species (impurity or Al in the near surface region). Figs. 4.8(a) and (b) depict Zn 2*p* and O 1*s* core level spectra corresponding to the 120 nm-thick AZO film. It is observed that XPS spectra of the Zn $2p_{3/2}$ and

Zn $2p_{1/2}$ levels are nearly centered at binding energy values of around 1021.4 eV and 1044.5 eV, respectively, corresponding to Zn atoms at regular sites of an AZO lattice [52]. The difference in the binding energies of Zn $2p_{3/2}$ and Zn $2p_{1/2}$ is found to be 23.1 eV, which is a characteristic value of AZO [53-55]. On the other hand, individual O 1*s* peak is deconvoluted to have three distinct curves centered at binding energies around 530, 531.4, and 532.1 eV. The lowest binding energy curve at 530 eV is attributed to O atoms at regular lattice site ($O_L$) i.e. O atoms in regular Zn-O bonds. In other words, the intensity of this peak is a measure of the amount of oxygen atoms in a fully oxidized stoichiometric surrounding [52,54]. The intermediate binding energy of 531.4 eV is associated with O atoms in the oxygen deficient regions ($O_v$) within the AZO matrix and hence, the intensity of this component may be attributed to the oxygen vacancies ($O_v$). The peak corresponding to the binding energy of 532.1 eV is attributed to the presence of loosely bound oxygen ($O_i$) at the surface of AZO films, belonging to either of the species such as adsorbed $H_2O$ or $O_2$ on the surface of AZO films [52,54,55].

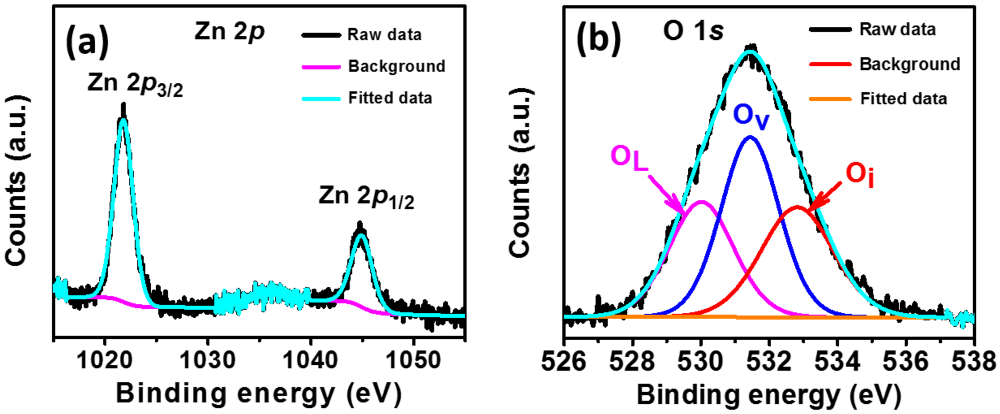

Figure 4.8: (a) and (b) depict Zn 2*p* and O 1*s* XPS spectrum, respectively of this film. Similar results are obtained for AZO films having different thicknesses [55].

Another crucial observation is the measured relative percentages of $O_L$, $O_V$, and $O_i$ are found to be 32, 40, and 28%, respectively, which indicate that the AZO film is oxygen deficient (because of the highest relative value of the $O_V$ component). However, Al concentration is below the detection limit of the present XPS setup and is thus, not discussed here. The presence of oxygen vacancy can generate a dipole inside the film which may be useful for charge induction [46]. In fact, the presence of defects increases the noncentrosymmetric nature of doped-ZnO system, leading to the induction of a spontaneous polarization in the same [6]. This spontaneous polarization generates electrostatic charges at the surface, causing a change in the work function of the AZO film.

In general, it is known that an electrostatic charge can be generated on the surface of a material by scanning a neutral metal-coated AFM tip on the same in cont-mode on the surface and this phenomenon is known as contact electrification [56]. Thus, to rule out the possibility of any contact electrification, first we scan a smaller area (5×5 $\mu m^2$) of the same film (120 nm-thick) in without any tip bias and then map $V_{CPD}$ over a bigger area (8×8 $\mu m^2$). Figs. 4.9(a) and (b) show the surface topography and the $V_{CPD}$ map of the film corresponding to the bigger scanned area, respectively. It is noticed that the surface potential does not change after scanning the tip at 0 V bias, confirming that sliding of the AFM tip on the AZO film does not generate any kind of charge on its surface.

On the other hand, if the above-mentioned steps are repeated with a tip bias, $V_{tip}$=+2 V then surface topography remains the same [Fig. 4.9(c)], albeit a clear change in $V_{CPD}$ (~40 mV) is observed from the first scan area, yielding a different work function [i.e. the central area of Fig. 4.9(d)] with respect to the surrounding one. In fact, $V_{tip}$=+2 V generates a higher electron density at the surface through electric field mediated charge induction process which in turn decreases the work function of the film over the scanned area. It is observed that the induced electrons are uniformly distributed over a desired scan area and are sustained for a long time. As a matter of fact, we have confirmed that without any external bias, $V_{CPD}$ remains in its mapped state for more than 24 h at RT, albeit after each 4 h, a 10% decrease takes place in the same. Similar effects are observed for films having different thickness values.

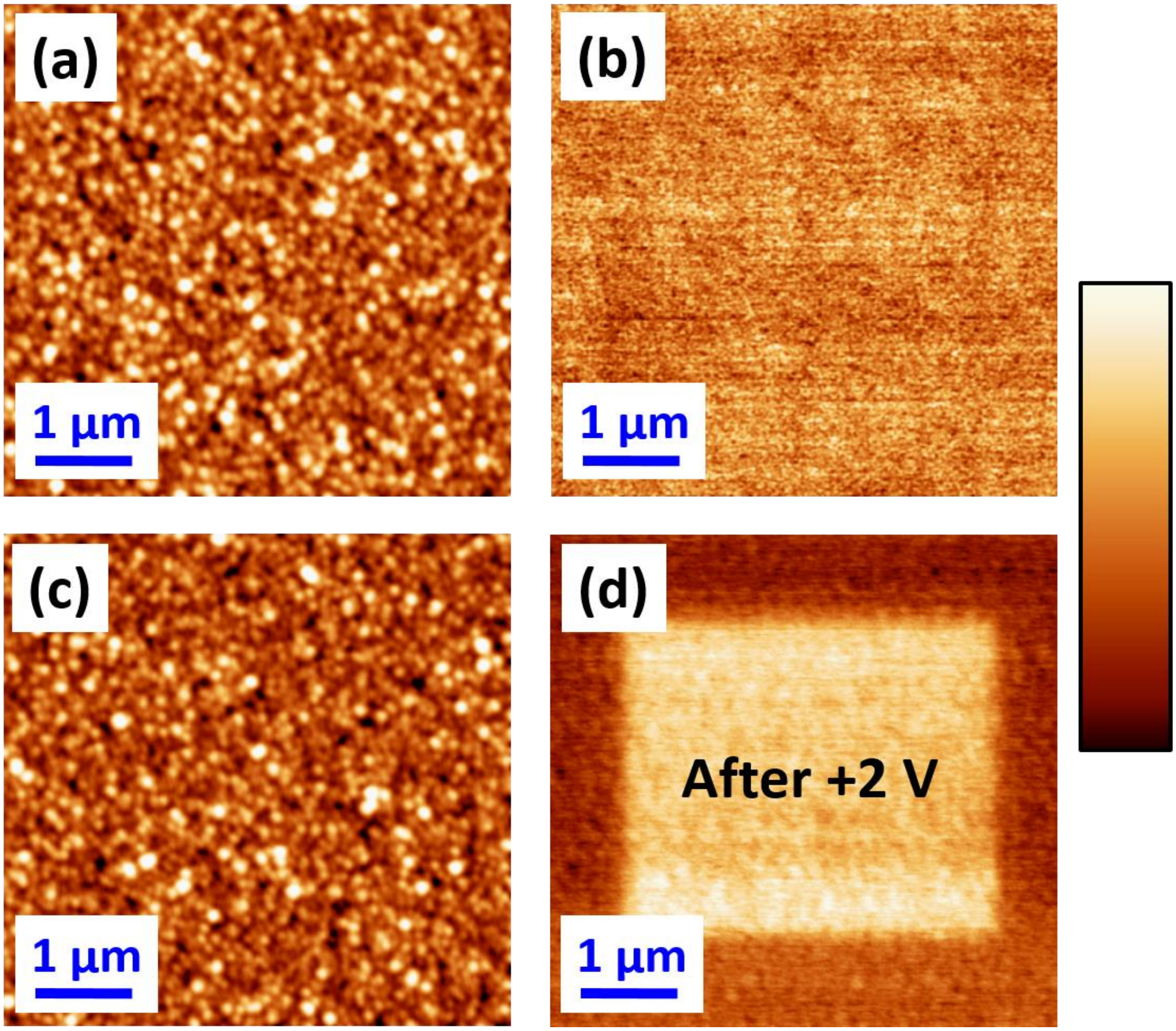

Figure 4.9: (a) and (b) represent the topography and the $V_{\mathrm{CPD}}$ map, respectively of the AZO film after scanning the AFM tip in cont-mode with 0 V at a central area, depicting no change in $V_{\mathrm{CPD}}$, while (c) and (d) represent the same but after scanning a central area of 5×5 µm$^2$ with +2V. Scale bar is 0 to 2.6 nm for (a) and (c), whereas it is 0.38 to 0.45 V for (b) and (d).

It may be mentioned that charge doping in an AZO film can also depend on the magnitude as well as polarity of the applied tip bias, $V_{\mathrm{tip}}$. Hence, charge doping due to $V_{\mathrm{tip}}$=+2 to +10 V [Fig. 4.10(a)] and -2 to -10 V [Fig. 4.10(b)] with an interval of 2 V, are performed over an area of 5×5 µm$^2$ and subsequently the $V_{\mathrm{CPD}}$ values are measured from the same. Interestingly, $V_{\mathrm{CPD}}$ increases in a systematic manner due to the scanning performed with positive values of the tip bias, whereas it decreases for the negative tip bias values (relative to the surrounded undoped region). For a better clarity, line profiles of Figs. 4.10(a) and (b) are shown in Figs. 4.10(c) and (d), respectively. A conspicuous behaviour is observed form both the figures: Initially, the surface potential (at low values of $V_{\mathrm{tip}}$) varies linearly and then it deviates at higher values of tip bias. In addition, it is observed that a change in the contact potential difference at negative $V_{\mathrm{tip}}$ values are much higher in magnitude compared to the corresponding positive ones, indicating that the induction of holes in the AZO film is relatively easy with respect to electrons. Such a behaviour can be attributed to the high electron affinity of AZO [57,58].

In fact, a negative tip bias induces positive charges (holes) at the surface which in turn decrease the effective electron density in an AZO film. As mentioned above, $V_{\mathrm{CPD}}$ can be converted into effective charge density at the surface. Thus, Eqn. (4.3) is used to calculate the respective effective donor density after applying different positive and negative tip voltages. After substituting $N_{\mathrm{C}}=1\times10^{21}$ cm$^{3}$ [57], $\chi$ = 4.5 eV [58], and $\Phi_{\mathrm{tip}}$=4.85 eV (measured with respect to a clean *highly ordered pyrolytic graphite, HOPG),* in Eqn. (4.3), each pixel of the KPFM image is converted into an effective donor concentration. The effective donor density corresponding to the unbiased, after scanning with positive bias (+2 V), and negative bias (-2 V) are found to be $1.83\times10^{19}$ cm$^{-3}$, $3.32\times10^{21}$ cm$^{-3}$, and $1.11\times10^{18}$ cm$^{-3}$, respectively. However, a large variation in the calculated carrier density values (obtained from the KPFM studies, performed at higher $V_{\mathrm{tip}}$ values) limits us to obtain any meaningful change in the measured effective donor concentration [19]. On the other hand, based on the measured $V_{\mathrm{CPD}}$ values, we do observe a meaningful change in the AZO work function corresponding to the different $V_{\mathrm{tip}}$ values (for both polarities).

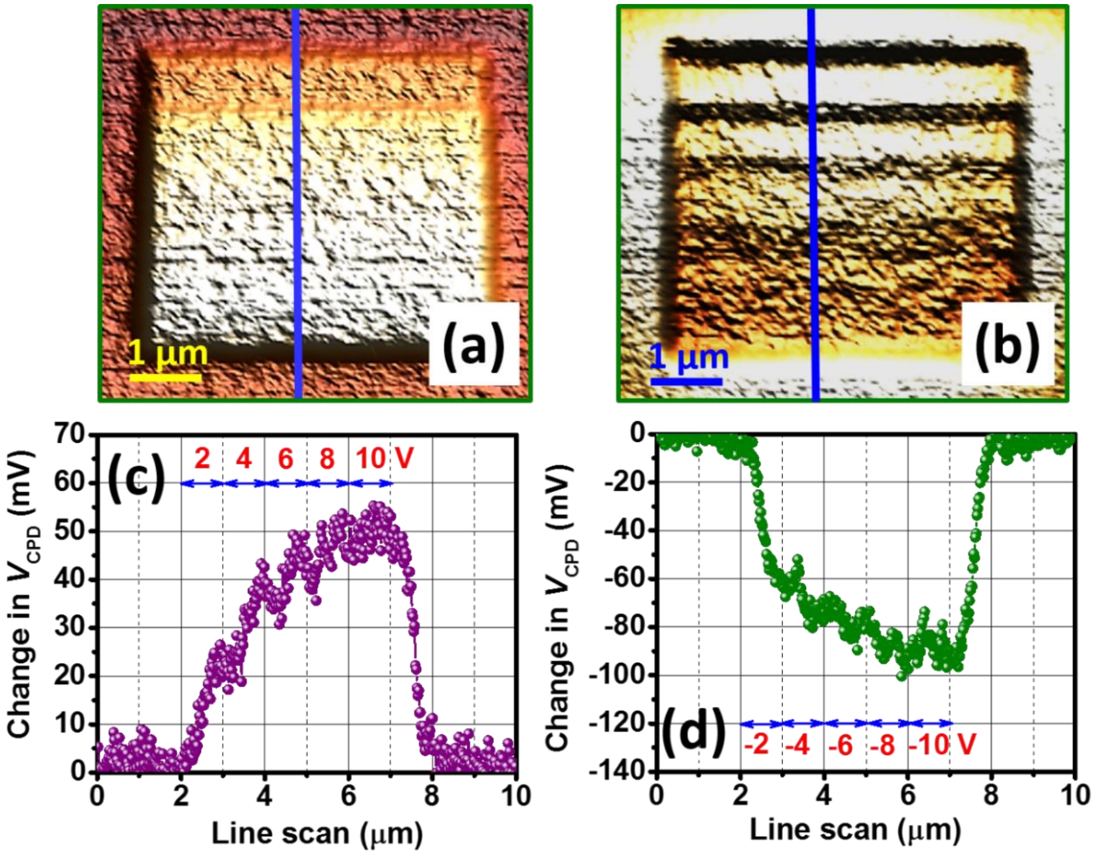

Figure 4.10: (a) and (b) show the relative change in the $V_{\text{CPD}}$ maps of an AZO film after scanning with $V_{\text{tip}}$=+2 to +10 V and $V_{\text{tip}}$=-2 to -10 V with an interval of 2 V. (c) and (d) depict the corresponding line profiles. Figures (a) and (b) are 3D images, showing the relative changes with the respective surrounding ones and hence, do not have any height scale bar.

The work functions of as-deposited and charged-AZO are shown schematically in Fig. 4.11(a), which clearly indicates that the measured work function will be different after charging. On the other hand, variation in the work function as a function of the applied tip bias is plotted in Fig. 4.11(b), which shows that the work function initially increases/decrease (for applied negative/positive tip bias), whereas it gets saturated (for both the polarities) at higher tip bias values. The observed saturation can be attributed to the presence of polarization in the AZO film. In fact, the saturation at higher tip bias values indicates that most of the dipoles in the AZO film flip along the electric field direction for $V_{\text{tip}}$ > 2 V and thus, no significant change in the work function is expected at higher applied fields. Similar behaviour is manifested by all the films having different thickness values. The presence of polarization in the films is also confirmed using piezoresponse force microscopy (data not shown).

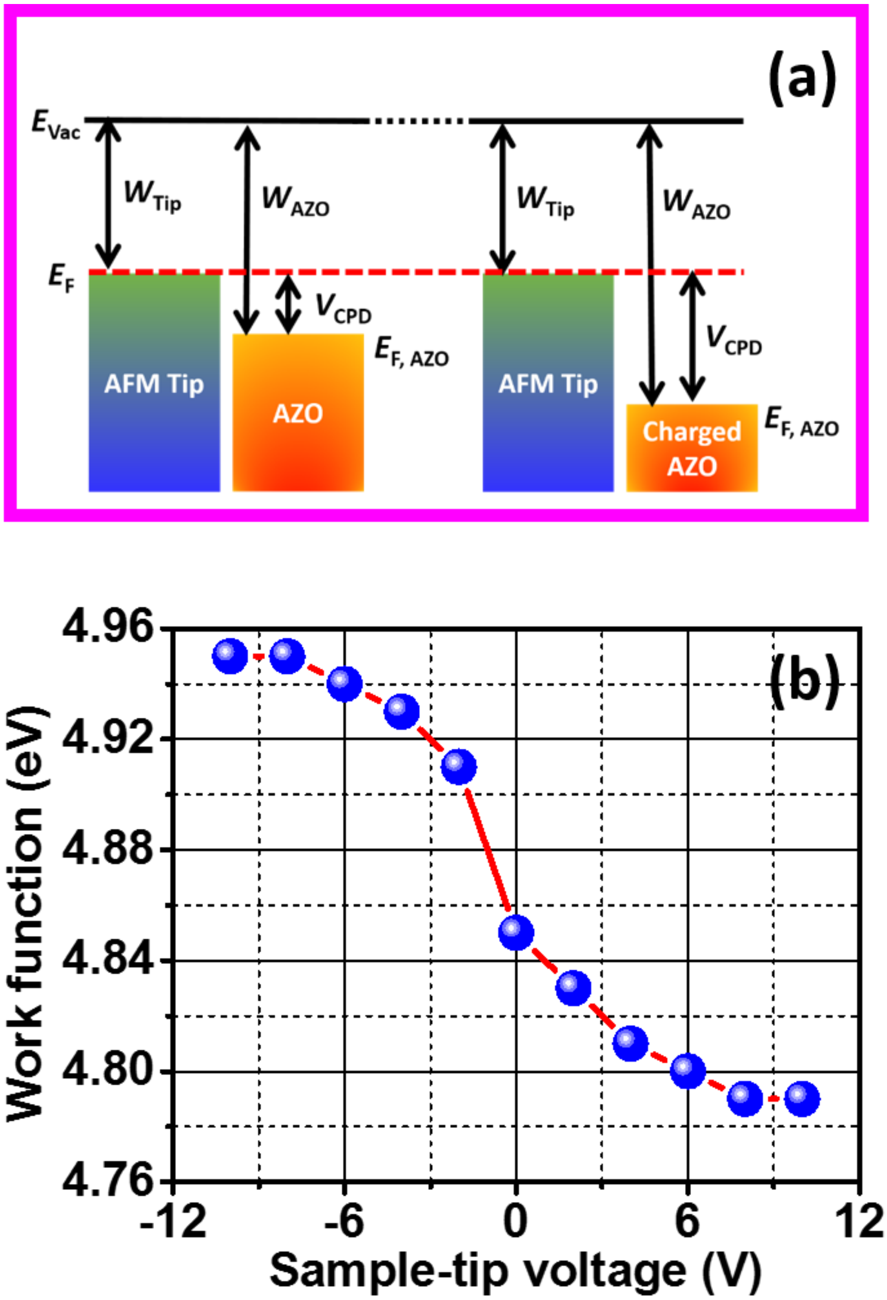

Figure 4.11: (a) Schematic representation of variation in the work function after charge doping and (b) shows the variation in the work function as a function of the applied tip bias.

Such an applied field-induced doping-mediated tuning of work function should play a role in charge transport across the AZO films. Thus, in order to explore the behaviour of charge transport due to the tuning of its work function, *I*-*V* measurements are performed using cont-mode AFM at a fixed point and for a large number of cycles. Likewise, the fixed point *I*-*V* measurements, for a large number of cycles, are performed at more than 150 randomly chosen spots on the film, which manifest the similar behaviour (within the experimental error). These results indicate the uniform nature of the film and a high degree of reliability in terms of field-induced doping-mediated tuning of the AZO work function. In fact, in the first cycle of the *I*-*V* measurements, the tip not only measures the current from the fixed point but also induces charge into the same. These induced charges modify the work function and in turn change the tip-sample barrier height for the next cycle. Indeed, the barrier height at the tip-sample junction for each subsequent cycle is different which in turn gets reflected in the turn-on potential (in comparison to the previous cycle) of *I*-*V* characteristics as described below.

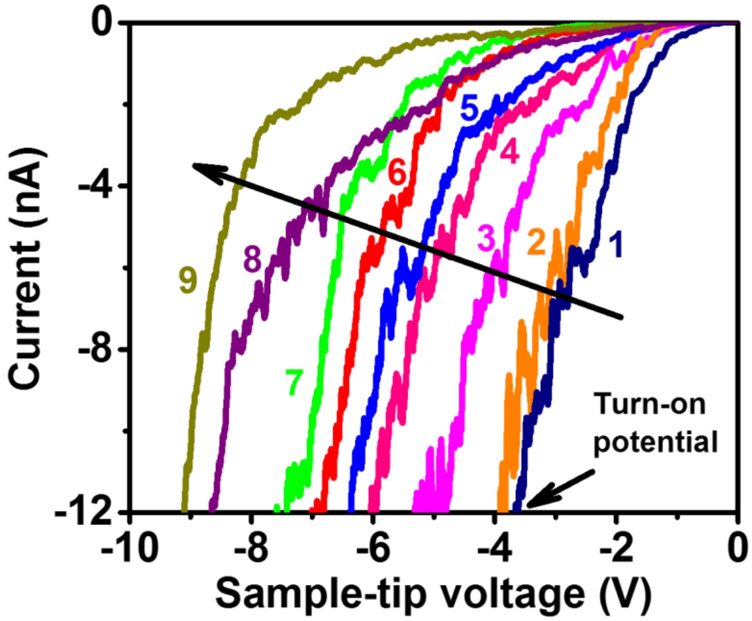

Figure 4.12: *I*-*V* characteristics obtained from cont-mode AFM measurements performed at a fixed point for nine different cycles for positive tip bias.

Fig. 4.12 shows the *I*-*V* characteristics for a large number of cycles obtained from cont-mode AFM measurements performed on the film. From this plot, it is observed that the turn-on potential decreases systematically for positive cycles (red arrows indicate an increase in the number of cycle). In addition, the *I*-*V* characteristics suggest the formation of a Schottky-like junction between the Pt-tip and the AZO film [19,59]. As discerned, a clear variation in the turn-on potential for different cycles (i.e. unipolar cases) is also observed which corroborates well with change in the work function with differently applied tip bias values. Another important point is that no change in the turn-on potential takes place for large number of cycles (data not shown) if the *I*-*V* characteristics are performed for both positive and negative cycles. These results depict that not only the work function but also charge transport can be tuned by an externally applied electric field on the sample surface (through the AFM tip).

The effect of field doping on the work function is also calculated using *ab initio* first-principle theory. Fig. 4.13(a) shows the side-view of a (3×3×3) AZO supercell where the big green spheres indicate the Zn atoms, small red spheres correspond to the O atoms, and the yellow sphere indicates the Al atom. In the present case, a Zn atom is replaced by an Al atom from randomly chosen sites, however, no significant change in the results is observed. It is known that the band gap ($E_g$) of AZO is around 3.4 eV (at RT), whereas the simple DFT result predicts the gap to be 0.7–0.95 eV, underestimating $E_g$ by more than 50% [60]. This is expected as a typical DFT error (band plots not shown) and can be improved by using the Coulomb parameter ($U$) [61]. Here, we use $U$=8.5 V as an optimal value (with respect to energy minimization) for a better understanding of the electronic structure to explain the work functions of a neutral and a charged unit cell. In addition, it needs to be mentioned that the experimentally calculated doped charge density is converted into the charge per unit cell, $n$ (i.e. $e$/unit cell, where $e$ is the elementary charge) and further used in DFT calculations [62]. Since the volume of a (3×3×3) unit cell is around 142.74 $Å^3$, the doping of one electron per unit cell corresponds to a doping density of $\sim 7\times10^{21}$ $cm^{-3}$. Therefore, the experimentally calculated doping density ($\sim 3.32\times10^{21}$ $cm^{-3}$) is converted into the charge per unit cell and it turns out to be 0.47.

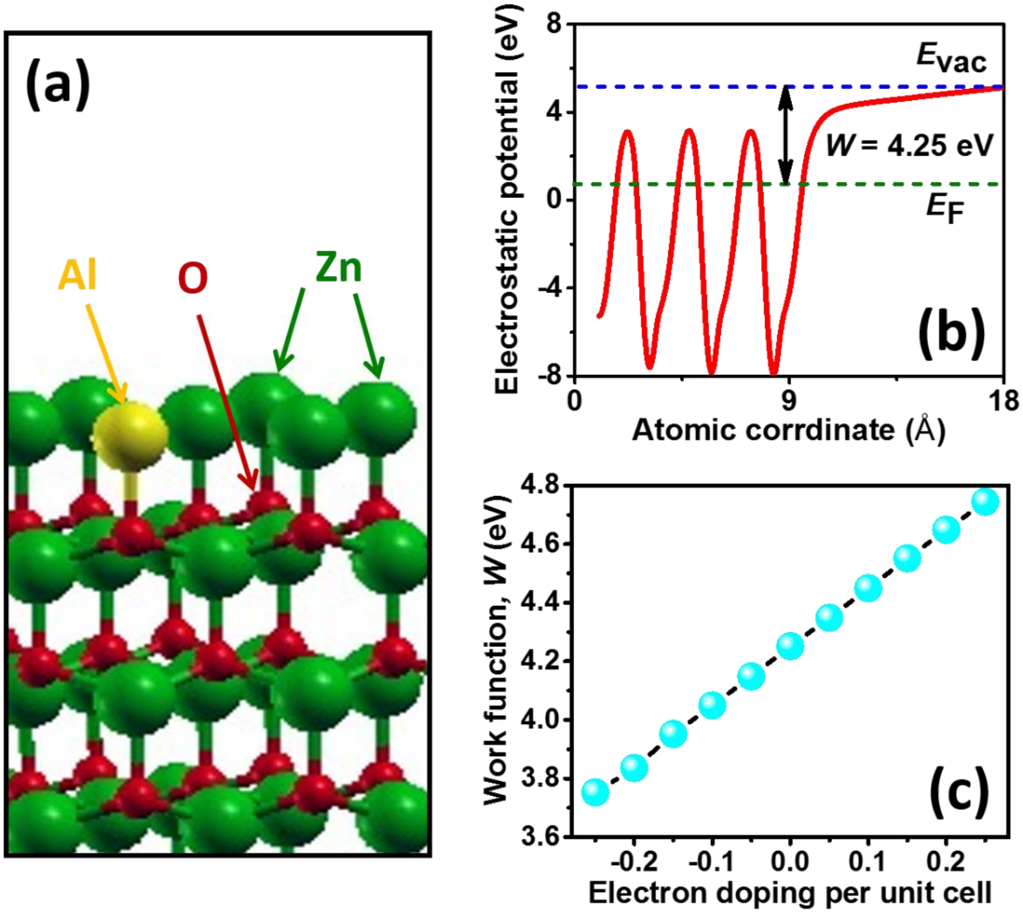

Figure 4.13: (a) Supercell of AZO, (b) shows the variation in electrostatic potential of AZO along the *z*-direction, and (c) shows the variation in work function as a function of field-induced charge doping.

Fig. 4.13(b) depicts the variation in electrostatic potential as a function of atomic coordinates for an AZO film. The vacuum potential was taken to be at the half way point of the vacuum slab because at this position, the influence of the adjacent unit cell may be negligible [63]. The work function is a difference between the vacuum potential ($E_{vac}$) and the Fermi energy ($E_F$) and mathematically it can be written as: $\Phi = E_{vac} - E_F$. The estimated work function is found to be 4.25

eV, which matches well with the existing report [64]. In addition, it is important to mention that we are using a defect-free AZO unit cell for our study, whereas the observed work function is due to get modified after using structural defects. However, here our main aim is the theoretical understanding of the behaviour of work function after charging and not to determine its absolute value form the DFT calculations. Interestingly, it is observed that the work function varies linearly with changing the electron doping per unit cell, confirming the charge doping-dependent change in the work function [Fig. 4.13(c)] [46,47]. In addition, it is interesting to note that at lower tip voltages, experimentally observed change in the work function varies linearly, which deviates at higher tip bias values. This is in contrast to the results obtained from DFT calculations where the work function also increases linearly with increasing applied $V_{\text{tip}}$ values. One of the possible reasons behind this mismatch is that in our DFT calculations, we are not considering the presence of polarization. In addition, we want to mention that a 120 nm-thick AZO film, simultaneously deposited on a glass substrate, shows a high average transparency (85%) (in the visible region) and low resistivity ($\sim 10^{-3}$ Ω-cm), confirming the fabrication of a transparent contact. Interestingly, similar behaviour is observed for two other different AZO film thicknesses, viz. 30 and 60 nm, grown on both Platinized-Si and glass substrates. Thus, we conclude that the present study provides important inputs towards tuning field-effect doping-mediated work function and the charge transport processes in a TCO like AZO.

### 4.2.5 Conclusions

In conclusion, we have grown AZO thin films on Platinized-Si substrates at room temperature using pulsed dc magnetron sputtering technique. The structural and compositional properties of highly oriented AZO films are confirmed by SEM, AFM, XRD, and XPS measurements. In addition, the tuning of work function of the AZO film due to an applied electric field-induced charge doping (through the AFM tip) is performed using KPFM measurements which corroborates well with the charge transport processes in the film, as is measured by cont-mode AFM. This is further substantiated by cAFM investigations, which show a systematic change in the turn-on potential at a fixed point as revealed from the local *I-V* characteristics, indicating the tunability of work function of AZO. Our experimental findings are further confirmed by calculations based on first-principle density functional theory. Tuning the work function and in turn charge transport of AZO by injected charge (field-induced doping) has a direct application in different optoelectronic devices, which use such optically transparent contacts materials.

# Bibliography

[1] K. Ellmer, A. Klein, B. Rech, *Eds*. Transparent Conductive Zinc Oxides: Basics and Applications in Thin Film Solar Cells. 2007: Springer, Berlin.

[2] J. T. Thienprasert, S. Rujirawat, W. Klysubun, J. N. Duenow, T. J. Coutts, S. B. Zhang, D. C. Look, and S. Limpijumnong, Phys. Rev. Lett. 110 (2013) 055502.

[3] M. Kumar, A. Kanjilal, and T. Som, AIP Advances 3 (2013) 092126.

[4] T. Makino, K. Tamura, C. H. Chia, Y. Segawa, M. Kawasaki, A. Ohtomo, and H. Koinuma, Phys. Rev. B 65 (2002) 12120.

[5] E. M. Likovich, R. Jaramillo, K. J. Russell, S. Ramanathan, and V. Narayanamurti, Phys. Rev. B 83 (2011) 075430.

[6] T. S. Herng, A. Kumar, C. S. Ong, Y. P. Feng, Y. H. Lu, K. Y. Zeng, and J. Ding, Sci. Rep. 2 (2012) 587.

[7] X. Ji, Y. Zhu, M. Chen, L. Su, A. Chen, X. Gui, R. Xiang, and Z, Tang, Sci. Rep. 4 (2014) 4185.

[8] D. Azullay, I. Balgerg, and O. Millo, Phys. Rev. Lett. 108 (2012) 076603.

[9]S. Chattopadhyay, S. Dutta, A. Banerjee, D. Jana, S. Bandyopadhyay, S. Chattopadhyay, and A. Sarkar, Physica B 404 (2009) 1509.

[10] D. Gupta, D. Dutta, M. Kumar, P. B. Barman, T. Som, and S. K. Hazra, J. Appl. Phys 118 (2015) 164501.

[11] A. K. Tagantsev, Appl. Phys. Lett. 93 (2008) 202905.

[12] V. Consonni, N. Baier, O. Robach, C. Cayron, F. Donatini, and G. Feuillet, Phys. Rev. B 89 (2014) 035310.

[13] A. Krtschil, A. Dadgar, N. Oleynik, J. Bläsing, A. Diez, and A. Krost, Appl. Phys. Lett. 85 (2005) 262105.

[14] X. B. Wang, C. Song, D. M. Li, K. W. Geng, F. Zeng, F. Pan, Appl. Surf. Sci. 253 (2006) 1639.

[15] Y. C. Yang, C. Song, X. H. Wang, F. Zeng, and F. Pan, Appl. Phys. Lett. 92 (2008) 012907.

[16] A. Bikowski and K. Ellmer, J. Appl. Phys. 114 (2013) 063709.

[17] E. Meyer, H. J. Hug, and R. Bennewitz, Scanning Probe Microscopy: The Lab on a Tip. 2004: Springer, Berlin.

[18] M. Kumar and T. Som, *Nanotechnology* 26 (2015) 345702.

[19] M. Kumar, T. Basu, and T. Som, J. Appl. Phys. 118 (2015) 055102.

[20] Y. Song and B. Bhushan, J. Phys.: Cond. Matt. 20 (2008) 225012.

[21] W. Wu, J. R. Guest, Y. Horibe, S. Park, T. Choi, S. W. Cheong, and M. Bode, Phys. Rev. Lett. 104 (2010) 217601; W. Wu, Y. Horibe, N. Lee, S-W Cheong, J. R. and Guest, Phys. Rev. Lett. 108 (2012) 077203.

[22] B. Singh, D. Varandani, and B. R. Mehta, Appl. Phys. Lett. 103 (2013) 051604.

[23] http://www.nanotec.es/products/wsxm/index.php for WSxM solutions.

[24] http://www.imagemet.com/index.php for SPIP software.

[25] B. C. Mohanty, Y. H. Jo, D. H. Yeon, I. J. Choi, and Y. S. Cho, Appl. Phys. Lett. 95 (2009) 062103.

[26] S. Nandy, G. Gonçalves, J. V. Pinto, T. Busani, V. Figueiredo, L. Pereira, R. F. P. Martins and E. Fortunato, Nanoscale **5** (2013) 11699.

[27] S. M. Sze, Jr D. J. Coleman and A. Loya, Solid-State Elect. 14 (1971) 1209.

[28] C. Maragliano, A. Glia, M. Stefancich, and M. Chiesa, J. Appl. Phys. 115 (2014) 124311.

[29] J. Shi, M. B. Starr, H. Xiang, Y. Hara, M. A. Anderson, J. H. Seo, Z. Ma, and X. Wang Nano Lett. 11 (2011) 5587.

[30] A. Kholkin, I. Bdikin, T. Ostapchuk, and J. Petzelt, Appl. Phys. Lett. 93 (2008) 222905.

[31] S. V. Kalinin and D. A. Bonnell, J. Mater. Res. 17 (2002) 936.

[32] H. N. Lin, S. H. Chen, S. T. Ho, P. R. Chen, and I. N. Lin, J. Vac. Sci. Technol. *B* 21 (2003) 916.

[33] https://www.asylumresearch.com/Applications/PFMAppNote/PFM-ANHR.pdf

[34] S. Mukherjee, A. Roy, S. Auluck, R. Prasad, R. Gupta, and A. Garg, Phys. Rev. Lett. 111 (2013) 087601.

[35] A. J. Hatt, N. A. Spaldin, and C. Ederer, Phys. Rev. B 81 (2010) 054109.

[36] A. R. Damodaran, E. Breckenfeld, Z. Chen, S. Lee, and L. W. Martin, Adv. Mater. 26 (2014) 6341.

[37] L. Pintilie and M. Alexe, J. Appl. Phys. 98 (2005) 124103.

[38] P. Gopal and N. A. Spaldin, J. Elec. Mater. 35 (2006) 538.

[39] A. G. Milnes, and D. L. Feucht, Heterojunctions and Metal-Semiconductor Junctions. 1972: Academic Press, New York.

[40] T. Basu, M. Kumar, T. Som, Mat. Letts. 135 (2014) 188.

[41] T. Iffländer, S. R. Pissarczyk, L. Winking, R. G. Ulbrich, A. A. Zubi, S. Blügel, and M. Wenderoth, Phys. Rev. Lett. 114 (2015) 146804.

[42] S. Ishibashi, Y. Higuchi, Y. Ota, and K. Nakamura, J. Vac. Sci. Technol. A 8 (1990) 1403.

[43] J. G. Lu, Z. Z. Ye, Y. J. Zeng, L. P. Zhu, L. Wang, J. Yuan, and B. H. Zhao, J. Appl. Phys. 100 (2006) 073714.

[44] B. E. Sernelius, K. F. Berggren, Z. C. Jin, I. Hamberg, and C. G. Granqvist, Phys. Rev. B 37 (1988) 10244.

[45] D. J. Yun, and S. W. Rhee, Thin Solid Films 517 (2009) 4644.

[46] M. F. Wong, T. S. Herng, Z. Zhang, K. Zeng, and J. Ding, Appl. Phys. Letts 97 (2010) 232103.

[47] A. Kumar, T. S. Herng, K. Zeng, and J. Ding, ACS Appl. Mater. Interfaces 4 (2012) 5276.

[48] P. Giannozzi et al. QUANTUM ESPRESSO: a modular and open-source software project for quantum simulations of materials. J. Phys.: Condens. Matter 21 (2009) 395502.

[49] W. Melitz, J. Shen, A. C. Kummel, and S. Lee, Sur. Sci. Rep. 66 (2011) 1.

[50] S. Chatterjee, M. Kumar, A. Pal, I. Thakur, and T. Som, J. Mater. Chem. C 3 (2015) 6389.

[51] O. Kappertz, R. Drese, and M. Wuttig, J. Vac. Sci. Technol. A 20 (2002) 2084.

[52] M. N. Islam, T. B. Ghosh, K. L. Chopra, H. N. Acharya, Thin Solid Films 280 (1996) 20.

[53] H. B. Fan, S. Y. Yang, P. F. Zhang, H. Y. Wei, X. L. Liu, C. M. Jiao, Q. S. Zhu, Y. H. Chen, Z. G. Wang, Chinese Physics Letters 24 (2007) 2108.

[54] T. P. Rao, M. C. S. Kumar, A. Safarulla, V. Ganesan, S. R. Barman, C. Sanjeeviraja, Physica B 405 (2010) 2226.

[55] T. Basu, M. Kumar, S. Nandy, B. Satpati , C. P. Saini, A. Kanjilal, and T. Som, J. Appl. Phys. 118 (2015) 104903.

[56] J. L. Daniel, and R. M. Sankaran, J. Phys. D: Appl. Phys. 44 (2011) 453001.

[57] J. J. Daniel and C. A. Wolden, Appl. Phys. Lett. 83 (2003) 3933.

[58] K. Ellmer Transparent Conductive Zinc Oxide. 2008: Springer Series in Materials Science, Springer Berlin.

[59] M. Kumar, S. K. Hazra, and T. Som, J. Phys. D: Appl. Phys. 48 (2015) 455301.

[60] C. C. Singh, T. A. Patel, and E. Panda, J. Appl. Phys. 117 (2015) 245312.

[61] T. R. Paudel and W. R. L. Lambrecht, Phys. Rev. B, 77 (2008) 205202.

[62] T. Brumme, M. Calandra, and F. Mauri, Phys. Rev. B 91 (2015) 155436.

[63] J. E. Jaffe and A. C. Hess, Phys. Rev. B 48 (1993) 7903.

[64] F. L. Kuo, Y. Li, M. Solomon, J. Du, and N. D. Shepherd, J. Phys. D: Appl. Phys. 45 (2012) 065301.

# CHAPTER 5

## 5. Role of structural defects on charge transport in Cu-O thin films

Generally, copper is found in two oxide states, viz. cuprous oxide ($Cu_2O$) and cupric oxide (CuO) having the band gaps of 2.1 eV and 1.2 eV, respectively [1]. The band gaps of these semiconductors make them good candidates for photovoltaic devices (e.g. solar cells and photolysis of water splitting), catalysts, sensors, stable electron sources, and optoelectronic devices [1]. Out of them, CuO is attractive as a selective solar absorber due to its high solar absorbance and a low thermal emittance. On the other hand, due to a smooth conduction, $Cu_2O$ is a very promising candidate for solar cell applications [1,2]. Thus, in order to make an efficient and stable solar cell, a polycrystalline thin film of Cu-O (e.g. a mixed phase of CuO and $Cu_2O$) is used [3]. Generally, copper oxide exhibits a *p*-type conductivity because of copper vacancies [4]. In fact, it is observed that the formation energy of copper vacancies in copper oxide is much lower than the oxygen vacancies, copper interstitial, and copper anti-site, which in turn make this an intrinsic *p*-type semiconductor [4]. Thus, the main conduction arises from the presence of holes in the valence band (VB). Polycrystalline films of Cu-O have been prepared by various techniques such as thermal oxidation, electro deposition, chemical conversion, chemical brightening, spraying, chemical vapor deposition, plasma evaporation, magnetron sputtering, and molecular beam epitaxy [5-8]. Out of these, the sputter deposition technique is a useful way to grow high quality Cu-O thin films under a controlled copper-rich (oxygen-poor) condition, which is a fundamental need to fabricate Cu-O based electronic and optical devices [9].

It is worth to mention here that the charge transport across the thin films depends on the crystallinity [10]. Thus, to get a better efficiency, an in-depth understanding on the role of crystalline nature in charge transport is needed [11]. In this chapter, we have studied the role of crystallinity on charge transport properties of polycrystalline Cu-O thin films using local probe techniques. This study will open a new avenue to design a solar cell, with Cu-O as the absorber layer, having an improved efficiency.

## 5.1 Structural defect-dependent charge transport in Cu-O/Si studied by Kelvin probe force microscopy and conductive atomic force microscopy

### 5.1.1 Introduction

The quest for memristor or resistive random access memory (ReRAM) is driven by a cost-effective process to develop a low power, dense, stable, and fast nonvolatile random access memories [12]. Generally, in ReRAM cells, a transition-metal oxide is used as a sandwich layer between two electrodes where the resistance of the oxide layer can be switched electrically from a low resistance state (LRS) to a high resistance state (HRS). As a result, a hysteresis loop appears in the current-voltage ($I$ -$V$) characteristics which is a signature of memory [12-14]. In fact, due to a suitably applied bias, dielectric break down takes place, leading to the formation of oxygen ions, their migration, and the formation of a subsequent conductive path which is known as a filament. This filament is responsible for LRS, whereas rupturing of the same, due to Joule heating, gives rise to HRS [12-14]. Transition-metal oxides such as NiO, Cu-O ($Cu_2O$ and/or CuO), $TiO_2$, $HfO_2$, ZnO, and $SiO_2$ are some of the promising materials for memristive applications [13,14-21]. Among these materials, copper oxide (Cu-O) has attracted a considerable attention not only due to an easy processing of efficient and compact ReRAM but also because of its nontoxic nature, relative abundance on earth, and for a range of advanced applications [22-24]. For instance, superior retention time and excellent cyclic endurance have been reported in Cu-O based memories [23]. In a recent report, Han *et al*. have shown the suitability of Cu-O thin films for integrated and wearable electronics [24]. In addition, they claim that an excellent performance in resistive switching (RS) can be achieved if copper oxide is present in the mixed phase and has a 8:1 ratio of $Cu_2O$ and CuO. As a matter of fact, it is suggested in various reports that a $Cu_2O$-rich film is needed to achieve an excellent device performance [18,22-24].

Generally, copper vacancies (defects) in Cu-O act as a *p*-type dopant (acceptor), which in turn makes this oxide a conductive *p*-type semiconductor, whereas oxygen vacancies are found at donor sites and responsible for *n*-type conductivity [25]. These vacancies not only govern the charge transport in Cu-O films but are also responsible for RS [21,23-26]. However, the influence of defects on charge transport and/or RS in copper oxides is still not clear. Therefore, it is important to study the role of structural defects to understand the RS behavior as well as the formation of conduction paths in Cu-O films.

In order to confirm the presence of RS in a material, various bulk and local techniques are applied. Versatile applications of scanning probe microscopy (SPM) have made it suitable to study the nanoscale physical properties of materials [15]. Among different modes of SPM, conductive atomic force microscopy is used extensively because it can build up simultaneous information on local electrical conduction and surface topography. In fact, a one-to-one correspondence between surface morphology and current mapping, with very high lateral resolution (~5 nm in topography and ~1 pA in current image), can be developed by cAFM [16]. In addition, in cAFM, a conductive tip is used as a top electrode which gives an easy control to perform *I-V* measurements at a desired location.

Normally, change in defects lead to a shift in the Fermi level position, which in turn changes the work function of a material [17,18]. Kelvin probe force microscopy is considered to be a suitable non-contact local probe technique which is used not only to map the work function but also to quantify the carrier concentration [27,28]. The measurement of doping concentration without any contact on the sample surface has a considerable advantage because this avoids the effect of an extra Schottky barrier at the contact-specimen junction. This local quantification of carrier concentration has a one-to-one correspondence with nanoscale conductivity [28,29].

In this work, we show the importance of structural defects on the RS behaviour of rf magnetron sputter deposited copper oxide thin films. X-ray diffraction is used to investigate the crystalline nature and evaluate the dislocation density of the films. In addition, KPFM is used to quantify the carrier density, whereas cAFM studies demonstrate the crystallinity-dependent presence and absence of bipolar resistive switching. Further, we present the experimental evidence on nanoscale filament formation from cAFM images and discuss the mechanism of switching behavior at nanoscale in detail.

### 5.1.2 Experimental detail

Cu-O thin films of thickness of 200 nm (measured by Ambios, XP-200 surface profilometer) were grown at room temperature on ultrasonically cleaned and native oxide covered low resistive ($\rho$=0.5 Ω cm), *n*-Si (100) substrates. Commercially available 99.99% pure $Cu_2O$ target (MTI Corporation, USA) was used for depositing Cu-O thin films. A base vacuum of $1\times10^{-7}$ mbar was achieved in the deposition chamber (Excel Instruments, India) and subsequently ultra-pure (99.999%) argon gas was injected (with a flow rate of 30 sccm) into the same to maintain the working pressure of $5\times10^{-3}$ mbar during sputtering. A rf power of 100 W (frequency=13.56 MHz) (Cesar, Advanced Energy, USA) was supplied to the target during deposition and the substrates were rotated with a speed of 3 rpm to achieve a uniform film thickness. The target-to-substrate distance was fixed at 8 cm. The deposition was carried out at 0° (called S1) and 50° (called S2) angles of incidence (measured with respect to the surface normal) of the flux. It may be mentioned that the film deposited at normal incidence (S1) had a growth rate of 8 nm min$^{-1}$, while it was 5 nm min$^{-1}$ for the case of growth at 50° oblique incidence (S2). Hence, a higher time was required to deposit the same thickness for the oblique incidence.

The crystallinity and phase identification of Cu-O films were performed by XRD (Bruker, D8-Discover) in Bragg-Brentano geometry, using the Cu-Kα radiation ($\lambda$=0.1542 nm). For the present study, similar slit width, sample areas, and scan speeds were chosen to achieve uniform results from S1 and S2. In addition, surface morphology and local electrical properties of Cu-O films were examined by *ex*-situ AFM in different modes using conductive Pt-coated tips having ~30 nm radius of curvature, ~2 N m$^{-1}$ stiffness, and a resonance frequency of ~70 kHz. It may also be mentioned that both cAFM and KPFM measurements were performed at large number of randomly chosen places with different scan speeds form 0.2 to 1 Hz and at various scan angles (by rotating the samples) on three sets of samples (for both S1 and S2), deposited under the similar conditions to minimize tip-related artifacts in the present data [30]. In addition, the present AFM setup is equipped with nanopositioning closed-loop sensors (NPS$^{TM}$), making it possible to reproducibly position the cantilever at a point of interest and measure the *I-V* characteristics on the same using the *pick a point* force curve interface [31].

A Pt-coated conductive probe was used as the top electrode, whereas the bottom electrode was made on the back of the Si substrate using silver paste. This led to the formation of a Pt/Cu-O/Si/Ag heterojunction. It would be important to mention that the electric transport properties at nanoscale, in particular performed by cAFM measurements, would strongly depend on the applied force [16].

Hence, the spring constant of the tip and the detector sensitivity were calibrated with the help of a quartz crystal. This helped us to find out a relation between the set-points and the applied force and we used a fixed set-point (applied force: 20 nN) during all cAFM measurements. In fact, the use of a constant force set-points should reduce tip-related artefacts to a significant extent [16]. All recorded images were analyzed using WSxM [31] and ImageJ [32] softwares.

### 5.1.3 Results and discussion

Therefore, to study the local electrical transport properties, information on the film topography will be useful. Thus, besides cAFM and KPFM measurements, Cu-O film morphologies are also recorded.

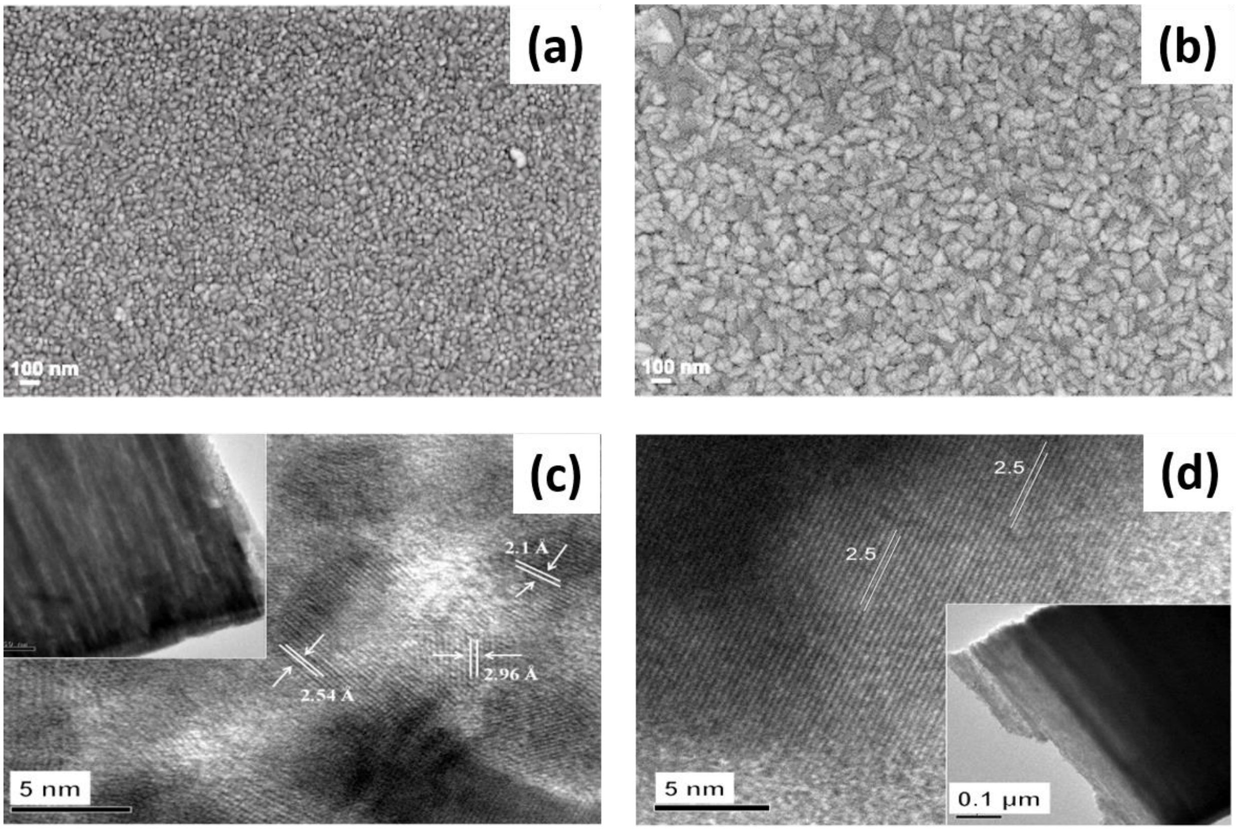

Figure 5.1: Plan-view SEM images of copper oxide thin films sputter deposited at (a) 0° (S1) and (b) 50º (S2). Plan view HRTEM images of (c) S1 and (d) S2. The insets show respective cross-sectional TEM images.

Scanning electron micrographs of copper oxide thin films deposited at normal incidence (S1) and an oblique angle of 50° (S2) are shown in Figs. 5.1(a) and 5.1(b), respectively. Top view of S1 thin film shows the presence of a granular morphology, having dimension of grains in the range of 20±10 nm [Fig. 5.1(a)]. On the other hand, in case of obliquely deposited films, the size of the grains becomes bigger (60±10 nm) and they evolve in triangular in shapes [Fig. 5.1(b)] [33,34]. The experimental parameters like target to substance distance (80 mm), radio-frequency power (100 W) and the oblique angle of deposition (50°) are chosen in such a way so that as-grown films will be continuous in nature and not sufficient enough to create a dominant shadowing effect at substrate to grow well-separated columnar structures of copper oxide films. In the plan-view HRTEM image of S1 film, three different lattice spacing (of about 2.1 Å, 2.5 Å and 2.9 Å) are found which closely correspond to *d*-spacing values of (200), (111), and (110) set of planes of $Cu_2O$ [Fig. 5.1(c)]. On the other hand, in the plan-view HRTEM image of the S2 film the measured *d*-spacing turns out to be 2.5 Å which corresponds to (111) set of planes of cubic $Cu_2O$ [Fig. 5.1(d)].

It is well-known that an AFM phase contrast image gives a better resolution, making it possible to detect very small features, which may otherwise remain hidden in a topographic image. A careful observation of AFM phase image (not shown) obtained from S1 and S2 reveal that films are granular in nature with average grain size of 30 and 70 nm, respectively. However, both films have nearly similar root mean square roughness 2.4 nm [35]. It is well-known that the carrier density available for the electrical transport in a material strongly depends on its crystallinity [36,37]. Thus, the XRD spectra are recorded under similar conditions to confirm the crystalline quality and nature of the films (i.e. S1 and S2).

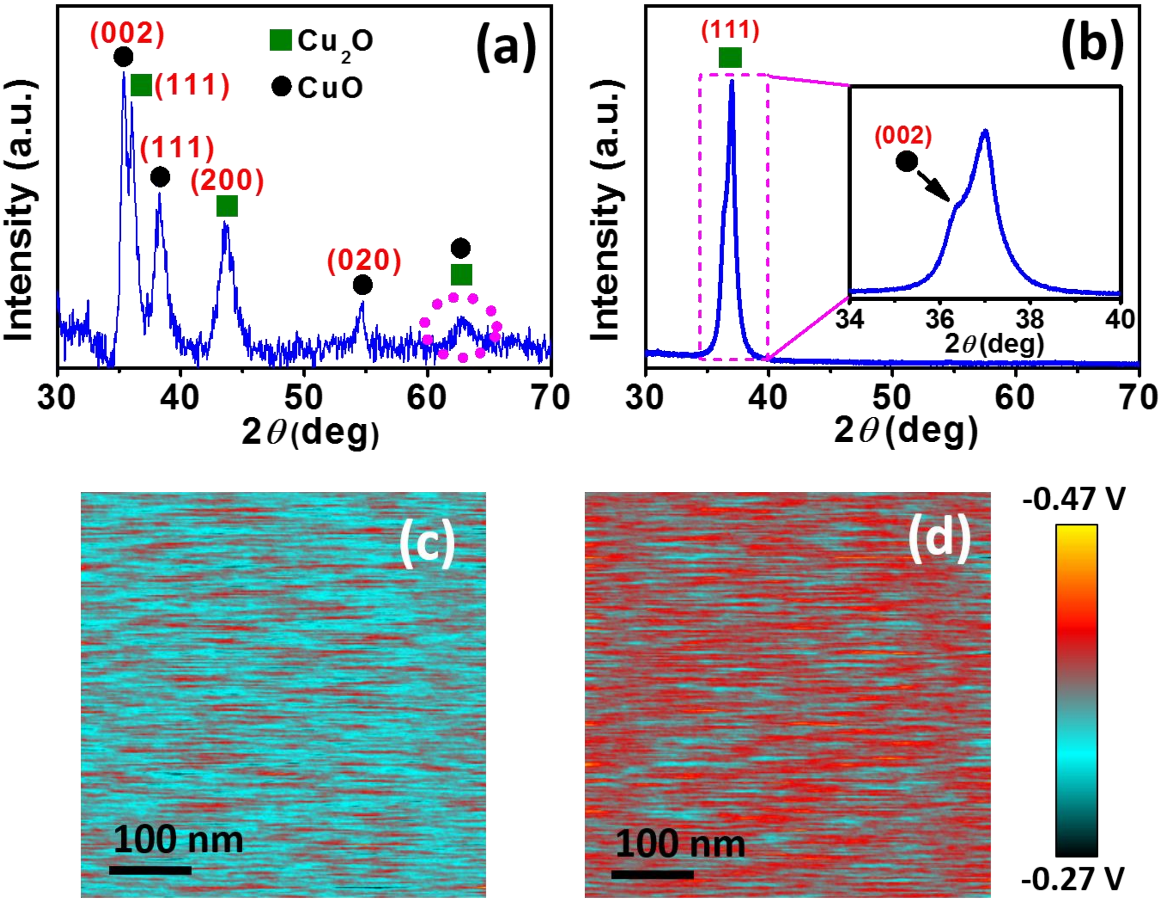

Figure 5.2: (a) and (b) show the XRD spectra of S1 and S2 films, respectively. The regime marked by a dashed circle in (a) indicates the presence of amorphous phases of Cu-O. The inset in (b) shows a magnified view of the marked region, showing the presence of CuO and $Cu_2O$ phases. (c) and (d) represent the contact potential difference, obtained from KPFM studies, for film: S1and S2, respectively.

Fig. 5.2(a) represents the XRD pattern for S1, exhibiting four prominent peaks at $2\theta$=35.38° ($d$=0.253 nm), 36.04° ($d$=0.249 nm), 38.32° ($d$=0.235 nm), and 43.60° ($d$=0.207 nm). The corresponding $d$-spacings match well with the (002) plane of CuO, (111) plane of $Cu_2O$, (200) plane of CuO, and (002) plane of $Cu_2O$, respectively [16]. In addition, a low intensity peak is also observed [marked in Fig. 5.2(a) by a dashed circle], which does not match with any reported peak of either CuO or $Cu_2O$. However, it matches well with the amorphous phases of CuO and $Cu_2O$ [38,39]. On the other hand, in Fig. 5.2(b), S2 film shows only one peak which is deconvoluted into two peaks: one is assigned to the CuO (002) reflection and the other one is assigned to $Cu_2O$ (111). In addition, it is interesting to note that unlike S1, no amorphous component of CuO and/or $Cu_2O$ is observed for S2 over the entire range of $2\theta$. The presence of only two peaks with excellent intensities in S2 film indicates that it has a better crystalline nature compared to S1. As mentioned above, S2 film has a relatively slower growth rate and hence, it tends to grow along the planes having minimum surface free energy [40] such as (111) for $Cu_2O$ and (002) for CuO [41].

From the respective diffractogram, we have calculated the average crystallite size ($D$) and dislocation density ($\delta$) for both the films (S1 and S2) using Scherer's formula: $D = 0.9\lambda/\beta cos\theta$, where $\beta$ is the FWHM, $\theta$ is the Bragg angle, $\lambda$ is the x-ray wavelength, and $\delta$ is defined ad $1/D^2$ [42]. In order to do the same, we have taken into account CuO (002) and $Cu_2O$ (111) peaks for both S1 and S2, yielding the average crystallite size to increase from 14 (for S1) to 50 nm (for S2) and the dislocation density to decrease from $5.1\times10^{15}$ (for S1) to $4\times10^{14}$ $m^{-2}$ (for S2). One can see that the measured grain sizes from AFM phase image are little bigger than the ones derived from the XRD data. This is because of the limitation of AFM to resolve smaller crystallites within a bigger grain [42]. It may also be noted that according to the theory of kinematic scattering, XRD peaks may get broadened either when crystallites become smaller than about a micrometer or if lattice defects are present in large enough abundance [43]. In the present case, S1 shows the broader XRD peaks compared to those of S2, confirming the presence of higher number of structural defects in S1 (as discussed above). Further, the ratio of the volume fraction of $Cu_2O$ and CuO phases in both films has been estimated by adding the intensity of individual diffraction peak belonging to both the phases: $\Sigma(I_{Cu_2O})/\Sigma(I_{CuO})$, where $\Sigma(I_{Cu_2O})$ and $\Sigma(I_{CuO})$ are summations of the intensity of all peaks for $Cu_2O$ and CuO, respectively [33]. It may be mentioned that during this calculation, we have not considered the contribution of any amorphous component [33]. The ratio of $Cu_2O$ to CuO volume fraction is found to be 1.31 and 1.56 for S1 and S2, respectively, which manifests that both films are rich in $Cu_2O$, albeit S2 has a nearly 20% higher $Cu_2O$ component. Thus, both films (S1 and S2) should have different degrees of structural defect density, leading to different charge transport processes.

Generally, charge transport in a film depends on its work function and the carrier concentration [44]. Thus, prior to the study of local electrical transport, KPFM is used to calculate the local carrier density. Mathematically, the work function of a sample ($\Phi_{\mathrm{sample}}$) can be expressed as:

$$\Phi_{\mathrm{sample}} = \Phi_{\mathrm{tip}} - eV_{\mathrm{CPD}} , \qquad (5.1)$$

where $\Phi_{\mathrm{tip}}$, $e$, and $V_{\mathrm{CPD}}$ are the work function of the AFM tip, electronic charge, and the contact potential difference measured by KPFM, respectively [28]. In addition, it is well-known that under the Boltzmann approximation, the concentration of holes ($H$) in a $p$-type semiconductor is given by:

$$H = N_A^- - N_D^+ = \sim N_A^- = C_A = N_{\mathrm{eff}}\, exp[(eV_{\mathrm{CPD}} + \chi - \Phi_{\mathrm{tip}})/k_BT] , \qquad (5.2)$$

where $N_A^-$ is the ionized acceptor density, $N_D^+$ is the donor density, $C_A$ is the acceptor concentration, $N_{\mathrm{eff}}$ is the effective density of states in the valance band, $\chi$ is the electron affinity, $k_B$ is Boltzmann constant, and $T$ is the absolute temperature [29]. Since, both the samples have mixed phases of Cu-O, it is very difficult to find out the accurate value of $\chi$. On the other hand, the above relation indicates that $H$ depends on $exp(eV_{\mathrm{CPD}}/k_BT)$. The measured $V_{\mathrm{CPD}}$ values for S1 and S2 are shown in Figs. 5.2 (c) and (d), respectively. Therefore, the ratio between the hole concentration ($H_{S2}/H_{S1}$) is given by $exp[e/k_BT\{(V_{\mathrm{CPD}})_{S2} - (V_{\mathrm{CPD}})_{S1})\}]$ and is found to be 2980. In this calculation, we have assumed that all other parameters such as $\chi$, $\Phi_{\mathrm{tip}}$, and $N_{\mathrm{eff}}$ remain constant. This indicates that a good crystalline sample (S2), having the lesser number of structural defects, has a much higher carrier density compared to the one having relatively poor crystallinity, which in turn gives rise to a difference in the charge conduction. cAFM measurements are carried out to study the local current-voltage (*I*-*V*) characteristics of both the films. Figures 5.3(a) and (b) show the local *I*-*V* characteristics for S1 and S2, respectively, obtained by sweeping a dc bias according to 0 V → 10 V → 0 V → -10 V → 0 V with a ramp rate of 0.2 V $s^{-1}$ at a fixed tip location on a randomly chosen grain and a grain boundary. The *I*-*V* curve, presented in Fig. 5.3(a), is separately analyzed for different branches: at positive voltages, the current is very low and remains constant (path #1) until the voltage reaches +7.5 V from where the current increases suddenly (path #2) and the corresponding voltage is identified as the 'set' voltage ($V_{\text{set}}$). Beyond 7.5 V, the current value reaches the compliance limit (20 nA) of the cAFM setup and hence, shows a straight line (path #3). On the other hand, during the decreasing cycle of voltage, the current remains saturated till far below $V_{\text{set}}$ (7.5 V). At much lower voltages (<3 V), the current decreases almost linearly, indicating the Ohmic nature of the tip-sample contact (path #4). In fact, the S1 film exhibits a well-defined *I*-*V* hysteresis which is a signature of the RS behaviour [12-22]. In addition, it is found that grain boundary shows a higher turn-on potential of 0.5 V [Fig. 5.3(a)] compared to a grain, albeit no significant change in the behaviour of *I*-*V* characteristics at G and GB is observed within the detection limit of the present AFM setup. In addition, we have studied the *I*-*V* characteristics at large number of randomly chosen points (plots not shown) to observe that behaviour of the curves remains nearly similar. Therefore, choice of the spots for *I*-*V* measurements (even for G and GB) on the films (in particular, for S1) is not expected to influence much in the present case.

One of the reasons behind observing nearly similar behaviour of the *I*-*V* data at G and GB stems from the fact that the Pt-coated AFM tip used here has a radius of ~30 nm, which may impede it to reach the bottom of the GBs. Instead, its lateral sides are likely to touch the surrounding grains.

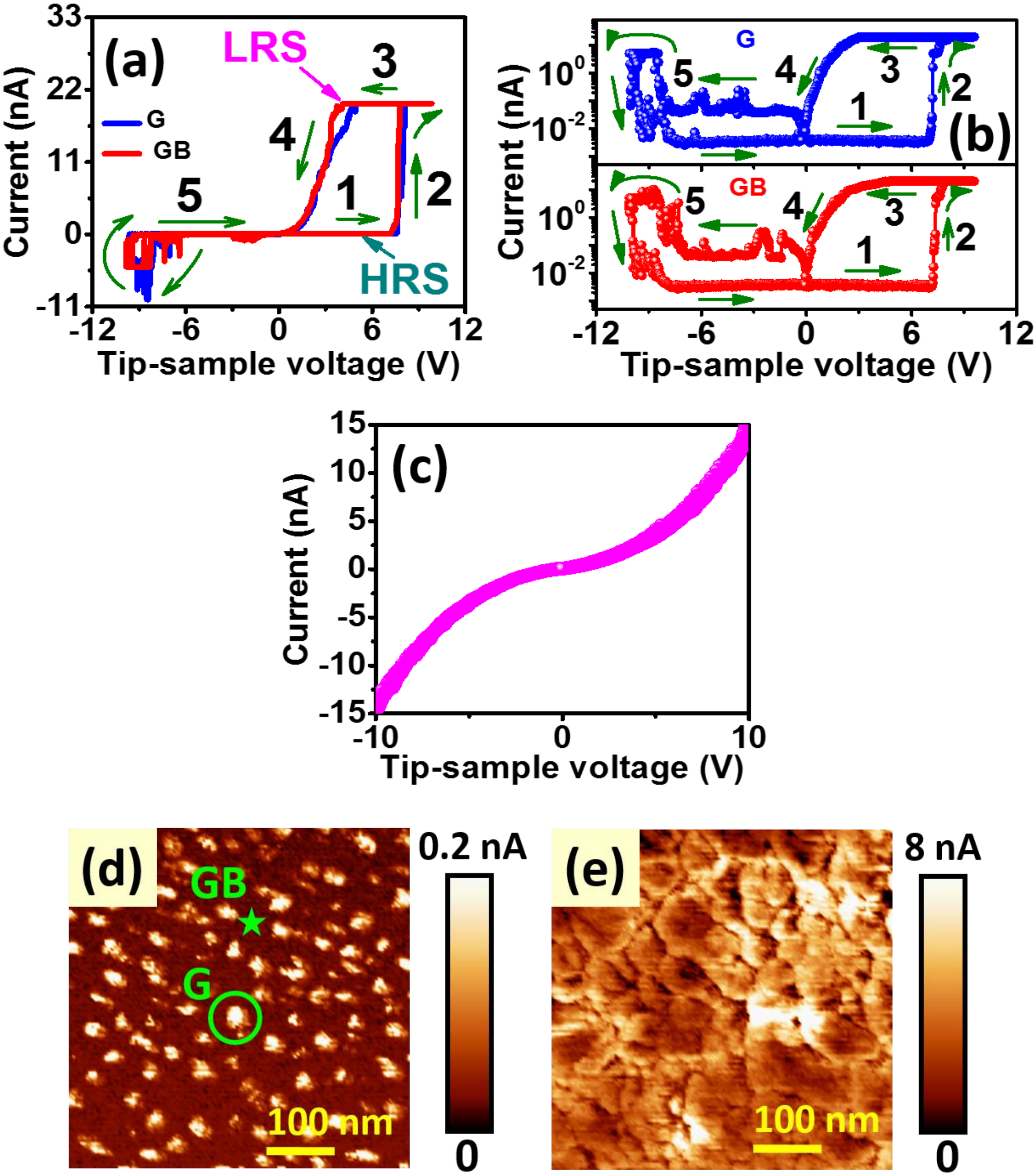

Figure 5.3: (a) and (b) show the local $I$-$V$ characteristics recorded for S1 in the linear and semi-log scale, respectively, whereas (c) represents the $I$-$V$ characteristic corresponding to S2 films. (d) and (e) represent cAFM images ($0.5\times0.5\ \mu m^2$) taken at $V_{tip}$=5 V for S1 and S2, respectively. The circle and the star on the current map in (c) indicate the positions from where $I$-$V$ measurements are performed from a grain and a grain boundary, respectively.

Further, to avoid any ambiguity regarding a possible reset transition at very low current at about -2.5 V due to the presence of small bumps in the *I-V* characteristics, corresponding to G and GB sites, we have plotted the same with the current values in log-scale and have presented in Fig. 5.3(b).

It should also be noted that a pronounced change in the resistance is observed for both increasing and decreasing voltages, corresponding to a tip bias, $V_{\text{tip}}$=5 V, which is known as the high resistance state (HRS) and the low resistance state (LRS), respectively. For this particular voltage (5 V), the conductance ratio is found to be $\approx 10^2$ and is defined as the window of memory [45]. Subsequently, an opposite 'reset' process is also observed when sweeping the voltage from 0 to -6 V ($V_{\text{reset}}$, path #5), as is evidenced by a two-step switching from LRS to HRS [Fig. 5.3(a)]. A similar behaviour of RS has also been reported by Singh *et al.* in case of a Cu hybrid interface device [46]. On the other hand, interestingly, S2 film does not show any loop in the *I-V* characteristics [Fig. 5.3(c)] under similar experimental conditions. For instance, here current increases continuously with increasing voltage and then decreases in the same manner. In fact, *I-V* characteristics for S2 matches well with Schottky-type behaviour of the tip-sample contact. It may be mentioned that since local *I-V* characteristics is performed at a fixed point, it is very difficult to predict the current conduction path over a large surface area. Hence, to address this issue, we have performed local current mapping at randomly chosen one hundred thirty places. Figs. 5.3(d) and (e) represent the corresponding cAFM images of S1 and S2 (taken at a fixed tip voltage of 5 V), respectively. Isolated current spots (in the range of pA) are observed for S1, while a uniform current (in the range of nA), except a small variation at grain boundaries, is observed in case of S2. It may be mentioned that similar current maps are observed from all the randomly chosen areas throughout the surfaces of S1 and S2. These images, thus, confirm that transport of charge carriers is much easier in S2 compared to that of S1.

To understand the statistical behaviour of the *I-V* characteristics, one hundred thirty curves are recorded for random tip positions (as mentioned above) and variation in the $V_{\mathrm{set}}$ for S1 is plotted in Fig. 5.4(a). This shows a fluctuation in $V_{\mathrm{set}}$ up to ~1 V to yield an average value of $V_{\mathrm{set}}$=7.5 V. In fact, different $V_{\mathrm{set}}$ values, obtained from different locations, reflect the local variation in the carrier density at those locations [28]. The existence of two resistance states (viz. HRS and LRS) in S1 is also reproduced using a two-fold overwriting process. In this process, first we scan an area in the contact mode by applying a positive tip bias, $V_{\mathrm{tip}}>(V_{\mathrm{set}})_{\mathrm{max}}$ (i.e. >8.5 V) which converts this area into a low resistance state. In the second step, a large area scan is performed, at a lower tip bias [$<(V_{\mathrm{set}})_{\mathrm{min}}$ (i.e. <6.5 V)], to map this converted area. Fig. 5.4(b) is a schematic diagram, showing both (first and second) scan areas by red and gray colours, respectively. We have performed the above mentioned steps for S1 which yields a high and saturated current (20 nA) [as seen from the 3D current map in Fig. 5.4(c)] from the first scan area [i.e. the central red box in Fig. 5.4(b)], indicating the presence of a LRS corresponding to $V_{\mathrm{tip}}>(V_{\mathrm{set}})_{\mathrm{max}}$=10 V. On the other hand, a very low current (in the range of pA) is observed from the surrounding gray area [in Fig. 5.4(b)] scanned at $V_{\mathrm{tip}}<(V_{\mathrm{set}})_{\mathrm{min}}$=5 V, depicting a HRS [Fig. 5.4(c)]. It may be mentioned that one should mostly expect the absence of LRS after scanning the first area with an applied tip bias of 6.5 V. However, upon applying higher tip voltages (e.g. $V_{\mathrm{tip}}$=7 V), one should observe more grains to be conducting in nature (image not shown). Likewise, for a first scan performed corresponding $V_{\mathrm{tip}}\geq$8.5 V, the entire area can be converted into a low resistance state (as discussed above).

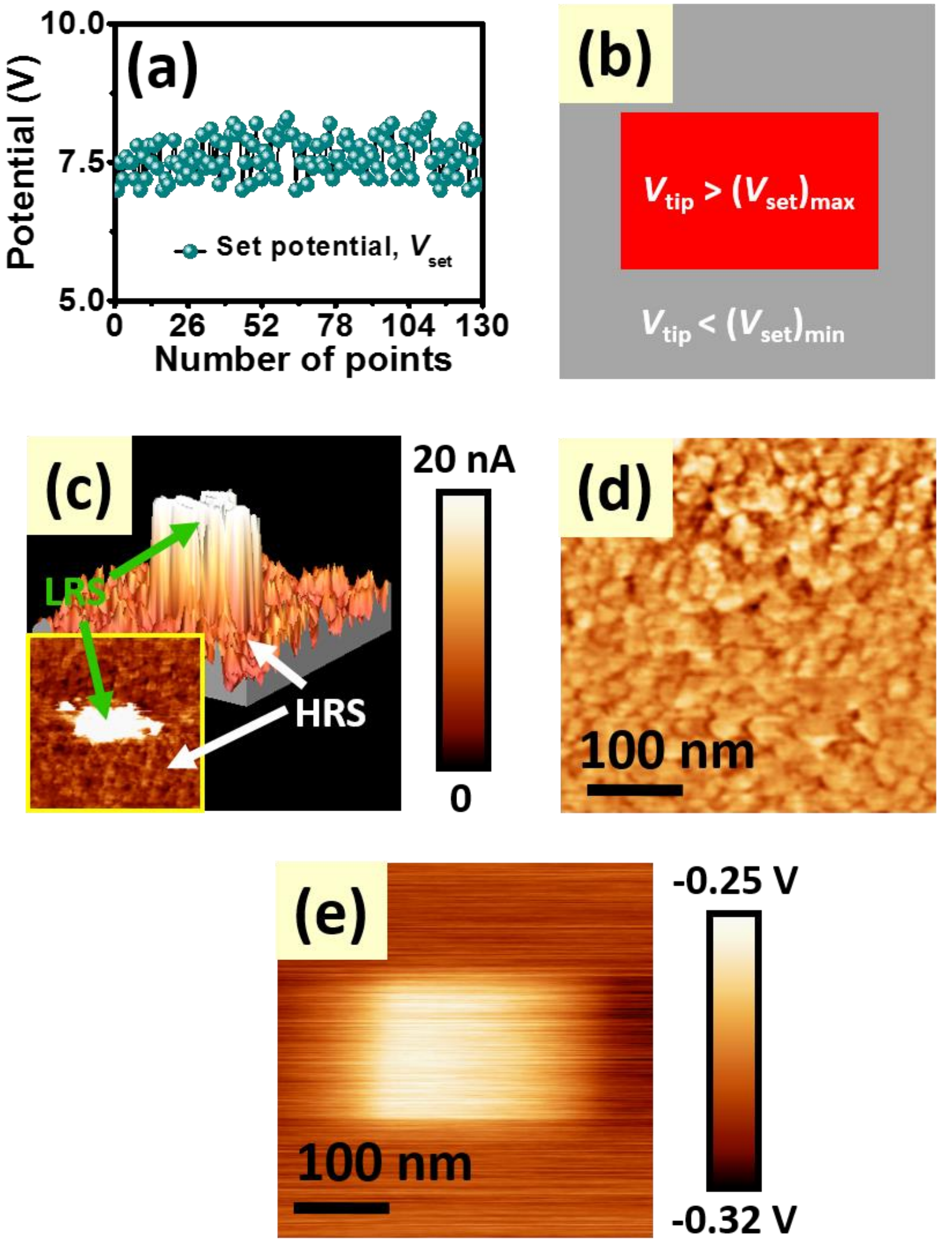

Figure 5.4: (a) Variation of set potential ($V_{set}$) at randomly chosen one hundred thirty places. The average value of $V_{set}$ is 7.5 V whereas $(V_{set})_{min}$ and $(V_{set})_{max}$ are found to be 6.5 and 8.5 V, respectively. (b) Schematic diagram, demonstrating the conversion to a low resistance state (LRS) as is indicated by the central red box, whereas the gray box surrounding the red one corresponds to the HRS achieved due to a scan performed at $V_{tip}<(V_{set})_{min}$ and over a large area, (c) 3-dimensional representation of the current image of S1 taken at a constant tip voltage, $V_{tip}$=5 V where the central bright spot represents the low resistance area [corresponding to the red box in (b)] converted at $V_{tip}$=10 V. The inset presents a two-dimensional view of this image, (d) the outcome of the same scan performed ($V_{tip}$=10 V) on sample S2. The scan areas for images shown in (c) and (d) are 0.5 × 0.5 $\mu m^2$, and (e) shows the map of $V_{CPD}$ (obtained from the KPFM measurement) corresponding to (c).

As a matter of fact, the inset in Fig. 5.4(c) shows a 2D-view of the current map where the central white patch corresponds to the LRS and the surrounding low current area represents the HRS.

We have also checked the sustainability of this memory, without any external power, and it is found that the LRS remains as it is for more than 24 h at RT. The same two-fold overwriting process is performed using the same experimental parameters, on S2, which shows the absence of any RS behaviour in the sample. For instance, it is evident from Fig. 5.4(d) that no change in the current map takes place even after applying a rather high tip voltage (+10 V) during the first scan itself. These results, thus, manifest a significant change in the local electrical transport properties in S1 and S2.

Since, the LRS of sample S1 shows a smooth charge conduction process, this state [red rectangular box in Fig. 5.4(b)] should have a higher carrier density. It is known that the change in carrier density has a one-to-one correspondence from the mapped $V_{\mathrm{CPD}}$ [28]. Thus, after the two-fold overwriting process, KPFM measurements are performed for both the samples on the respective areas. Fig. 5.4(e) depicts the $V_{\mathrm{CPD}}$ map corresponding to Figure 5.4(c), for S1, where only the central area has a white contrast and corresponds to the LRS but the surrounding area does not show any change and thus, represents the HRS. In fact, a positive voltage may produce a large amount of charged oxygen vacancies in the surface region by extracting oxygen ions from the lattice which in turn generates a LRS [19]. However, no such change in the $V_{\mathrm{CPD}}$ map is observed corresponding to the sample S2.

In addition, to understand the main current conduction path in S1, a topographical image [Fig. 5.5(a)] is superimposed on the corresponding cAFM current image [Fig. 5.5(b)] and is shown in Fig. 5.5(c). From these figures, it is interesting to note that, corresponding to $V_{\mathrm{tip}}$=+5 V, grains are the preferential conduction paths for charge carriers in S1, whereas grain boundaries remain neutral. The present observation that grains are more conducting is consistent with the larger Pt-coated tip radius, causing the tip-sample area on a grain boundary to be lesser than that on a grain.

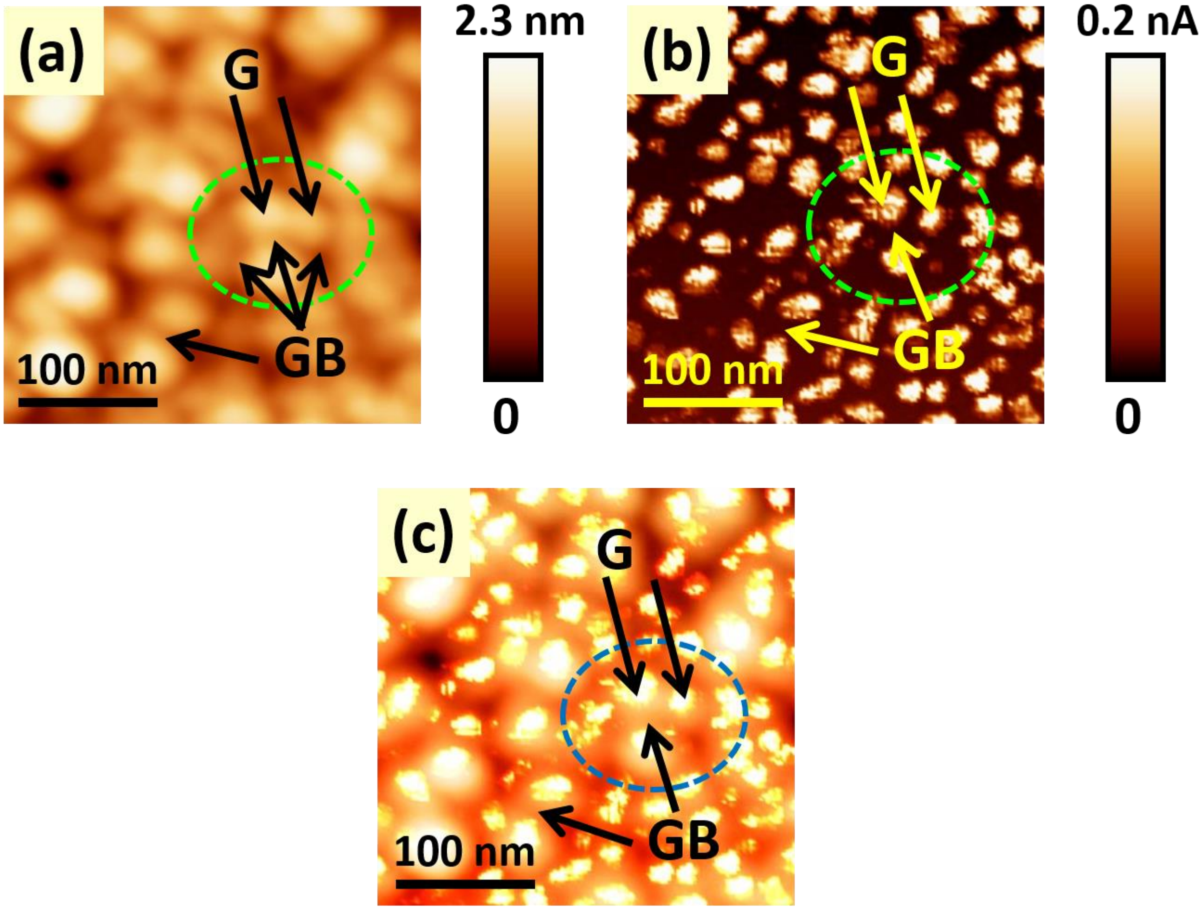

Figure 5.5: (a) Surface topography of S1 measured during current mapping, (b) corresponding current image, and (c) represents the superimposed topographic and the current images [0.3×0.3 $\mu m^2$] and hence, does not have any scale bar. G and GB represent grains and grain boundaries in (a)-(c).

On the other hand, as discussed above, a much higher current flows through a desired area, which gets transformed into a LRS [Fig. 5.4(c)] due to an applied tip voltage of +10 V across it. As a matter of fact, this low resistance state, surrounded by the corresponding high resistance state, manifests the filament formation [2D representation of the current map shown as the inset in Fig. 5.4(c)] within S1.

Presently, RS in a material like Cu-O is explained on the basis of the formation of conducting filaments and their subsequent rupturing [12-14]. In the present case, the resistive switching in Cu-O film (viz. S1) can also be attributed to the formation of conducting filamentary paths, presumably in the form of copper nanowires [12-14]. As mentioned above, the copper (acceptor) and oxygen (donor) vacancies are likely to be present simultaneously in a Cu-O film, although at thermal equilibrium, the charge generated inside the film due to the $O^-$ ions is balanced by the $Cu^+$ ions [25]. After applying a positive bias to the cAFM tip, $O^-$ ions migrate towards the anode and get neutralized due to the recombination with positive charges (holes). Due to the recombination of $O^-$ ions or vacancies, the density of $Cu^+$ ions increases and in turn forms a metallic conduction channel, known as a *filament* in RS [set state, path #2, Fig. 5.3(a)] [20-25]. In fact, $Cu^+$ ions are responsible for the metallic behaviour (i.e. LRS) whereas $O^-$ ions give rise to the semiconducting nature (i.e. HRS) of Cu-O films. In the present scenario, recently, Zhang *et al*. have shown that the RS behaviour depends on oxygen vacancies [25]. However, they do not find any absence of RS behavior even after changing the oxygen concentration. This confirms that the absence of RS (in S2) in the present study, is not governed by oxygen vacancies alone and some other effect is also responsible for the same, e.g. variation in the compositional and structural defects (arising due to growth-dependent crystalline quality). It is worth mentioning that the ratio of $Cu_2O$:CuO in S1 is 20% greater than that of S2 and S1 exhibits the presence of amorphous components of both CuO and $Cu_2O$ as well. Thus, in the present study, the most crucial factor responsible for the presence and absence of RS, in two-types of Cu-O films, can be attributed to different degrees of structural defects.

As mentioned above, S1 consists of more structural defects (as is seen from the calculated dislocation density and the presence of amorphous components of CuO and $Cu_2O$) in comparison to S2. It has been reported that, in case of a poor polycrystalline oxide material, oxygen vacancies can be present at non-lattice sites and be loosely bound in comparison to the lattice oxygen vacancies [25,26]. Following this argument, non-lattice oxygen vacancies can easily move at low electric field and give rise to the observed RS behavior. These oxygen vacancies can play a crucial role in the reset process by direct heating effect as well [28]. On the other hand, a better crystalline sample (viz. S2) has relatively lower defect density (and also a lesser resistivity) which is not expected to be mobile due to an applied electric field. Thus, such a sample is due to exhibit smooth conduction, as is seen in Fig. 5.3(e) [47]. Our results are well supported by the existing theoretical [47] model since according to the same, the RS behaviour is governed by defects.

### 5.1.4 Conclusions

In conclusion, the resistive switching (at room temperature) and the formation of conductive filament in an rf sputter deposited Cu-O thin film is demonstrated by cAFM and KPFM measurements. XRD is used to evaluate the crystalline quality, dislocation density, and the ratio of $Cu_2O$:CuO crystalline phase present in two-types of Cu-O specimen. We observe the resistive switching behaviour in a relatively poor crystalline film, whereas it disappears for the one having a better crystalline quality. These observations are explained on the basis of structural defect-dependent variation in the local carrier density and match well with the existing theoretical model based on the conducting filament formation. The present findings are not only useful for fundamental understanding of local electrical transport in Cu-O/Si heterostructures but also improve our knowledge for not only to design advanced nanoscale memory devices but also for an efficient solar cell.

# Bibliography

[1] S. H. Wee, P. S. Huang, J. K. Lee, and A. Goyal, Sci. Rep. 5 (2015) 16272.

[2] A. A. Ogwu, T. H. Darma, E. Bouquerel, J. Achiev. Mater. Manuf. Eng. 24 (2007) 172.

[3] I. Platzman, R. Brener, H. Haick, and R. Tannenbaum, J. Phys. Chem. C 112 (2008) 1101.

[4] H. Raebiger, S. Lany, and A. Zunger, Phy. Rev. B 76 (2007) 045209.

[5] http://repo.lib.nitech.ac.jp/bitstream/123456789/6200/1/ko2011_muhibbullah.pdf

[6] M. R. Johan, M. S. M. Suan, N. L. Hawari, H. A. Ching, Int. J. Electrochem. Sci., 6 (2011) 6094.

[7] J. Su, Y. Liu, M. Jiang, X. Zhu, arXiv: 1412.2031.

[8] F. K Mugwang, P. K. Karimi, W. K. Njoroge, O. Omayio, and S. M. Waita, Int. J. Thin Film Sci. Tec. 2 No. 1 (2013) 15.

[9] S. Ghosh, D. K. Avasth, P. V. Shah, V. Ganesan, A. Gupta, D. Sarang, R. Bhattacharya, W. Assmann, Vacuum 57 (2000) 377.

[10] J. S. Rossier, P. Bercier, A. Schwarz, S. Loridant, and H. H. Girault, Langmuir, 15 (1999) 5173.

[11] Y. S. Woo, D. Y. Jeon, I. T. Han, Y. J. Park, H. J. Kim, J. E. Jung, J. M. Kim, N. S. Lee, J. Vac. Sci. Technol. B 21 (2003) 1660.

[12] E. Linn, R. Rosezin, C. Kügeler, and R. Waser, Nat. Mater. 9 (2010) 403.

[13] B. R. Waser, R. Dittmann, G. Staikov, and K. Szot, Adv. Mater. 21 (2009) 2632.

[14] K. M. Kim, D. S. Jeong, and C. S. Hwang, Nanotech. 22 (2011) 254002.

[15] E. Meyer , H. J. Hug, and R. Bennewitz, Scanning Probe Microscopy: The Lab on a Tip. 2004: Springer, Berlin, 2004.

[16] B. Singh, D. Varandani, and B. R. Mehta, Appl. Phys. Lett. 103 (2013) 051604.

[17] J. Sun, Q. Liu, H. Xie, X. Wu, F. Xu, T. Xu, S. Long, H. Lv, Y. Li, L. Sun, and M. Liu Appl. Phys. Lett. 102 (2013) 053502.

[18] A. A. Ogwu and T. H. Darma, J. Appl. Phys. 113 (2013) 183522.

[19] Y. Du, A. Kumar, H. Pan, K. Zeng, S. Wang, P. Yang, and A. T. S. Wee, AIP Adv. 3 (2013) 082107.

[20] M. Lanza, K. Zhang, M. Porti, M. Nafrıa, Z. Y. Shen, L. F. Liu, J. F. Kang, D. Gilmer, and G. Bersuker, Appl. Phys. Lett. 100 (2012) 123508.

[21] G. S. Tang, F. Zeng, C. Chen, H. Y. Liu, S. Gao, S. Z. Li, C. Song, G. Y. Wang, and F. Pan, J. Appl. Phys. 113 (2013) 244502.

[22] A. Chen, S. Haddad, Y. C. Wu, Z. Lan, T. N. Fang, and S. Kaza, Appl. Phys. Lett. 91 (2007) 123517.

[23] S. Y. Wang, C. W. Huang, D. Y. Lee, T. Y. Tseng, and T. C. Chang, J. Appl. Phys. 108 (2010) 114110.

[24] J. W. Han and M. Meyyappan, AIP Adv. 1 (2011) 032162.

[25] L. Zhang, H. Y. Xu, Z. Q. Wang, H. Yu, X. N. Zhao, J. G. Ma, and Y. C. Liu Appl. Phys. Lett. 104 (2014) 093512.

[26] M. K. Yang, J. W. Park, T. K. Ko, and J. K. Lee Appl. Phys. Lett. 95 (2009) 042105.

[32] Nanotech: WSxM Program. [http://www.nanotec.es/products/wsxm/].

[33] M. Pelliccione, T. Karabacak, T. M. Lu, Phys. Rev. Lett. 96 (2006) 146105.

[34] C. A. Schneider, W. S. Rasband and K. W. Eliceiri, ImageJ: Nat. Methods 9 (2012) 671.

[35] S. Chatterjee, M. Kumar, A. Pal, I. Thakur and T. Som, J. Mat. Chem. C 3 (2015) 6389.

[36] W. Bollmann, Crystal Defects and Crystalline Interfaces. 1970: Springer, Berlin.

[37] K. Han, M. Tao, Sol. En. Mater. Sol. Cells 93 (2009) 153.

[38] J. W. Park, H. Jang, S. Kim, S. H. Choi, H. Lee, J. Kang, and S. H. Wei. J. Appl. Phys. 110 (2011) 103503.

[39] C. Zhu and M. J. Panzer, Chem. Mater. 26 (2014) 2960.

[40] L. Chen, T. M. Lu, and G. C. Wang, J. Appl. Phys. 112 (2012) 024303.

[41] M. Ohring, Materials Science of Thin Films: Deposition and Structure. 2002: Academic Press.

[42] M. Kumar, A. Kanjilal, and T. Som, AIP Adv. 3 (2013) 092126.

[43] T. Ungar, Scr. Mater. 51 (2004) 777.

[44] S. M. Sze and K. K. Ng, Physics of Semiconductor Devices. 2007: Wiley-Interscience, New York.

[45] J. Qi, M. Olmedo, J. Ren, N. Zhan, J. Zhao, J.-G. Zheng, and J. Liu, ACS Nano 6 (2012) 1051.

[46] B. Singh, B. R. Mehta, D. Varandani, Govind, A. Narita, X. Feng, and K. Mullen, J. Appl. Phys. 113 (2013) 203706.

[47] Assimos, J. A; Trivich, D. Phys. Stat. Solidi a 26 (1974) 477.

# CHAPTER 6

## 6. Study of the hole blocking behaviour in$TiO_2$ thin films

In the present work, the sandwich layer between the window (AZO) and the absorber (Cu-O) layers is $TiO_2$. Generally, $TiO_2$ is widely used in emerging technologies because it can prevent the shunting and leakage currents under reverse bias condition [1]. It shows the ability to selectively block the flow of holes (via valence band barrier). In fact, due to a mismatch in the band gaps, the band bending at the interface of $TiO_2$ and the coexisting layer is formed, which in turn blocks both the ionic and electronic charge carriers across the junction [2]. This property makes this material useful to augment or replace the traditional *p-n* junction to achieve similar effects [2]. Generally, for high efficiency solar cells, a wider *p-n* junction with a smooth band bending at the interface is required, although the design of the same is time consuming and costly. On the other hand, as mentioned above, the hole blocking behaviour depends on the band bending due to mismatch in the band gaps and thus, can have relatively thinner junction. However, the charge transport across $TiO_2$ its interfaces with other constituent layers of the cell is still not fully understood. In fact, it depends a lot on the film properties and thus, in this chapter, first we describe the growth of $TiO_2$ thin films and study their structural properties. Following this, we study the charge transport across $TiO_2$ films having an optimal thickness.

In this chapter, we investigate the growth of $TiO_2$ thin films using radio frequency (rf) sputter deposition technique. The as-prepared thin films are characterized by scanning electron microscopy, atomic force microscopy, x-ray diffraction, and x-ray photoelectron spectroscopy. Following this, using Kelvin probe force microscopy and temperature-dependent current-voltage characteristics, we study the charge transport across the $TiO_2$/Si heterojunction. In particular, the KPFM results show a variation in the work function on $TiO_2$ surface. On the other hand, temperature-dependent current-voltage characteristics depict a non-ideal hole blocking behavior. In addition, the measured barrier height is found to decrease with temperature and not following the thermionic emission theory, strongly suggesting an inhomogeneous nature of the interface. The observed result of barrier inhomogeneities is attributed to the interfacial disorders, arising due to the growth dynamics and corroborates well with the KPFM map. Further, as a main content of the present thesis, we go ahead to demonstrate that like $TiO_2$/Si, the $TiO_2$/Cu-O heterojunction also shows the hole blocking property.

## 6.1 Experimental detail

Thin films of $TiO_2$ were deposited at RT using an rf magnetron sputtering setup at normal and different oblique angles (viz. 45° and 87°) of incidence on *p*-type Si(100) (B-doped, resistivity of 0.01–0.02 Ω-cm) and soda lime glass substrates simultaneously. Before deposition, the substrates were ultrasonically cleaned in trichloroethylene, alcohol, acetone, and de-ionized water to remove the organic contaminants. Commercially available $TiO_2$ target (99.99%) of diameter 50 mm (Testbourne, UK) was used as the target material. The deposition chamber was evacuated to a base pressure of $5\times10^{-7}$ mbar. Sputtering was performed in pure Ar atmosphere at a pressure of $5\times10^{-3}$ mbar under an rf power of 100 W (Cesar, Advanced Energy system). The target-to-substrate distance was kept fixed at 80 mm. The deposition time was chosen in a way so that it yields the same film thickness for each angle, which was confirmed by thickness calibration using a surface profilometer (described earlier in section 2.2). Films having different thicknesses (in the range of 5-80 nm) were grown and during each deposition, the substrates were continuously rotated at a constant speed of 3 rpm. The nature of crystallinity of the films was investigated using the x-ray diffractometer with Cu-$K_\alpha$ radiation ($\lambda$=0.15418 nm). In addition, the compositional analysis was carried out using x-ray photoelectron spectroscopy. Detail microstructural analysis of the films were performed using a field emission scanning electron microscopy operated at 20 keV. Film morphologies were studied by *ex*-situ atomic force microscopy in the tapping mode. Root mean square (*rms*) surface roughness (*w*) was extracted using the WSxM software. KPFM studies were carried out in the tapping mode using conductive tips having a radius of curvature of ~30 nm, a stiffness of ~2 N $m^{-1}$, and a resonance frequency of ~70 kHz. For each sample, a large number of micrographs were collected from different regions to check the uniformity in the results.

Silver paste was used to make electrical contacts on top of the $TiO_2$ films and back side of the Si substrates. An indigenously developed sample holder assembly (having a heating stage), whose temperature was precisely controlled (±0.5 K) by a proportional-integral-derivative temperature controller and sensed by a Platinum resistance temperature detector (RTD, A-class) thermocouple, was coupled with a source meter to perform the temperature-dependent electrical studies [3]. The *I-V* data were recorded using a commercially available software (Lab-Tracer 2.0) during annealing (203-313 K) of the $TiO_2$/Si heterojunction in air. Following the similar experimental procedure, $TiO_2$ thin films were also deposited on Cu-O/Mo/Si substrate to study the hole blocking nature of the same.

## 6.2 Physical properties of $TiO_2$ thin films: Role of growth angle

Prior to the electrical measurements, $TiO_2$ films are analyzed by XRD, XPS, SEM, and AFM to look for a possible correlation between the charge transport and the structural properties as well as composition of the film. Fig. 6.1(a) presents XRD data of as-prepared $TiO_2$ films deposited at all three deposition angles (0°, 45° and 87°). The diffractograms (corresponding to the film thickness of 80±3 nm) do not show any peak, which indicate that as-prepared films are amorphous in nature in all three cases [4].

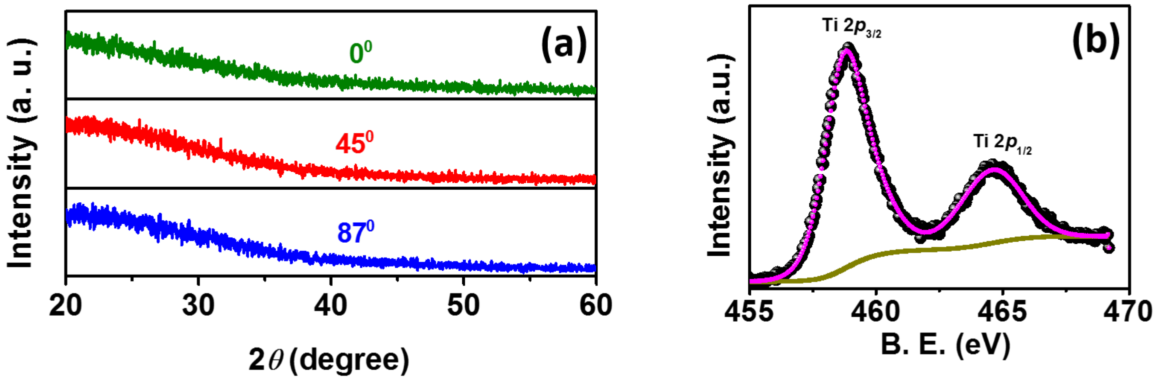

Figure 6.1: (a) XRD patterns of $TiO_2$ thin films sputter deposited at normal as well as oblique incidences. (b) XPS spectra of the Ti 2*p* line corresponding to the film (80 nm-thick) deposited at normal incidence.

On the other hand, Fig. 6.1(b) shows the XPS spectrum of Ti 2*p* line in which two main peaks, corresponding to the binding energies of 458.8 and 464.6 eV, are observed. The main peak at 458.8 corresponds to the Ti $2p_{3/2}$ for $Ti^{4+}$ in $TiO_2$ (458.6–459.2 eV), whereas the second peak can be due to the spin orbit coupling [5]. It is noted that the observed peaks are significantly different from the Ti $2p_{3/2}$ peak of $Ti^{2+}$ (454.9–455.2 eV) and $Ti^0$ (453.7–454.2 eV) states [5]. In addition, the calculated intensity ratio of the two peaks at 458.8 eV and 464.6 eV is 2.3:1, which is very close to the branching ratio of 2:1, expected for the 2*p* lines. Further, the difference between the two peaks is found to be 5.8 eV, which is more likely due to the spin-orbit splitting of $Ti^{4+}$ (5.5 eV) rather than the $Ti^0$ (6.2 eV) [5]. In fact, the XPS measurement confirms the presence of titanium dioxide on the surface of the Si substrate. Similar XPS results are also observed for $TiO_2$ thin films deposited at under the oblique angles geometries.

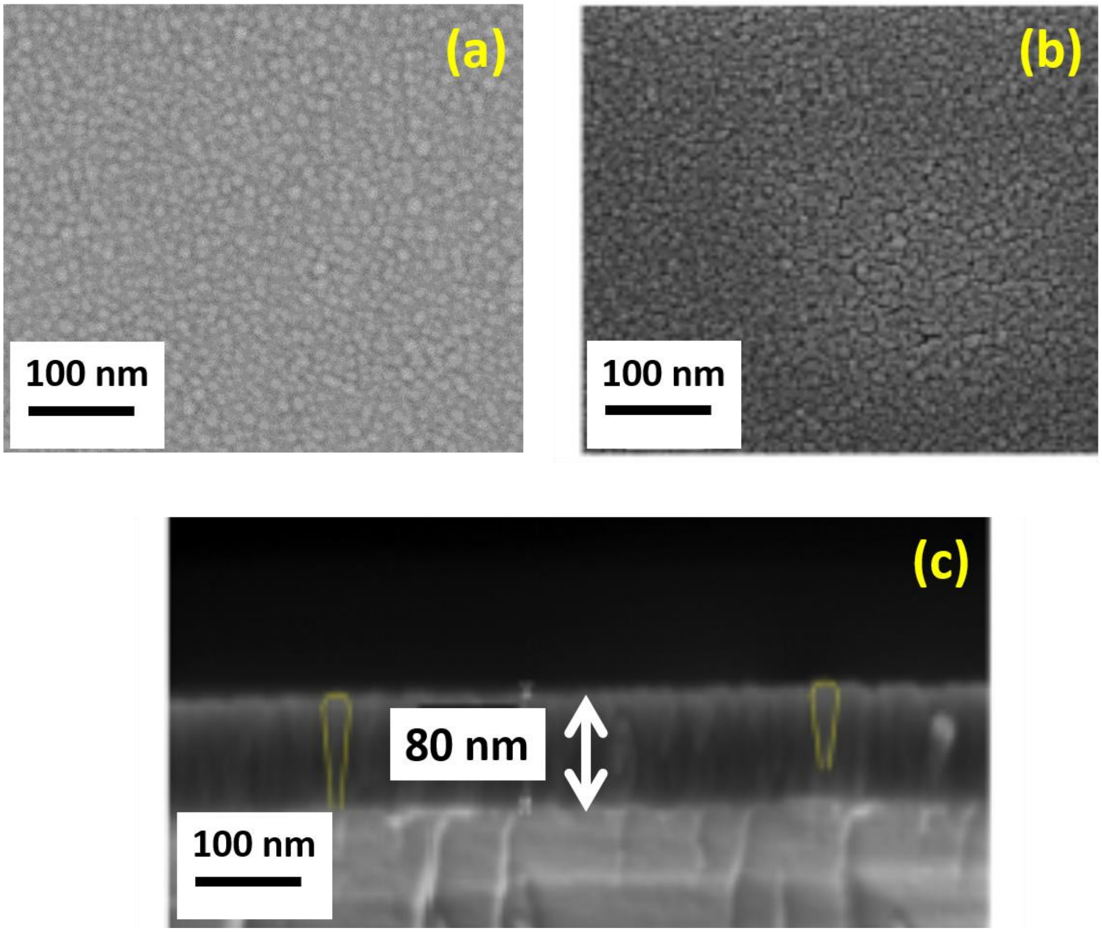

Figure 6.2: SEM images of $TiO_2$ thin films: (a) plan-view for deposition at 0°. (b) and (c) plan- and cross sectional-view, respectively for deposition at 87° where the columnar nanostructures are evident and marked by yellow lines.

Fig. 6.2 shows the SEM images which depict the angle-dependent change in the surface morphology. Figs. 6.2(a) and (b) are plan-view SEM micrographs corresponding to films deposited at 0° and 87°, respectively. In the case of normal incidence [Fig. 6.2(a)], a granular microstructure is observed and the film is largely uniform. In contrary, the film deposited at 87° shows the presence of porosity spreaded over the entire surface [Fig. 6.2(b)]. The cross-sectional view [Fig. 6.2(c)] of the same film (i.e. the one deposited at 87°) shows the presence of well-aligned nanocolumns of height 80-90 nm and width 15-20 nm. It is also seen that tips of the nano-structures are wider than their bases. This kind of widening of the top end compared to the base occurs due to the fast rotation of substrate applied during sputter deposition in glancing angle mode. In case of normal incidence (i.e. for 0°) no such nano-columnar structures is observed in the cross-sectional view (micrographs not shown).

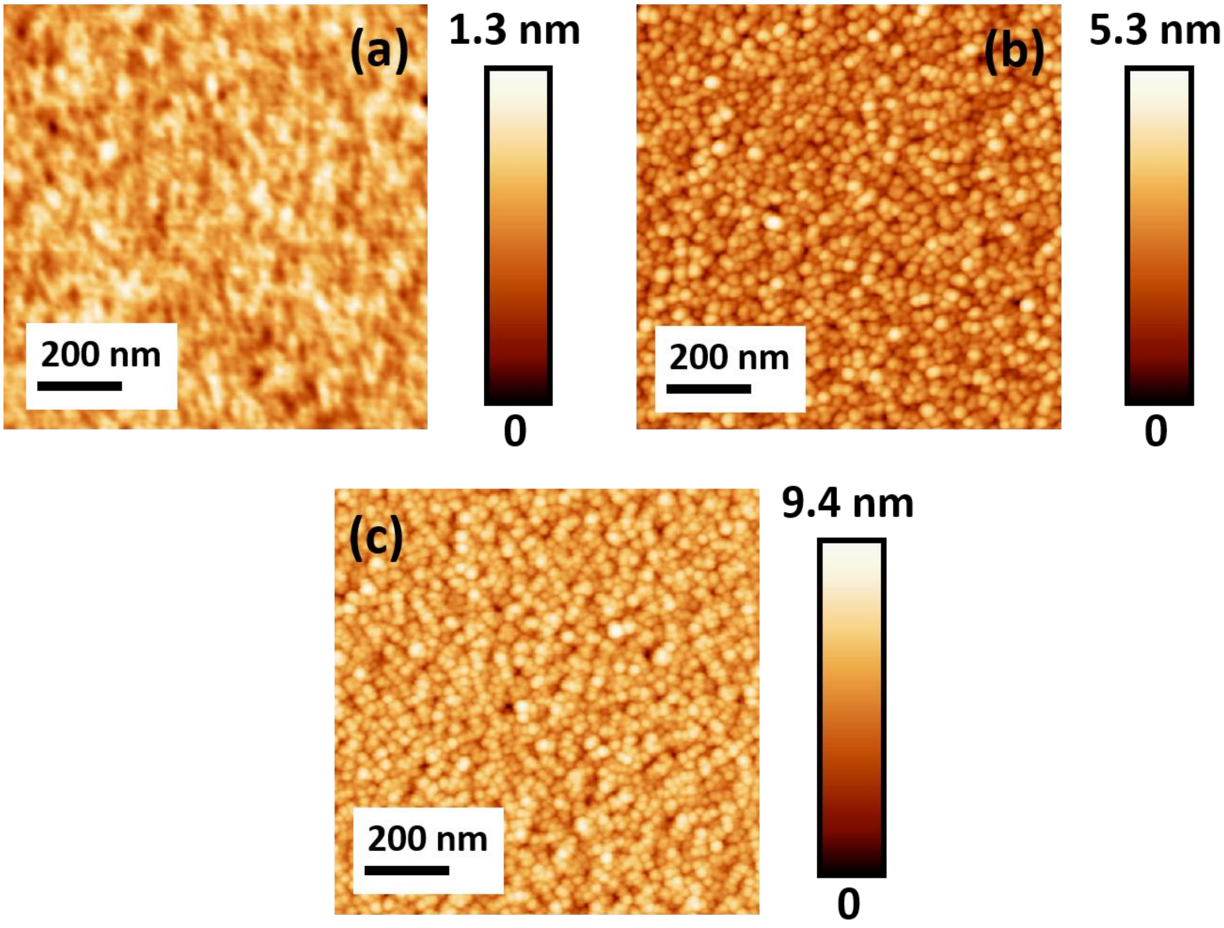

Figure 6.3: Surface morphologies of $TiO_2$ thin films sputter deposited at various angles: (a) 0°, (b) 45°, and (c) 87°, respectively.

Fig. 6.3 shows AFM images of the $TiO_2$ thin films deposited at incidence angles of 0°, 45°, and 87°. Fig. 6.3(a) presents an AFM image of the film corresponding to normally incident flux, which shows the presence of an ultra-smooth surface (surface rms roughness 0.10 nm). On the other hand, AFM images of films grown under incidence angles of 45° and 87° are shown in Figs. 6.3(b) and (c), respectively, which show granular microstructures. It is interesting to note that roughness value is the lowest for the deposition angle of 0° (0.10 nm), which increases to 0.57 nm for the deposition angle of 45°, and finally reaches 1.13 nm for the film deposited at 87°. This behavior can be realized as follows. As the deposition angle increases, the shadowing effect becomes more and more prominent and controls the granular morphology [6]. For instance, films grown at higher incidence angle show more porosity as well [4]. Surface roughness is known to play an important role in case of charge transport. In fact, a low interfacial roughness is desired to obtain a smooth charge transport across a device [7]. For the present study, the lowest roughness is found corresponding to the $TiO_2$ film deposited under normal indigence and thus, for further studies, we deal with the film grown under normal incidence to study the charge transport across it.

It is known that for an efficient hole blocking junction, a low reverse leakage (due to blocking of holes) and high forward current (due to a smooth flow of electrons) are desired [2]. Thus, in order to get an optimized hole blocking nature, various thicknesses of $TiO_2$ (e.g. 5, 20, and 80 nm) are deposited on Si substrates at normal incidence and study the charge transport across the same. It may be mentioned here that the heterojunction made with a 5 nm-thick $TiO_2$ layer shows a high reverse leakage current, while a low forward current is observed for the junction made by 80 nm-thick $TiO_2$ (data not shown). On the other hand, the junction made with a 20 nm-thick $TiO_2$ layer shows a low reverse leakage current and a smooth forward current and thus, for the further study, we will deal with 20 nm film thickness as the optimal one. In addition, it is mentioned that the 20 nm-thick films also show the lowest roughness (i.e. 0.1 nm).

## 6.3 $TiO_2$ hole blocking properties

Generally, electrical transport in a film depends on its work function and the carrier concentration. Thus, to understand the local electrical transport, we have undertaken KPFM studies for two-dimensional mapping of the work function of the optimized film. As discussed earlier, in such cases, mathematically, the work function of a sample ($W_{\text{sample}}$) is expressed as: $W_{\text{sample}} = W_{\text{tip}} -$

$qV_{\mathrm{CPD}}$ , where $W_{\mathrm{tip}}$, $q$, and $V_{\mathrm{CPD}}$ are work function of the tip, the electronic charge, and the contact potential difference, respectively [8]. Figs. 6.4(a) and (b) show the topography and the surface potential distribution, respectively. It is interesting to note that although the surface of the film is uniform and smooth (surface roughness of 0.10 nm), a variation (~30 meV) in the $V_{\mathrm{CPD}}$ is observed. Since, the work function of the tip is found to be 4.85 eV [measured with respect to a cleaned, highly ordered pyrolytic graphite, *(*HOPG)], the calculated work function of the $TiO_2$ film turns out to be 4.62±*0.2* eV which matches well with the existing report [8]. It is interesting to note that the measured nanoscale surface potential is found to be inhomogeneous throughout the mapped area [Fig. 6.4(b)].

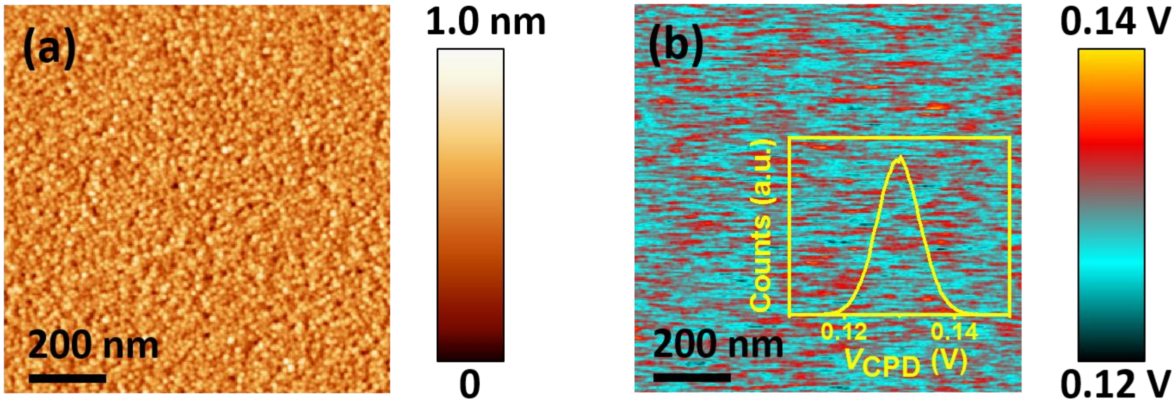

Figure 6.4: (a) AFM surface topography of a 20 nm-thick $TiO_2$ film deposited on the *p*-Si substrate and (b) KPFM map corresponding to (a).

In fact, the nanostructured film surface with blue contrasts correspond to a lower work function with respect to the adjacent areas and the maximum variation is found to be up to ~30 meV. It is interesting to note that this variation in the work function does not have any one-to-one correlation with the surface topography, confirming the role of growth dynamics. On the other hand, due to different electron affinities of the Pt-tip and the $TiO_2$ film, an electrostatic potential barrier is generated at the interface and for a uniform film, this is expected to remain spatially invariant, leading to a uniform value of the work function [8]. However, the observed variation in the work function indicates that some other factor may be responsible for the same. The existence of this inherent spatial inhomogeneity in $V_{CPD}$ value at the $TiO_2$ surface leads to a variation in the barrier height ($\Phi_b$), as is determined by carrying out the temperature-dependent *I*-*V* measurements.

Fig. 6.5(a) shows the *I*-*V* characteristics of an *n*-$TiO_2$/*p*-Si heterojunction at different temperatures, varying from 203 to 313 K, where all the *I*-*V* curves show a rectifying property. It is interesting to note that relatively low current flows corresponding to the negative applied bias in comparison to the positive one, indicating the blocking nature of holes [Fig. 6.5(a)]. It is evident from this figure that both the currents, viz. forward and reverse bias are not only dependent on the applied voltage but also on the sample temperature [3,8]. Generally, temperature-dependent charge transport is governed by thermally excited charge carriers and can be understood on the basis of thermionic emission (TE) model [9-10]. Mathematically, the TE model is written as follows: $I = I_s(T)\left[\exp\left(\frac{eV}{\eta k_B T}\right) - 1\right]$, where $V$ is the applied voltage, $k_B$ the Boltzmann's constant, and $\eta$ is the ideality factor. The $\Phi_{b0}$ is the zero bias barrier height and can be extracted from the extrapolation of $I_s$(T) in the semi-log forward bias ln(*I*)–*V* using the formula: $\Phi_{b0} = \frac{k_B T}{q}\ln(\frac{AA^*T^2}{I_s})$, where A is the diode area and A* is the effective Richardson constant of the semiconductor. Since, it is known that the ideality factor is a dimensionless parameter and it should be 1 for an ideal diode [10], any change in $\eta$ is related to the deviation from the standard TE theory. Here, ln(*I*)-*V* is used to calculated $\eta$ using the following formula: $\eta = \frac{q}{k_B T}\ [\frac{dV}{d\ln(I)}]$. In addition, the temperature-dependent forward bias ln(*I*)–*V* plots are depicted in Fig. 6.5(a), which remain linear at low voltages and deviate at the higher ones, which is likely due to the presence of series resistance [10].

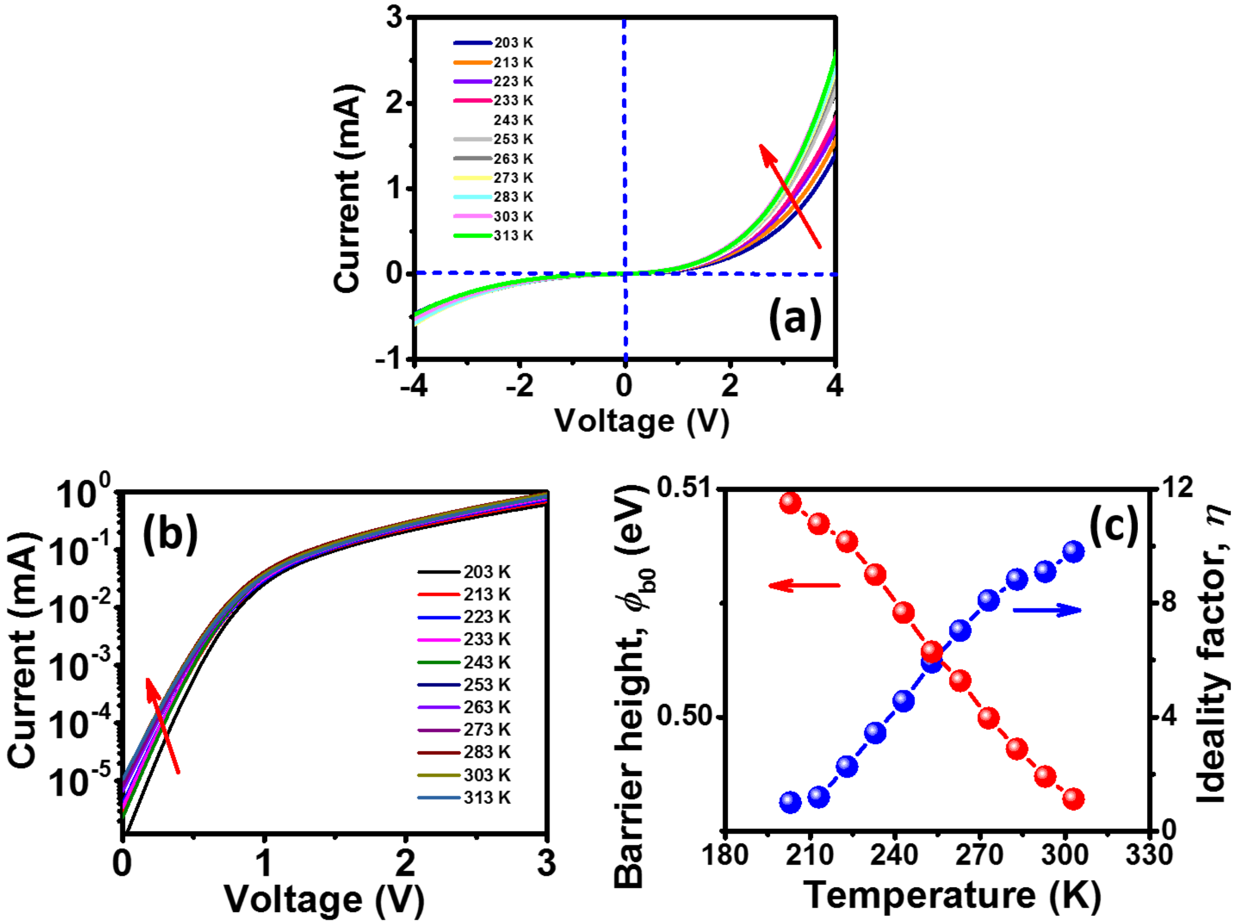

Figure 6.5: (a) Temperature-dependent current-voltage characteristics of $TiO_2$/Si junction, (b) the semi-log plot of the forward bias, and (c) variations in the zero bias barrier height and the ideality factor with temperature.

On the other hand, Fig. 6.5(b) shows the temperature-dependent zero bias Schottky barrier height (SBH), $\Phi_{b0}$, and the ideality factor, $\eta$. The calculated barrier height decreases with increasing temperature, while the ideality factor increases with the same. It is worth mentioning here that according to the TE theory, the barrier height and ideality factor should behave in different manners. For instance, the ideality factor should increase as $1/T$, although the observed results do not match with the TE theory, suggesting the presence of an inhomogeneous barrier height [10] at the $TiO_2$/Si interface. In the present case, the $TiO_2$ layer is grown by sputtering where, depending on the thermodynamic driving forces, isolated islands coalesce and form the film. Thus, due to the growth dynamics, the interfacial disorders get generated, which in turn give rise to an intrinsic inhomogeneity in the barrier height.

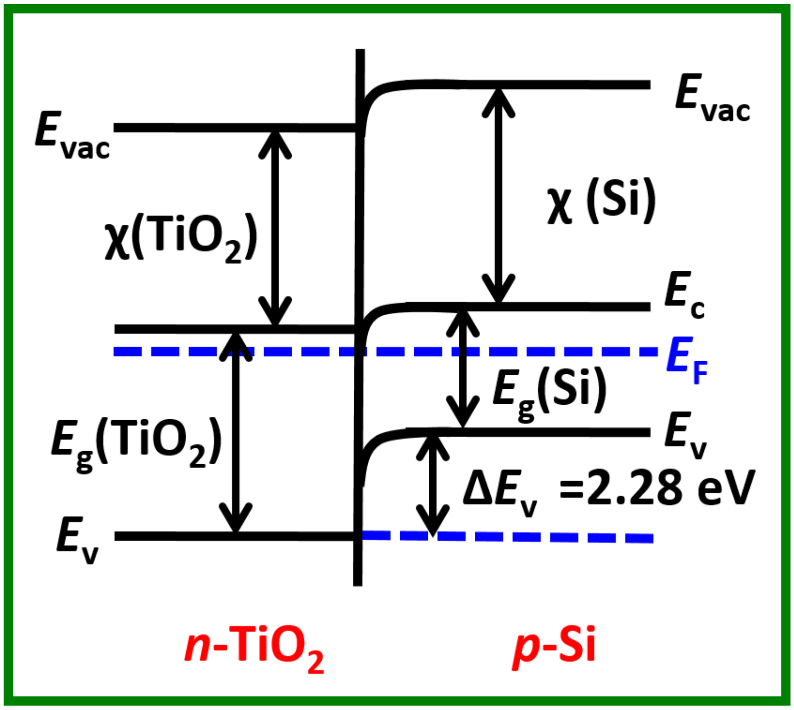

Figure 6.6: Schematic band diagram of $TiO_2$/Si heterojunction, indicating a large barrier ($\Delta E_v$) at the interface [11].

The hole blocking properties of a $TiO_2$/Si heterojunction can be understood on the basis of the schematic band diagram shown in Fig. 6.6. In fact, the conduction band edge (electron affinity, $\chi$) and valance band edge (ionization energy) are at about 4.30 eV and 7.45 eV below the vacuum level, respectively. On the other hand, the conduction band edge at about 4.05 eV and the valance band edge at about 5.17 eV of Si below the vacuum level, leads to the band gap energies ($E_g$) of $TiO_2$ and Si to be 3.15 eV and 1.12 eV, respectively. The energy barrier ($\Delta E_c$) for an electron is $\Delta E_c=\chi(TiO_2)-\chi(Si)=4.30-4.05=0.25$ eV, while the potential barrier ($\Delta E_v$) for a hole is: $\Delta E_v=E_g(TiO_2)+\Delta E_c-E_g(Si)=3.15+0.25-1.12=2.28$ eV (Fig. 6.6)[11]. As is seen form this figure, there is a large barrier at the valance band interface, which in turn blocks the transport of holes from silicon to the titanium dioxide layer. On the other hand, a small barrier in the conduction band would allow the transport of electrons from silicon to the titanium dioxide film. This interesting property opens up a new way to control the charge transport in an oxide solar cell. In the context of the present thesis work, the band gap of Cu-O ($E_g$~1.4 eV) is similar to that of Si and thus, it is expected that the $TiO_2$ layer should also show a hole blocking nature, if it is grown on Cu-O layer [12].

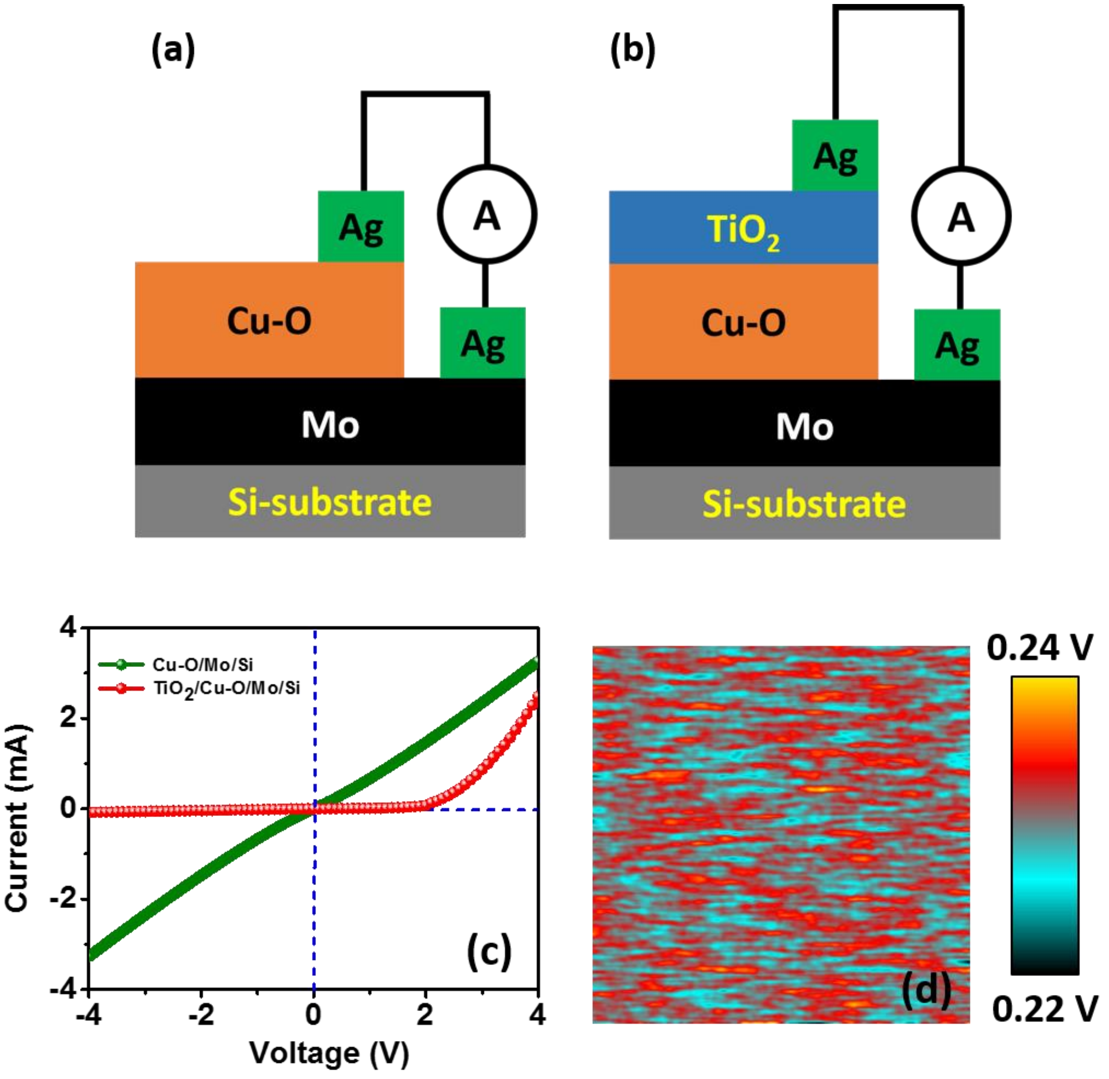

Figure 6.7: (a) and (b) depict the schematic representations of Cu-O/Mo/Si and $TiO_2$/Cu-O/Mo/Si heterostructures, respectively. (c) shows the current-voltage characteristics corresponding to (a) and (b). (d) KPFM map of the $TiO_2$ thin film deposited on Cu-O/Mo/Si heterojunction.

In fact, the hole blocking nature of $TiO_2$, deposited on a Cu-O layer, is also confirmed by studying the current-voltage characteristics at RT. In order to do so, two types of junctions (e.g. Cu-O/Mo/Si and $TiO_2$/Cu-O/Mo/Si) have been fabricated [Figs. 6.7 (a) and (b)]. It is interesting to note that the Cu-O/Mo/Si shows a nearly linear *I-V* characteristics, which is almost similar to that of an Ohamic nature of the Mo back contact and the top Ag contact [Fig. 6.7(c)]. The observed little deviation from the exact linear *I-V* characteristics can be due to different top and bottom contacts. In fact, both the contacts (top and bottom) have different work functions and thus, can give rise to this behaviour. On the other hand, a non-liner behaviour in current-voltage characteristics of the $TiO_2$/Cu-O/Mo/Si heterojunction is observed, which confirms the charge blocking nature of $TiO_2$ [Fig. 6.7(c)]. In fact, similar to the $TiO_2$/Si junction, Cu-O/$TiO_2$ interface also allows the conduction of electrons, while it blocks the flow of holes, although it is more prominent (reverse bias current: 500 μA) to that of $TiO_2$/Si heterojunction (reverse bias current: 80 μA). On the other hand, the variation in the work function for the $TiO_2$/Cu-O/Mo/Si heterojunction is also measured using KPFM, which is found to be inhomogeneous [Fig. 6.7].

## 6.5 Conclusions

We report here the growth of ultrathin $TiO_2$ films at RT on Si and glass substrates by rf magnetron sputtering. It is found that the surface roughness increases with increasing growth angle. Using Kelvin probe force microscopy and temperature-dependent current-voltage characteristics, we have studied the charge transport across the $TiO_2$/Si heterojunction. In particular, KPFM result shows a variation in the work function at the $TiO_2$ surface. In addition, the temperature-dependent current-voltage characteristics show an intrinsic non-ideal hole blocking behavior in the $TiO_2$ layer. The measured barrier height is found to decrease with temperature, strongly suggesting its inhomogeneous nature at the interface. Further, in the context of the present thesis work, the hole blocking nature of $TiO_2$ is also confirmed by depositing it on a Cu-O thin film. As a matter of fact, this study is very important, in particular for solar cell applications, because the hole blocking nature of $TiO_2$ will reduce the leakage current which in turn open a new avenue to design an efficient solar cell.

# Bibliography

[1] ] Y. N. Tan, C. L. Wong, A. R. Mohamed, Mater. Sci. 2011 (2011) 18.

[2] S. Avasthi, W. E. McClain, G. Man, A. Kahn, J. Schwartz, and J. C. Sturm, Appl. Phys. Lett. 102 (2013) 203901.

[3] M. Kumar, S. K. Hazra and T. Som, *J. Phys. D: Appl. Phys.* 48 (2015) 455301.

[4] S. Chatterjee, M. Kumar, S. Gohil, and T. Som, Thin Solid Films, 568 (2014) 81.

[5] T. Basu, M. Kumar, and T. Som, Mat. Lett. 135 (2014) 188.

[6] Y. P. Zhao, S. B. Chaney, S. Shanmukh, and R. A. Dluhy, J. Phys. Chem. B 110 (2006) 3153.

[7] A. Konar, T. Fang, N. Sun, and D. Jena, Phys. Rev. B 82 (2010) 193301.

[8] W. B. Nottingham, Thermionic Emission in Encyclopedia of Physics (Edited by S. Fliigge). 1956: Springer, Berlin.

[9] D. Tomer, S. Rajput, L. J. Hudy, C. H. Li, and L. Li, Appl. Phys. Lett. 105 (2014) 021607.

[10] D. Tomer, S. Rajput, L. J. Hudy, C. H. Li and L. Li, Nanotechnology 26 (2015) 215702.

[11] M. Perego, G. Seguini, G. Scarel, M. Fanciulli, and F. Wallrapp, J. Appl. Phys. 103 (2008) 043509.

[12] M. Heinemann, B. Eifert, and C. Heiliger, Phys. Rev. B 87 (2013) 115111.

# CHAPTER 7

# 7. Introduction

The back contact is an essential part of a solar cell and thus, in order to design an efficient solar cell, the optimization of the same is desired. This contact should have a low resistivity and high reflectivity such that it can not only helps flowing the charge carriers smoothly but also reflects the incident photons back into the absorbing layer. In the present chapter, first we will study the growth of molybdenum (Mo) thin film towards achieving the above mentioned properties. Following this, the optimized Mo thin film will be used as a back contact to grow other necessary overlayers. In addition, we present the structural and charge transport properties of the full solar cell structure chosen in this work.

## 7.1 Growth of low resistive and highly reflective Mo thin films

### 7.1.1 Introduction

Mo thin films show high stability and good electrical conductivity and are thus, considered to be better suitable for making electrical contacts in different nano-electronics applications, compared to other materials [1]. In addition, Mo is also used as a back electrode for solar cell applications where it is used not only as a conducting layer but also as a reflecting mirror [2]. As discussed earlier, using oblique angle deposition, tunable structural properties, surface reflection, and electrical transport properties have been demonstrated for large number of materials, including metals and semiconductors [2-8]. However, to the best of our knowledge, a systematic study of structural, electrical, and optical properties of molybdenum thin films, deposited at oblique angles, is still lacking.

In this study, we investigate on tunable structural, optical, and electrical properties of radio-frequency (*rf*) sputter-deposited Mo thin films by changing the growth angle during deposition. The surface morphology of Mo thin films is studied by atomic force microscopy (AFM) which shows an enhancement in the grain size and root mean square (rms) roughness with increasing angle of deposition. Since the surface morphology is known to play a crucial role in controlling the refractive index and charge transport, we have measured the surface reflectance and resistivity of these films. In fact, as a novelty, we show that the film deposited under the normally incident flux can be used as a good reflecting surface with a very low resistivity, leading to its use as a back contact.

### 7.1.2 Experimental

Molybdenum films of 500 nm thickness, measured by a surface profilometer, were deposited on ultrasonically cleaned soda lime glass substrates at room temperature (RT) using *rf* magnetron sputtering technique. Commercially available (Testbourne) 99.99% pure Mo target (50.8 mm dia.×6.35 mm-thick) was used for deposition. The deposition was carried out at $0^0$, $20^0$, $65^0$, and $85^0$ angles of incidence (with respect to the surface normal). Ultra-pure (99.999%) argon gas was injected into the chamber with a flow rate of 30 sccm to maintain the working pressure of $5\times10^{-3}$ mbar during sputtering. An *rf* power of 100 W (frequency = 13.56 MHz) was supplied to the target and the substrate was rotated with a speed of 3 rpm to achieve uniform film thickness, where the target-to-substrate distance was 80 mm. Surface morphology of Mo films were examined by *ex-situ* AFM studies in tapping mode using a silicon tip. For each sample, several images were taken from different randomly chosen regions to check the uniformity of the films. WSxM software was used for AFM image analysis [9]. The optical reflectance measurements were carried out using a UV-Visible spectrophotometer in the wavelength range of 300 to 800 nm with unpolarized light. The angle-dependent variation in resistivity was measured by the linear four-probe technique using a source meter.

### 7.1.3 Results and discussion

Figs. 7.1(a)-(d) show AFM images of all four samples, exhibiting a gradual change in the surface morphology with increasing deposition angle. Fig. 7.1(e) depicts the variation in average grain size and rms roughness as a function of deposition angle. It becomes evident that rms surface roughness and average grain size increase monotonically with increasing oblique angle of deposition [Fig. 1(e)]. In fact, as the deposition angle increases, the shadowing effect becomes more and more prominent, which in turn controls the surface morphology [3,4,7]. Besides investigating the topographical evolution of Mo films, as a function of deposition angle, the growth of 3D nano-columnar structures of the films is also confirmed from the corresponding cross-sectional scanning electron microscopic (XSEM) images [Figs. 7.2(a) and (b)], for films grown at $0^0$ and $85^0$, respectively. It may be noted that the film deposited at normal incidence has closely packed granular nanostructures, which transforms into a well-defined columnar nanostructures.

Figs. 7.3(a)-(c) show the x-ray diffraction patterns obtained from the Mo thin films, grown under normal as well as oblique incidences, depicting a strong peak at 40.6°. In fact, the phase identification reveals a *bcc* crystal structure with a very strong [110] preferential orientation, which is along the direction normal to the substrate. It is interesting to note that the peak becomes quite narrow and its position shifts towards a higher $2\theta$-value (viz. 44°) for the film grown at 85°, which can be attributed to much bigger grain size and a large compressive strain arising from the tilting of the columnar nanostructures (by 12.5°), respectively [7].

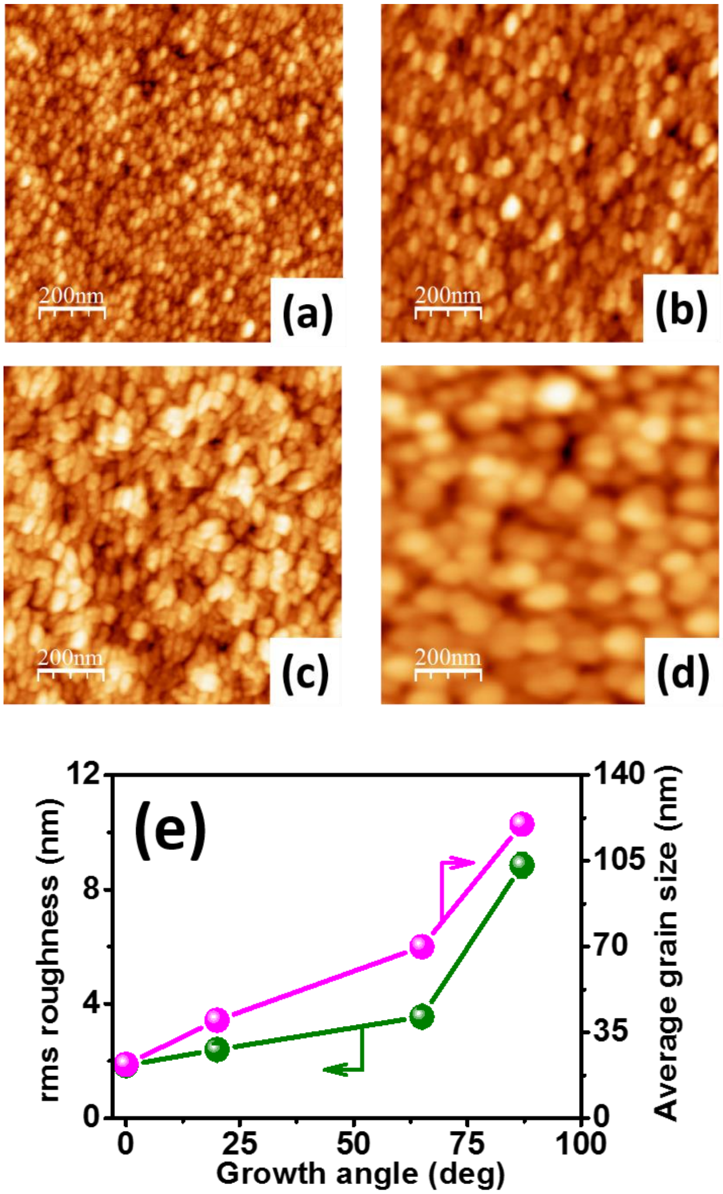

Figure 7.1: AFM images of Mo films grown at different angles: (a) $0^0$, (b) $20^0$, (c) $65^0$, and (d) $85^0$ with the individual height scale of 14, 16, 22, and 73 nm, respectively. (e) Variations in the rms roughness and average grain size with angle of deposition.

Since the charge transport in a material depends on the surface roughness, *I*-*V* characteristics are recorded under similar conditions. Fig. 7.4(a) shows the *I*-*V* plots for all the films measured by the linear four-probe technique. Note that, the linear variation in the *I*-*V* characteristics of Mo films confirms the Ohmic nature of the contacts, and hence, the slope of these *I*-*V* characteristics gives rise to the sheet resistance of the films.

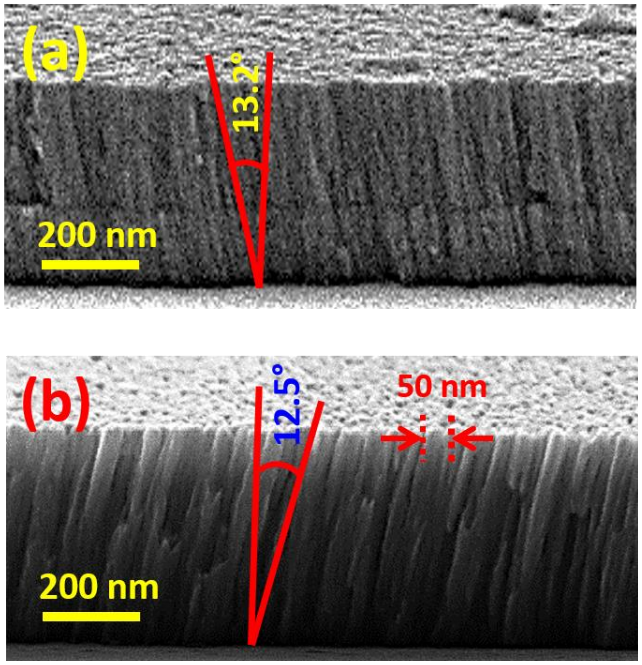

Figure 7.2: (a) and (b) Show the cross-sectional SEM images of the film grown at 0$^0$ and 85$^0$, respectively.

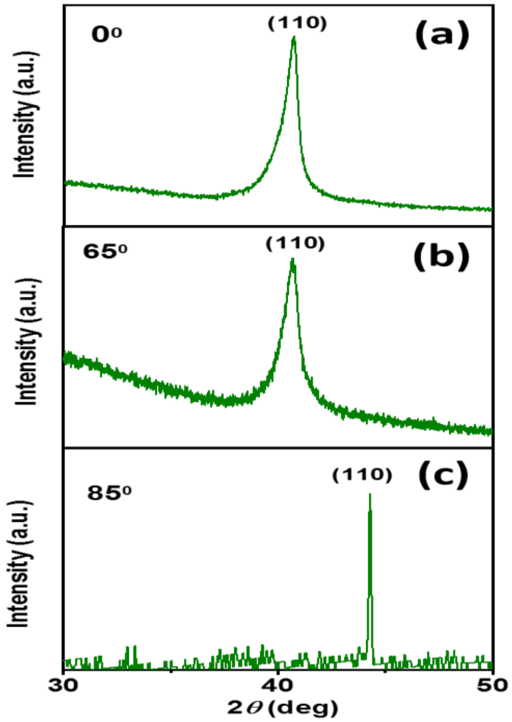

Figure 7.3: (a), (b), and (c) show the XRD patterns of Mo films grown under different angles.

Interestingly, a systematic variation in the resistance is observed for all of them. In fact, the resistance increases by nearly an order of magnitude for the film grown at $20^0$ in comparison to the one grown under normal incidence. A similar enhancement takes place in the resistivity when one compares the cases of $65^0$ and $85^0$. For instance, the resistivity of these films from $7.9\times10^{-6}$ to $1.4\times10^{-6}$ to $7.5\times10^{-5}$ to $8.1\times10^{-4}$ Ω-cm for growth angles of $0^0$, $20^0$, $65^0$, and $85^0$, respectively.

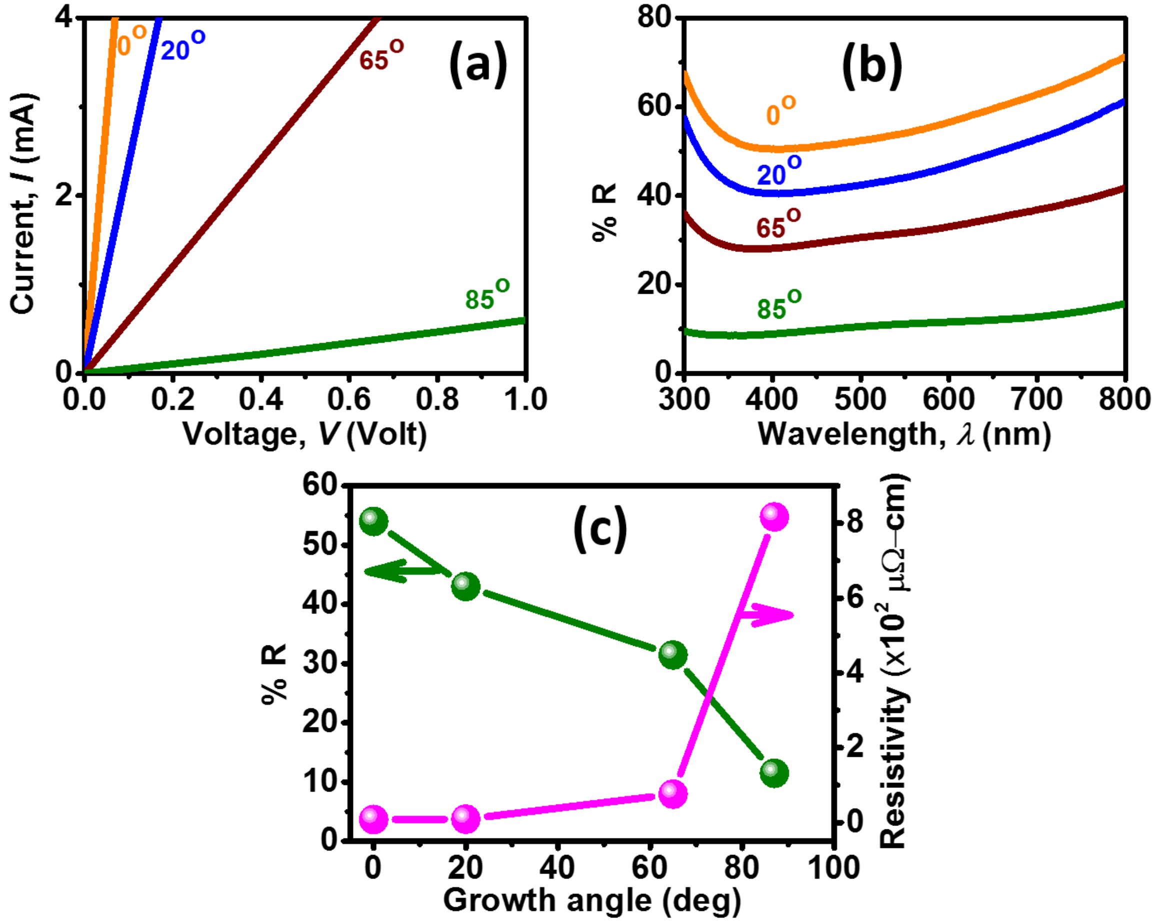

Figure 7.4: (a) *I-V* characteristics and (b) surface reflectance of Mo films grown at different angles. Angle-dependent variations in surface reflectance (at 400 nm) and resistivity of Mo films are shown in (c).

It is clear that the resistivity increases by two orders of magnitude due to an increase in the growth angle from $0^0$ to $85^0$. Such a large change can be attributed to a variation in the porosity as well as surface roughness of the films with increasing deposition angle [6,7,10]. Porosity of thin films is known to govern not only the charge transport in the films but also has a bearing on the optical reflectance spectra [6,11]. In fact, reflectance of a film is inversely proportional to the porosity [7]. Fig. 7.4(b) shows the reflectance spectra of Mo films deposited at different angles. A careful observation of these reflectance spectra reveals that the local reflectance minimum of each spectrum appears at 400 nm. It is also observed that the reflectance decreases in a sequential manner with increasing angle of deposition. As a matter of fact, the calculated average residual surface reflectance of the films (deposited at $20^0$, $65^0$, and $85^0$) reduces by 20%, 42%, and 80%, respectively with respect to the one deposited under normal incidence, which can be attributed to the presence of porosity in the films.

### 7.1.4 Conclusions

In this section, the tunability of microstructural, electrical, and optical properties of *rf* sputter-deposited Mo films, by changing the growth angle, has been demonstrated. Atomic force microscopy measurements show an increase in the average grain size and rms roughness with the angle of deposition. A sequential increment in the resistivity and decrement in the reflectance is observed with an increase in the growth angle. Thus, in the context of the present thesis work, it is found that the film grown under normal incidence shows the lowest resistivity ($7.9\times10^{-6}$ Ω-cm) and the highest average reflectance (~65%) and has been used to deposit several overlayers (included active one) to construct a copper oxide-based solar cell (as described below).

## 7.2 An efficient hole blocking copper oxide-based solar cell

### 7.2.1 Introduction

Generally, a *p-n* junction is needed to design a solar cell where the *p*-type material works as an absorber and the *n*-type material generates an electric field at the junction which can be used to separate out the electron-hole pairs [12]. In particular, for a Cu-O based solar cell, it is very difficult to achieve a high efficiency because of the difficulty in obtaining a suitable *n*-type semiconductor as well as the chemical instability of the $Cu_2O$ surface [13]. In the present scenario, Avasthi *et al*. have shown a new concept of holes blocking solar cell [14]. In fact, they have demonstrated that the $TiO_2$ thin film shows the ability to selectively block the flow of holes (via valence band barrier). Due to a mismatch in the band gaps, the band bending at the interface of $TiO_2$ and the coexisting layer is formed, which in turn blocks both the ionic and electronic charge carriers across the junction [14]. This property makes this material useful to replace a traditional *p-n* junction to achieve similar effects [14]. As described in the previous chapter, a $TiO_2$/Cu-O heterostructure shows a better hole blocking property in comparison to that of a $TiO_2$/Si heterostructure and thus, can be used to design an efficient solar cell. However, to the best of our knowledge, the construction of a hole blocking Cu-O based solar cell deposited at room temperatures is still lacking.

In this study, the structural properties of individual as well as the full solar cell is studied using SEM, EDX, and XRD. In particular, SEM images of the individual layers show granular structures, while their crystalline nature is confirmed by XRD. We also investigate the current-voltage (*I-V*) characteristics (in dark) of an Al-doped ZnO (AZO) and Cu-O heterostructure, fabricated without $TiO_2$ layer, which shows a high leakage current. In contrast, a significant reduction in the leakage current is noticed after introducing a $TiO_2$ layer between the AZO and Cu-O layers, confirming the hole blocking nature of the same. Finally, it is found that the AZO/$TiO_2$/Cu-O/Mo/Si heterostructure solar cell shows an eight times higher efficiency compared to the AZO/Cu-O/Mo/Si heterostructure.

### 7.2.2 Experimental

Cu-O, $TiO_2$, and AZO thin films having optimal thickness values were deposited sequentially on ~400 nm-thick Mo-coated Si substrate at room temperature using a magnetron sputtering system. As described earlier, commercially available 99.99% pure targets of $Cu_2O$, $TiO_2$, and $ZnO:Al_2O_3$ (2 wt.%) were used to deposit 120 nm-thick AZO, 20 nm-thick $TiO_2$, and 600 nm-thick Cu-O layers in a sequential manner. We also constructed a cell configuration having similar thicknesses but without having a $TiO_2$ layer. For each deposition, ultra-pure (99.999%) argon gas was injected into the chamber with a flow rate of 30 sccm to maintain the working pressure of $5\times10^{-3}$ mbar during sputtering. An *rf* power of 100 W was applied for $Cu_2O$ and $TiO_2$ targets, while a pulsed dc power of 100 W (frequency=150 kHz, reverse time=0.4 µs) was put on the AZO target. The substrates (kept at a fixed target-to-substrate distance of 8 cm) were rotated at a speed of 3 rpm to achieve uniform film thickness values. We have also used separate substrates to grow individual layers, which were taken out after the growth of each layer. In addition, separate substrates were also used to grow Mo/Si, Cu-O/Mo/Si, and $TiO_2$/Cu-O/Mo/Si multilayers.

Change in microstructures after each deposition was monitored by a field emission gun scanning electron microscopy (FEGSEM) in the plan- and cross sectional-view geometries using 5 keV electrons. FEGSEM-based energy dispersive x-ray (EDX) spectrometric analysis was performed for compositional analysis of the AZO/$TiO_2$/Cu-O/Mo/Si heterostructure. The crystallinity and phase identification of the used layers were performed by x-ray diffraction (XRD) studies using the Bragg-Brentano geometry and the Cu-$K_\alpha$ radiation ($\lambda$=0.1548 nm). Silver paste was used to make electrical contacts on top of the AZO layer and the Mo back contact. The *I-V* data were recorded using a commercially available software (Lab-Tracer 2.0).

### 7.2.3 Results and discussion

In order to look for a possible correlation between the charge transport and structural properties of different layers in both the heterostructures, SEM, EDX, and XRD studies are carrier out. Fig. 7.5(a) shows a schematic diagram of the studied solar cell. Figs. 7.5(b)-(e) show the plan-view SEM images of Mo/Si, Cu-O/Mo/Si, $TiO_2$/Cu-O/Mo/Si, and AZO/$TiO_2$/Cu-O/Mo/Si, respectively. It is observed that the Mo film deposited on a Si substrate [Fig. 7.5(b)] shows elongated granular structures with an average grain size of 35 nm, while after the growth of Cu-O layer on top of it, spherical grains are observed (average grain size of 30 nm) [Fig. 7.5(c)]. On the other hand, no significant change in the topography (apart from a little enhancement in the grain size) is noticed after $TiO_2$ deposition on top of Cu-O/Mo/Si and this can be attributed to a low thickness of the same. It is interesting to note that the grain size increases further after the growth of AZO layer on top of $TiO_2$/Cu-O/Mo/Si substrate. However, no other drastic change in the surface topography is observed even after the deposition of AZO thin film on top of, confirming the conformal nature of growth. Besides investigating the topographical evolution, the growth of solar cell structures using different layers is also confirmed from the corresponding cross-sectional scanning electron microscopic (XSEM) images. Fig. 7.6(a) shows a XSEM image of the film deposited on the Si substrate. The XSEM image not only confirms the intended thicknesses of the grown layers but also shows the formation of microstructures with in these films. On the other hand, Fig. 7.6(b) shows magnified view of the AZO/$TiO_2$/Cu-O interface. The elemental composition of the heterostructure is studied by EDX spectrometric analysis, which clearly shows the presence of Zn, Cu, Ti, and O but the absence of Al (due to its very low concentration) or any other metallic impurity in the film. An EDX spectrum corresponding to the heterostructure grown on the Si substrate is depicted in Fig. 7.6(c).

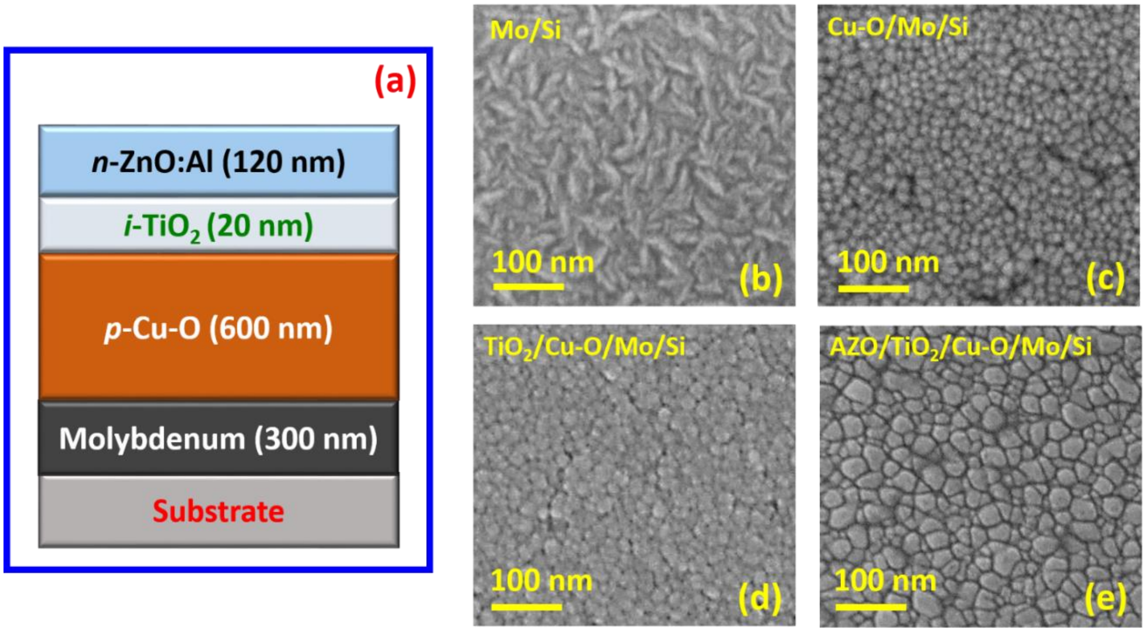

Figure 7.5: (a) Schematic diagram of the full solar cell configuration, (b)-(e) present the plan-view SEM images of Mo deposited on Si, Cu-O deposited on Mo/Si, $TiO_2$ deposited on Cu-O/Mo/Si, and AZO deposited on $TiO_2$/Cu-O/Mo/Si substrate, respectively.

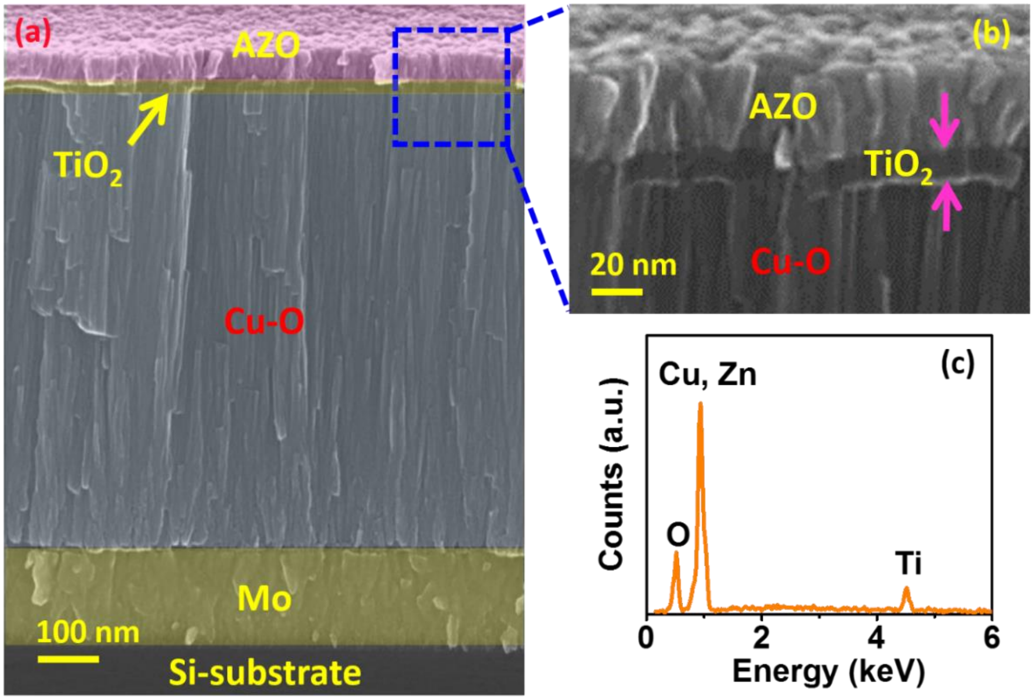

Figure 7.6: (a) XSEM image of the complete hole blocking solar cell where various colour corresponds to the different layers, viz. bottom yellow: Mo, light blue: Cu-O, yellow on top of Cu-O: $TiO_2$, and light magenta: AZO. (b) Magnified part of (a), and (c) present the EDX spectrum collected from (b).

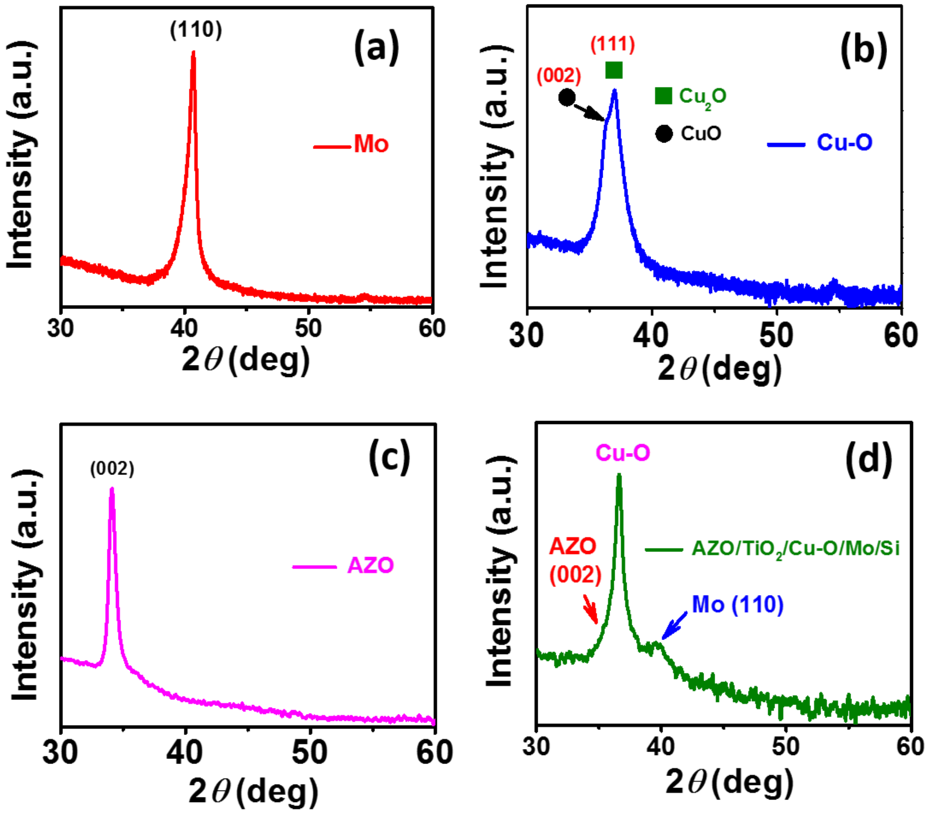

Figure 7.7: (a)-(c) XRD plots of Mo, Cu-O, AZO individual layers deposited on Si substrate, respectively. (d) Represents the XRD plot of full solar cell.

It is well-known that the carrier density available for electrical transport in a material strongly depends on its crystallinity. The XRD spectra of the individual layer as well as the whole AZO/$TiO_2$/Cu-O/Mo/Si cell configuration are recorded under similar conditions to confirm the phase and crystalline nature of the films (i.e. AZO, $TiO_2$, Cu-O, and Mo). Fig. 7.7(a) shows the x-ray diffractogram obtained from the Mo thin film, depicting a strong peak at $2\theta$=40.6° corresponding to this peak, the phase identification reveals a *bcc* crystal structure with a very strong (110) preferential orientation along the direction normal to the substrate. On the other hand, $TiO_2$ film turns out to be amorphous in nature (diffractogram not shown) [7]. Fig. 7.7(b) represents the XRD pattern corresponding to the Cu-O layer, exhibiting one prominent peak which is deconvoluted into two peaks: one is assigned to the CuO (002) reflection and the other one is assigned to $Cu_2O$ (111) [15]. Further, Fig. 7.7(c) shows the XRD pattern of the AZO layer which confirms the crystalline nature of the film. In this case, the dominant peak at $2\theta$=34.1° can be attributed to the (002) reflection of hexagonal wurtzite structure, indicating the formation of highly oriented grains along the *c*-axis. It may be mentioned that no signature of Al or $Al_2O_3$ is observed in the films [15]. The XRD spectra of the full solar cell configuration is depicted in Fig. 7.7(d) where a combination of all possible peaks are observed. Similar XRD lines are observed for the AZO/Cu-O/Mo/Si heterojunction (plot not shown to maintain the clarity).

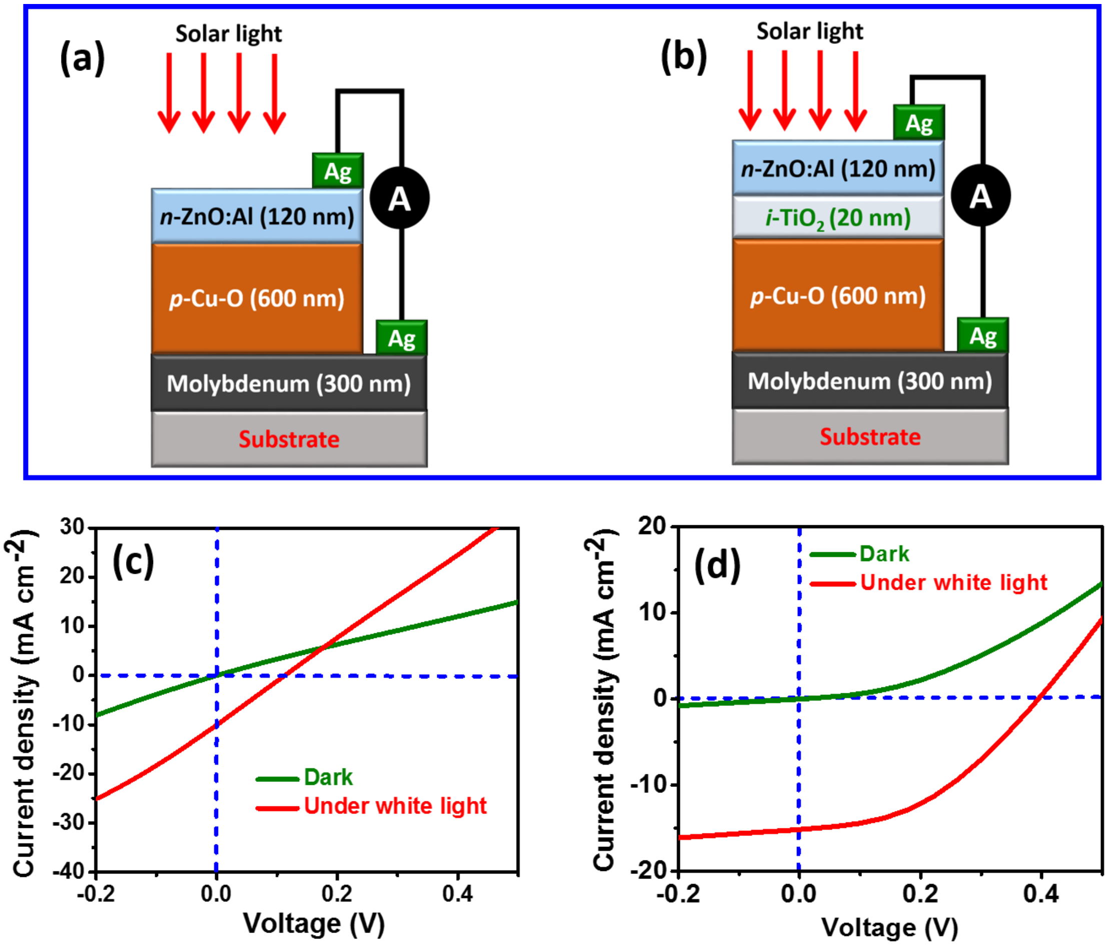

Figure 7.8: (a) and (b) Represent the schematic diagrams of solar cells built up with and without $TiO_2$ sandwich layer, respectively. The *I-V* characteristics under dark and white light conditions corresponding to (a) and (b) are depicted in (c) and (d), respectively.

The hole blocking nature of the $TiO_2$ layer is confirmed by making two types of heterostructures viz. AZO/Cu-O/Mo/Si and AZO/$TiO_2$/Cu-O/Mo/Si [Figs. 7.8(a) and (b)]. The I-$V$ characteristics (under dark and white light) of both types of junctions are presented in Figs. 7.8(c) and (d), respectively (olive color). It is interesting to note that a high reverse leakage current is observed for the configuration without $TiO_2$ [olive color, Fig. 7.8(a)], while it turns out to be very low after introducing the same [Fig. 7.8(b)], confirming the hole blocking nature. In the similar way, the behaviour of photocurrent is also observed.

To evaluate the performance of such simplistic solar cells, photocurrent density-voltage characteristics of both the heterojunctions, under white light illumination of 100 mW $cm^{-2}$, are performed [Figs. 7.8(c) and (d)]. These plots indicate that light absorption takes place in both the cells, leading to the formation of electron-hole pairs and in turn the generation of photocurrent. Following this, the cell configuration in (a) shows an open-circuit voltage ($V_{oc}$) of 0.11 V and a short-circuit current ($I_{sc}$) of 10 mA $cm^{-2}$. Subsequently, the fill factor (FF) and the power conversion efficiency (or cell efficiency) of this cell are found to be 43% and 0.58%, respectively. On the other hand, for the hole blocking cell configuration shown in (b), both $V_{oc}$ and $I_{sc}$ get enhanced and are found to be 0.4 V and 15 mA $cm^{-2}$, respectively which correspond to a cell efficiency of ~5.2%. It is interesting to note that comparatively the FF (68%) does not increase much, albeit the efficiency increases by a factor of nine in comparison to the cell based without $TiO_2$. This enhancement in the cell efficiency can be attributed to the hole blocking nature of the $TiO_2$ layer. For instance, when light falls on the heterojunctions, both the generation and recombination of electron-hole pairs take place. $TiO_2$ layer in between the AZO and Cu-O layers reduces the flow of holes, while it allows the movement of electrons and in turn reduces the recombination rate, resulting in an improvement in the cell efficiency.

### 7.2.4 Conclusion

In summary, two types of heterojunction solar cell viz. AZO/Cu-O/Mo and AZO/$TiO_2$/Cu-O/Mo have been grown and studied their charge transport properties. In is observed that the heterostructure grown with $TiO_2$ sandwich layer between AZO and Cu-O shows a much higher efficiency in comparison to without the same. The observed results is attributed to the hole blocking nature of $TiO_2$.

## Bibliography

[1] H. M. Latuske and T. P. Drusedau, Phys. Rev. B 58 (1998) 10933.

[2] X. Jiao, J. Yang, R. Zhang, N. Zhang, H. Zhong, Y. Shi, Mat. Lett. 124 (2014) 318.

[3] M. M. Hawkeyea and M. J. Brett, J. Vac. Sci. Tech. A 25 (2007) 1317.

[4] M. T. Taschuk, M. M. Hawkeye, M. J. Brett, P. Martin (Eds), Handbook of Deposition Technologies for Films and Coatings: Science, Applications and Technology (3rd Edition), 2010: William Andrew (Elsevier, Oxford).

[5] J. B. Sorge, A. C. Popta, J. C. Sit, and M. J. Brett, Opt. Exp. 14 (2006) 10550.

[6] J. Q. Xi, M. F. Schubert, J. K. Kim, E. F. Schubert, M. Chen, S. Y. Lin, W. Liu, and J. A. Smart, Nat. Photo. 1 (2007) 176.

[7] S. Chatterjee, M. Kumar, S. Gohil, and T. Som, Thin Solid Films 568 (2014) 61.

[8] M. Kumar and T. Som, Nanotechnology 26 (2015) 345702

[9] http://www.nanotec.es/products/wsxm/index.php.

[10] F. C. Hsu, V. N. Prigodin and A. J. Epstein, Phys. Rev. B 74 (2006) 235219.

[11] A. Ghosh, P. Kant, P. K. Bandyopadhyay, P. Chandra, O.P. Nijhawan, Infr. Phys. and Tech. 40 (1999) 49.

[12] M. H. Kang, K. Ryu, A. Upadhyaya, and A. Rohatgi, Prog. Photovolt: Res. 19 (2011) 983.

[13] Y. Abdu, A.O. Musa, J. Pure Appl. Sci. 2 (2009) 8

[14] S. Avasthi, W. E. McClain, G. Man, A. Kahn, J. Schwartz, and J. C. Sturm, Appl. Phys. Lett. 102 (2013) 203901.

[15] D. Tomer, S. Rajput, L. J. Hudy, C. H. Li and L. Li, Nanotechnology 26 (2015) 215702.

[16] M. Kumar, A. Kanjilal, and T. Som, AIP Adv. 3 (2013) 092126.

# CHAPTER 8

## 1. Summary and future scope

In summary, we have carried out extensive experimental investigations on the growth and characterization of individual layers as well as copper oxide-based full solar cell. As a starting point, we have deposited AZO films at different growth angles (using pulsed dc magnetron sputtering) at room temperature and demonstrated that the optoelectronic properties of AZO films can be tuned by varying the growth angle. The observed grain growth with increasing deposition angle is confirmed from the SEM and XRD results. In addition, optical transmittance of the AZO films, in the visible region, is found to be more than 80% and a blue shift is also observed till the growth angle of 70°. Further, we have demonstrated that low resistive films ($5.6\text{-}4.3\times10^{-3}$ Ω-cm) can be obtained for the growth angle between 50° to 70°. A continuous change in the work function with the growth angle is also observed, which becomes the highest (4.78 eV) corresponding to 50°. Thus, the AZO film, grown at 50° shows the best optimized physical properties to use it as a transparent conductive contact to the construct the solar cell in the present study.

Following this, we have varied the AZO film thicknesses at 50° angle of deposition on SLG and *p*-Si substrates and performed temperature-dependent *I*-*V* studies. *I*-*V* characteristics of *n*-AZO/*p*-Si heterojunction diodes, at different temperatures, reveal unusual behaviour, which is correlated with the temperature-dependent resistivity of the AZO film deposited on the SLG substrates. At higher temperatures, an increase in the resistivity takes place which is attributed to the annihilation of oxygen vacancies. The metallic-like of conductivity of the AZO film, at relatively higher temperatures, is concluded to be responsible for the transition of the conduction mechanism from diffusion to the thermionic emission mode.

In addition, the roles of UV absorption on bulk and nanoscale charge transport in AZO film are also studied. cAFM investigation shows an enhancement in the local electrical conductivity at grains after UV-exposure, which gives a smooth conduction in the film. In particular, it is observed that a smooth charge transport takes place not only in the bulk but also at the nanoscale. In fact, our experimental observation of enhancement in the photoresponsivity of an AZO/Si heterojunction diode in the visible range, after UV-exposure, manifests that UV absorption in the AZO overlayer should not be considered as an optical loss for the underlying absorber layer of a solar cell which is in contrary to the common belief.

Further, we demonstrate a first conclusive experimental evidence on nanoscale room temperature pseudoferroelectricity in preferentially oriented thin films of AZO. Local probe microscopic measurements like cAFM, KPFM, and PFM indicate that pseudoferroelectricity in AZO gives rise to the polarization-driven barrier formation, which in conjunction with the defect-induced electrostatic potential barrier matches well with the experimentally observed local band bending at the grain boundaries. The present observation of the polarization-driven potential barrier formation can be a benchmark for understanding the charge transport process across the GBs even in other pseudoferroelectric materials. However, more detail investigations are underway to address the local band bending at AZO grain boundaries in light of roles played by the type and nature of the grains and GBs.

The polarization in the AZO film opens a new way to control the charge transport. Thus, the tuning of the work function of an AZO film due to an applied electric field-induced charge doping (through the AFM tip) is performed using KPFM measurements, which corroborates well with the charge transport processes in the film, as is measured by contact-mode AFM. This is further substantiated by cAFM investigation, which shows a systematic change in the turn-on potential at a fixed point (as revealed from the local *I-V* characteristics), indicating a tunability in the work function of AZO. Our experimental findings are further confirmed by calculations based on first-principle density functional theory. Tuning the work function and in turn charge transport of AZO by injected charge (field-induced doping) has a direct application in different optoelectronic devices, which use such optically transparent contacts materials.

The growth and characterization of the main absorbing layer in the form of copper oxide layer is performed. In fact, XRD is used to evaluate the crystalline quality, dislocation density, and the ratio of $Cu_2O$:CuO crystalline phase present in two-types of Cu-O specimen. We observe the resistive switching behaviour in a relatively poor crystalline film, whereas it disappears for the one having a better crystalline quality. These observations are explained on the basis of structural defect-dependent variation in local carrier density and match well with the existing theoretical model based on conducting filament formation. It is found that the film deposited at 50° have a smooth charge transport and thus, it is used for the growth of full solar cell.

It order to get a better efficiency, the hole blocking nature of $TiO_2$ is also studied. In particular, we have studied the growth of ultrathin $TiO_2$ films at RT on Si and glass substrates by rf magnetron sputtering. It is found that the surface roughness increases with increasing growth angle. Using KPFM and temperature-dependent current-voltage characteristics, we have studied the charge transport across the $TiO_2$/Si heterojunction. In particular, KPFM result shows a variation in the work function at the $TiO_2$ surface. In addition, the temperature-dependent current-voltage characteristics show an intrinsic non-ideal hole blocking behavior in the $TiO_2$ layer. The measured barrier height is found to decrease with temperature, strongly suggesting its inhomogeneous nature at the interface. Further, in the context of the present thesis work, the hole blocking nature of $TiO_2$ is also confirmed by depositing it on a Cu-O thin film. As a matter of fact, this study is very important, in particular for solar cell applications, because the hole blocking nature of $TiO_2$ helps reducing the reverse leakage.

As a back contact, the growth and characterization of Mo thin film is also studied. The bottom electrode for the presently studied cell configuration is a Mo thin film. For a better efficiency, this electrode should have a high optical reflectivity and a good charge collection efficiency. Thus, in chapter 7, first we have optimized the growth of Mo thin films at various angles and studied their structural, electrical, and optical properties. It is observed that the resistivity increases with the increasing growth angle, and thus, the film deposited under normal incidence shows the lowest resistivity (~$10^{-6}$ Ω-cm) and the highest reflectivity (~65%), which are considered to be the optimised ones for the present architecture of the Cu-O based cell. Finally, based on our experimental findings on individual layers, we have constructed a full solar cell and demonstrated that the efficiency of a hole blocking copper oxide-based solar cell can be increased up to 5.2%. This is nine times higher compared to the one where $TiO_2$ has not been used as a sandwich layer between AZO and Cu-O.

In the last chapter, we provide a summary of the present thesis work, which deals with the growth and characterization of heterostructures towards constructing a copper oxide-based solar cell. In particular, we have studied the bulk as well as nanoscale charge transport properties across the used layers. For the optimization of growth, different thin films have been deposited over a large angular window (0°-80°). Following the same, structural, morphological, microstructural, compositional, and electrical properties of all the different layers have been critically evaluated. Finally, based on our experimental findings on individual layers, we have optimized the growth conditions at RT and thicknesses of different layers, viz. Mo, Cu-O, $TiO_2$, and ZnO:Al and constructed a fully functioning Cu-O based solar cell whose efficiency has been demonstrated to be 5.2%. This, to the best of our knowledge, is by far the highest among the Cu-O based solar cells, using the similar architecture and thus, shows an improvement by a factor of 2.5 times. We believe that the cell efficiency can be increased further by enabling more light trapping in the active layers through the use of textured substrates and/or individual layer.